TU Delft

Delft University of Technology

Reconstituting microtubule-actin coordination by cytolinkers

Alkemade, Celine

DOI
10.4233/uuid:209dce6d-bc95-43fd-9203-9204dd561684

Publication date
2021

Document Version
Final published version

Citation (APA)
Alkemade, C. (2021). *Reconstituting microtubule-actin coordination by cytolinkers*. [Dissertation (TU Delft), Delft University of Technology]. https://doi.org/10.4233/uuid:209dce6d-bc95-43fd-9203-9204dd561684

Important note
To cite this publication, please use the final published version (if applicable).
Please check the document version above.

Copyright
Other than for strictly personal use, it is not permitted to download, forward or distribute the text or part of it, without the consent of the author(s) and/or copyright holder(s), unless the work is under an open content license such as Creative Commons.

Takedown policy
Please contact us and provide details if you believe this document breaches copyrights.
We will remove access to the work immediately and investigate your claim.

This work is downloaded from Delft University of Technology.
For technical reasons the number of authors shown on this cover page is limited to a maximum of 10.

RECONSTITUTING MICROTUBULE-ACTIN COORDINATION BY CYTOLINKERS

RECONSTITUTING MICROTUBULE-ACTIN COORDINATION BY CYTOLINKERS

Proefschrift

ter verkrijging van de graad van doctor
aan de Technische Universiteit Delft,
op gezag van de Rector Magnificus prof. dr. ir. T. H. J. J. van der Hagen,
voorzitter van het College voor Promoties,
in het openbaar te verdedigen op
maandag 13 december 2021 om 15:00 uur

door

Celine ALKEMADE

Master of Science in Physics, Universiteit van Amsterdam, Nederland,
geboren te Utrecht.

Dit proefschrift is goedgekeurd door de promotoren.

Samenstelling promotiecommissie:

Rector Magnificus	voorzitter
Prof. dr. G.H. Koenderink	Technische Universiteit Delft, promotor
Prof. dr. M. Dogterom	Technische Universiteit Delft, promotor

Onafhankelijke leden:

Prof. dr. ir. S.J. Tans	Technische Universiteit Delft
Prof. dr. B.M. Mulder	AMOLF and Universiteit Utrecht
Prof. dr. A. Straube	University of Warwick (United Kingdom)
Dr. Z. Lánský	Institute of Biotechnology, BIOCEV (Czech Republic)
Dr. J.L. Henty-Ridilla	Upstate Medical University (USA)
Prof. dr. C. Dekker	Technische Universiteit Delft, reservelid

Keywords: Microtubules, actin filaments, cytoskeletal crosstalk, in vitro reconstitution, cytolinkers, Gas2L1, Shot

Printed by: Gildeprint

Cover design: Celine Alkemade

Copyright © 2021 by C. Alkemade

Casimir PhD Series, Delft-Leiden 2021-38

ISBN/EAN 978-94-6384-272-3

An electronic version of this dissertation is available at
http://repository.tudelft.nl/.

Dear Sir or Madam, will you read my book?
It took me years to write, will you take a look?

The Beatles

SUMMARY

The human body is composed of about $3-4\times10^{13}$ (30-40 trillion) cells [1]. These cells are all functioning consistently, and working elegantly together, to sustain the organism. Not only humans, but all other living things on earth (from plants to parrots) are composed of cells. Cells are the smallest living building blocks of plants and animals, and in fact some organisms are built from a single cell, such as bacteria.

To be able to sustain life, cells are dynamic entities that need to grow, divide, and interact with their environment. They accomplish this by a number of complex and dynamic processes. For instance, to perform vital functions such as cell division, a key factor of life, cells need to dramatically change their shape. In addition to shape changes, the internal cellular organization needs to be tightly controlled to properly function. For example, cells need to establish a front-back polarity to drive directional migration, like immune cells that hunt for intruders. Furthermore, the proper functioning of brain cells (also named neurons), which depends on finding and connecting to other neuronal cells, is closely related to their internal organization and cellular shape.

For cells, essentially small bags filled with proteins, to change their shape and internal organization, they depend on an internal filamentous scaffold named the cytoskeleton. Unlike the name might suggest, this 'cellular skeleton' is actually very dynamic, with constant assembly and disassembly of the constituent filaments and changes in filament organization. In addition to organizing the cellular interior, this cytoskeleton provides mechanical support for cells and allows them to generate forces.

Two main cytoskeletal components are microtubules and actin filaments. They are usually studied as separate systems, despite a growing body of work indicating their functions are closely intertwined and interdependent. This thesis studies how these two cytoskeletal components influence each other. More specifically, we focus on the question how actin and microtubules co-organize and affect each other via proteins that physically link them to each other, named cytolinkers.

To study how cytolinkers impact cytoskeletal crosstalk, we move away from the complex environment of the cell, where many other proteins are present and different processes take place. We took the cytoskeletal building blocks and cytolinking proteins out of the cell, rebuilt a cytoskeleton from these building blocks and characterized the effects of the cytolinkers on cytoskeletal co-organization by fluorescence microscopy. In addition to natural cytolinkers, we engineered our own cytolinkers to better understand how these proteins influence microtubule/actin coordination and in the absence of ill-defined regulatory processes in the cell. This isolated context is a powerful tool to study cellular functions, as the simplification allows us to tightly control all variables and identify the underlying mechanisms.

MAIN FINDINGS OF THIS THESIS

The work in this thesis uses a bottom-up (also referred to as an *in vitro*) approach to reconstitute the biological process of microtubule/actin coordination. Most experiments were performed using total internal reflection fluorescence (TIRF) microscopy to obtain high spatial and temporal resolution. We combine characterization of natural cytolinkers with studies on actin filament re-organization and on microtubule dynamics using simpler engineered cytolinkers. Obtaining a detailed understanding of how cytolinkers impact microtubule/actin crosstalk provides new insights in the question how actin filaments impact microtubule polymerization dynamics, which determines microtubule organization in the cell, and also in the question how microtubule growth impacts actin organization.

In Chapter 1, we provide a general introduction to the topic, our motivation, and the aim of this thesis. In Chapter 2, we explain the methods and materials used to perform the *in vitro* reconstitution studies.

Chapter 3 combines experimental and theoretical studies to show that microtubules can transport actin filaments bound to their growing end via an EB/cytolinker complex. We demonstrate that this new form of crosslinker-driven transport is governed by an interplay between an affinity-driven forward condensation force driving transport and an opposing friction force. We show that microtubule/actin coupling via passive crosslinkers is a new mechanism by which cytoskeletal elements can coordinate and exert forces on each other, in this case resulting in the transport of actin filaments.

In Chapter 4, *in vitro* reconstitution assays are combined with experiments in neurons to characterize the natural cytolinker Gas2Like1 (Gas2L1). We demonstrate that Gas2L1 is auto-inhibited, but that this autoinhibition is relieved when Gas2L1 can bind at microtubule/actin overlaps, providing an elegant mechanism to localize the cytolinker specifically to the place where it is required. In addition, we observe that in the presence of actin, Gas2L1 changes microtubule dynamics by greatly increasing the microtubule rescue rate. Furthermore, we show that in neurons, Gas2L1 primarily localizes to the actin cytoskeleton and functions as an actin stabilizer, which is spatially modulated by microtubules.

Since most cytolinking proteins contain two different binding domains to connect to microtubules (namely via EBs to the tip, or directly to the microtubule lattice), we wonder how the molecular anatomy of cytolinkers influences MT/actin crosstalk. Therefore, in Chapter 5, we use the *Drosophila* cytolinker Shot as a model protein and designed and engineered simpler cytolinkers where we controlled the cytoskeletal binding domains and the spacer domains. We specifically focused on cytoskeletal co-organization and on microtubule dynamics, and found that linking actin filaments to the growing microtubule plus-end resulted in dynamic actin re-organization. Conversely, linking actin filaments to the microtubule lattice resulted in longer-lived actin re-organization, and more persistent MT growth with many MT rescue events.

In Chapter 6, we present a new method to study microtubule/actin co-organization in 3D cell-sized compartments based on water-in-oil emulsion droplets. Whereas all reconstitution experiments in previous chapters were performed in quasi-2D to enable high-resolution imaging by TIRF microscopy, this chapter shows that centrosome-nucleated dynamic microtubules can be made to interact with actin filaments in a 3D spher-

ical cell-sized container via engineered cytolinker TipAct. In addition, we provide detailed protocols and discuss optimization steps required in order to build these more complex *in vitro* model systems of cytoskeletal interactions.

The work in this thesis shows the power of *in vitro* reconstitution assays to study microtubule/actin crosstalk by cytolinkers. We show that a new mechanism of microtubule/actin coordination (namely actin transport) can be understood from studying the underlying molecular interactions of the cytolinker. In addition, we demonstrate that cytolinker regulation in neurons (namely Gas2L1) can be understood from *in vitro* characterization. Furthermore, we show that by modifying engineered cytolinkers, we can start to understand how the molecular anatomy of natural cytolinkers impacts microtubule/actin coordination. And finally, we demonstrate that reconstitution assays can also be used to study microtubule/actin coordination in cell-like geometries. This thesis can serve as a basis for future studies to unravel microtubule/actin coordination by cytolinkers. The final Chapter 7 of this thesis presents a brief outline of some examples for future research directions, illustrated by proof-of-concept data.

CONTENTS

1 Introduction **1**
- 1.1 The cytoskeleton . . . 2
  - 1.1.1 Actin filaments . . . 2
  - 1.1.2 Microtubules . . . 3
- 1.2 Cytoskeletal crosstalk . . . 5
  - 1.2.1 Mechanisms for MT/actin crosstalk . . . 5
  - 1.2.2 Cytolinker-mediated crosstalk . . . 8
- 1.3 Aim of this thesis . . . 11
- 1.4 Thesis outline . . . 12

2 Material and Methods **15**
- 2.1 General experimental procedures . . . 16
- 2.2 Flow cell preparation and surface passivation . . . 17
- 2.3 Buffer conditions . . . 18
- 2.4 Proteins used in this thesis . . . 18
- 2.5 Total internal reflection fluorescence (TIRF) microscopy . . . 22
- 2.6 Data analysis . . . 22

3 Crosslinkers at growing microtubule ends drive actin transport **25**
- 3.1 Introduction . . . 26
- 3.2 Results . . . 27
  - 3.2.1 Growing microtubules plus ends can transport actin filaments . . . 27
  - 3.2.2 Simulations reproduce microtubule-mediated actin transport . . . 30
  - 3.2.3 Theory for crosslinker-driven transport and force generation . . . 31
  - 3.2.4 Simulations and theory correctly predict actin transport times . . . 35
  - 3.2.5 Crosslinker binding creates a significant condensation force . . . 39
- 3.3 Discussion . . . 39
- 3.4 Supplemental Information . . . 42
  - 3.4.1 Material and methods . . . 42
  - 3.4.2 Supplementary figures . . . 44
  - 3.4.3 Supplementary tables . . . 55
  - 3.4.4 SI Appendix . . . 56

4 Actin-microtubule coordination in axons by the cytolinker Gas2L1 **73**
- 4.1 Introduction . . . 74
- 4.2 Results . . . 75
  - 4.2.1 Gas2L1 affects axon branching and outgrowth in developing neurons . . . 75
  - 4.2.2 Gas2L1 specifically localizes to actin-MT overlaps in *in vitro* reconstitution assays . . . 77

4.2.3 Autoinhibition of Gas2L1 is a result of the interaction between the CH domain and MT-binding tail . . . 81
4.2.4 The Gas2L1 Tail fragment contains at least two MT binding regions . 82
4.2.5 Gas2L1 localizes to neuronal F-actin and regulates axon development by influencing actin stability . . . 84
4.2.6 MT behaviour appears unaffected in neurons depleted of Gas2L1 but is affected by Gas2L1 *in vitro* . . . 88
4.2.7 MTs guide Gas2L1 activity in neurons . . . 91
4.3 Discussion . . . 92
4.4 Supplemental Information . . . 97
4.4.1 Materials & Methods . . . 97
4.4.2 Supplemental Figures . . . 104

5 Role molecular anatomy of cytolinkers on actin/MT co-organization 117
5.1 Introduction . . . 118
5.2 Results . . . 119
5.2.1 Engineered cytolinkers . . . 119
5.2.2 Actin slows down microtubule growth . . . 121
5.2.3 Shot localizes to MT/actin overlaps and promotes rescues . . . 124
5.2.4 Linking F-actin to microtubule plus-ends via TipAct . . . 128
5.2.5 Linking F-actin to the microtubule lattice via TipActLong . . . 132
5.3 Discussion . . . 144
5.4 Supplemental Information . . . 149
5.4.1 Materials and methods . . . 149
5.4.2 Supplemental figures . . . 152

6 Reconstituting dynamic MT/actin co-organization in droplets 167
6.1 Introduction . . . 168
6.2 Materials . . . 170
6.2.1 Buffer conditions . . . 170
6.2.2 Proteins . . . 170
6.2.3 Lipids, oils and surfactants . . . 171
6.2.4 Materials . . . 171
6.3 MT asters in emulsion droplets with end-binding protein comets . . . 171
6.3.1 Lipid mix preparation . . . 172
6.3.2 Reaction mix preparation . . . 172
6.3.3 Emulsion droplets . . . 172
6.3.4 Microfluidic chips . . . 173
6.3.5 Microfluidic setup . . . 175
6.3.6 Coverslip silanization with Rain-X . . . 175
6.3.7 PDMS well preparation . . . 176
6.3.8 Rhodamine tubulin versus SiR-tubulin . . . 176
6.3.9 Imaging and data analysis . . . 177

6.4 Increasing complexity: adding cytolinkers and actin filaments 178
6.4.1 Actin mix. 178
6.4.2 Final reaction mix 180
6.4.3 Imaging 180
6.5 Supplemental Notes 182

7 Outlook **187**

Bibliography **193**

Samenvatting **213**

Curriculum Vitæ **217**

List of Publications **219**

Acknowledgements **221**

1

INTRODUCTION

It's like a jungle sometimes, it makes me wonder,
How I keep from going under.

Grandmaster Flash

Cells are the smallest living building blocks of life. To be able to sustain life by growing and proliferating, cells require an internal biopolymer network, named the cytoskeleton. This cytoskeleton organizes their internal structure, mechanically supports them, and allows them to generate forces. Two main cytoskeletal components are microtubules and actin filaments. In this thesis, we study how these two components co-organize and affect each other via cytolinkers: proteins that physically link them together. This chapter provides a general introduction into actin filaments and microtubules. Next, we focus on the mechanisms by which actin and microtubules coordinate with each other. We focus in particular on actin-microtubule crosstalk that is mediated by cytolinkers. Finally, we describe the aim of this thesis and an outline of the further chapters.

1

1.1. THE CYTOSKELETON

The smallest unit of life is a cell, which is an incredibly complex container inside of which dynamic processes take place continuously. A large number of cellular activities that are essential for sustaining life, such as cell division and motility, depend on an internal filamentous scaffold named the cytoskeleton. Unlike the name might suggest, this 'cellular skeleton' is actually very dynamic, with constant assembly and disassembly of the constituent filaments and changes in filament organization. By controlling these filamentous biopolymers, cells are able to change their shape while maintaining mechanical integrity and organize their interior and establish asymmetric organizations (e.g., front-back polarity to drive directional migration).

The cytoskeleton of animal cells consists of three filamentous components, namely microtubules, actin filaments, and intermediate filaments [2]. All three contribute to the mechanical rigidity of cells and the internal organization of the cytoplasm. Actin filaments and microtubules are more dynamic than intermediate filaments, and can also actively generate forces; this may explain why they are the most studied components of the cytoskeleton. They are usually studied individually, despite a growing body of work indicating their functions are closely intertwined and interdependent [2–9].

In the following sections, we summarize the main properties of actin filaments and microtubules, the two cytoskeletal components we focus on in this thesis. Next, we review microtubule/actin-crosstalk, specifically focussing on crosstalk via cytolinking proteins. And finally, we provide the aim and outline of the thesis.

1.1.1. ACTIN FILAMENTS

Actin filaments (also referred to as F-actin) are structurally polar filaments with two distinct ends referred to as the plus (or barbed) and minus (or pointed) end. They assemble via longitudinal addition of actin monomers (also referred to as G-actin, globular actin), as is illustrated in Fig. 1.1A(top), and form thin double-stranded helical polymers. Although actin filaments can form in the absence of the chemical fuel ATP (adenosine triphosphate), the presence of ATP enables filament treadmilling behavior [10]. Since the ATP on newly added actin subunits hydrolyzes, this maintains a difference between the fast-growing plus ends and slowly-growing minus ends, and effectively subunits are added on one end and lost on the other end (Fig. 1.1A, bottom).

The assembly of actin filaments is a process that is rate-limited by the formation of dimer and trimers of G-actin in absence of any cofactors [11–13]. However, after the formation of these thermodynamically unfavorable nuclei, the filaments grow rapidly with an elongation rate that is directly proportional to the monomer concentration [14]. This allows cells to regulate actin polymerization in space and time using accessory proteins that alter the dynamics, including capping proteins, monomer-binding proteins such as profilin, filament-severing proteins such as cofilin, and actin nucleators and polymerizers such as Arp2/3, formins and APC (reviewed in [15]).

In cells, dynamic actin filaments are often organized into higher order structures, such as bundles or networks, to perform their function (Fig. 1.1C) [15]. The organization of these actin structures is also dependent on accessory proteins. For example, actin-binding proteins such as α-actinin and fascin connect filaments to form networks and bundles. In addition, contractile forces that reorganize and reinforce these structures

are generated by myosin motor proteins. Typical examples of these actin structures in animal cells are for instance the actomyosin cortex (a thin actin network right underneath the cell membrane), stress fibers (actin filaments bundled into thick fibers), cytokinetic rings (membrane-anchored ring-shaped actin bundles that drive cell division), and complex networks such as the lamelipodium (a dense actin meshwork that drives cell migration). These organized actin structures are important for reinforcing the membrane and actively driving cell migration and cytokinesis.

1.1.2. MICROTUBULES

Microtubules are also structurally polar filaments that self-assemble via longitudinal addition of tubulin dimers in the presence of the chemical fuel GTP (guanosine triphosphate). We term the linear arrays of these tubulin dimers protofilaments, of which usually 13 associate laterally to form hollow tubes, as illustrated in Fig. 1.1B. Microtubules are thicker and stiffer than actin filaments. Furthermore, microtubules have the ability to switch between growing and shrinking phases, a process known as 'dynamic instability' [16, 17]. The switching from a growing to a shrinking state is known as a catastrophe event. Conversely, the switching from a shrinking to a growing state is known as a rescue event. The switching behaviour, and thus the addition or loss of tubulin subunits, is a stochastic process that depends on the nucleotide-state of the subunits [18]. GTP-bound tubulin dimers favour longitudinally binding [19], promoting the correct incorporation of the tubulin dimer into the microtubule lattice at the ends. Once bound, GTP hydrolysis takes place, causing a transition from GTP- to GDP-bound tubulin for dimers further behind the tip region. However, this transition occurs with a delay, causing a so-called GTP-cap region at the growing microtubule end [20].

In many cells, microtubules are anchored with their minus ends to an organizing structure such as the centrosome. This leads to a radial organization of microtubules, with their plus ends pointing towards the cell periphery (Fig. 1.1C). The structural organization of microtubules is important to perform their functions, such as serving as molecular tracks for motor proteins to transport a variety of cargoes, segregating chromosomes during cell division [21], and maintaining front-rear polarity in migrating cells [5].

Dynamic instability is the basis for remodelling the microtubule network in cells. In addition, dynamic instability can serve as a platform for force generation, since microtubules reaching the cell front can exert pushing forces during growth, but also, when transiently anchored to the cortex, exert pulling forces during depolymerization. Thus it is not surprising the cell uses a plethora of proteins to regulate microtubule dynamics. Via either direct interactions or through other proteins, Microtubule Associated Proteins (MAPs) are able to alter various parameters of microtubule dynamics. A specific subclass of MAPs are the plus-end tracking proteins (+TIPs), that specifically recognize and bind to the growing microtubule end [22]. An important +TIP is the conserved family of End Binding (EB) proteins, that contains three main members in mammals: EB1, EB2, and EB3. It was shown that EB1 and EB3 increase microtubule growth velocity, both *in vitro* and *in vivo* [23]. In addition, EB proteins increase the catastrophe rate *in vitro* by accelerating the GTP-to-GDP transition, which destabilizes the GTP-cap [24–26]. Interestingly, when EB1 and EB3 are depleted in cells, an increase of catastrophe rate was

1

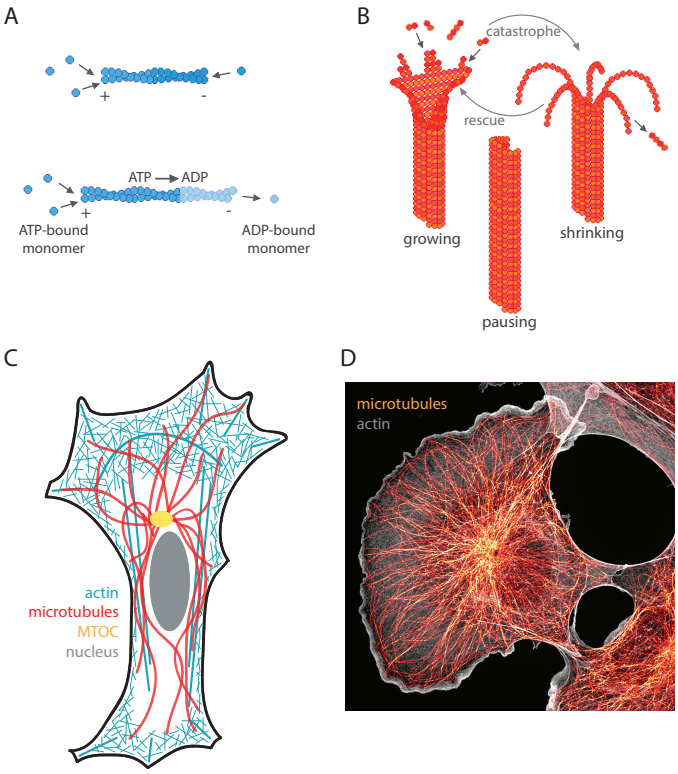

Figure 1.1: **Polymerization dynamics and cellular organization of actin filaments and microtubules. (A)** Actin filament polymerization. After the rate-limiting nucleation step, actin filaments can grow from both ends, although in the presence of ATP faster addition of G-actin subunits occurs at the barbed (+) end than at the pointed (-) end (top). At steady-state, polymerization occurs at the barbed (+) end, while dissociation of ADP-bound G-actin occurs at the minus (-) ends, leading to filament treadmilling. **(B)** Microtubule dynamic instability. Depicted are the three phases between which the microtubule can switch. During the growing phase, GTP-bound tubulin dimers are added, while GDP-bound tubulins dissociate during the shrinking phase. We name a microtubule pausing, when neither growing nor shrinking occurs. Switching between the growing and shrinking phase is called 'catastrophe', and the converse switch is called 'rescue', as indicated. **(C)** Schematic depiction of the cellular organization of actin filaments (blue) and microtubules (red) in a typical mesenchymal cell adhered on a rigid 2D-substrate in interphase. Actin usually forms a thin cortex, stress fibers and complex networks. At the protrusive front of the cell (upper side in the drawing), actin forms a branched network, while the actin at the cell's rear is contractile. Microtubules often grow with the minus-ends attached to a microtubule organizing center (MTOC). **(D)** Super-resolution spinning disk image of fibroblast-like COS cells labelled for actin (grey) and microtubules (orange), illustrating the radial organization of microtubules and the denser actin cortex at the cell membrane. Panel C adapted from [2]. Panel D credits to Christophe Leterrier (NeuroCyto, INP, CNRS-Aix Marseille University, France).

observed [24]. The different effect of EB on microtubule catastrophes *in vitro* and *in vivo* is probably a consequence of other +TIPs that are recruited to the microtubule plus ends by EB *in vivo* [27]. Typically, plus-end tracking proteins can bind EB via a so-called 'SxIP motif', a binding domain that recognizes EBs [22]. In addition to MAPs, cells can modulate microtubule dynamics by regulation of β-tubulin isotype expression levels or post-translational modifications [28].

1.2. CYTOSKELETAL CROSSTALK

In the past decades, the behaviour and regulation of the actin and microtubule cytoskeletons have been studied extensively in a variety of cellular contexts. However, it is becoming increasingly clear that interactions between the two cytoskeletal components are essential for many cellular functions [3, 5–7]. In this section, we briefly review the different mechanisms underlying MT/actin-crosstalk. For more details, we refer the reader to several recent reviews [3, 4, 9]. We specifically focus on the proteins that are involved in physically linking microtubules to actin filaments, which are often referred to in the literature as cytolinkers.

1.2.1. MECHANISMS FOR MT/ACTIN CROSSTALK

The coordination between the actin and microtubule cytoskeletal systems can be accomplished through different mechanisms, which we classify under three main categories: (i) coordination via biochemical signalling pathways; (ii) coordination via steric or mechanical interaction; and (iii) coordination via physical crosslinking, as is also depicted in Fig. 1.2. Through these mechanisms, MT/actin crosstalk can cause the filaments to affect each other's polymerization dynamics and/or network organization.

MT/actin crosstalk via signalling pathways is enabled via shared regulators, of which Rho-GTPases play an important role (Fig. 1.2A). Small GTPases, such as RhoA, Rac1 and Cdc42, function as switches by cycling through an active (GTP-bound) phase and an inactive (GDP-bound) phase. The switching is regulated by GTPase-activating proteins (GAPs) for deactivation, by guanine-nucleotide exchange factors (GEFs) for re-activation, and by guanosine dissociation inhibitors (GDIs). Both actin and microtubules are regulated by GTPases, as depicted in Fig. 1.2A. For actin, active GTPases promote actin polymerization (via either formin or Arp2/3) and actin organization by stimulating myosin contractile activity. For microtubules, GTPases influence microtubule dynamics via MAPs (reviewed in [29]): they recruit formin mDia1 and IQGAP that, together with MAPs such as APC, CLIP-170 and CLASP, capture and stabilize microtubules; or they de-activate MT-destabilizing factors such as stathmin, thereby again stabilizing microtubules. Interestingly, stabilized microtubules collect GEFs along their lattice, thereby indirectly promoting GTPase inactivity, and thus generating a negative feedback loop on their own stability. Upon microtubule depolymerization, these GEFs are released again [30] and are able to activate GTPases again, generating a positive feedback loop on microtubule stability. Moreover, microtubule depolymerization in cells stimulates actin-myosin contractility. Thus, although actin organization and polymerization are mostly regulated by GTPases, microtubules have a reciprocal relationship with these GTPases, consequently coordinating actin. Conversely, since microtubule-mediated GTPase-regulation is de-

pendent on microtubule dynamics, actin can influence this regulation by affecting microtubule dynamics, closing the crosstalk-circle.

Another, more recent, identification of MT/actin crosstalk via shared regulators is based on profilin [31, 32]. Although mainly associated with actin polymerization due to its G-actin-sequestering capabilities, it was recently shown that profilin can directly bind microtubules [33], and speed up microtubule growth in neuronal cells [34]. Since there is no evidence that profilin can bind actin and microtubules simultaneously, which would allow it to perform as a cytolinker, profilin-mediated crosstalk apparently arises from competition between actin and microtubules for profilin binding [33].

Microtubule-actin coordination via steric or mechanical interactions is another mechanisms through which actin can influence microtubule dynamics. More specifically, a dense actin network can function as a barrier, thereby sterically hindering microtubule growth (Fig. 1.2B, left). *In vitro* experiments have shown that a physical barrier impedes microtubule growth, subsequently promoting catastrophes [35]. That actin networks can indeed similarly function as a barrier was shown in a recent *in vitro* study, where an Arp2/3-crosslinked actin network decreased average microtubule length and growth velocity [36]. In fact, Colin *et al* observed that an entangled, thus non-crosslinked, actin network did not alter microtubule growth dynamics, suggesting that actin network properties are important to function as a barrier. In addition, another study demonstrated that with increasing actin concentration, the number of microtubules grown from a centrosome decreased [37]. As a consequence, microtubules might be prevented to reach the membrane and might be blocked from membrane anchoring, from delivering cargoes, and from exerting protrusive forces.

Besides influencing microtubule dynamics, actin can also affect microtubule organization via steric interactions. For example, retrograde flows of actin, generated by both actin polymerization and myosin-driven network contraction, can translocate micro-

Figure 1.2 *(facing page)*: **Mechanisms of actin-microtubule crosstalk. (A)** Crosstalk via shared regulators of actin and microtubule dynamics. Members of the RHO family of small GTPases regulate both actin and microtubule dynamics via their interaction with both actin and microtubule-associated proteins. In addition, microtubules may contribute to the local regulation of actin dynamics via their influence on RHO GTPase activity. **(B)** Crosstalk via steric or mechanical interactions. Actin can act as a physical barrier for microtubule growth (left): the actin cortex may act as a physical barrier that prevents growing microtubules from reaching the plasma membrane by blocking growth and inducing catastrophes. Buckling and breaking of microtubules by actin flows (middle): retrograde actin flows, generated by actin polymerization and network contractions, can buckle and break microtubules. Mechanical cooperation in membrane protrusions (right): stiff microtubules may provide mechanical support against membrane retraction in events of membrane protrusion driven by actin polymerization. **(C)** Crosstalk by physical crosslinking, via cytolinking proteins, motors, or cytolinking complexes. Guidance of microtubule growth (left): actin–microtubule crosslinking proteins that associate with growing microtubule ends via microtubule plus-end trackers (+TIPs) provide dynamic links between microtubules and actin bundles, which can redirect microtubule growth along actin bundles. Anchoring and stabilization of microtubule ends (middle): protein complexes associated with cortical actin networks can capture both the plus and minus ends of microtubules, leading to stable connections between the two cytoskeletal systems. In the example shown, a plus end is stabilized by a complex involving a motor protein, but the composition of the complex may vary depending on the context. Nucleation of actin filaments at microtubule ends (right): actin nucleation factors such as formins may associate with growing microtubule ends, which leads to microtubule-mediated local stimulation of actin polymerization. GAP, GTPase-activating protein; GEF, guanine nucleotide exchange factor; MAP, microtubule-associated protein. Figure adapted from [3].

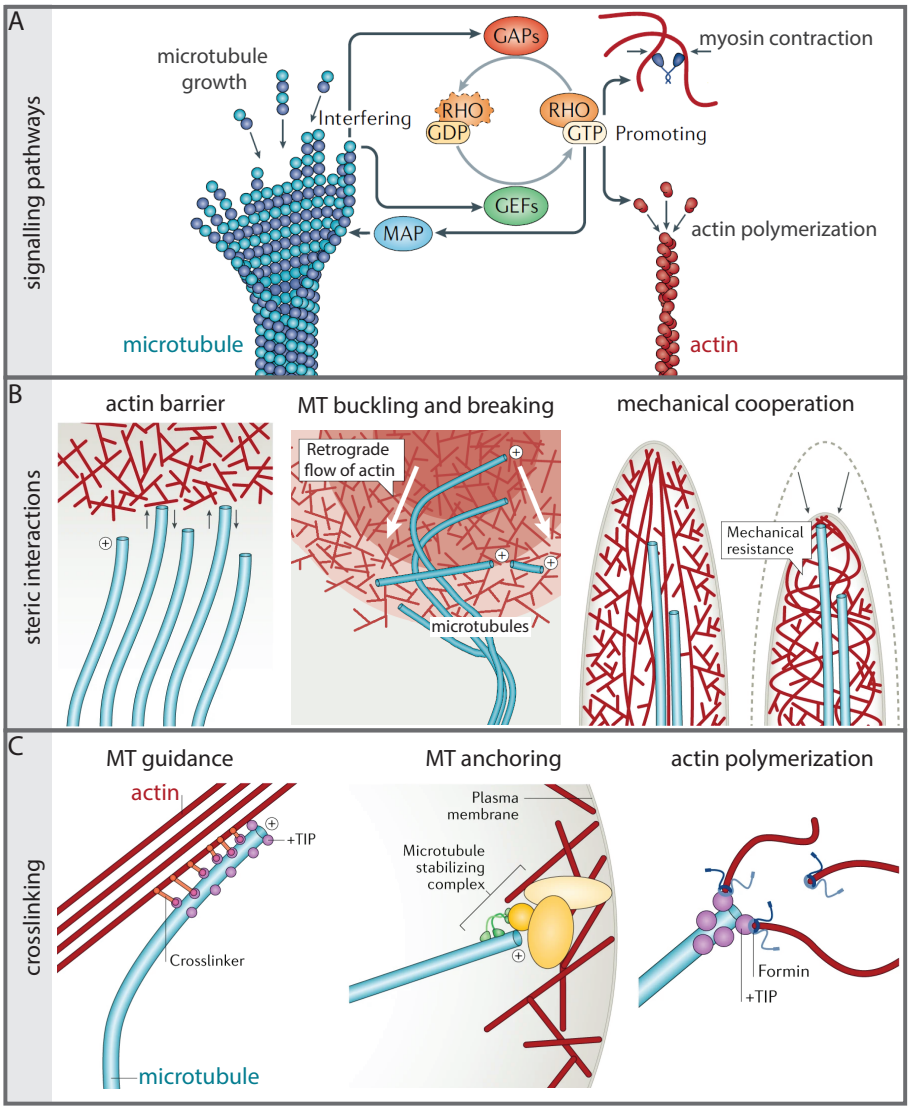
A
signalling pathways
microtubule growth
Interfering
GAPs
RHO GDP
RHO GTP
Promoting
myosin contraction
GEFs
MAP
actin polymerization
microtubule
actin
B
steric interactions
actin barrier
MT buckling and breaking
mechanical cooperation
Retrograde flow of actin
microtubules
Mechanical resistance
C
crosslinking
MT guidance
MT anchoring
actin polymerization
actin
+TIP
Crosslinker
microtubule
Plasma membrane
Microtubule stabilizing complex
Formin
+TIP

tubules (Fig. 1.2B, middle). A well-know example is a migrating cell, where retrograde flows in the lamellipodium cause rearward movement of microtubules [38, 39] and can buckle and break microtubules [40, 41]. Furthermore, in neurons, translocating actin arcs in the neuronal growth cone push microtubules into densely-packed bundles [42], while actin-dependent cytoplasmic flows towards neurite tips transiently widen neurite shafts to create more space for microtubules to grow into and deliver axon-promoting proteins [43]. In addition, actin network organization and contractions in oocytes drive microtubule spindle translocation towards the cell cortex [44–47], although direct linking of actin to microtubules could be at play here too.

Conversely, microtubules can also affect actin organization via steric interactions, namely via mechanical cooperation (Fig. 1.2B, right). It was shown with *in vitro* rheology experiments that microtubules added to a crosslinked actin network enhance its nonlinear stiffening in response to an applied mechanical stress [48]. Since microtubules are stiff polymers, they are able to bear large compressive loads [49–51], which is thought to help reinforcing the actin network at cell protrusions. This mechanical support leads to cooperative behaviour of the actin and microtubule cytoskeletons in cell motility. By providing mechanical resistance, microtubules can counteract membrane retractions and thus maintain actin-driven protrusions [52].

1.2.2. CYTOLINKER-MEDIATED CROSSTALK

While microtubule-actin coordination via signalling pathways or via steric interactions does (in principle) not require mechanical coupling of the two cytoskeletal systems, many known instances of MT/actin crosstalk in cells are mediated via physical linking (Fig. 1.2C). In this section, we focus on the different proteins or protein complexes that accomplish the physical crosslinking, namely cytolinkers. In addition to potentially further enhancing the effects of microtubule-actin coordination as described above (Fig. 1.2A,B), physical linking allows three new mechanisms for crosstalk, as depicted in Fig. 1.2C. Via cytolinkers, actin bundles can guide microtubule growth (Fig. 1.2C, left), microtubule growth can be stabilized by capturing microtubule ends and anchoring them to actin networks (Fig. 1.2C, middle), or actin filaments can be polymerized locally at the growing microtubule end (Fig. 1.2C, right).

In recent years, many proteins have been identified to function as cytolinkers. Here, we discuss three separate ways to physically link actin and microtubules, namely via: (i) direct linking by passive cytolinkers; (ii) linking by motor proteins; and (iii) linking by multiple proteins, forming cytolinking complexes. Although some cytolinkers form complexes with EBs to localize to the growing microtubule end, we classify them as passive cytolinkers that are specific for microtubule tips rather than lattices.

CYTOLINKERS

Spectraplakins

There are many protein families that can function as cytolinkers, although it is not yet understood what the different effects of these cytolinkers are on microtubule-actin coordination. Maybe the proteins most studied in this context are the spectraplakins, a family of giant proteins that can bind both actin filaments and microtubules [53, 54]. Mammals contain two spectraplakin genes: microtubule-actin crosslinking factor (MACF1,

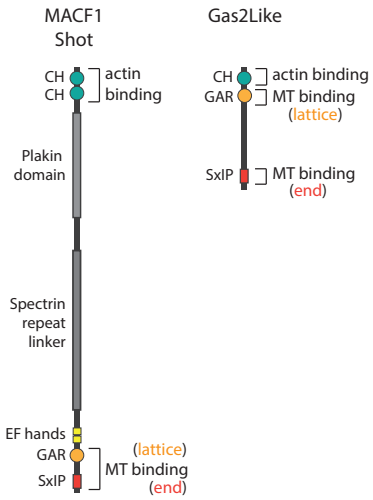

Figure 1.3: **Cytolinker domain structures.** Protein domains for spectraplakins like MACF1 and Shot (left) and for Gas2Like cytolinkers (right). Indicated are the actin- and microtubule-binding domains. CH, calponin-homology; GAR, GAS2-related.

also known as ACF7) and Dystonin (also known as DST or BPAG1). However, a large variety of isoforms increase the functional diversity by using alternative splicing and different promotors (i.a. reviewed in [55]), although the tissue distribution for each isoform remains largely unknown. The domain structure of spectraplakins (Fig. 1.3) is conserved among different species, and includes: an N-terminal region for actin binding, that usually contains two calponin homology (CH) domains; a plakin domain that acts as scaffold for many protein-protein interactions; a domain with multiple spectrin repeats, which acts as a flexible linker domain and as scaffold for signalling pathway interactions; C-terminal region for microtubule binding, containing two EF-hand motifs, a GAR domain and GSR repeats, and a SxIP motif. Although the predominant domain for microtubule lattice binding is the GAR domain [56], spectraplakins like MACF1 (and its *Drosophila* homolog Shot) also contain a SxIP motif that enables them to track the growing microtubule end tracking via EB proteins [57].

The spectraplakin MACF1 has been identified to play a crucial role in a number of cellular processes, such as cell migration, cell-cell connections, vesicular transport, cell polarity and cell division. During cell migration, MACF1 is found at growing microtubule ends and enriched at the leading edge [58–60]. Without MACF1, microtubules are less stable and the microtubule network is disorganized with microtubules oriented in random directions and dissociated from actin bundles. In this context, it was shown that MACF1 plays a key role in guiding microtubules along actin bundles (Fig. 1.2C, left) towards focal adhesions, where motor proteins deliver factors for focal adhesion turnover [60]. In addition, MACF1 plays a role in microtubule anchoring (Fig. 1.2C, middle) at the leading edge, where it is recruited to the membrane via ELMO and promotes microtubule plus-end capture and stabilization, which in turn promotes membrane protrusions via Rac activation [61]. Furthermore, together with CAMSAP3 (also called Nezha),

MACF1 anchors noncentrosomal microtubule minus-ends to actin filaments to keep microtubule orientation perpendicular to the cell edge [62].

Besides cell migration, an important role of MACF1 was also identified in the context of tight junctions that hold epithelial cells together, since MACF1 knockout in Caco2 (colorectal adenocarcinoma) epithelial cells caused microtubules to dissociate from these junctions, resulting in junction stabilization and impaired wound closure [63]. Using a MACF1 mutant where microtubule binding was inhibited by mutations in the GAR domain, it was shown that microtubule lattice binding is important to restore the junction dynamics. In addition, MACF1 is important to keep the cytoskeleton organized during cell division, although this function seems cell-specific. For example, in osteoblastic cells, MACF1 knockdown inhibits cell proliferation and induces MTOC disappearance [64], and in neurons, MACF1 is involved in regulating centrosome movement [65]. In contrast, for epidermal or endodermal cells, the suppression of MACF1 had no impact on cell proliferation [59, 60, 66].

In addition to MACF1, another well-studied spectraplakin is the *Drosophila* spectraplakin named Short stop (Shot, also known as Kakapo) [54, 67]. Since it is the only spectraplakin in *Drosophila*, it is involved in many functions. Typical examples are studies of Shot in neurons, where it plays a key role in axon and dendrite growth. It was shown that Shot is involved in microtubule guidance (Fig. 1.2C, left), where Shot's linkage to actin is essential [68, 69]. In addition, Shot is involved in microtubule stability, since Shot helps stabilize microtubules against drug-induced depolymerization, but also promotes microtubule growth, since microtubule growth in Shot-deficient neurons was drastically stopped [70]. Earlier studies had shown that Shot's impact on microtubule growth velocity in neurons depends on its ability to bind EB1 [71]. In addition to neurons, recent studies show that Shot also play important roles in other cellular contexts. For example at the ovary ring canals, where Shot controls the transport direction of cytoplasmic materials that are required for oocyte growth from the sister cells to the oocyte [72].

With affinities for microtubule lattices, microtubule ends and actin filaments, the binding activity of Shot/MACF1 must be tightly controlled. One way for the cell to control microtubule/actin linking is via phosphorylation. In MACF1, two sites have been identified to play important roles: (i) near the second CH domain, which is required for microtubule targeting to focal adhesions [73]; and (ii) at the C-terminus, which results in MACF1 detaching from microtubules [65, 66]. In addition, it was shown for Dystonin that Ca^{2+}-binding to the EF-hand motifs turns it from an EB1-binding mode towards microtubule lattice binding [74]. Although it is not clear whether Shot/MACF1's EF-hands are also regulated by Ca^{2+}, they can be involved in another regulatory mechanism, namely auto-inhibition. Applewhite *et al* showed that Shot is in a closed conformation due to association of the EF-hand motif domain with the actin binding domain [75]. According to their model, when Shot is in this closed conformation, it is recruited and following growing microtubule plus ends. However, Shot opens once it binds to both the microtubule lattice and actin simultaneously, thus at the cell cortex.

Other cytolinkers

In addition to spectraplakins, another family of cytolinking proteins has been identified, namely the growth-arrest-specific 2 (GAS2) family [76] (Fig. 1.3). Similar to spectraplakins, the GAS2 proteins also contain an actin binding (CH) domain and a micro-

tubule binding (GAR) domain, but they are much smaller than spectraplakins. There are four members (Gas2, Gas2Like1, Gas2Like2, and Gas2Like3) and a few isoforms, and they mostly differ structurally in containing no or multiple domains for End Binding (EB) recognition that allows microtubule plus end tracking. The members are expressed in a wide variety of cell types, and the different isoforms have also been found at different cellular locations, sometimes predominantly along microtubules, while others are co-localizing to actin filaments, near the plasma membrane or at the nucleus (reviewed in [77]). In U2OS osteosarcoma cells, it was shown that Gas2Like proteins play an important role in microtubule guidance along actin bundles (Fig. 1.2C, left), which depended on EB binding. Similar to spectraplakins, *Drosophila* express only a single member of the GAS2 family, namely 'Pigs'. Pigs is mostly found tracking microtubule plus ends, and, similar to Shot, an auto-inhibitory model was suggested because of a mutual inhibitory relationship between the actin binding CH-domain and the microtubule lattice binding GAR-domain [78].

Besides the spectraplakin and GAS2 family of proteins, the list of cytolinkers is steadily increasing. For example members of the formin family, proteins that are classically characterized as actin polymerizing proteins, since they nucleate and processively elongate (unbranched) actin filaments [79], have also been identified to directly bind microtubules and influence their dynamics [80–82]. Other proteins that can act as cytolinkers include (but are not limited to) CLASP, Tau, MAP2C, Plectin, Doublecortin, Pod1, Drebrin, NAV1, XMPA215, MISP, anillin, moesin, and septin. Which cytolinkers are involved in a given biological process is often context-specific. For details, we refer the reader to Ref. [3, 6].

CYTOLINKING MOTORS

In addition to passive cytolinkers, microtubules and actin can be linked via motor proteins. For example, Myosin X binds both F-actin and microtubules simultaneously and thus contributes to mitotic spindle positioning [83]. Furthermore, cytolinking complexes that involve motors can perform active cytolinking, such as the dynein/dynactin-complex [84], which is involved in microtubule anchoring (Fig. 1.2C, middle), or complexes involving Bim1/Kar9/Myo2 in budding yeast [85, 86].

CYTOLINKING COMPLEXES

Finally, linking microtubules and actin can also occur via multiple proteins that form cytolinking complexes. For example, a CLIP170/mDia complex binds microtubule plus-ends through an EB-CLIP170 interaction, while mDia can nucleate and elongate actin filaments [87]. This causes localized actin nucleation at the growing microtubule end (Fig. 1.2C, right). Also other protein complexes at microtubule ends, involving for instance APC [88], have been shown to couple microtubule growth to actin nucleation.

1.3. AIM OF THIS THESIS

As the section above already indicates, the cell possesses many different cytolinkers to physically link actin and microtubules. This probably allows the cell to control the MT/actin cytoskeletons both spatially and temporally, depending on the cellular context. Although we can distinguish a few general mechanisms for MT/actin crosstalk via

cytolinkers (Fig. 1.2C), it remains difficult to understand how these cytolinking components influence MT/actin crosstalk. The functional analysis of a specific cytolinker is complicated by the redundancy of its function with other cytolinkers. For example in *Drosophila*, where cytolinkers Shot and Tau functionally overlap in stabilizing microtubules [67, 71, 89].

In addition to overlapping functions of cytolinkers, often multiple mechanisms for MT/actin crosstalk are at play too. Although we subdivided the different mechanisms for MT/actin crosstalk, that does not mean that these mechanisms are also divided in the cell. In fact, there are many cellular contexts known where a combination of different mechanisms is required. For example, the formation of primary lumen during subcellular branching (a developmental process where single cells form branched structures such as neurons or cells of the respiratory system), where actin and microtubules require linking via Shot [89, 90]. The physical linkage results in both cytoskeletons being properly organized, where microtubules serve as tracks to deliver membrane material and provide mechanical support (Fig. 1.2B, right) to the actin-driven protrusions (Fig. 1.2C, right) [91]. The complexity to investigate MT/actin crosstalk in cells is also illustrated by a study on Myosin IIA in cell migration [39]. It was shown that MyoIIA negatively regulates cell migration through involvement in actin contractions that block microtubules from reaching the membrane. Interestingly, both cells without MyoIIA and cells where MyoIIA activivity was inhibited by blebbistatin displayed more stable microtubules, raising the question whether this is a direct effect of MyoIIA on microtubule stability, or whether this stability arises from more microtubules reaching the membrane and thus interacting with stabilizing anchors.

The overlapping functions of different cytolinkers and the combination of crosstalk mechanisms make it difficult to understand and study the underlying mechanisms of MT/actin crosstalk. In addition, the same cytolinker might fulfil different roles, depending on the cell type or context. To circumvent this complexity and to characterize the underlying mechanisms of microtubule-actin coordination via cytolinkers, we use a bottom-up *in vitro* approach and reconstitute the biological process of microtubule-actin coordination, using the minimal components within a controllable environment. In addition, this approach enables us to change one parameter at the time and study its effect on coordination. Using fluorescently labelled purified proteins and total internal reflection fluorescence (TIRF) microscopy, we can image the microtubule-actin interactions with high spatial and temporal resolution. In addition, using engineered cytolinkers, we can eliminate regulatory domains and thus avoid the need for additional regulatory factors, so that we can focus on the biophysical principles of MT/actin coordination.

1.4. THESIS OUTLINE

This thesis describes a series of experiments and analyses conducted to find the underlying mechanisms of microtubule-actin crosstalk by cytolinkers, using *in vitro* reconsitution experiments. We combine characterization of natural cytolinkers with studies of actin filament re-organization and microtubule dynamics using simpler engineered cytolinkers.

Chapter 2 first describes the methods and the materials used to perform the *in vitro*

reconstitution studies throughout the thesis.

Next, in Chapter 3, we study a new example of MT/actin crosstalk, namely actin transport by growing microtubules. This new mechanism allows growing microtubules to locally remodel actin by transporting actin filaments tethered to the growing ends via an engineered tip-binding cytolinker TipAct. We use *in vitro* reconstitution experiments, computer simulations, and a minimal theoretical model to investigate the required conditions and mechanism for actin transport. We show that transport results from two antagonistic forces that arise from crosslinkers transiently binding at the MT/actin overlap region.

In Chapter 4, we study MT/actin interactions mediated by a natural cytolinker, namely Gas2like1, by combining *in vitro* reconstitution experiments with imaging of neurons. We characterize the MT- and actin-binding ability of Gas2L1, and demonstrate that it is autoinhibited. This autoinhibition is relieved when Gas2L1 can bind at the MT/actin overlap regions, providing an elegant mechanism to localize the cytolinker specifically to the place where it is needed. In neurons we find that Gas2L1 primarily localizes to the actin cytoskeleton, where it promotes axon branching, restricts axon elongation, and acts as an actin stabilizer. Our *in vitro* reconstitutions indicate that Gas2L1 is also able to affect MT dynamics by increasing MT rescue rate. However, MT organization and dynamics appear normal in Gas2L1-depleted neurons. These combined results suggest that Gas2L1 does not promote axon branching by guiding MTs into actin-rich areas. Instead, we propose that Gas2L1 acts as an actin regulator, the function of which is spatially modulated by microtubules.

In Chapter 5, we study how the molecular anatomy of cytolinking proteins influences MT/actin crosstalk. Using *Drosophila* spectraplakin Shot as a model protein, we engineered several cytolinking proteins where we controlled the cytoskeletal binding domains and the spacer domains. We specifically focused on cytoskeletal organization and on microtubule dynamics, and found that linking actin filaments to the growing microtubule plus-end resulted in dynamic actin re-organization. Conversely, linking actin filaments to the microtubule lattice resulted in longer-lived actin re-organization, and more persistent MT growth with many MT rescue events.

Whereas previous chapters studied MT/actin crosstalk in quasi-2D, we present in Chapter 6 a method to study MT/actin organization in 3D. Using cell-sized water-in-oil emulsion droplets, we show that centrosome-nucleated dynamic microtubules can be made to interact with actin filaments via TipAct. We provide detailed protocols and discuss optimization steps required in order to build these more complex *in vitro* model systems of cytoskeletal interactions.

Finally, in Chapter 7, we summarize the main conclusions and provide an outline for possible future research directions, including more complex actin networks.

2

Material and Methods

You're something beautiful,
A contradiction.
I wanna play the game,
I want the friction.

Muse

The majority of experimental assays in this thesis are in vitro reconstitutions with dynamic microtubules and pre-polymerized actin filaments. Dynamic microtubules were grown from surface-immobilized seeds stabilized with a slowly hydrolyzable nucleotide analogue and incubated with fluorescently labeled tubulin. Actin filaments were pre-polymerized and stabilized with phalloidin, and were added in solution, so they were freely diffusible and able to rearrange in response to interactions with microtubules. The microtubule dynamics and actin organizations were imaged by total internal reflection fluorescence (TIRF) microscopy to obtain high temporal and spatial resolution. This chapter introduces the general experimental methods used in this thesis. It provides detailed protocols for surface and buffer preparations, the purification and handling of all proteins used in this thesis and the source of all chemical components. In addition, general methods for image analysis are provided. Experimental or analysis methods specific to a particular chapter are explained there.

2.1. GENERAL EXPERIMENTAL PROCEDURES

To achieve conditions that promote the reconstitution of microtubules as well as actin filaments, our experimental assays were all based on MRB80 buffer conditions (details are provided in the next sections). Although traditionally used as a microtubule polymerization buffer, MRB80 also allows actin polymerization and is thus used to pre-polymerize actin (details are provided in the next sections). To achieve the high spatial and temporal resolution required for measuring microtubule dynamics and single-protein interactions, we used total internal reflection fluorescence (TIRF) microscopy. This microscopy method only allows imaging near the glass surface, consequently requiring us to bring the events of interest towards the surface. We accomplished this by a functionalized glass surface (details are provided in the next sections), on which microtubule seeds are immobilized. Microtubule seeds are stabilized microtubules (details on preparations are provided in the next sections), from which new microtubules can nucleate and grow. By controlling the tubulin concentration and temperature, we are able to selectively allow microtubules to grow from these seeds and inhibit nucleation of new microtubules in solution. A schematic of our experimental assay is shown in Fig. 2.1.

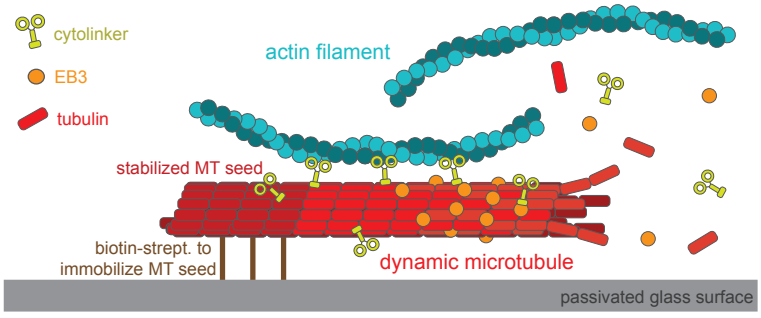

Figure 2.1: **Schematic of our experimental reconstitution assays for TIRF microscopy.** Typical assay with dynamic microtubules (red) and stabilized actin filaments (blue) in the presence of EB3 (orange) and cytolinkers (yellow). The GMPCPP-stabilized microtubule seeds are immobilized on the surface via biotin-streptavidin chemistry. Actin filaments are pre-polymerized and phalloidin-stabilized.

To prepare our experimental assay, actin filaments were pre-polymerized and stabilized with phalloidin while in the meantime glass slides and coverslips were cleaned and flow cell channels were prepared and functionalized. Then, final protein mixes were prepared, containing tubulin and other proteins like end binding (EB3) proteins and cytolinkers, in addition to other components like an oxygen scavenging system. This final mix was clarified at 149,000×g for 5 min before the addition of the actin filaments. At the microscope, microtubule seeds were flushed into the flow channels, and their binding was monitored with TIRF microscopy. Any non-attached seeds were rinsed out with MRB80, before the final microtubule polymerization mix, including actin filaments, was added.

2.2. FLOW CELL PREPARATION AND SURFACE PASSIVATION

Glass coverslips and microscope slides need to be thoroughly cleaned to avoid non-specific binding of (fluorescent) proteins to the glass. Besides having better control over the protein concentrations in solution, avoiding non-specific binding to the surface also reduces the 'background' signal since TIRF microscopy specifically illuminates a thin region near the glass surface. In addition to surface passivation, we also functionalized the surface to allow stable microtubule seeds to bind to the glass surface.

Glass coverslips and slides (Menzel-Glässer, Braunschweig, Germany) were cleaned in base piranha solution, as was previously described [92]. Although base piranha is a safer alternative to acid piranha since it only becomes reactive when heated to 60°C or above, preparations should be handled with great caution. Base piranha was prepared under the fume hood by mixing milliQ water, 30% H_20_2, and 30% NH_4OH at a 5:1:1 volume ratio in a glass beaker. The mixture was heated to 80°C on a hot plate, and once this temperature was reached, a home-made Teflon®rack holding the glass coverslips or slides was immersed into the solution. After 10 min incubation, the coverslips and slides were thoroughly rinsed with milliQ water, and finally stored at room temperature (RT) in milliQ for no longer than 5 days.

When preparing for experiments, clean glass slides and coverslips were carefully blow-dried with pressurized N_2 gas. Flow cell channels were assembled by cutting parafilm in thin pieces, which were spaced ~ 2 mm apart to form 10-15 µL channels when sandwiched between the dried glass slides and coverslips [92]. The flow channel was placed for ~ 20 s on a 120°C hot plate while gently applying pressure to melt the parafilm and prevent leaking between the channels. After cooling down, the surface functionalization of the flow channels was started.

Flow channels were functionalized with biotin and streptavidin to bind the biotinylated microtubule seeds. In principle, this linkage could also be used to immobilize individual actin filaments to the surface. Surface functionalization was obtained as described before [92]. Briefly, biotinylated glass surfaces were obtained by sequentially incubating (at room temperature) the flow cell channels with the following solutions: 0.1 mg/ml PLL-PEG-Biotin (PLL(20)-g[3.5]-PEG(2)/PEG(3.4)-Biotin(20%), SuSos AG, Dübendorf, Switzerland) for 30-60min, 0.25 mg/ml streptavidin (Thermo Scientific Pierce Protein Biology Products, Rockford, IL, USA) for 10 min, 0.5 mg/ml κ-casein (Merck, the Netherlands) for 10min and 1% (w/v) Pluronic F-127 (Merck, the Netherlands) for 10min, all diluted in MRB80, with 40-70 µL rinses with MRB80 in between steps. To avoid drying during the incubation steps, the flow channels were stored in a humid environment.

For assays with centrosomes (details on centrosome isolation are provided in next sections), the surface functionalization was slightly different, since centrosomes can adhere to the surface non-specifically. First, the centrosomes were thawed quickly (in your hands) and placed in a 37°C water bath for about 15 minutes, which increases the nucleation capability of the centrosomes, as was empirically found. Next, the centrosomes were gently diluted in MRB80 (at RT) to the desired concentration, before addition to the flow channel and incubation for 5 min to allow for surface adhesion. The channel was rinsed with 70-100 µL MRB80, before incubation with 0.1 mg/ml PLL-PEG (SuSos AG, Dübendorf, Switzerland) for 10 min. Next, 40-70 µL MRB80 rinses and another 15 min incubation with 1.0 mg/ml κ-casein mixed with 1% (w/v) Pluronic F-127 followed,

before finally rinsing with 40-70 µL of 1.0 mg/ml κ-casein solution. It is essential to rinse with solutions at RT to prevent decreased centrosome nucleation.

2.3. BUFFER CONDITIONS

The core (final) reaction mix is MRB80 buffer-based (pH 6.8 with KOH, 80 mM PIPES [piperazine-*N,N'*-bis(2-ethanesulfonic acid)], 4 mM $MgCl_2$, 1 mM EGTA [ethylene glycol-bis(β-aminoethyl ether)-*N,N,N',N'*-tetraacitic acid]), supplemented with 0.5 mg/ml κ-casein, 0.2% (v/v) methyl cellulose, 75 mM KCl, 1 mM GTP, 0.2 mM Mg-ATP, 4 mM DTT (dithiothreitol), 2 mM PCA (protocatechuic acid), and 100 nM PCD (protocatechuate-3,4-dioxygenase) (all compounds from Merck, the Netherlands). The final reaction mix contains κ-casein to balance the dynamic (un)binding of κ-casein to the surface and thus to prevent non-specific binding of proteins. We used 0.2% (v/v) methyl cellulose to push actin filaments and microtubules near the surface, thus confining them to the shallow region illuminated in TIRF mode. Furthermore, we used a slightly higher salt concentration (compared to other *in vitro* reconstitution assays) to promote microtubule plus-end binding of EB3, since higher salt concentrations reduce microtubule lattice interactions [93, 94]. Finally, DTT, PCA and PCD function as an oxygen scavenging system that reduces photo-damage and photobleaching of the proteins during imaging [95].

In addition to buffer components, our final mix for the dynamic microtubule assays also contained proteins. The tubulin concentration was kept at 20 µM (6 mole% labelled and 94% unlabelled tubulin), unless stated otherwise. This tubulin concentration avoids spontaneous nucleation while ensuring proper microtubule dynamics in combination with a temperature of 30°C and in presence of EB3 proteins. Pre-polymerized F-actin (co-assembled from 15 mole% labelled and 85% unlabelled G-actin monomers) was diluted to a final concentration between 10 nM and 1 µM. The EB3 concentration was kept at 133 nM, to be able to compare data on microtubule instability. In addition, a cytolinker concentration of 30 nM was used, unless stated otherwise. This concentration was chosen based on previous work [96], and to favor MT/actin interactions over actin/actin interactions for our dimeric engineered cytolinkers.

2.4. PROTEINS USED IN THIS THESIS

Below we list information for all the proteins used in this thesis, such as their origin, their storage, and how to handle and prepare them for the *in vitro* reconstitution assays.

ACTIN

G-actin was purified in-house from rabbit skeletal muscle acetone powder [97], filtered on a Superdex 200 10/60 size-exclusion column (GE Healthcare, Waukesha, WI, USA) to remove any oligomers and stored at -80°C in G-buffer [5 mM tris(hydroxymethyl)-aminomethane (Tris), pH 7.8 with HCl, 0.1 mM $CaCl_2$, 0.2 mM ATP, 1 mM dithiothreitol (DTT)]. Fluorescent actin was prepared by labelling monomers with Alexa Fluor 649 carboxylic acid succinimidyl esther (Molecular Probes, Life Technologies, Carlsbad, CA, USA), as described before [98]. Before use, G-actin was thawed overnight at 4°C, and clarified by centrifugation for 10-15 min at 149,000 x *g*, using an Airfuge® ultracentrifuge (Beckman Coulter, Brea, CA, USA). Next, actin was stored at 4°C for no longer than two

weeks.

Phalloidin-stabilized actin filaments were first polymerized at 7.5 µM G-actin concentration (15% labelled and 85% unlabelled G-actin) in MRB80 (with 50 mM KCl, 0.2 mM Mg-ATP, 4 mM DTT) at room temperature. Only after 30-90 minutes of polymerization, phalloidin was added in 1:1 molar ratio, to prevent its interference with actin polymerization.

TUBULIN

Lyophilized porcine brain tubulin was obtained from Cytoskeleton (Denver, CO, USA), resuspended at 50–100 µM in MRB80 buffer [80 mM PIPES, pH 6.8 with KOH, supplemented with 4 mM $MgCl_2$ and 1 mM EGTA], snap-frozen and stored at -80°C until use.

Microtubules were grown from surface-immobilized microtubule seeds, which were stabilized using the slowly hydrolysable GTP analogue guanylyl-(α,β)-methylene-diphosphonate (GMPCPP, Jena Biosciences, Jena, Germany). We followed the double-cycling protocol as described before [92, 99]. In short, a 20 µM tubulin mix was prepared in MRB80 on ice, containing 12% labelled tubulin (either TRITC Rhodamine, HiLyte®488, or HiLyte®635), 18% biotinylated tubulin, and 70% unlabelled tubulin, and supplemented with 1 mM GMPCPP. After incubation on ice for 5 min, the mix was incubated in a 37°C water bath for 30 min, to trigger microtubule polymerization. Next, the seeds were pelleted using an Airfuge®ultracentrifuge (Beckman Coulter, Brea, CA, USA) for 5 min at 149,000 x *g* in RT, before resuspending in MRB80 to a final 20 µM tubulin concentration, assuming 80% tubulin recovery. Before the second cycle of seed polymerization, the resuspended microtubules were incubated on ice for 20 min to trigger depolymerization. Fresh GMPCPP was added (1 mM), and the 5 min ice incubation and 30 min 37°C steps were repeated as above. After pelleting the seeds again via centrifugation (as described above) and discarding the supernatant, the seeds were resuspended in MBR80 containing 10% glycerol to a final concentration of 5 µM tubulin (again assuming 80% tubulin recovery). Thereafter, the seeds were aliquoted, flash-frozen in liquid N_2 and stored at -80°C until use.

Microtubule seeds were thawed on the same day as experiments were performed. Thawing of seeds was done quickly in a 37°C water bath to prevent depolymerization, and the seeds were kept dark and at RT to prevent bleaching. Typically, seeds were diluted to a 50-60 nM tubulin concentration when added to the surface functionalized flow channels. Incubation and binding of seeds was followed live via TIRF microscopy to tune the surface density, before the remaining (unbound) seeds were flushed away through rinsing with MRB80.

EB3

6xHis-tagged recombinant human EB3, GFP-EB3 and mCherry-EB3, purified from bacteria [24, 100], were kind gifts from Michel Steinmetz (Laboratory of Molecular Research, Paul Scherrer Institute, Switzerland) and Anna Akhmanova (Department of Biology, Utrecht University, the Netherlands). They were stored in -80°C at 5 µM concentrations.

CENTROSOMES

Centrosomes were isolated from human lymphoblastic KE37 cells by Sophie Roth and Florian Huber (Living Matter Department, AMOLF, the Netherlands) and Anne Doerr and Esengul Yildirim (Department of Bionanoscience, Technical University Delft, the Netherlands) following a previously described protocol [101]. They were stored in a high sucrose buffer (50-60%) at -80°C.

TIPACT AND TIPACTLONG

The engineered cytolinkers TipAct and TipActLong were used in Chapters 3 and 5 and in Chapter 5 of this thesis, respectively. eGFP-TipAct is an engineered cytolinking protein designed and used previously [92, 96]. In short, this 74 kDa small protein contains a microtubule tip-binding domain and an actin-binding domain, hence the name 'Tip-Act'. These binding domains come from the human spectraplakin MACF1 [55]. The N-terminal eGFP-tag is followed by the actin binding domain, consisting of tandem calponin-homology (CH) domains. Next, a spacer domain consisting of the coiled-coil domain of cortexillin (and additional amino acid residues) is placed to induce dimerization [102], which enhances microtubule plus-end localization [100]. Finally, the C-terminal microtubule tip-binding domain consists of an SxIP motif to bind EB-proteins [71, 100]. GFP-TipActLong is very similar in design to TipAct, except that it contains an additional microtubule lattice-binding GAR domain in between the coiled-coil domain and the SxIP motif, also originating from MACF1.

TipAct and TipActLong were expressed in E coli T7 cells and purified using a His-tag affinity column, as previously described for TipAct [96, 103]. In short, *E. coli* strains T7-express (New England Biolabs, Ipswich MA) were grown at 37°C in LB (lysogeny broth) containing 50 µg/ml kanamycin. By adding isopropyl β-D-1-thiogalactopyranoside (IPTG) to a final concentration of 0.4 mM and incubation at 20°C overnight, protein expression was induced. Next, cells were pelleted at 4°C and 15,000 rpm for 8 min, resuspended in 50 mL ice-cold lysis buffer [20 mM Tris pH 7.6, 10% (v/v) glycerol, 5 mM β-mercaptoethanol (BME), 500 mM NaCl, 45 mM imidazole, protease inhibitor cocktail (Roche, 1 tablet per 50 mL solution), 1 mg/mL lysozyme, and 20 µg/mL benzonase], and lysed by a cell disrupter. The insoluble material was removed by centrifugation (20,000g for 60 min). Next, the N-terminal 6xHis-tagged proteins were purified using immobilized metal-affinity chromatography on Ni-NTA agarose (Qiagen Benelux B.V., Venlo, Netherlands) at 4°C and diluted to 5 mg/ml, before thrombin-based cleavage of the 6xHis-tag [96]. To store the purified proteins (Fig. 2.2A,B), the buffer was exchanged to MRB80-KGβ (pH 6.8 with KOH, 80 mM PIPES, 4 mM $MgCl_2$, 1 mM EDTA, supplemented with 250 mM KCl, 10% (v/v) glycerol and 5 mM β-mercaptoethanol), and proteins were aliquoted, snap-frozen in liquid N_2 and stored at -80°C until use.

For more details on the behaviour of these cytolinkers, including the TALonger and TALmono variants, we refer the reader to Chapter 5 of this thesis.

GAS2LIKE1

The natural cytolinker Gas2Like1 was used in Chapter 4 of this thesis. The N-terminal GFP-Gas2L1 fusions were purified from HEK293 cells by Dieudonnée van de Willige (Department of Biology, Utrecht University, the Netherlands), using Strep(II)-streptactin affin-

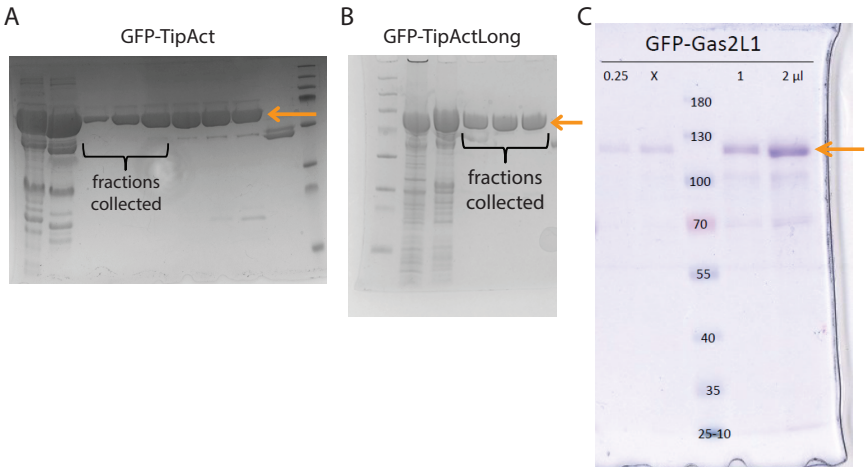

Figure 2.2: **Purified proteins for *in vitro* reconstitutions.** **(A)** Purified TipAct from bacteria. SDS-PAGE gel of eGFP-TipAct after histidine cleavage, showing which fractions were collected and used for *in vitro* reconstitutions in Chapter 3. **(B)** Purified TipActLong from bacteria. SDS-PAGE gel of eGFP-TipActLong after histidine cleavage, showing which fractions were collected and used for *in vitro* reconstitutions in Chapters 3 and 5. **(C)** Isolated Gas2L1 (G2L1) from HEK-cells. Commassie-stained SDS-PAGE gel showing the purity of isolated G2L1 used for *in vitro* reconstitutions in Chapter 4. Orange arrows indicates bands of cytolinkers.

ity purification protocols as described before [104]. In short, HEK293 cells were cultured in 50/50 DMEM/Ham's F10 medium (DMEM: Lonza or Biowest; Ham's F10: Lonza) supplemented with 10% FCS (Sigma) and 1% penicillin-streptomycin (Sigma), and routinely tested for mycoplasma. The cells were transfected with tandem StrepII-tagged GFP-Gas2L1 fusions constructs using MaxPEI (Polysciences) in a ratio of 3:1 PEI:DNA. After 24-48h expression, cells were washed with ice-cold PBS supplemented with 0.5x protease inhibitor cocktail (Roche) and 5 mM MgCl2. Next, cells were lysed for 15 minutes on ice in purification lysis buffer (50 mM HEPES pH 7.4, 300 mM NaCl, 0.5% Triton X-100, 1x protease inhibitors), followed by centrifugation for 20 minutes at 13.2 krpm/4°C. Supernatants were incubated for 45 minutes in the presence of pre-washed StrepTactin Sepharose High Performance beads (GE Healthcare) at 4°C. Following incubation, beads were washed three times in ice-cold wash buffer (50 mM HEPES pH 7.4, 300 mM NaCl, 0.5% Triton X-100). StrepII-GFP-Gas2L1 was then eluted in standard elution buffer (50 mM HEPES pH 7.4, 150 mM NaCl, 1 mM $MgCl_2$, 1 mM EGTA, 0.05 % Triton X-100, 1 mM DTT, 2.5 mM d-Desthiobiotin) by incubating beads with elution buffer for ten minutes on ice. To prevent aggregation, the elution buffer used to purify Gas2L1 truncation mutants was supplemented with 50 mM arginine, 50 mM glutamic acid and 10% glycerol. After incubation with elution buffers, supernatants were collected by centrifuging for 1 minute at 3000 rpm/4°C, and cleared a second time by centrifuging for 1 minute at 13.2k rpm/4°C. The remaining supernatant was aliquoted in single-use vials, snap frozen in liquid nitrogen and stored at -80°C.

The purity of purified Gas2L1 fusions was determined by Coomassie blue staining of SDS-PAGE gels (Fig. 2.2C). Concentration was determined by set amounts of purified

Gas2L1 ran alongside a range of standardized BSA concentrations (100 ng - 2000 ng). The resulting Gas2L1 band intensities were compared to the BSA concentration curve, using the *Gel Analyzer* tool in Fiji, and used to calculate the amount of protein in ng/µl from which molarity could be determined.

SHOT

The natural cytolinker Shot was used in Chapter 5 of this thesis. Shot (aka Short stop or Kakapo) is the only spectraplakin in *Drosophila*, and the homolog of mammalian spectraplakin MACF1. N-terminal GFP-Shot fusions were purified from HEK293 cells with help of Dipti Rai (Department of Biology, Utrecht University, the Netherlands). We used Strep(II)-streptactin affinity purification protocols as described before [104] and similar to Gas2Like1 purification (described above). Purified proteins were aliquoted, snap frozen in liquid N_2 and stored at -80°C.

2.5. TOTAL INTERNAL REFLECTION FLUORESCENCE (TIRF) MICROSCOPY

Triple-colour TIRF microscopy experiments were performed on a Nikon Eclipse Ti-E inverted microscope (Nikon Corporation, Tokyo, Japan) equipped with an Apo TIRF 100 x 1.49 N.A. oil objective, a motorized stage, Perfect Focus System, a motorized TIRF illuminator (Roper Scientific, Tucson, AZ, USA) and a QuantEM:512SC EMCCD camera (Photometrics, Roper Scientific). For excitation, we used a 561 nm (50 mW) Jive (Cobolt, Solna, Sweden), a 488 nm (40mW) Calypso (Cobolt) diode-pumped solid-state laser, and a 635 nm (28 mW) Melles Griot laser (CVI Laser Optics & Melles Griot, Didam, Netherlands). Most of the imaging of dynamic microtubules was performed at 3 s per frame with 50-100 ms exposure time at 8-18 % laser power. The sample temperature was kept fixed using a custom-build (by Roland Dries at AMOLF) objective heater to 30±1°C. The microscope hardware was controlled with MetaMorph 7.8.8.0 (Molecular Device).

2.6. DATA ANALYSIS

All image processing and data analysis were performed using Fiji [105] and custom-written codes in MATLAB or Python. General procedures to quantify microtubule dynamics are explained here. Details on other specific analyses are found in each chapter.

To characterize microtubule dynamics, we measured the parameters of microtubule dynamic instability, namely microtubule growth and shrinkage velocity, and catastrophe and rescue frequencies. We construct a kymograph, i.e. a space-time plot, along the length of the microtubule to obtain these parameters. First we project a movie in time (Fig. 2.3A,B) and then draw a line along a microtubule to construct the kymograph. From the microtubule tip position as a function of time, thus the slope, we can extract the microtubule growth velocity (Fig. 2.3C). For each microtubule growth event, we obtained one manual fit, thus averaging the growth and shrink velocities over the complete growth and shrink phase, respectively. The average velocity was then taken as the average over all events weighted with the duration of the individual events. The error is the weighted standard deviation of this weighted mean.

Catastrophe rates were calculated as the number of catastrophe events divided by the total time microtubules spent growing. The error is given by the rate divided by the square-root of the number of events. Similarly, the rescue rates were calculated as the number of rescue events divided by the total time microtubules spent shrinking, thereby excluding the 'recues' that occur at the microtubule seed. Often, the seed contained the same fluorescent label as the free tubulin, but at higher molar ratio. Thus, the seed was distinguishable from the dynamic lattice by brightness. Because of the diffraction limit, we only counted rescues that occurred further than 0.5 µm away from the seed.

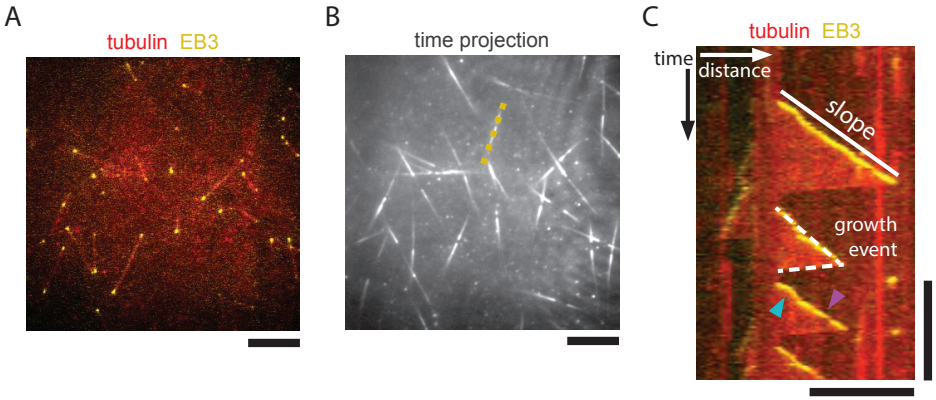

Figure 2.3: **Kymograph analysis to obtain microtubule dynamics. Schematic of our experimental reconstitution assays for TIRF microscopy. (A)** Frame from a movie showing a typical field-of-view with microtubules (red) and EB3 protein comets (yellow) tracking the growing microtubule ends. **(B)** Time projection of the EB3 signal from the movie shown in (A). The yellow dashed line indicates how a line is drawn along a microtubule to create a kymograph. **(C)** A kymograph, i.e. a space-time plot, of the microtubule indicated in (B). The slope of a growing microtubule is used to determine the microtubule growth velocity. The dashed lines indicate the manual fit of a single microtubule growth event, including a growing phase and a shrinking phase. Although during such a single growth event, several slopes, thus growth velocities, might be observed (as indicated with blue and purple arrowheads), we take the average slope over the complete growing phase. Scale bars: 10µm (horizontal) and 3 min (vertical).

3

CROSSLINKERS AT GROWING MICROTUBULE ENDS GENERATE FORCES THAT DRIVE ACTIN TRANSPORT

For a while now,
I can't stay very far,
I can't stay much longer.

The Killers

The actin and microtubule cytoskeletons form active networks in the cell that can contract and remodel, resulting in vital cellular processes as cell division and motility. Motor proteins play an important role in generating the forces required for these processes, but more recently the concept of passive crosslinkers being able to generate forces has emerged. So far, these passive crosslinkers have been studied in the context of separate actin and microtubule systems. Here, we show that crosslinkers also allow actin and microtubules to exert forces on each other. More specifically, we studied single actin filaments that are crosslinked to growing microtubule ends, using in vitro reconstitution, computer simulations, and a minimal theoretical model. We show that microtubules can transport actin filaments over large (micrometer-range) distances, and found that this transport results from two antagonistic forces arising from the binding of crosslinkers to the overlap between the actin and microtubule filaments. The crosslinkers attempt to maximize the overlap

This chapter is based on the pre-print *Cross-linkers at growing microtubule ends generate forces that drive actin transport* by Celine Alkemade, Harmen Wierenga, *et al*, (2021) [106]. Celine Alkemade contributed the *in vitro* reconstitution experiments, co-wrote the article and adapted for thesis chapter. Theory and simulations were performed by H. Wierenga. Optical tweezer experiments were performed by V. Volkov.

between the actin and the tip of the growing microtubules, creating an affinity-driven forward condensation force, and simultaneously create a competing friction force along the microtubule lattice. We predicted and verified experimentally how the average transport time depends on the actin filament length and the microtubule growth velocity, confirming the competition between a forward condensation force and a backward friction force. In addition, we theoretically predicted and experimentally verified that the condensation force is of the order of 0.1 pN. Thus, our results reveal a new mechanism for local actin remodeling by growing microtubules.

3.1. INTRODUCTION

Vital cellular processes such as cell division and motility are driven by contraction and remodeling of active networks within the cell: the actin and microtubule cytoskeletons. These contraction and remodeling processes require the generation of forces and relative movement of filaments. It is well known that motor proteins can cross-link filaments, and organize the network by driving the relative movements of the filaments [107]. Besides the well-appreciated role of motor proteins, also polymerization dynamics have been shown to generate forces required for self-organization and remodeling [108, 109]. In addition, the importance of passive (non-motor) crosslinkers has recently been increasingly recognized. It is now clear that passive crosslinkers can generate driving forces too, as has been shown for anillin in the contractile ring [110] and Ase1 in the spindle [111]. These forces are generated via the entropy associated with the crosslinker's diffusion within the overlap region [111], or via the condensation (or preferential binding) of crosslinkers to the overlap between filaments [110, 111], therefore named 'condensation force'. In addition, passive crosslinkers create frictional forces [111, 112], which not only affect the speed at which cytoskeletal structures are remodeled, but can even be essential for their stability by opposing the motor proteins [113, 114].

The studies on force generation by passive crosslinkers have so far focused on individual cytoskeletal systems. However, passive crosslinkers could also be a way for two systems to exert forces on each other. In particular, there is a growing body of work showing the importance of microtubule/actin crosstalk in vital cellular functions [3]. Besides crosstalk via signalling pathways, it has been shown that crosstalk via motor proteins such as myosin-X (Myo10) is among the drivers of remodeling the microtubule spindle network during cell division [83, 115]. In addition, crosstalk via various passive crosslinking proteins such as MACF1 and Tau have been shown to result in guidance and stabilization of the actin and microtubule networks [60, 71, 96, 116].

Recent experiments suggest that the driving condensation forces and friction forces associated with passive crosslinkers can also couple to the growth dynamics of filaments, and thereby allow passive crosslinkers to play a central role not only in contraction but also in transport. It was shown that an engineered passive crosslinker called TipAct can mediate transport of actin filaments by binding to the tips of growing microtubules [96]. The microtubule tip region is chemically different from the microtubule lattice region, due to delayed hydrolysis of GTP that is associated with tubulin subunits that incorporate into growing microtubules. This region is recognized by microtubule end-binding (EB) proteins [22, 25, 117] as well as EB-binding partners such as TipAct. However, the processivity of the actin transport mechanism and its dependency on relevant parame-

ters such as actin filament length and microtubule growth velocity, as well as the magnitude of the generated forces are currently unresolved.

Here, we investigated the conditions necessary for microtubule-mediated actin transport and elucidated the crosslinker-dependent mechanism. We combined biochemical reconstitution experiments with coarse-grained computer simulations and a minimal theoretical model, and showed that in the presence of passive crosslinkers, microtubules can transport actin filaments over large (micrometer-range) distances during periods that last up to several minutes. We proposed and tested a new mechanism to explain this movement, in which actin transport is the result of a competition between a forward force that tends to maximize the overlap of the actin filament with the plus end of a growing microtubule and a backward force caused by the friction between the actin and microtubule lattice. These two antagonistic forces are both caused by the binding of crosslinkers. The preferential binding of crosslinkers at the interface between two objects (such as filaments) creates a driving force that tends to maximize the overlap region. This type of force, which, following earlier work [111, 112], we called condensation force, can drive the movement of intracellular cargoes [118–121] and the contraction of filament bundles [110, 111, 122, 123] in various biological contexts. However, the combination of a processive transport of cargo by a crosslinker based condensation force that is simultaneously hindered by a friction force caused by the same crosslinkers is specific to filament transport and has to our knowledge not been studied before. The active transport of filaments by the growing microtubule plus ends thus provides a new minimal mechanism by which two cytoskeletal systems can interact, which is distinct from cytoskeletal crosstalk that is driven by motor proteins [83, 124–127].

3.2. RESULTS

3.2.1. GROWING MICROTUBULES PLUS ENDS CAN TRANSPORT ACTIN FILAMENTS

To study actin filament transport by growing microtubule plus ends, we used the engineered cross-linking protein TipAct that contains both a domain that specifically binds actin filaments and a domain that recognizes end-binding (EB) proteins to target it to the growing ends of microtubules (Fig. S3.7A,B) [96]. Dynamic microtubules were grown from surface-immobilized seeds stabilized with the nucleotide analogue GMPCPP and incubated with fluorescently labeled tubulin. The microtubules grew in the presence of TipAct, EB3, and freely diffusible stabilized actin filaments and were imaged by total internal reflection fluorescence (TIRF) microscopy (Fig. 3.1A). We observed a 54µm×54µm sized region of interest, which typically contains on the order of 30 microtubules (Fig. 3.1B), and we looked for instances where growing microtubules interact with actin filaments (see Materials&Methods for criteria). Figure 3.1C shows a typical example of an encounter of a growing microtubule with an actin filament. Once the microtubule starts growing, an EB3-TipAct complex localizes at its growing end (yellow arrow). After several seconds, an actin filament binds and co-localizes to this tip-tracking complex (blue arrows) and is transported over a distance of several micrometers, before finally unbinding while the microtubule continues growing (white arrows).

To analyze the effect of actin transport on microtubule growth dynamics, we con-

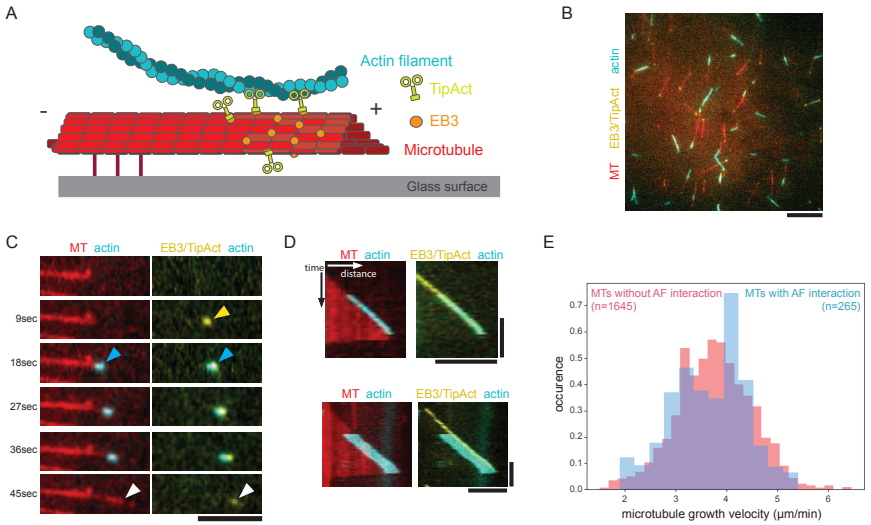

Figure 3.1: **Actin transport by growing microtubule plus ends.** **(A)** Schematic of the experimental assay for observing microtubule-mediated actin transport, showing a stabilized actin filament (cyan), the engineered cytolinker TipAct (green-yellow), and the microtubule end-binding protein EB3 (orange) moving freely in solution, while the growing microtubule (red) is anchored to the surface of a functionalized and passivated glass slide. **(B)** Experimental field of view, showing a typical cropped region that was used for analysis, including microtubules/tubulin (red), EB3 (yellow), TipAct (yellow), and stabilized actin filaments (cyan). **(C)** Time series of the growing plus end of a microtubule that recruits and transports an actin filament via EB3/TipAct complexes. Arrowheads show the localization of the EB3/TipAct-complex (yellow), the binding of a short actin filament (cyan), and the unbinding of this actin filament while the microtubule continues to grow (white). **(D)** Kymographs (space-time plots) of actin filament transport by the growing plus end of a microtubule, showing the microtubule (red), EB3 and TipAct (yellow), and an actin filament (cyan). From these kymographs, we measure parameters of the microtubule dynamics, such as the growth velocity. **(E)** Normalized distribution of microtubule growth velocities for growth events where the microtubules does not interact with actin filaments (red) and for microtubules that transport an actin filament (blue). The average growth velocities are 3.5±0.6 µm/min and 3.7±0.7 µm/min for non-interacting and interacting events, respectively. Separate channels are shown in Fig. S3.7 and S3.6. Scale bars: 10 µm in B, 5 µm in C, 5 µm (horizontal) and 60 s (vertical) in D.

struct a kymograph, i.e. a space-time plot along the length of the microtubule (Fig. 3.1D). From the microtubule tip position as a function of time, we can extract the microtubule growth velocity. In the example kymographs in Fig. 3.1D, actin transport does not affect the growth velocity. This finding is confirmed by an analysis of 265 transport events (Fig. 3.1E).

To further analyze transport parameters such as the transport rate and duration, we again turn to kymographs. Fig. 3.2A shows an example kymograph corresponding to the transport event shown in Fig. 3.2C. It clearly visualizes the recruitment of the actin filament shortly after the microtubule starts growing, and its unbinding before the microtubule undergoes a catastrophe. For each event, we measure the transport time from the moment when the actin filament begins to move along with the growing microtubule tip region until this directed motion stops.

We observed long-range actin filament transport (Fig. 3.2F) for actin filaments with a wide range of lengths from around 0.5 µm to 8 µm (Fig. 3.2G). In the example of Fig. 3.2A,

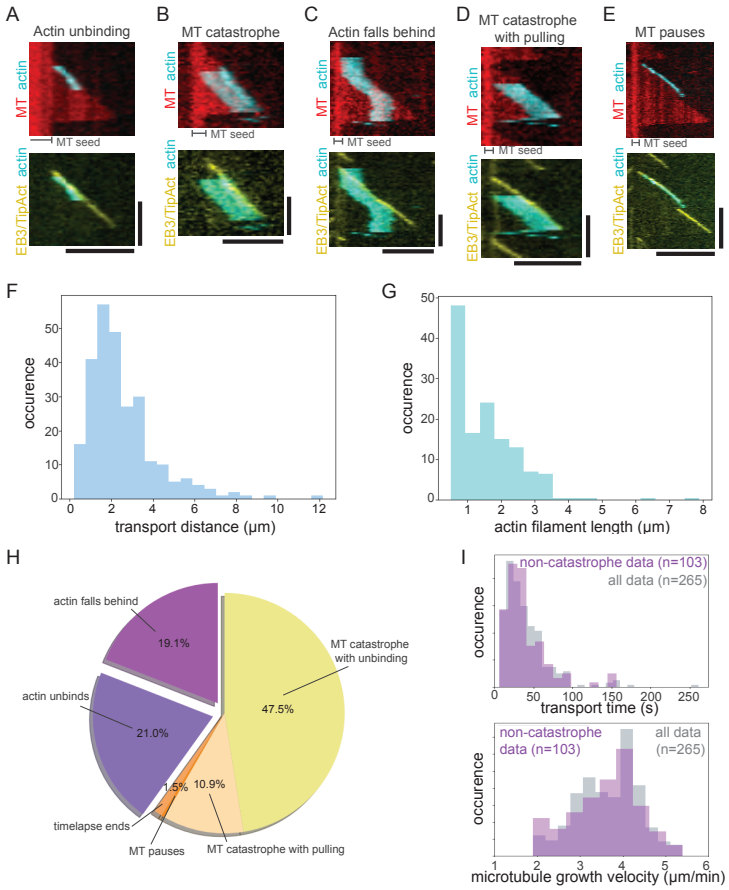

Figure 3.2: **Mechanisms limiting the actin transport time.** **(A)** Kymograph of the actin transport event depicted in Fig. 3.1C, showing that the event ends by the unbinding of the actin filament while the microtubule continues growing for a while. **(B)** Kymograph of a typical transport event that ends upon a microtubule catastrophe. **(C)** Kymograph of a typical transport event that ends by loss of contact of the actin filament with the tip resulting in the actin filament falling behind and lingering on the MT lattice. **(D)** Kymograph of a typical transport event that ends upon a microtubule catastrophe, but where the shrinking microtubule pulls an actin filament backwards. **(E)** Kymograph of the transport event that ends by the disappearance of the comet at a pausing microtubule. **(F)** Distribution of transport distances for actin filaments transported by growing microtubule plus end. Median distance of 2.1 µm (and mean of 2.5 µm) and range of 0.8-12.2 µm. **(G)** Length distribution of transported actin filaments. Median length of 1.4 µm (and mean of 1.6 µm) and length range of 0.5-7.9 µm long filaments. Note that all filaments shorter than 0.5 µm are binned as 0.5 µm because of the diffraction limit. The maximal length is limited by the tendency of longer filaments to form bundles, which are excluded from further analysis. **(H)** Categories of termination events together with their observed frequency (n=265). Typical examples of the categories are shown in A-E. **(I)** Distributions for the transport times (top) and microtubule growth velocities (down) are indistinguishable when we consider the complete dataset (n=265) or just a subset of transport events that end by actin filament unbinding and therefor are independent of microtubule catastrophe (*i.e.*, both the 'actin unbinds' and 'actin falls behind' events, n=103). Separate channels of the kymographs are shown in Fig. S3.8. Scale bars: 5 µm (horizontal) and 60 s (vertical).

the actin filament is only 0.6 µm long, which is not much longer than the length of the microtubule tip region where EB3 preferentially binds. Actin filaments that are longer than the tip length sometimes land largely behind the microtubule tip and immediately start following it (Fig. 3.2B), while others land with part of the filament in front of the tip (Fig. 3.2C). In the latter situation, we observed that actin transport only starts once the microtubule tip has caught up with the front of the actin filament. Upon analyzing 265 actin transport events, we observed a broad distribution of transport times with a median transport time of 48 s and a long tail that extends up to several minutes (Fig. 3.2I top, in grey).

The kymographs in Fig. 3.2A-E demonstrate several mechanisms by which actin transport can end: the actin filament unbinds (21% of events), the microtubule undergoes a catastrophe whereby actin unbinds (48%), the actin filament falls behind the growing microtubule tip region, leaving the filament bound to the microtubule lattice region behind the tip (19%), or the microtubule undergoes a catastrophe while the actin filament remains attached and is pulled along with the shrinking microtubule (11%). In addition, a small fraction of events corresponds to events truncated by the end of the timelapse movie or to a microtubule pausing (1.5%). A summary of the distribution of events is shown in Fig. 3.2H. Irrespective of whether we include all transport events in the distributions or only subsets, the distributions of microtubule growth velocities and of the actin transport times remain similar (Fig. 3.2I). Specifically, the distribution of transport times excluding those events that end by microtubule catastrophe is indistinguishable from the distribution including all events, in line with the assumption that the three main mechanisms of ending the actin transport, i.e. actin unbinding, microtubule catastrophe, and actin falling behind, are independent Markovian processes (see SI Appendix).

3.2.2. SIMULATIONS REPRODUCE MICROTUBULE-MEDIATED ACTIN TRANSPORT

We hypothesized that actin transport can be explained by a competition between two crosslinker induced forces: (i) a driving condensation force that originates from the binding free energy of the cross-linking TipAct proteins that should act to maximize the overlap between the actin filament and the microtubule tip region, and (ii) a friction force due to the presence (at lower affinity) of crosslinkers at the interface between the actin filament and the microtubule lattice that hinders actin transport. To test this hypothesis, we performed kinetic Monte Carlo simulations of the simple model presented in Fig. 3.3A. We modeled the microtubule and the actin filament as one dimensional lattices of binding sites, where the microtubule is immobile while the actin filament can move along its long axis. For simplicity, we assumed the same lattice spacing δ between the binding sites on both filaments (see SI Appendix). Microtubule growth is modeled through the addition of new binding sites with a fixed rate r_g. We assumed that the microtubule contains a chemically different microtubule tip region of l_t =200 nm long. To maintain a constant size of the tip region, we transformed the oldest site in the tip region to a lattice site upon each addition of a new tip site, as indicated in Fig. 3.3A. We treated TipAct and EB3 proteins as a single complex that can bind to and unbind from the microtubule. Based on the EB3 fluorescence intensity at the microtubule tip (Fig.S3.9),

we assumed that the affinity of the cross-linking complex is 20-fold higher for the tip compared to the lattice region. Since we observed in experiments that TipAct strongly localizes to microtubules, but barely to isolated actin filaments (Fig. 3.1B), we assumed that the crosslinkers always bind to the microtubule first and can then bind to the actin filament. We included the microscopic reverse reactions for all binding reactions, such that microtubule growth is the only process that breaks detailed balance. Free actin filaments diffuse at a rate D_a that depends on the viscosity of the solution. When the actin filament gets cross-linked to the microtubule, its diffusive movement is limited mainly by the transient crosslinker binding events, strongly reducing its effective diffusion constant.

We modeled the diffusive movement of the actin filament using Brownian Dynamics with a fixed time-step. To allow for movement of the actin filament, the crosslinkers can stretch as Hookean springs with spring constant k. We modeled the (un)binding of crosslinkers and the addition of new subunits to the microtubule tip as continuous-time Markov processes, which were described by the reaction rates shown in Fig. 3.3A. We simulated these reactions using a kinetic Monte Carlo algorithm, as described in [112]. We omitted microtubule catastrophes from the computational model, since these occur at a constant Markovian rate, as shown in Fig. S3.6C.

We used experimental observations to estimate all parameters shown in Fig. 3.3A (for details see SI Appendix). In particular, we measured the actin diffusion coefficient on the microtubule lattice, which depends on the spring constant and binding rates of the crosslinkers, fluorescence recovery after photobleaching (FRAP) experiments on fluorescently labeled TipAct proteins to measure the off-rate of microtubules, and the actin transport time for one specific combination of actin length (4 μm) and growth velocity (3 μm min^{-1}).

Simulations using this parameter set systematically showed that the actin filament follows the growing microtubule tip region, as shown in Fig. 3.3B. In this example, the actin filament initially overlaps with its front end with the microtubule tip and is transported. At some point it transiently falls behind the tip, but then catches up again (black arrow). We observed the same transient diffusion events in our experiments, as shown in Fig. S3.10. Eventually the filament completely loses its interaction with the tip and performs random diffusion on the microtubule lattice. Hence, the transition from transport to diffusion occurs when the actin filament loses its interaction with the microtubule tip and does not rebind to the microtubule tip before the microtubule grows away.

3.2.3. THEORY FOR CROSSLINKER-DRIVEN TRANSPORT AND FORCE GENERATION

To complement our simulations and identify the requirements for actin transport by growing microtubules, we developed a general coarse-grained theory based on the model schematically shown in Fig. 3.3C. On timescales longer than the crosslinker (un)binding time, the stochastic motion of the actin filament can be characterised as a biased diffusion process. In this coarse-grained description, the microscopic interactions of the crosslinkers with the filaments give rise to a condensation force that tends to maximize the overlap between the actin filament and the tip of the growing microtubule, and a stochastic force that not only modulates the effective diffusion constant of the actin fil-

ament but also generates a friction force that opposes the driving condensation force. We described this diffusion process via a Fokker-Planck equation, where the actin position x is defined in a reference frame that is co-moving with the growing microtubule, as indicated in Fig. 3.3C. An actin filament moving with the growing microtubule tip thus remains at a constant position x.

The actin filament performs 1D diffusion along the microtubule with an effective diffusion constant that depends on the crosslinker binding dynamics. This effective diffusion constant of the actin filament D_{eff} decreases with an increasing average number of connections between the actin filament and the microtubule [112, 123, 128, 129]. In turn, the average number of connections depends on the length of the overlap between the actin filament and the microtubule lattice region y_ℓ and between the actin filament and the microtubule tip region y_t (see Fig. 3.3C). Short actin filaments, or filaments that barely overlap with the microtubule tip, can be in states where no crosslinkers connect the actin to the microtubule. Hence, the effective diffusion constant of the actin filament is the average over the diffusion constants of the unbound and bound states of the actin filament. In the unbound case, the diffusion constant is set by the viscosity of the solution to $D_a = 1\ \mu\text{m s}^{-1}$ (see SI Appendix). In the microtubule-bound state, the actin diffusion constant is dominated by the binding dynamics of the crosslinkers which we capture by an effective friction coefficient $\zeta_{\text{bound}}(y_t, y_\ell)$. The effective diffusion constant is related to this friction coefficient through the Einstein relation,

Figure 3.3 *(facing page)*: **Computer simulations and analytical theory of a mechanism for actin transport by growing microtubules (MTs). (A)** The model used for simulating the interaction between an actin filament (blue, top) cross-linked to a growing MT (red, bottom). Both filaments are modeled as one dimensional inflexible chains of binding sites with lattice constant δ. Crosslinkers are modeled as springs with spring constant k that can first bind to the MT and from there to the actin filament. These crosslinkers represent a complex of TipAct and EB3, which has a higher affinity for the tip region of the MT (dark red, right) compared to the lattice region (light red, left). The distance between the filaments remains fixed, so the actin filament can only move forward and backward. Viscous interactions with the solution result in a diffusion constant D_a for the actin filament, while the longitudinal components of the pulling forces from the crosslinkers provide additional movement of the actin filament. **(B)** A typical time trace of the MT and the actin filament. Compare to Fig. 3.1C. The actin filament is transported when it interacts with the MT tip region (dark red, front of MT), and can recover from quick detachments from this tip region through diffusion (black arrow). However, after a stochastic transport time T_t, the actin filament falls behind the tip region and then performs random diffusion on the MT lattice. **(C)** Parameter definitions for an analytical theory in a co-moving frame. We define x as the position of the front of the actin filament compared to the back of the MT tip region. Since the tip region advances upon MT growth, this constitutes a co-moving frame of reference. The theory describes the dynamics of x using the crosslinker induced effective diffusion constant of the actin filament $D_{\text{eff}}(x)$, the MT growth velocity v_g and the effective forward condensation force F_f. The actin filament has a length l_a, the microtubule tip region has a length l_t, and the microtubule lattice region is assumed to extend leftward. The overlap lengths between the actin filament and the microtubule tip and lattice regions are denoted y_t and y_ℓ, respectively, and the bottom schematics show the relations between these overlap lengths and the other parameters in three regimes. **(D)** The effective actin diffusion constant $D_{\text{eff}}(x)$ decreases with the overlap between the actin filament and MT lattice region (blue) and the MT tip region (green). Simulations give the proportionality constants of the actin friction coefficients ζ_t and ζ_ℓ by fitting Eq. 3.1 (lines) to the simulation results (points). **(E)** Using an analytical expression for the condensation force and the fits from panel D, the theory predicts a free-energy well (blue line), where a co-moving actin position $x > 0$ within the well represents meta-stable transport, whereas a barrier crossing at $x = 0$ and the subsequent slide towards $x < 0$ represents the actin falling behind the MT tip. Direct sampling of the positional distribution of x in simulations (blue points) confirms the validity of the theoretical prediction.

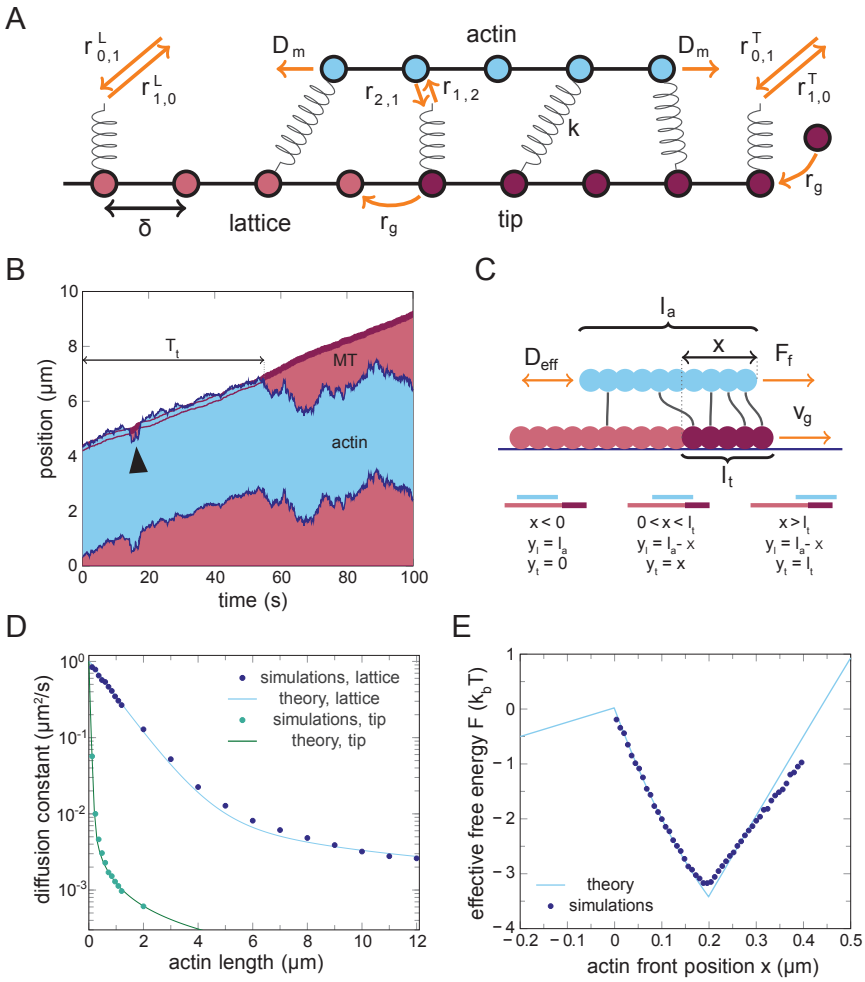
A
actin
lattice
tip
δ
B
position (μm)
time (s)
MT
actin
C
D
diffusion constant (μm²/s)
actin length (μm)
simulations, lattice
theory, lattice
simulations, tip
theory, tip
E
effective free energy F (k_bT)
actin front position x (μm)
theory
simulations

$D_{\text{bound}} = k_B T/\zeta_{\text{bound}}$ [130]. Put together, the average diffusion coefficient averaged over unbound and bound states is given by

$$D(y_t, y_\ell) = p_0(y_t, y_\ell)\, D_a + \left(1 - p_0(y_t, y_\ell)\right) \frac{k_B T}{\zeta_{\text{bound}}(y_t, y_\ell)}. \tag{3.1}$$

The probability $p_0(y_t, y_\ell)$ that the actin filament is not bound to the microtubule is given by (see SI Appendix for details)

$$p_0(y_t, y_\ell) = \mathrm{e}^{-y_t/\lambda_t} \mathrm{e}^{-y_\ell/\lambda_\ell}. \tag{3.2}$$

The length scales λ_t and λ_ℓ depend on the binding affinities of the crosslinkers for the tip and overlap region, respectively, since these determine the likelihood of crosslinker binding to these regions. We assumed that the friction coefficient scales linearly with the actin overlap lengths,

$$\zeta_{\text{bound}}(y_t, y_\ell) = \zeta_t y_t + \zeta_\ell y_\ell, \tag{3.3}$$

since the average number of crosslinkers is proportional to the overlap lengths y_t and y_ℓ, and friction scales linearly with the number of crosslinkers when the spring constant is low enough and exclusion effects between the crosslinkers are insignificant [123, 128, 129]. To find the proportionality constants ζ_t and ζ_ℓ, we performed two separate sets of simulations where we kept y_ℓ or y_t at 0 and varied the other one, and then measured the diffusion constant of the actin filament. In Fig. 3.3D, we fitted Eq. 3.1 to the simulated diffusion constants, using ζ_t and ζ_ℓ as the fitting parameter for the curve varying the actin length y_t or y_ℓ, respectively. The effective diffusion constant has an exponential regime for small y due to Eq. 3.2, and a linearly decreasing regime for large y due to Eq. 3.3. Fig. 3.3D shows that Eq. 3.1 fits the diffusion constants in the simulations remarkably well over the whole range of y, confirming that the motion of the actin filament is well described by an effective diffusion process.

The diffusive motion of the actin filament is biased forward when the actin filament happens to overlap with the microtubule tip region, because the crosslinkers have a higher affinity for the microtubule tip than for the microtubule lattice. The resulting forward pointing condensation force F_f provides a drift term to this diffusion process. This force is present as long as the actin filament overlaps with the microtubule tip region of size l_t, but does not fully cover it, $0 < x < l_t$. When the actin filament extends in front of the microtubule tip region, $x > l_t$, a negative, backward condensation force F_b attempts to increase the overlap between the actin filament and the microtubule lattice region. We derived analytical expressions for these forces in the SI Appendix, yielding estimated force values of F_f = 0.10 pN and F_b = -4.6 fN using the parameter set given in Table S3.1.

Using these forces and Eq. 3.1, we could describe the effective drift of the actin filament observed in the co-moving frame x. The effective net force $F_{\text{eff}}(x)$ that acts on the actin filament is the sum of the driving condensation force and the opposing friction force:

$$F_{\text{eff}}(x) = F_f \mathbb{1}(0 \le x < l_t) + F_b \mathbb{1}(x > l_t) - \frac{k_B T}{D(x)} v_g. \tag{3.4}$$

Here, $\mathbb{1}(c)$ is the indicator function returning 1 if the condition c is true and 0 otherwise. The condensation force is thus either the forward driving force F_f when the actin overlaps only partially with the microtubule tip, or the backwards moving force F_b when the actin fully overlaps with the tip but only partially with the microtubule lattice. The diffusion constant $D(x) = D\big(y_t(x), y_\ell(x)\big)$, where the x dependence of the overlap lengths y is given in Fig. 3.3C, and the diffusion constant follows Eq. 3.1. The last term in the effective force is indeed the opposing friction force, which equals the effective friction coefficient $k_B T / D_x$ times the microtubule growth velocity v_g since that determines the relative speed between the actin filament and the microtubule.

We integrated the effective force from Eq. 3.4 to find the emergent generalized free energy $\mathscr{F}(x)$ shown in Fig. 3.3E. The free energy shows three regimes, corresponding to the three situations indicated in the bottom of Fig. 3.3C. For actin filaments behind the tip ($x < 0$), there is no condensation force since the actin filament does not interact with the microtubule tip region. The negative slope is caused by the effective backward drift of the actin filament in the co-moving frame. For actin filaments that (partially) overlap with the tip ($0 \le x \le l_t$), the condensation force F_f acts to maximize the overlap region, because the free energy decreases with increasing overlap length. For actin filaments protruding ahead of the tip ($x > l_t$), the overlap between the actin filament and the microtubule tip region can no longer increase, so the forward condensation force disappears. A very small negative backward force F_b remains, since the actin filament loses overlap with the microtubule lattice as x increases. However, the largest contribution of the upward slope of the free energy for $x > l_t$ is again caused by the effective backward motion in the co-moving frame. The combination of these three regimes creates an energy well, showing that actin transport is a meta-stable state. Interestingly, since the probability distribution $P(x)$ of the actin position x in the simulations is given by $P(x) \propto \exp(-\beta F(x))$ where $F(x)$ is the free-energy of the computational model, we could compare the theoretically predicted free-energy profile to $-\log P(x)$ as obtained from the simulations. The generalized free-energy profile obtained from the simulations (symbols in Fig. 3.3E) closely agreed with the theoretical prediction without any adjustable parameters, supporting the idea that actin transport arises from the balance between a driving condensation force and an opposing friction force.

3.2.4. SIMULATIONS AND THEORY CORRECTLY PREDICT ACTIN TRANSPORT TIMES

The simulations and the analytical theory made predictions about actin transport that could be directly tested against the experimental data. Specifically, we studied how the mean duration of transport $\langle T_t \rangle$ by growing microtubules changes with the microtubule growth velocity and actin filament length. We observed in Fig. 3.1C that actin transport ends by microtubule catastrophes, actin unbinding, or actin falling behind the tip region of the microtubule.

The likelihood that crosslinker unbinding will terminate actin transport is low when the overlap between the actin filament and the microtubule tip region is large, $x \gg 0$, since there will be many crosslinkers holding the actin filament and microtubule tip together. In the other limit that the actin filament falls behind the tip ($x < 0$), the transport event most likely ends by the actin filament rapidly falling even further behind. Hence,

the rate at which actin unbinding from the microtubule tip region ends actin transport is dominated by the probability that the actin filament starts to loose overlap with the microtubule tip region, i.e. reaches the top of the free-energy barrier at $x \approx 0$ (see Fig. 3.3C). This probability $P(x \approx 0)$ could be calculated using the effective free-energy profile, and scales exponentially with the growth velocity v_g (see SI Appendix). Once the actin filament has climbed up the energy barrier for unbinding and lost all connections with the microtubule tip region, unbinding still requires the filament to lose all connections to the microtubule lattice as well. Using Eq. 3.2, we calculated how the probability to be disconnected changes with the actin length l_a,

$$r_u = r_u^0 \mathrm{e}^{-l_a/\lambda_\ell} \mathrm{e}^{v_g/\gamma}. \tag{3.5}$$

Here, λ_ℓ is the same as in Eq. 3.2, and γ follows from the free energy and measures how fast the barrier height changes with the microtubule growth velocity v_g (see SI Appendix). Analytical expressions for λ_ℓ and γ are given in the SI Appendix. Only the prefactor r_u^0 remains unknown, so we fitted it once to the complete set of simulated average transport times that is shown in Fig. 3.4A and B.

To compute the rate at which the actin filament falls behind the tip region, $x < 0$, we noted that the filament has to cross a free-energy barrier to leave the tip region, as shown in Fig. 3.3E. Hence, we employed Kramers theory [131] to calculate the rate r_e at which

Figure 3.4 *(facing page)*: **Comparing experimental, simulation, and theoretical results for the mean transport times.** The transport time T_t is defined in Fig. 3.3B. **(A)** Mean actin transport time plotted against the growth velocity. Simulations and theoretical predictions shown for three different actin filament lengths. Experimental data is sorted according to the growth velocity and grouped into four sets with 63 or 64 data points each. The error bars represent $\left(\overline{v}_{g,i} \pm \mathrm{SD}_i, \overline{T}_{t,i} \pm \mathrm{SEM}_i\right)$, where i labels the four groups, a bar on a random variable represents the sample mean, SD is the standard deviation of the distribution of growth velocities, and the SEM is the standard error of the mean of the transport times over that group. The experimental data samples over a distribution of actin lengths $\overline{l}_a = 1.5 \pm 0.8$ µm (mean ± SD). The theory correctly predicts both the order of magnitude and the declining trend of the mean transport times. **(B)** Mean actin transport time plotted against the actin length. Simulations and theoretical predictions shown for three different microtubule growth velocities. The same experimental data as in A is sorted according to the actin length and divided into four equally sized groups of 63 or 64 data points each, with $v_g = 3.8 \pm 0.7$ µm min^{-1} (mean ± SD). The experimental data confirms the order of magnitude and the trends of the theoretical predictions. There is insufficient experimental data to test the declining transport times due to increased friction for $l_a > 4$ µm. However, for $l_a < 4$ µm, the experimental data confirms that the transport time increases due to an increase of the actin binding times when the actin length increases. **(C)** Fractions of transport events that end by microtubule catastrophes, actin falling behind the microtubule tip region, or actin unbinding from the tip region as a function of actin filament length. The fractions calculated from theoretical values of the catastrophe rate r_c, rate of falling behind r_e, and unbinding rate r_u are plotted as the indicated colored regions. We group the experimental data into two bins of equal size, because the four data bins used in B provide insufficient statistics per bin to calculate two numbers per bin. We calculate the mean actin length (horizontal error bars are the SD) and the fractions at which each mechanism ends the transport events in both bins. We report the borders between these three regions (vertical error bars are the SEM). Microtubule catastrophes either lead to backward actin transport or to actin unbinding, but are always counted as catastrophes in these fractions. The theory overestimates the fraction of unbinding events, but it correctly shows that unbinding events become less important with increasing actin length.

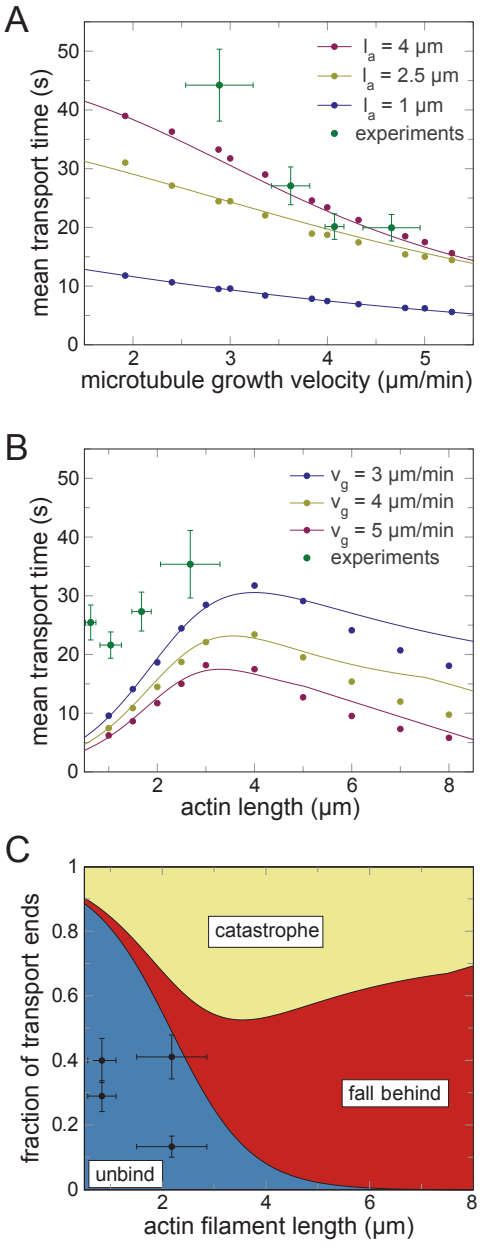
A
mean transport time (s)
microtubule growth velocity (μm/min)
l_a = 4 μm
l_a = 2.5 μm
l_a = 1 μm
experiments
B
mean transport time (s)
actin length (μm)
v_g = 3 μm/min
v_g = 4 μm/min
v_g = 5 μm/min
experiments
C
fraction of transport ends
actin filament length (μm)
catastrophe
fall behind
unbind

the actin filament escapes from the free-energy well,

$$r_e = \left[\int_{-\infty}^{l_t} \frac{e^{\mathcal{F}(x)/k_B T}}{D(x)} dx \int_0^{\infty} e^{-\mathcal{F}(x)/k_B T} dx \right]^{-1}. \tag{3.6}$$

Finally, we treated microtubule catastrophes as an independent process that occurs at a fixed rate r_c. The total rate at which transport ends is given by $r_t = r_u + r_e + r_c$, and the average transport time is simply the inverse of this rate, $\langle T_t \rangle = 1/r_t$.

We calculated $\langle T_t \rangle$ using this theoretical description, and additionally sampled T_t in computer simulations as a function of the microtubule growth velocity v_g and the actin length l_a. As shown in Fig. 3.4, the theory successfully described the simulation data, showing that the coarse-grained analytical theory is valid for all regimes probed in the simulations. Only the single parameter r_u^0 was directly fitted once to the complete set of lines in Fig. 3.4, otherwise all parameters in the theory are based on analytically calculable expressions or on ζ_ℓ and ζ_t, which were separately fitted to the diffusion constants in Fig. 3.3D. The curves in Fig. 3.4A show that higher growth velocities lead to shorter transport times. This is because the friction force between the filaments increases while the condensation force remains unchanged, lowering the free-energy barrier for unbinding. Fig. 3.4B shows that the theory also predicts a decrease of the transport time with increasing actin filament length, again due to an increased friction. However, the transport time is also small for short actin filaments, because in this case transport ends predominantly through actin unbinding. The model therefore predicted an optimal length for processive transport.

Experimentally, we observed a set of transport events, each characterised by a microtubule growth velocity v_g, actin length l_a, and transport time T_t. Since both v_g and l_a vary stochastically in the experiments, we sorted the experimental data according to the microtubule growth velocity (or actin length), and grouped the data into four sets with an equal number of data points each. Then, we calculated the mean $\overline{v}_g$ (l_a) and the mean $\overline{T}_t$ for each set, giving the four green data points in Fig. 3.4A (Fig. 3.4B).

The experimental data showed decreasing transport times for increasing growth velocities (Fig. 3.4A, see also Fig. S3.12A), a trend that was confirmed by calculations of Spearman correlation coefficients (Table S3.2). The experiments, having an average actin filament length of $\overline{l}_a = 1.5$ µm, both confirmed the predicted theoretical order of magnitude of mean transport times and the trends with varying the growth velocity (Fig. 3.4A). In addition, the experimental data showed increasing transport times for increasing filament length (Fig. 3.4B, see also Fig. S3.12B), which was also confirmed by calculations of Spearman correlation coefficients (Table S3.2). Again, having an average growth velocity of $\overline{v}_g = 3.8$ µm s^{-1}, the experimental data confirmed the order of magnitude and trends with varying actin length that were predicted by the theory in the small actin length regime (Fig. 3.4B). The experimentally observed actin filaments were not long enough to also probe the regime $l_a > 4$ µm where the transport time is predicted to decline again due to increased filament friction. The direct unbinding of short actin filaments from the microtubule tip region ends a significant fraction of the transport events, as shown in Fig. 3.2H. We can also use the theory to predict the fraction of the different events that can terminate transport: microtubule catastrophes, actin falling behind, and actin unbinding. As shown in Fig. 3.4C, we observed that the model parameters overestimate the

direct unbinding rate of the actin filaments, but does correctly predict that the fraction of unbinding events decreases strongly with increasing actin filament length.

3.2.5. CROSSLINKER BINDING CREATES A SIGNIFICANT CONDENSATION FORCE

As explained above, the analytical theory predicts a forward condensation force. To test this prediction, we used optical tweezer measurements in a simplified geometry where TipAct is attached to a bead in the absence of actin filaments (Fig. 3.5A). Each experiment started with placing such a TipAct-coated bead in front of a growing microtubule end with the trap. Successful binding of the bead to the microtubule tip region is evident from its movement towards a microtubule (Fig. S3.15A). The bead then gradually returned to the center of the trap as the microtubule grows (Fig. 3.5A,B), after which it continued to move against an opposing trap force until contact with the microtubule tip was lost and the bead returned to the trap center. We considered the signal starting at the first positive displacement of the bead against the opposing force until the smoothed bead trajectory crosses the zero displacement again as the force signal. Further analysis of these force signals are shown in Fig. S3.15B. From typical force signals as shown in Fig. 3.5C, we measured forces with a mean of 0.12 pN (±0.07, SD) for the same conditions as the previously described actin transport experiments (Fig. S3.15C). The measured force provided an estimate for the condensation force, since the opposing friction force is expected to be very small because of the low velocity.

In this simplified experimental geometry, where the TipAct-coated bead replaces the actin filament, our theory predicted a condensation force of roughly 0.2 pN on the bead (Eq. S3.26 of the SI Appendix), which is close to the value measured experimentally. We also observed experimentally that the force magnitudes decreased when we lower the crosslinker affinity for the microtubule by raising the salt concentration (Fig. S3.15C), consistent with Eq. S3.25 of the SI Appendix. This experimentally confirmed the predictive power of our theoretical model, and demonstrated that actin transport is indeed driven by a condensation force.

3.3. DISCUSSION

In this study, we have reconstituted transport of actin filaments by growing microtubule plus ends in the presence of transiently binding crosslinkers. We have shown that this transport is governed by a condensation force and a competing friction force that are both caused by the crosslinkers. Microtubule growth leads to the net motion of the chemically distinct microtubule tip region. The actin filament recognizes the microtubule tip region through cross-linking proteins that bind more strongly to the tip region compared to the lattice region, creating a force that tries to maximize the overlap between the actin filament and the microtubule tip region. The resulting mechanical movement of the actin filament is opposed by a friction force with the static microtubule lattice, and actin movement is only possible if the crosslinkers adjust their binding positions on the actin filament through (un)binding dynamics. Hence, increasing the condensation force by increasing the crosslinker density does not necessarily lead to longer-range actin transport, since the crosslinker induced friction force between the filaments

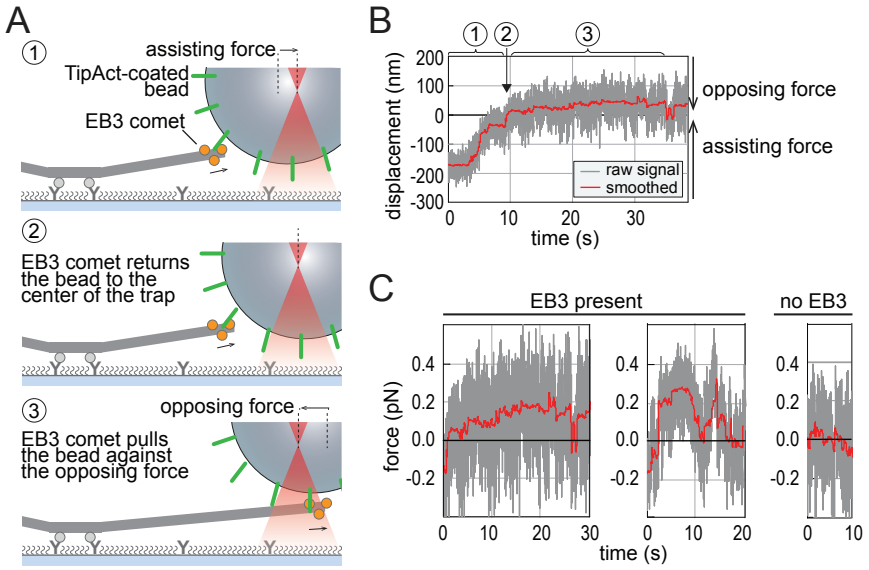

Figure 3.5: **Optical tweezer measurement of the force developed by cargo-bound TipAct at the growing microtubule plus end.** **(A)** Schematic diagram of the experimental setup. A TipAct-coated bead is initially attached to a growing microtubule carrying an EB3 comet. The bead moves back to the center of the trap under the assisting force (1). After having arrived in the trap center (2), the bead is pulled by the EB3 comet against the opposing force from the trap (3). **(B)** A typical recording of a bead moving against the opposing trap force with experimental steps numbered according to (A). **(C)** Examples of forces exerted by growing microtubule ends through the TipAct coupling in presence or absence of EB3.

is also increased.

In recent years, it is becoming increasingly clear that, in addition to motor-driven and (de)polymerization-driven forces, passive crosslinkers can also generate active forces. One mechanism for passive crosslinkers to generate active forces is via entropic expansion [111], where the overlap region between two filaments is maximized to increase the entropy of a fixed number of diffusible crosslinkers, as was shown for Ase1 crosslinkers that connect anti-parallel microtubules in the mitotic spindle [111]. A second mechanism to generate active forces by passive crosslinkers is via their binding affinity for overlap regions when the crosslinkers are present in the solution. This mechanism creates an effective affinity between the filaments, which can result in bundle contractions as was shown for FtsZ filaments in bacteria [122] and for actin filaments [110, 123]. Here we show that this condensation force can also cause directed transport of actin filaments by growing microtubules biased forward by the higher density of crosslinkers present at the growing tip.

The mechanism that we describe is reminiscent of a previously proposed mechanism for cargo transport by shrinking microtubules binding in a sleeve, originally proposed as a mechanism for chromosome transport via kinetochores [118]. Also in that case, the force that drives the transport is simultaneously countered by a friction force between the sleeve and the microtubule. However, previous theoretical analysis of chro-

mosome transport focused on finding the meta-stable distribution of microtubule positions within the sleeve [118]. In contrast, we not only calculate the free energy profile (Fig. 3.3E) but also the transport time distribution that results from this meta-stable state. Furthermore, while actin transport is driven by the higher affinity of the actin filament for the tip of the growing microtubule than for its lattice, the sleeve-based transport is driven by a depolymerizing microtubule.

Another example of condensation forces that result in processivity is a recent experimental study on pulling of membrane-tubes by growing microtubules [121]. Similar to the transport of actin filaments, the forward force on the membrane tubes is driven by the affinity of the membrane for the growing microtubule plus-end. However, the actin filament slides relative to the microtubule, causing a friction force, whereas the fluid nature of the membrane means that the pulled tubes can spread over the microtubule like a continuous track without creating any friction force.

Actin transport by growing microtubule plus ends results in much lower forces than are measured for microtubule motor proteins 0.10 pN for microtubule growth compared to 1-10 pN for single motors or collectives of motor proteins) [132, 133]. In direct competition, motor forces would therefore likely dominate over the condensation forces. However, condensation forces can remodel actin filaments specifically at the growing microtubule plus end, whereas motor-driven forces remodel actin filaments along the microtubule lattice, or at depolymerizing microtubule ends [83, 134]. Tip-localized transport of actin filaments may be relevant given recent studies that uncovered two distinct pathways to specifically nucleate new actin filaments at the growing microtubule plus end [87, 88]. The transport mechanism identified in our study could rapidly relocate those filaments to the leading edge of the cell, where they influence the formation of new actin-based protrusions. See also a recent theoretical study which investigates how microtubule-based transport could influence the actin distribution within spherical cells [135]. Finally, we note that the transport mechanism we describe might also be used to transport other cytoskeletal filaments in cells, such as intermediate filaments [136–139], and that the theoretical description we present may be applicable not only to filament transport, but also to transport by propagating reaction-diffusion patterns on membranes, such as the transport of plasmids by ParA [140–142].

ACKNOWLEDGEMENTS

We thank Jeffrey den Haan and Marjolein Vinkenoog for actin purification, and Andrea Martorana for TipAct purification. We thank Michel Steinmetz for the gift of EB3's. We thank Maurits Kok for help with image analysis. We thank Michele Monti for many useful discussions. This work was supported by the European Research Council (Synergy grant 609822 to M.D. and A.A.).

3.4. SUPPLEMENTAL INFORMATION

3.4.1. MATERIAL AND METHODS

ACTIN TRANSPORT ASSAYS

Experiments were prepared as previously described in Chapter 2. In short, actin filaments were pre-polymerized at 7.5 μM G-actin concentration (15 mol % labelled and 85 mol % unlabelled premixed monomers) in MRB80 for 30–90 min at room temperature, before adding phalloidin (Sigma-Aldrich) in 1:1 molar ratio to stabilize the filaments. Dynamic microtubules were nucleated from guanylyl-(α, β)-methylene-diphosphonate (GMPCPP) stabilized microtubule seeds, which were bound to the biotinylated surface and prepared according to standard double-cycling protocols [92, 99]. Any non-attached seeds were rinsed off with MRB80 before adding the final imaging mix. The core imaging buffer consisted of MRB80 supplemented with 0.5 mg/ml κ-casein, 0.2% (v/v) methyl cellulose (M0512, Sigma-Aldrich Chemie B.V., the Netherlands), 75 mM KCl, 1 mM guanosine triphosphate(GTP), 0.2 mM Mg-ATP and an oxygen scavenging system [4 mM dithiothreitol (DTT), 2 mM protocatechuic acid (PCA) and 100 nM protocatechuate-3,4-dioxygenase (PCD)]. This solution futher contained tubulin concentrations ranging from 20 to 30 μM (6 mol % Rhodamine labeled), 7.5-10 nM F-actin, 133 nM EB3 (mCherry or GFP labeled), and 50 nM TipAct (GFP). The pre-polymerized actin filaments were shortened in length by harsh pipetting of the actin mix after dilution.

ACTIN TRANSPORT DATA ANALYSIS

Image processing and analysis were performed using plugins for Fiji [105] or ImageJ and custom-written programs in Python or MATLAB. Timelapse series of TIRF images were drift-corrected using a custom-written Matlab program. Kymographs of microtubule growth were created using the reslice tool in Fiji [105]. Plus and minus ends were distinguished based on their growth rates: faster-growing ends were identified as the plus ends and the slower-growing ends as the minus ends. The parameters characterizing actin transport and microtubule dynamics were determined from these timelapses and kymographs.

A microtubule/actin interaction event was classified as transport and included in further analysis when (1) an actin filament colocalized with an EB3/TipAct-complex at the growing microtubule plus end, (2) moved for at least 0.5 μm (3 pixels) and for 9 sec (3 pixels) along with the microtubule tip, and (3) was not interacting with other actin filaments or microtubules. The actin filament length and tracking time were obtained from manual fits on the kymographs. From the original time lapse image series, the binding states of the actin filament before and after the transport event were determined.

SIMULATIONS AND THEORETICAL MODELING

The simulations are based on a modified version of the algorithm described in [112]. All details are described in the SI Appendix.

OPTICAL TWEEZERS

Silica beads (1 μm in diameter) functionalized with carboxy groups (Bangs Laboratories) were conjugated PLL-PEG-Biotin (PLL(20)-g[3.5]-PEG(2)/PEG(3.4)-Biotin(10%), SuSoS AG, Switzerland) as described [143]. 10 μL of PLL-PEG-coated beads (ca 0.2% w/v) were

washed in washing buffer (80mM K-Pipes pH 6.9 with 1mM EGTA, 4mM $MgCl_2$, 1mM DTT and 0.5 mg/ml casein) by centrifugation for 1 min at 16000 g, then resuspended in 20 µL of 8 µM Neutravidin (Thermo Scientific) in the same buffer. After 30min incubation at 23°C with frequent mixing, the beads were washed twice in 100 µL of the washing buffer, resuspended in 20 µL of 0.2 µM biotinylated anti-GFP IgG (Rockland) and further incubated for 30 min at 23°C with frequent mixing. After two more washes in the washing buffer, the beads were resuspended in 20 µL 120nM GFP-TipAct and incubated for 1 hour on ice with frequent mixing. Finally, the beads were washed 3 times and resuspended in 50 µL of the washing buffer.

To attach microtubule seeds to glass, we used digoxigenin (DIG)-labelled tubulin to prevent interactions with the biotinylated beads. Briefly, tubulin was purified from porcine brain [144] and chemically labelled with NHS-DIG [145]. GMPCPP stabilized microtubule seeds were prepared using 30% DIG-labelled tubulin and according standard double-cycling protocols [99].

Optical trapping was performed as described previously [121]. Slides and coverslips were silanized using Plus-One Repel Silane (GE Life Sciences), then assembled into flow chambers using double-sided tape and functionalized with 0.2 µM anti-DIG IgG (Roche), then passivated with 1% Pluronic F-127 in MRB80, before DIG-labelled seeds were introduced. The reaction mix (80 mM K-Pipes pH 6.9, 50 or 75 mM KCl, 1 mM EGTA, 4 mM $MgCl_2$, 1mM GTP, 1 mg/ml κ-casein, 4 mM DTT, 0.2 mg/ml catalase, 0.4 mg/ml glucose oxidase, 20 mM glucose and either 25 mM unlabelled tubulin with addition of 133 nM EB3, or 10 mM unlabelled tubulin in the absence of EB3) was centrifuged at 30 psi for 5 min. TipAct-coated beads were added to the supernatant at a ratio of 1:33-1:50. This final mix was then introduced into the flow chamber, and experiments were carried out at 25°C.

DIC microscopy and optical trapping were performed as described previously [143]. Measurements were performed at nominal trap power of 0.2W (the lowest setting of our instrument), and then the trap stiffness was additionally softened down to 4-6·10-3 pN/nm using a circular polarizing filter placed in the wave path of the trapping laser. The QPD signal was recorded at 10 kHz.

3.4.2. SUPPLEMENTARY FIGURES

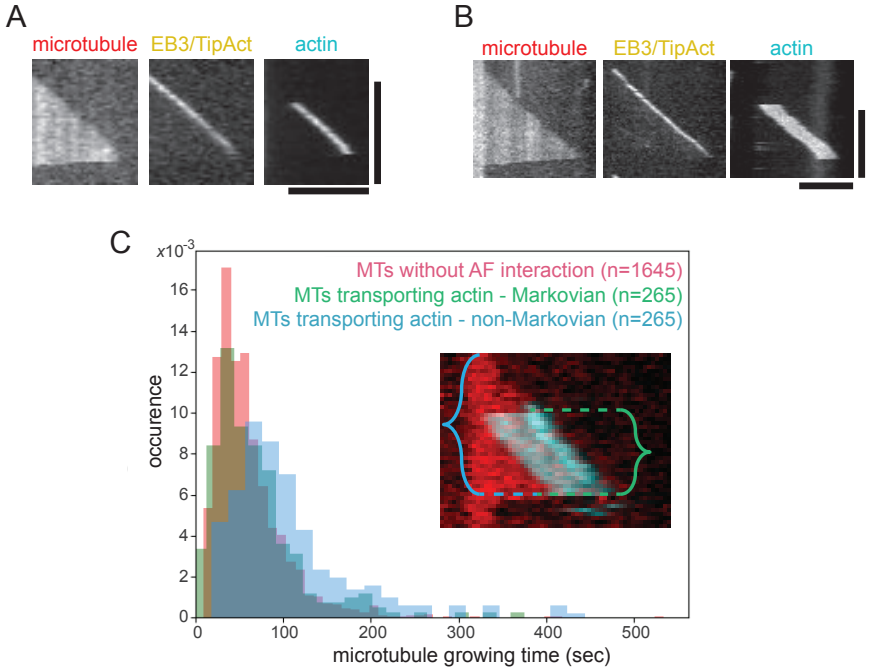

Figure 3.6: **Supplemental for main Figure 1.** **(A)** Kymograph (a space-time plot) of actin transport event, as is also shown in Fig. 3.1D (top). **(B)** Kymograph (a space-time plot) of actin transport event, as is also shown in Fig. 3.1D (bottom). **(C)** Normalized distribution of microtubule growing times for growth events where the microtubule does not interact with actin filaments (red) and for growth events where microtubules transport an actin filament (blue). For the actin-transporting microtubule growth events, we also show the growing time starting at the binding of the actin filament (green, a Markovian process), as is indicated by the accolades in the inset too. Average catastrophe rates of 1.00±0.03, 0.89±0.05 and 0.57±0.03 events/min for non-interacting MTs, actin-transporting MTs measured upon actin binding, and complete growth events of actin-transporting MTs, respectively. Number of measured growth events indicated in figure. Scale bars: 5 µm (horizontal) and 2 min (vertical).

Figure 3.7 *(facing page)*: **Supplemental for main Figure 1.** **(A)** TipAct in the absence of actin filaments tracks the growing microtubule plus tip. Images show microtubule seeds and EB3 in red, tubulin in cyan, TipAct in yellow, and the merged image. **(B)** TipAct is present at the growing microtubule plus tip during actin transport events. Images show microtubule seeds and EB3 in red, TipAct in yellow, actin filaments in cyan, and the merged image. Note that in this experiment, tubulin is not labeled. **(C)** Separate channels for typical field of view shown in Fig. 3.1B. A cropped region of 54 by 54 µm was used for analysis. **(D)** Time series of the growing plus ends of a microtubule that recruits and transports an actin filament via EB3/TipAct complexes, as is shown in Fig. 3.1C. Scale bars: 5 µm (horizontal) and 2 min (vertical) in A,B; 20 µm in C; and 5 µm in D.

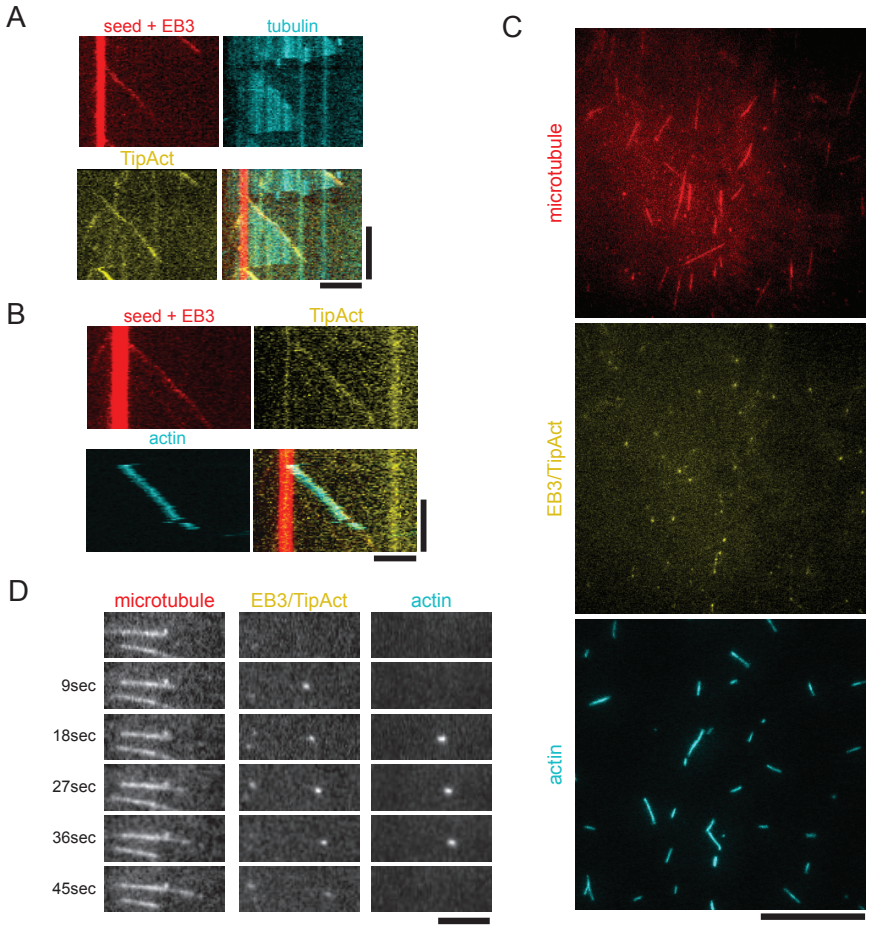
A
seed + EB3
tubulin
TipAct
B
seed + EB3
TipAct
actin
C
microtubule
EB3/TipAct
actin
D
microtubule
EB3/TipAct
actin
9sec
18sec
27sec
36sec
45sec

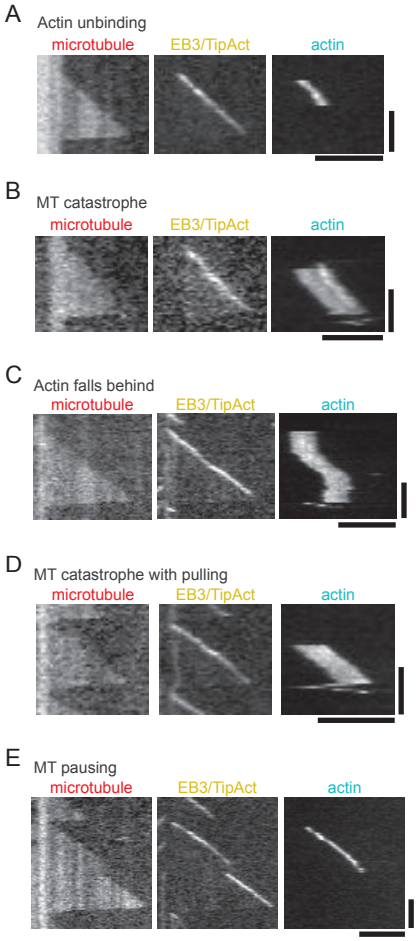

Figure 3.8: **Individual channels of transport events shown in main Figure 2.** **(A)** Kymograph of a typical transport event that ends by the unbinding of the actin filament, as is also shown in Fig. 3.2A. This is the same transport event that is also depicted as a time series in Fig. 3.1C and Fig. 3.7D. **(B)** Kymograph of a typical transport event that ends upon a microtubule catastrophe, as is also shown in Fig. 3.2B. **(C)** Kymograph of a typical transport event that ends by loss of contact of the actin filament with the tip resulting in the actin filament falling behind and lingering on the MT lattice, as is also shown in Fig. 3.2C. **(D)** Kymograph of a typical transport event that ends upon a microtubule catastrophe where the actin filaments is pulled along by the shrinking microtubule, as is also shown in Fig. 3.2D. **(E)** Kymograph of a typical transport event that ends upon a microtubule catastrophe, as is also shown in Fig. 3.2E. Scale bars: 5 µm (horizontal) and 60 s (vertical).

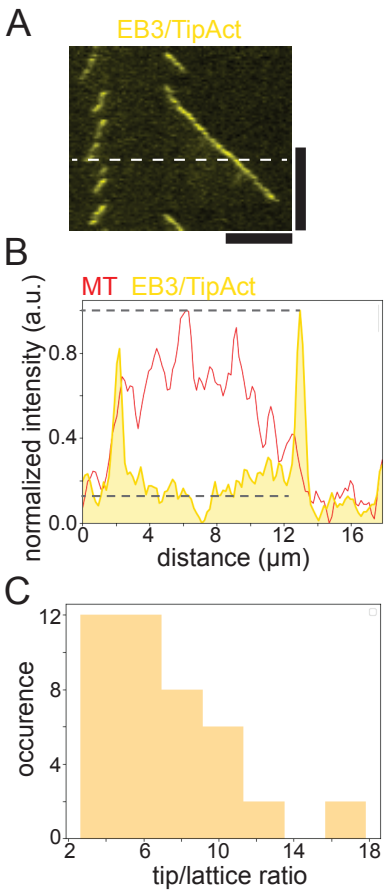

Figure 3.9: **Ratio between the signal of EB3 and TipAct on the microtubule tip and on the lattice.** **(A)** Example kymograph showing the (GFP) signal of both EB3 and TipAct, from which tip/lattice-ratios can be calculated. The dashed line was used to produce an intensity profile. **(B)** Intensity profile showing the lattice (red) and plus end intensity of EB3 and TipAct (yellow). Dashed lines on the profile, showing the maximum value and the mean value along the microtubule lattice for GFP, were used to estimate the 1:10 lattice:tip ratio of the tiptracking-complex. **(C)** Distribution of tip/lattice ratios for 42 analysed profiles of EB3/TipAct intensity while transporting an actin filament, with 6.9 and 5.9 as the mean and median values of this distribution, respectively. Scale bars: 5 µm (horizontal) and 2 min (vertical)

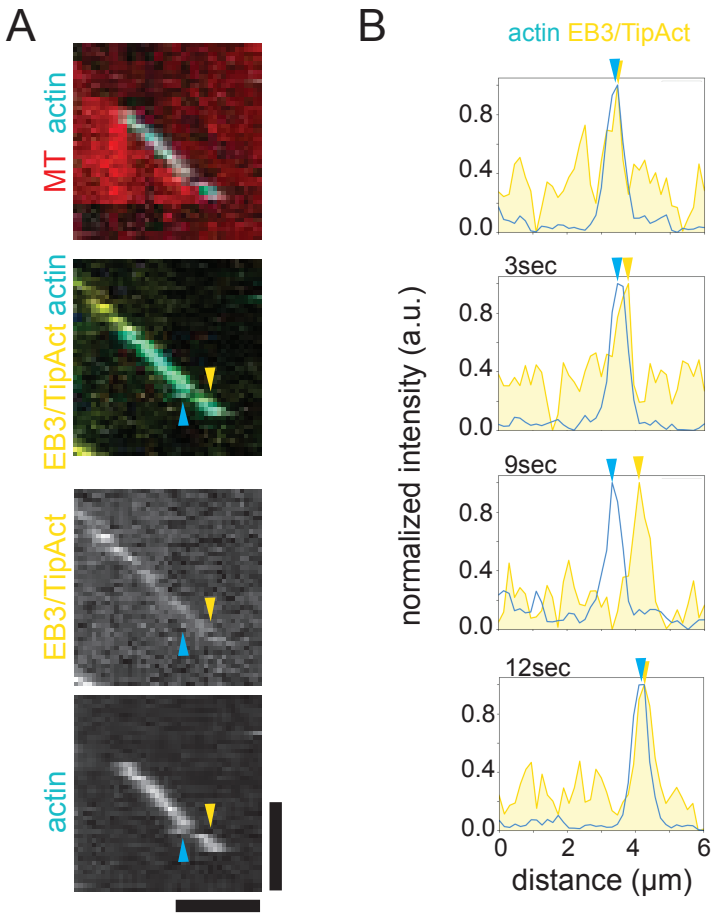

Figure 3.10: **Catching-up of actin filament to tip-tracking-complex. (A)** Kymograph showing a growing microtubule (red), the tip-tracking-complex consisting of EB3 and TipAct (both yellow), and a transported actin filament (cyan). At one point, the actin filament (cyan arrow) falls behind the tip (yellow arrow), but remains at the microtubule lattice and quickly catches up with the tip-tracking-complex again to continue transport. **(B)** Line profiles along the kymograph in *A*, showing an actin filament catching up with the tip-tracking-complex. Arrows indicate the locations of the actin filament (cyan) and of the tip-tracking-complex (yellow). Scale bars: 3 µm (horizontal) and 60 sec (vertical).

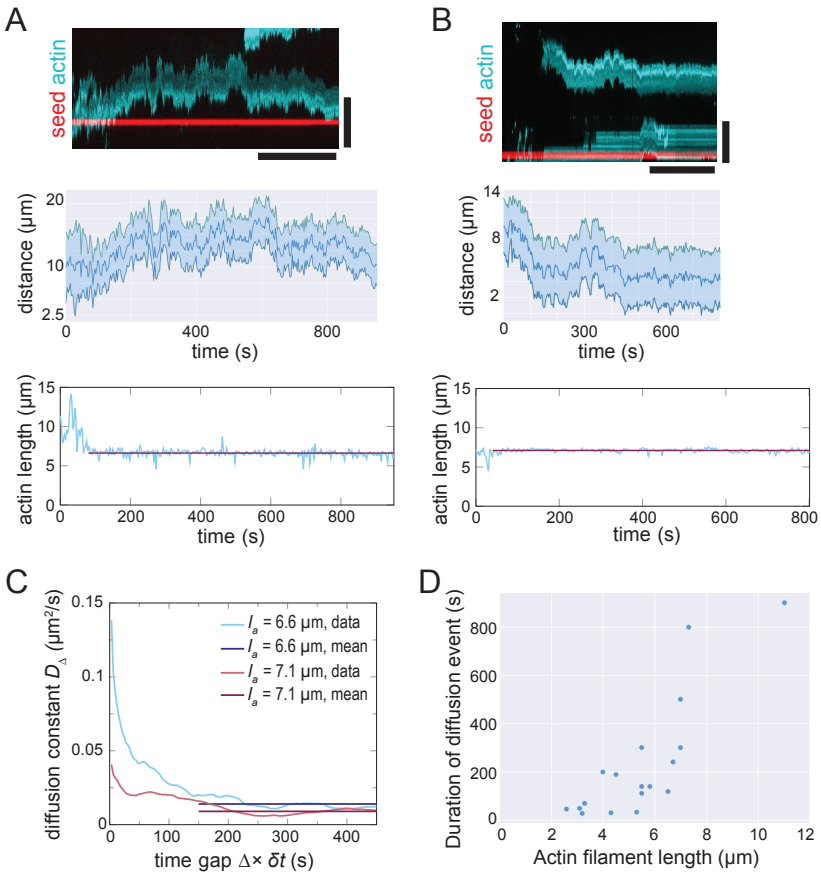

Figure 3.11: **Diffusion of actin filaments along the microtubule lattice.** **(A)** Diffusion of 7.1 μm long actin filament along the microtubule lattice in a kymograph (top), corresponding time trace of the filament front and rear end positions (middle), and the filament length fluctuations used to determine the actin filament length (bottom). **(B)** Another example, showing diffusion of a 6.6 μm long actin filament. **(C)** Diffusion constant estimates given by Eq. S3.15. For small time scales, the observed actin position fluctuations are influenced by external noise and length fluctuations, so we can only extract the diffusion constant at large time scales. We take the sample mean of the estimator over the window between 150 s and 450 s, yielding $\overline{D} = 0.014(3)\ \mu m^2 s^{-1}$ (l_a = 6.6 μm) and $\overline{D} = 0.009(3)\ \mu m^2 s^{-1}$ (l_a = 7.1 μm). **(D)** The typical duration of diffusion events increases with the actin filament length, since the rate at which the actin filament unbinds from the microtubule lattice region decreases with the number of crosslinkers that connect the two filaments. Scale bars in panels A,B: 5 min (horizontal), 10 μm (vertical).

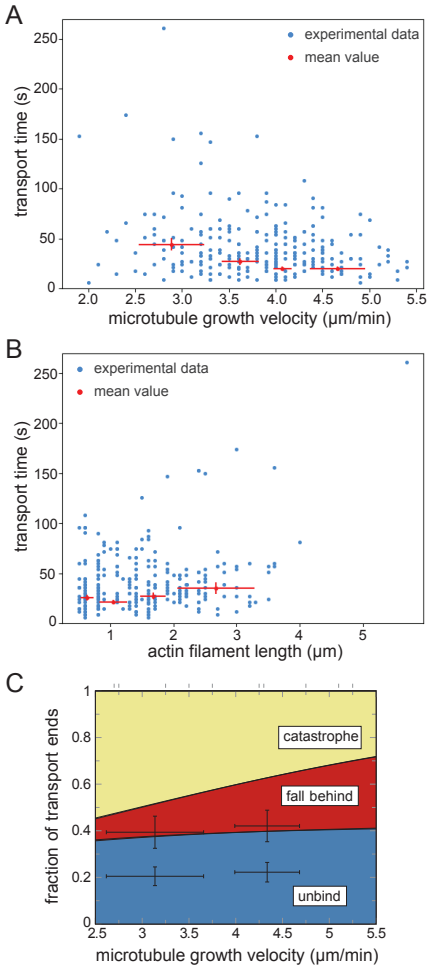

Figure 3.12: **Unbinned and binned experimental data for actin transport. (A)** The transport time versus the microtubule growth velocity and **(B)** the transport time versus the actin filament length. This data is complementary to the data shown in main text Fig. 3.5A,B. Single data points are shown in blue; binned experimental means (when distributing data in 4 bins of equal size) are shown in red and are also depicted in main text Fig. 3.5A,B. Horizontal error bars represent the standard deviation of the growth velocities or the actin filament length within the bin, and vertical error bars represent the standard deviation of the mean transport time. **(C)** The fractions of the categories of transport ends as a function of the microtubule growth velocity. The fractions were calculated from experimental values of the catastrophe rate (constant r_c), falling behind rate (Eq. 3.6 of the main text) and unbinding rate (Eq. 3.5 of the main text). Experimental data was binned into two bins of equal size, shown as points with errors. Transport events ending by microtubule catastrophes include both events where actin is pulled back with the depolymerizing microtubule and events where the actin unbinds upon a catastrophe. The horizontal error bars show the weighted standard deviation of the microtubule growth velocity and of the actin filament length, and the vertical error bars show the standard error of the estimated mean ratio. Since we have to estimate two data points per bin with sufficient statistics, we only divided the growth velocities and actin lengths into two bins.

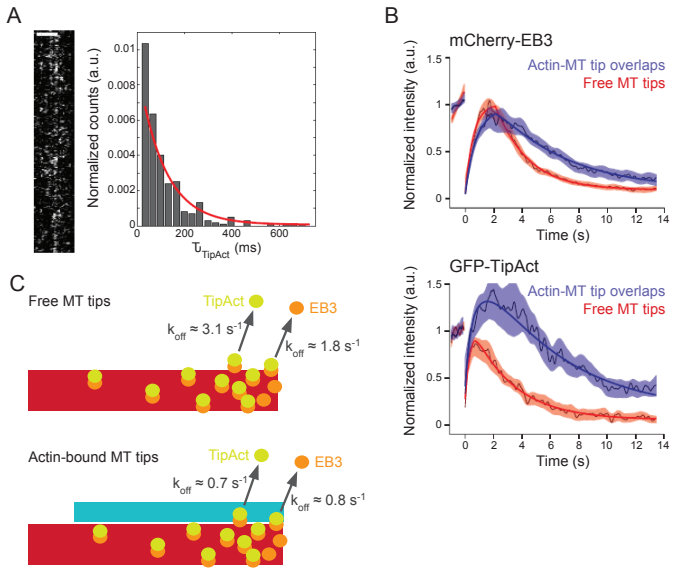

Figure 3.13: **Binding dynamics of the tip-tracking complex. (A)** TipAct single-molecule dwell times on actin filaments. High temporal resolution kymograph of TipAct molecules showing multiple binding and unbinding events at a surface-bound actin filament (left), and a normalized distribution of TipAct dwell times (right), including single-exponential fit (red curve) which yielded an average dwell time of 111±6 ms (n=301) and corresponds to a single-molecule off-rate of about 0.01 s^{-1}. **(B)** FRAP experiments to probe protein off-rates at microtubule plus-ends. We analyze the recovery curves for mCherry-EB3 (top) and GFP-TipAct (bottom) at both free (red) and actin-bound (blue) microtubule tips. The solid lines show fits (see methods description below), and the thin colored lines and shaded areas show the average curves and SEM for n = 19 (free) and n = 13 (actin-bound) recovery profiles for mCherry-EB3, and n = 7 (free) and n = 6 (actin-bound) recovery profiles for GFP-TipAct, respectively. Note that the maximum recovery intensity of GFP-TipAct at actin-bound microtubule tips reaches values larger than one due to the variable amount of GFP-TipAct that can localize to the F-actin bundles independently of microtubules. **(C)** Schematics to interpret the FRAP experiments. Top, showing the unbinding rates for EB3 and TipAct at free microtubule plus ends. Bottom, showing the unbinding rates for EB3 and TipAct at actin-bound microtubule plus ends.
Methods for the results presented in this figure: (A) Actin filaments were bound to the coverslip surface via biotin-streptavidin links. Thereafter, TipAct was added to the flow cell at a concentration of 25 nM and TIRF microscopy imaging was performed at 33 ms/frame. (B) Fitting of FRAP data: for the free microtubule tips (i.e. not bound to an actin bundle), a reaction-limited recovery curve multiplied by a decaying single-rate exponential envelope was sufficient to describe the recovery. Thus, the equation used to fit the free MT tips data was: $I(t) = (A - B * exp[-t * k_{off-free}]) * exp[-H(t-t_0) * (t-t_0) * k_{decay-free}] + D + (1 - exp[-H(t-t_0) * (t-t_0) * k_{decay-free}]$, where A, B and D are constants, $k_{off-free}$ the off-rate of mCherry-EB3 (or GFP-TipAct) at microtubule tips, k_{decay_free} the transition rate from a tip-like to a lattice-like binding profile (related to GTP hydrolysis), and $H(t-t_0)$ the Heaviside function to account for the fact that this transition occurs with a time delay. For microtubule tips bound to actin, we used a modified version of this equation to fit the data, namely: $I(t) = (A - B * exp[-t * k_{off-free}] - C * exp[-t * K_{off-bound}]) * exp[-H(t-t_0) * (t-t_0) * k_{decay-bound}] + D + (1 - exp[-H(t-t_0) * (t-t_0) * k_{decay-bound}]$, where $k_{off-free}$ is the off-rate of mCherry-EB3 (or GFP-TipAct) bound only to microtubule tips and $k_{off-free}$ is the off-rate of mCherry-EB3 (or GFP-TipAct) bound both to the microtubule tip and actin.

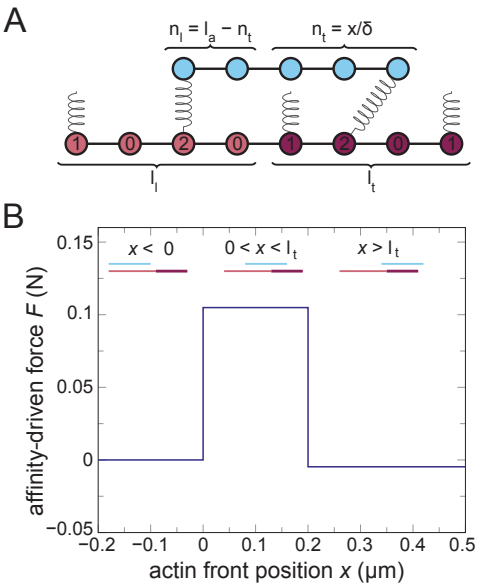

Figure 3.14: **Analytical calculations of the condensation forces.** **(A)** Parameter definitions: ℓ_ℓ is the number of binding sites in the microtubule lattice region, and ℓ_t is the number of binding sites in the microtubule tip region. The actin filament contains ℓ_a binding sites, which are split into n_ℓ sites that overlap with the microtubule lattice and n_t sites that overlap with the microtubule tip. The actin position x, defined as the distance between the front of the actin filament and the back of the microtubule tip region (see main Fig. 3.3C), equals $n_t \times \delta$, where δ is the lattice spacing between binding sites. We describe the full configuration of all crosslinkers by labeling each microtubule binding site with its binding state: no crosslinker is bound (0), a dangling crosslinker is bound (1), or a crosslinker is bound that connects with the actin (2). To calculate the condensation force, we take into account all possible extents to which the crosslinker can stretch. **(B)** The calculated condensation force on the actin filament as a function of the actin position x. When the actin filament is behind the tip ($x < 0$, top-left cartoon), the condensation force vanishes. When the actin filament is partially overlapping with the microtubule tip region ($0 < x < l_t$, top-center cartoon), there is a forward affinity driven force caused by the crosslinker affinity for the microtubule tip region compared to the lattice region. When the actin filament is sticking out in front of the microtubule ($x > l_t$, top-right cartoon), a tiny negative force acts on the actin filament due to the crosslinker affinity for the microtubule lattice region.

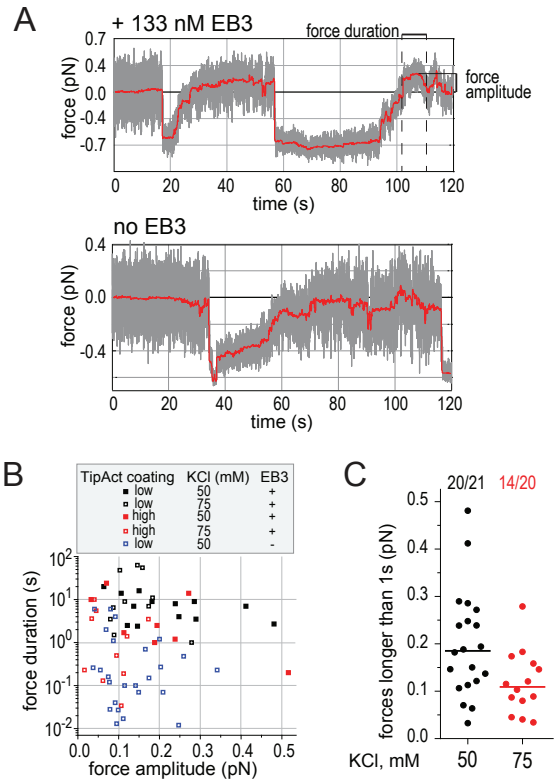

Figure 3.15: **Additional optical tweezer force measurements. (A)** Examples of full recordings of TipAct-coated beads interacting with growing microtubule ends in presence or absence of EB3. **(B)** Distribution of duration and amplitude of forces obtained in conditions indicated in the legend. In absence of EB3, most forward force events last shorter than 1 s. **(C)** Distribution of force amplitudes for force events lasting longer than 1 s, comparing two different salt concentrations, with average forces of 0.20±0.11 pN for 50 mM KCl and 0.12±0.07 pN for 75 mM KCl (mean±SD). For the actin transport assays, we used 75 mM KCl. Straight lines are the median forces (0.19 pN for 50 mM KCl and 0.11 pN for 75 mM KCl). The number on top indicates the number of force events included in the distribution, where both low- and high-density TipAct coatings are combined and events lasting shorter than 1 s are excluded, compared to the total force events measured for each salt concentration.

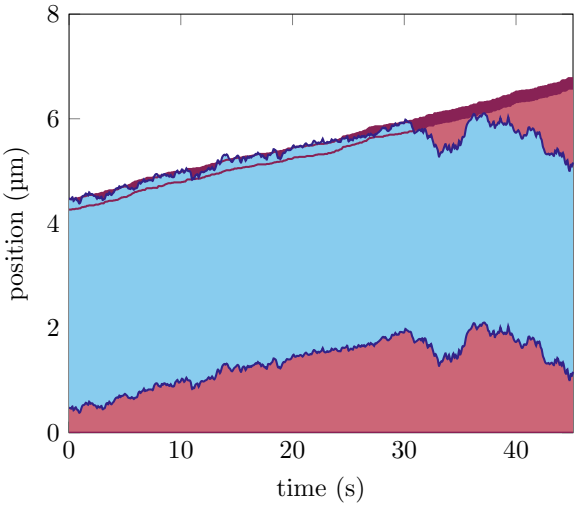

Figure 3.16: **Simulations show that actin transport by growing microtubules also occurs when tip sites hydrolyse stochastically, resulting in an exponentially decaying density of tip sites.** New sites are added with a rate of 6.25 s^{-1} (microtubule growth velocity of $v_g = 3$ µm min^{-1} from experimental data) and all tip sites decay to lattice sites with a rate of 0.25 s^{-1}. These values lead to a density of tip sites that decays exponentially with a length scale of 0.2 µm, matching the experimentally observed approximate tip length. The other parameter values are listed in Table S3.1.

3.4.3. SUPPLEMENTARY TABLES

Parameter	Value	Sources
Lattice spacing binding sites δ	0.008 µm	literature [96], [146–149];
Microtubule tip size l_t	0.2 µm	imaging;
Binding rate to microtubule tip $r^T_{0,1}$	3 s^{-1}	literature [23, 103], transport;
Unbinding rate from microtubule tip $r^T_{1,0}$	4 s^{-1}	FRAP, transport, literature [23, 103];
Binding rate to microtubule lattice $r^L_{0,1}$	1 s^{-1}	fluorescence, diffusion, transport, unbinding;
Unbinding rate from microtubule lattice $r^L_{1,0}$	60 s^{-1}	fluorescence, diffus., transport, unbind.;
Basic binding rate to actin filament $r^0_{1,2}$	75 s^{-1}	diffusion, transport, unbinding;
Basic unbinding rate from actin filament $r^0_{2,1}$	300 s^{-1}	diffusion, transport, unbinding;
Effective spring constant k	$2 \times 10^4\, k_B T$ µm^{-2}	literature [112], [150–152], diffusion, transport, unbind.;
Diffusion constant bare actin filament D_a	1 µm^{2}s^{-1}	literature [149], [153–155], viscosity;
Actin unbinding time τ_a	5×10^{-3} s	viscosity;

Table 3.1: **Model parameters, their values used in the simulations, and the sources used for determining the parameter values.** As explained in the supplemental text, we use a combination of experimental observations to self-consistently choose the model parameters, and most of these observables are influenced by multiple parameters. Hence, we manually varied the parameters and searched for a parameter set that is consistent with all experimental observations. The sources that influenced each parameter value are previously published data (literature), direct microscopy observations (imaging), the typical duration of actin transport events without the effects of actin unbinding or microtubule catastrophe (transport), fluorescence recovery after photobleaching experiments determining effective unbinding rates (FRAP), experimental observations of the actin diffusion constant (diffusion) or binding duration (unbinding) on the microtubule lattice, and calculations of the viscous drag of the solution on an actin filament (viscosity, Eq. S3.17).

	MT growth velocity and transport time		Actin filament length and transport time	
	Correlation	Permutation	Correlation	Permutation
Experiments (n=265)	−0.16	0.01 ± 0.06	0.17	0.01 ± 0.06
Experiments selective ends (n=103)	−0.25	0.00 ± 0.09	0.33	0.00 ± 0.09
Simulations (n=60000)	−0.252	0.000 ± 0.004	0.113	0.000 ± 0.004

Table 3.2: **Spearman correlation coefficients show that the transport time observed experimentally decreases with the microtubule growth velocity while it increases with the actin length.** By making 100 random permutations of the transport times linked to the growth velocities or the actin lengths, we find the range of Spearman coefficients that can be expected for an uncorrelated data set (mean ± SD), showing that the measured correlation coefficients are significantly outside of this range. By selecting only those events that end by actin falling behind the microtubule tip region ('selective ends' in the table), we find similar correlation coefficients. Finally, we perform the same analysis on the two simulation data sets shown in Figs. 4A,B. Each data point in those figures is the result of simulating 2000 events, giving 66 000 events for the set varying the growth velocity and 60 000 events for the set varying the actin length. The correlation coefficient between the transport time and the growth velocity obtained in the simulations is comparable to the correlation coefficient found in experiments, while the correlation coefficient between the transport time and the actin length agrees in the sign, but is lower in magnitude for the simulations than for the experiments. The reason for this discrepancy is that the simulation data extends to larger actin lengths where the transport time decreases again.

3.4.4. SI APPENDIX

EFFECT OF MICROTUBULE CATASTROPHES ON THE TRANSPORT TIME DISTRIBUTION

As shown in Fig. 3.2H of the main text, transport events typically end in one of three ways: (i) actin can fall behind the growing microtubule tip and escape to the microtubule lattice, (ii) actin can unbind directly from the microtubule tip and escape to the solution, or (iii) a microtubule catastrophe occurs. We call stochastic times at which these events happen T_e, T_u, and T_c, respectively. Our model assumes that these three random variables are independent, and the shortest time decides which event actually occurs. In this section, we discuss a framework to separate the events that end with the actin falling behind the tip or unbinding from simple catastrophe events. We are interested in this separation of events, because, accounting for the crosslinker properties in our model, we want to check whether it can explain how long actin filaments remain associated with growing microtubule tips. Hence, we group the former two event types, $T_i \equiv \min(T_e, T_u)$, and refer to them as events of interest. In case of a microtubule catastrophe, the actin filament either unbinds from the microtubule or it is transported back by the shrinking microtubule (see Fig. 3.2B and Fig. 3.2D), but we consider the microtubule catastrophe itself to be responsible for terminating transport in both cases, since we only focus on forward transport. We call $r_i = r_e + r_u$ the rate at which the events of interest occur, and we call the rate of microtubule catastrophes r_c. Then, the experimentally measurable rate r_t at which the transport events end is given by

$$r_t = r_i + r_c. \tag{3.7}$$

The observed transport time T_t obeys

$$T_t = \min(T_i, T_c)\,. \tag{3.8}$$

Since events ending with versus without a microtubule catastrophe are independent and exponentially distributed, we have

$$\mathbb{P}(T_t > t) = \mathbb{P}(T_i > t \wedge T_c > t) = \exp[-(r_i + r_c)\,t]\,, \tag{3.9}$$

consistent with Eq. S3.7.

If we cut out the events that end in catastrophes, we observe the transport time distribution

$$\mathbb{P}(T_t > t \mid T_i < T_c) = \frac{\mathbb{P}(T_i > t \wedge T_i < T_c)}{\mathbb{P}(T_i < T_c)}, \tag{3.10}$$

where we rewrite the first probability using Bayes' theorem and Eq. S3.8. We can calculate the probability density of T_c (events ending by a microtubule catastrophe) happening at time t', and integrate over all possible t',

$$\begin{aligned}\mathbb{P}(T_i > t \wedge T_i < T_c) &= \int_0^\infty \mathbb{P}\left(t < T_i < t'\right) r_c \exp\left[-r_c t'\right] \mathrm{d}t' \\ &= \int_t^\infty \left(\exp[-r_i t] - \exp\left[-r_i t'\right]\right) r_c \exp\left[-r_c t'\right] \mathrm{d}t' \\ &= \frac{r_i}{r_i + r_c} \exp[-(r_i + r_c)\,t]\,.\end{aligned} \tag{3.11}$$

In a similar fashion, one can show that

$$\mathbb{P}(T_i < T_c) = \frac{r_i}{r_i + r_c}. \tag{3.12}$$

Hence, Eq. S3.10 gives

$$\mathbb{P}(T_t > t \mid T_i < T_c) = \exp[-(r_i + r_c)\,t] = \exp[-r_t t] = \mathbb{P}(T_t > t)\,. \tag{3.13}$$

The cumulative distribution function (CDF) we look for is simply $\mathbb{P}(T_t \le t \mid T_i < T_c) = 1 - \mathbb{P}(T_t > t \mid T_i < T_c)$, and Eq. S3.13 shows that this distribution equals the CDF $\mathbb{P}(T_t \le t)$. Naively, one may expect that removing the catastrophe data and looking only at the events of interest would lead to measuring the CDF $\mathbb{P}(T_i \le t)$, the distribution that is measured when catastrophes never occur. However, the actual distribution in Eq. S3.13 is biased compared to $\exp[-r_i t]$. To explain this, it is helpful to estimate the likelihood that an event ends in a catastrophe when the event time T_i is short ($T_i < 1/r_c$) or when it is long ($T_i > 1/r_c$). When T_i is short, and catastrophes do occur, it is likely that the catastrophe takes place after the actin filament escapes, or $T_i < T_c$. When the events that end in catastrophe are then discarded, it is likely that the short T_i is still observed. However, when T_i is long, the catastrophe is more likely to happen before the event of interest, and usually $T_i > T_c$. The selection then discards these events more often. Hence, short T_i are selected more often than long T_i, which introduces a negative bias in the distribution of transport times of those events that do not end in a microtubule catastrophe. Eq. S3.13

shows that the CDF for the selected transport times $\mathbb{P}(T_t \leq t \mid T_i < T_c)$ equals the CDF of the complete data set of transport times $\mathbb{P}(T_t \leq t)$, and is biased compared to the desired CDF $\mathbb{P}(T_i \leq t)$. Hence, we proceed by simply measuring the mean transport time using all events T_t, and then separately measure the microtubule catastrophe rate in order to separate the contributions of r_i and r_t.

CROSSLINKER PARAMETERS IN THE SIMULATED MODEL

The simulation model (see Fig. 3.3A of the main text) is based on a model previously developed to describe microtubules [112] interacting via crosslinker proteins. It uses discrete time step dynamics for the movement of the actin filament, while using a kinetic Monte Carlo algorithm for simulating the Markovian reactions that take place with time-varying rates. Here we explain in detail how the actin-microtubule crosslinkers are implemented in the simulation. The parameters are based on the experimental characterization of the interactions of TipAct with actin filaments and microtubules. TipAct has a binding site that can bind to actin directly [96]. In the presence of EB3, we observe that TipAct has a higher binding affinity for microtubules than for actin filaments, as is indicated by the co-localization of TipAct to growing microtubule ends as opposed to co-localization of TipAct to actin filaments (Fig. 3.1B of the main text, quantified in Fig. 3.13). TipAct interacts with microtubules through EB3, which in turn has a high affinity for the microtubule tip region and a low affinity for the microtubule lattice region [23]. In the model, we make the simplifying assumption that there is a single crosslinker that represents the complex of TipAct and EB3, but could also represent states where TipAct binds to microtubules and actin on its own. We will refer to this single crosslinker as TipAct, except when we need to specifically distinguish between internal binding states.

To form a cross-link between a microtubule and an actin filament, there are two different pathways. TipAct can first bind to the microtubule or first to the actin filament. Next, it can bind to the opposite filament. All these binding transitions are reversible. Hence, there are eight (un)binding rates; two for the transition between the unbound and actin-bound states, two between the unbound and microtubule-bound states, two between the actin-bound and fully bound states, and two between the microtubule-bound and fully bound states. Detailed balance reduces this to a set of seven different rates. Our in vitro experiments show that the binding of TipAct to single actin filaments is negligible compared to the binding to single microtubules (Fig. 3.1B, Fig. 3.7C and Fig. 3.13), meaning that we can remove one of the pathways, and we are left with four (un)binding rates per pair of binding sites on the microtubule and actin filament, as shown in Fig. 3.3A of the main text. These are the two rates for the transition between a fully unbound state and a state where TipAct is solely bound to the microtubule, and two rates for the transition from this dangling crosslinker state to the state where the crosslinker binds both the microtubule and the actin filament.

Since TipAct binds strongly to the microtubule tip region through EB3, but it also has a low but significant affinity for the microtubule lattice through EB3, we use two separate sets of (un)binding rates for TipAct binding from the solution to the microtubule lattice and tip regions. However, we assume that the rates to bind to or unbind from the actin filament are the same for dangling TipAct crosslinkers bound to the microtubule

tip or lattice. For convenience, we label the unbound state as 0, the state with a dangling crosslinker bound to the microtubule as 1, and the fully bound state where the crosslinker also binds to the actin filament as 2, and we distinguish between the microtubule lattice region L and the microtubule tip region T. As Fig. 3.3A shows, this gives us the rates $r^T_{0,1}$, $r^T_{1,0}$, $r^L_{0,1}$, $r^L_{1,0}$, $r^0_{1,2}$, and $r^0_{2,1}$. Here, a rate $r_{i,j}$ corresponds to the transition from state i to state j, and the 0 in the superscript indicates that the rate will depend on the amount that the linker has to stretch,

$$r_{1,2}(d) = r^0_{1,2} \exp\left[-\frac{U(d)}{2k_B T}\right], \tag{3.14}$$

where d is the amount by which the linker is stretched after the transition, and $U(d)$ gives the potential energy for a crosslinker with extension d. The same equation holds for the reverse rate $r_{2,1}(d)$ if we change the sign of the potential energy. Detailed balance sets a Boltzmann factor for the ratio between the forward and backward rates, but not for the rates individually. We make the model choice to distribute this factor evenly between the forward and backward reactions, explaining the factor $1/2$ in the exponent in Eq. S3.14. This choice ensures that the binding rate to a site that requires a crosslinker stretch d decreases with d, and the corresponding unbinding rate increases with d.

Even though there are typically multiple crosslinkers connecting the actin filament to the microtubule, the filaments can occasionally disconnect due to the stochastic nature of the (un)binding dynamics of the crosslinkers. However, upon the unbinding of the last remaining crosslinker, the filaments are still in close enough proximity such that new crosslinkers can bind. Hence, crosslinker rebinding can keep the filaments connected. To simulate this rebinding dynamics, we introduce a time scale τ_a and end a simulation when there are no connections between the two filaments for longer than τ_a. This time scale accounts the time it takes the actin filament to diffuse over a distance corresponding roughly to the size of a crosslinker, such that the probability of rebinding becomes negligible [156], and is estimated in Eq. S3.17.

Since we keep the distance between the filaments fixed in the simulations, we only have to describe the longitudinal component of the stretch of the crosslinkers d, and we assume that the potential energy obeys a simple harmonic function $U(d) = kd^2/2$. This potential provides forces on the actin filament and also influences the (un)binding rates through Eq. S3.14. When a crosslinker is bound to the microtubule and dangling, there are many binding sites on the actin filament that the crosslinker could bind to, but the harmonic potential sets very low rates for binding to the ones that require the crosslinker to stretch far. Hence, we improve the efficiency of the simulations by setting a maximum stretch for the crosslinkers, such that the simulations do not check binding positions that are unrealistically far away. We set this maximum stretch to 4δ, where δ is the spacing between binding sites on either filament. Using the parameter values from Table 3.1, the springs store a potential energy of 10.4 $k_B T$ at a stretch of 4δ. Hence, thermal fluctuations are unlikely to cause a stretch that large, justifying the simulation choice. For consistency, we also disallow the actin filament to change its position in a way that would stretch linkers more than 4δ.

Another model choice we explain in the main text is that the density of microtubule tip sites follows a step function, such that the tip is a well-defined region on the micro-

tubule of length l_t. This simple structure simplifies calculations and expresses our ignorance about the precise structure of the microtubule tip region where EB3 binds, which remains under discussion [23, 157, 158]. To confirm that the proposed mechanism of tip tracking also works with different microtubule tip region structures, we performed simulations where the density of tip sites decreases exponentially with the distance from the front of the microtubule. Leaving the other parameter values as they are listed in Table 3.1, we still observed actin transport, as shown in Fig. 3.16. Hence, the mechanism of a forward condensation force caused by transiently binding crosslinkers works independent of the exact shape of the tip region.

ACTIN FILAMENT DIFFUSION MEASUREMENTS

We experimentally observed that actin filaments occasionally land on the microtubule lattice and perform one-dimensional diffusion while remaining bound via TipAct. By raising the tubulin concentration to 30 μM, we obtained longer microtubules that allowed us to measure the diffusive motion of the actin filaments on the microtubule lattice, away from the tip region. The estimation of the diffusion constant is complicated by thermal fluctuations of the apparent actin filament length as observed by TIRF illumination. We quantify this apparent length by manually measuring the positions of the beginning and the end of the actin filament, called x_b and x_e, respectively, as a function of time with time steps of $\delta t = 3$ s. Two kymographs of diffusing actin filaments are shown in Fig. 3.11AB, along with the trajectories of x_b and x_e and the apparent actin length $l_a = x_e - x_b$. Besides small fluctuations around a constant length, we observe large transient deviations of the actin length at the beginning of the time traces (in the bottom panels of Fig. 3.11AB). These length fluctuations are probably caused by the binding process of the actin filaments, since binding will bring the whole actin filament from solution closer to the surface, therefore bringing it in the TIRF field. To estimate the length of the part of the actin filament that interacts with the microtubule, we remove the initial part of the time traces and take the mean value of l_a over the cropped time trace, as shown in Fig. 3.11AB. Then, we define the actin position x as the center point of the actin filament, $x = (x_b + x_e)/2$, and estimate the diffusion constant from the time trace of x in the cropped window.

Since the recorded data for x is noisy and contains a finite number of time points, it is difficult to find a reliable estimate of the diffusion constant from a single time trace [159]. The data set consists of $N+1$ time points x_i, which are acquired at $t_i = i\delta t$ and $i = \{0, 1, \ldots, N\}$. For the diffusion constant, we use a family of estimators based on the time-averaged square displacement [160],

$$\overline{D}_\Delta = \frac{1}{2\Delta\,(N-\Delta+1)\,\delta t} \sum_{i=0}^{N-\Delta} (x_{i+\Delta} - x_i)^2 , \tag{3.15}$$

which depends on a choice of the number of time steps $\Delta \in \mathbb{N}$ over which we probe the fluctuations. The movement of the actin filament is likely correlated for small times, and when Δ is smaller than the largest correlation time, the estimate of the diffusion constant will be influenced by these correlations. Furthermore, measurement noise and thermal length fluctuations have a larger influence on $\overline{D}_\Delta$ when Δ is small, because the actin steps $(x_{i+\Delta} - x_i)$ are typically smaller. However, when Δ is too large, the number of

time points $N - \Delta$ decreases, and the uncertainty in the estimate grows. As shown in in Fig. 3.11D, we measured time traces that last for only 30 s to 950 s before cropping, giving between 9 and 291 data points after cropping. We focus on the two time traces that are longer than 500 s to obtain reliable estimates of the actin diffusion constants.

Since estimates of the diffusion constant will be influenced by the number of time steps, we show the results of Eq. S3.15 as a function of the time gap $\Delta\delta t$ for the two long time traces in Fig. 3.11C. These two time traces are obtained from actin filaments with lengths $l_a = 6.6$ µm and $l_a = 7.1$ µm, and after cropping the time traces to a total duration of 873 s and 762 s, respectively. For small times, the estimate $\overline{D}_\Delta$ decreases strongly with Δ and reaches a plateau value after roughly 150 s. We believe that the strong bias in $\overline{D}_\Delta$ contains contributions from actin filament length fluctuations and external measurement noise. Furthermore, actin movement is different for time scales shorter than the time scales over which crosslinker remodeling occurs, and we expect that these effects also contribute to the bias in $\overline{D}_\Delta$. We therefore estimate the true diffusion constant as the sample mean of $\overline{D}_\Delta$ over a window between 150 s and 450 s, and report the standard deviation of the mean over this window as the error in our estimate. This results in the values $\overline{D} = 0.014(3)$ µm^2 s^{-1} ($l_a = 6.6$ µm) and $\overline{D} = 0.009(3)$ µm^2 s^{-1} (l_a =7.1 µm).

SIMULATION PARAMETER VALUE ESTIMATION

The simulation model presented in Fig. 3.3A of the main text contains many parameters, which are listed in Table 3.1. We constrain these parameters by combining several experimental observations.

First, for model simplicity, we chose to have a single lattice spacing between crosslinker binding sites both on the microtubule and on the actin filaments. We take this lattice spacing to be equal to the distance between subunits of the microtubule, which is $\delta = 8$ nm [148]. The actual distance between binding sites on the actin filament is around 5 nm [146, 147]. However, the actin binding domain of TipAct consists of a tandem of CH domains and TipAct forms a dimer [96], making it likely that TipAct typically fills two neighboring binding sites. Moreover, due to the helical twist of the actin filament [149], it is unclear how many binding sites are available on average. Hence, we can only find an approximate value for the lattice spacing between binding sites on the actin filament. Importantly, our model results do not depend qualitatively on the values of the lattice spacings on the microtubule and the actin filament.

A second parameter that can be estimated relatively easily from experiments is the size of the microtubule tip region. In our model, the tip region is a deterministic step function. In experiments, the EB3-TipAct comet fills roughly a single pixel of the camera, which has a size of 0.2 µm. Therefore, we take the length of this tip region $l_t = 0.2$ µm as a rough estimate, which sets the number of tip sites to 25 using the previously introduced choice for lattice spacing δ.

Next, the longitudinal friction coefficient of F-actin due to its viscous interactions with the solution can be calculated theoretically for a thin rod [153–155],

$$\zeta_{||} = \frac{2\pi\eta l_a}{\log(l_a/d) + \gamma_{||}}. \tag{3.16}$$

Here, the correction parameter $\gamma_{||} = -0.114$, as confirmed experimentally for actin filaments [155], and the actin diameter $d = 9e^{-9}$ m [149]. Furthermore, the viscosity is taken

to be that of water, $\eta = 1e^{-3}$ Pa s, and we use a filament length of $l_a = 3$ µm here, which falls within the experimental length distribution shown in Fig. 3.2G. Using the Einstein relation [130] and thermal energy $k_B T = 4.1e^{-21}$ J, this gives us $D_a \approx 1$ µm^{2}s^{-1}. For simplicity, we will not vary the value of D_a with the actin length, which is justified by the fact that the crosslinkers limit the motion of the actin filament much more strongly than the viscous drag by the solvent.

Another parameter in our model is τ_a, the time it takes for the actin filament to diffuse far enough away from the microtubule such that it is unlikely to be recaptured. To estimate this time scale, we use the time it takes diffusion of the actin filament to produce a standard deviation of 0.1 µm in the perpendicular position. This is roughly three times the length of the TipAct-EB3 complex [103], and also accounts for the possibility that the actin filament could slightly bend. Using an equation for the friction coefficient $\zeta_\perp$ similar to Eq. S3.16 [155], we arrive at

$$\tau_a \approx 5e^{-3} s. \tag{3.17}$$

As Fig. 3.3A shows, we have to constrain the rates $r^T_{0,1}$, $r^T_{1,0}$, $r^L_{0,1}$, $r^L_{1,0}$, $r^0_{1,2}$, and $r^0_{2,1}$, and also the spring constant k. Since these parameters are difficult to access directly, we estimate them based on a comparison between experimental observations and simulation results. Firstly, we use the observed diffusion constants of actin filaments on the lattice. Secondly, we measure the duration of actin diffusion on the microtubule lattice before unbinding as a function of the actin length. Thirdly, we fit our parameter set to the order of magnitude of the duration of actin transport events. Fourthly, we label TipAct and EB with the same fluorescent tag, and measure the difference in the fluorescence signal between the microtubule lattice and tip regions as a read-out of the binding affinity of the complex. Lastly, we use several specific observations on the (un)binding rates obtained by fluorescence recovery after photobleaching (FRAP) measurements. We explain all these experimental sources in detail below.

We discussed above that the actin diffusion constant is roughly $D_{\text{eff}} = 0.01$ µm^{2}s^{-1} at $l_a = 7$ µm, as shown in Fig. 3.11. This diffusion constant is affected by the average number of crosslinkers that bind to the actin filament. If there are many crosslinkers, the diffusion on the lattice slows down. The number of bound linkers is set by all binding rates on the lattice, $r^L_{0,1}$, $r^L_{1,0}$, $r^0_{1,2}$, and $r^0_{2,1}$. The parameter $r^0_{2,1}$ is also important for actin movement in another way, since movement is limited by how fast the crosslinkers can remodel. Hence, a higher $r^0_{2,1}$ will quickly increase the effective diffusion constant of actin on the microtubule lattice by reducing the number of crosslinkers and by increasing the rate of crosslinker remodeling. Additionally, the actin diffusion constant decreases by lowering the spring constant k, since this increases the numbers of bound crosslinkers by increasing the accessibility of the actin binding sites.

Another experimental observation that constrains the binding rates is the average duration of actin diffusion on the microtubule lattice. Fig. 3.11D shows that this duration depends exponentially on the actin length, since it becomes exponentially more likely that at least one crosslinker binds to the actin filament when more binding sites are available. The experimentally observed duration is strongly stochastic, and since we only have 19 events where actin diffuses on the lattice, we can only make an order of magnitude estimate of the average time of being bound for a diffusing actin filament of

a certain length. The experiments show that the actin stays on the microtubule lattice for roughly 40 s at $l_a = 4$ µm, so we fit the order of magnitude of the actin binding time in our simulations to this value. Specifically, we perform simulations in which a 4 µm long actin filament is transported by the microtubule, and then record both the time until the actin falls behind the tip and the time until the actin unbinds from the microtubule lattice. Several parameters influence the duration of lattice diffusion in the simulations. Increasing the average number of crosslinkers on the lattice by changing $r^L_{0,1}$, $r^L_{1,0}$, $r^0_{1,2}$ or $r^0_{2,1}$ makes this binding time larger. Additionally, the actin binding time can be increased by reducing the time scale of crosslinker remodeling, so by increasing both $r^0_{1,2}$ and $r^0_{2,1}$ while keeping the number of crosslinkers fixed. The actin unbinds when no crosslinkers connect the filaments for a duration of τ_a, and rebinding events often rescue the actin filament from unbinding if the crosslinkers remodel quickly.

Then, we use a rough estimate of the average time an actin filament is transported by a growing microtubule tip in cases where microtubule catastrophes and actin unbinding play no role. We used data sets that were limited in number of analysed transport events, which are part of the data presented in Fig. 3.12AB, Fig. 3.1E and Fig. 3.6C, together with Eq. S3.7 to estimate the average time $T_e \approx 80$ s for an actin filament of $l_a = 4$ µm and a microtubule growth velocity of $v_g = 3$ µm min^{-1}. We hence excluded simulation parameter sets that showed order of magnitude deviations from this value of T_e.

All binding parameters have an influence on the transport time T_e. Increasing the condensation force leads to longer transport times, and a larger condensation force can be created by increasing the binding affinity on the tip compared to the lattice. This can be seen in Eq. S3.23, where changing k, $r^T_{0,1}$, $r^T_{1,0}$, $r^L_{0,1}$ or $r^L_{1,0}$ changes the condensation force. Increasing the number of crosslinkers by altering $r^0_{1,2}$ and $r^0_{2,1}$ also increases the force, since the stronger interaction between the actin filament and the microtubule amplifies the effect of the stronger affinity for the lattice as set by $r^T_{0,1}$ and $r^T_{1,0}$. However, simply increasing the force by increasing the number of crosslinkers is not generally favorable, since it also increases friction between the moving actin filament and the fixed microtubule.

Another set of experiments shows that TipAct has a significant affinity for the microtubule lattice, which we can directly compare to the affinity for the microtubule tip. Specifically, we observe that the intensity of TipAct and EB3 is roughly $R = 20$ times higher on the tip than on the lattice when no actin is present, as shown in Fig. 3.9. This ratio is set by the rates $r^T_{0,1}$, $r^T_{1,0}$, $r^L_{0,1}$ and $r^L_{1,0}$,

$$R = \left(\frac{K^t_{0,1}}{1 + K^t_{0,1}} \right) / \left(\frac{K^\ell_{0,1}}{1 + K^\ell_{0,1}} \right), \tag{3.18}$$

where the equilibrium constants $K^t_{0,1}$ and $K^\ell_{0,1}$ are defined in Eq. S3.20. These same parameters also influence the condensation force, as seen in Eq. S3.23. Hence, the ratio R sets a limit on the condensation force in the limit where $K_{1,2} \to \infty$,

$$F_{f,max} = \frac{k_B T}{\delta} \log[R] \approx 1.5 \text{ pN}. \tag{3.19}$$

The true force $F_f = 0.10$ pN is more than an order of magnitude lower, since $K_{1,2}$ is far from ∞ using our final parameter set. So far, we have only talked about the effects of the

ratios $K_{0,1}$, but we do not have data on the specific rates $r^L_{0,1}$ or $r^L_{1,0}$. Hence, we make a choice that makes $r^L_{0,1} < r^T_{0,1}$ and $r^L_{1,0} > r^T_{1,0}$, but the specific choice has little effect as long as the factors $K_{0,1}$ stay the same.

To gain insight into the rate $r^0_{2,1}$ at which TipAct unbinds from the actin while it remains connected to the microtubule, we use in vitro TIRF measurements of the TipAct fluorescence signal on single actin filaments, as shown in Fig. 3.13A. We find that TipAct barely binds to actin filaments when no microtubule is present, and the binding events that do happen are quickly followed by unbinding events. From measurements with an inter-frame duration of ΔT = 33 ms, a mean binding time of $\overline{T}$ = 111 ms is deduced (Fig. 3.13A), giving an off-rate of $r_{\text{off}} \approx 9$ s^{-1} from actin without a microtubule present. However, the rate $r^0_{2,1}$ used in the simulations does not simply equal r_{off}. In the simulations, TipAct unbinds from the actin filament but remains bound to a microtubule that is very close. Furthermore, in the experiments shown in Fig. 3.13A, unbinding means that the crosslinker has not only detached but also that it has diffused away, since it is no longer in the proximity of the actin filament. In the simulations, what is required is only a short moment where the crosslinker is not bound, and we consider a quick rebinding to a neighboring location to be a new binding event. Hence, the binding and unbinding rates in our model will be higher than the r_{off} observed in full (un)binding experiments.

The (un)binding rates for the TipAct on the microtubule tip also require some interpretation. Since the protein is assumed to bind in a complex with EB3, TipAct and EB3 could in principle unbind individually. In the simulations, we consider only a single crosslinker, ignoring the possibility of the complex dissociating. To estimate the (un)binding rates $r^T_{0,1}$ and $r^T_{1,0}$, kinetic data is available on EB1 [23], and on TipAct and EB3 on microtubule tips as shown in Fig. 3.13BC. The binding rate of EB1 to the microtubule tip is 0.15 nM^{-1}s^{-1} [23]. With an EB concentration of 100 nM, we would get a binding rate of 15 s^{-1}. However, we assume that the concentration of the complex equals the (limiting) TipAct concentration, which is 30 nM in our experiments.

For the unbinding rate of the complex from the microtubule tip $r^t_{1,0}$, Fig. 3.13BC shows that we found unbinding rates of 1.8 s^{-1} for EB3 on microtubule tips, 0.8 s^{-1} on microtubule tips associated with actin bundles, 3.1 s^{-1} for TipAct on microtubule tips, and 0.7 s^{-1} for TipAct cross-linked between microtubules and actin bundles. The reported unbinding rate of EB1 from microtubule tips equals 3.4 s^{-1} [23]. We need to assume a higher unbinding rate $r^t_{1,0}$, since a rate of 3.4 s^{-1} makes partial binding very likely and makes it impossible for sites not to be bound. We justify this choice by seeing that this rate is an effective parameter that combines the unbinding of EB3 from the microtubule and of TipAct from EB3. Furthermore, the floppiness of the actin makes the binding of crosslinkers less likely because the actin is occasionally at a distance from the microtubule, but this flexibility is completely ignored in our model. Hence, we overestimate the likelihood of the fully bound state of the crosslinkers, which we can compensate for by increasing $r^t_{1,0}$. An additional reason why $r^t_{1,0} > 3.4$ s^{-1} is that the rate of 3.4 s^{-1} obtained by FRAP measures the effective unbinding rate after possible rebinding events [23], whereas we consider the short-time unbinding events to be separate events.

The value for the spring constant k of the crosslinkers is also not easily accessible by direct measurements. We choose a value of $2 \times 10^4 k_B T$ μm^{-2}, which is lower than the range of previously reported spring constants $6 \times 10^4 - 3e^5 k_B T$ μm^{-2} for other cytoskele-

tal cross-linking proteins [112, 150–152]. This low value accounts for the flexibility of a complex of EB3 dimers and TipAct dimers, and for the floppiness of actin. We chose several values of k going down from $1\times10^5\,k_BT$ µm^{-2} [112] to $1\times10^4\,k_BT$ µm^{-2}, then varying the binding rates until we found parameter sets that roughly complied with all considerations listed in this section. The value of $k = 2\times10^4\,k_BT$ µm^{-2} leads to a parameter set where the effective diffusion constant of the cross-linked actin filament is consistent with the experimental measurements. Lowering the spring constant even more leads to frequent events where the actin filament stochastically moves to $x \sim 1$µm in the comoving reference, making it protrude beyond the front of the growing microtubule tip. An actin filament that sticks so far past the front of the microtubule should be observable in TIRF microscopy. Since we do not observe such events experimentally, we did not lower the spring constant further.

We finally arrive at a set of parameters that accounts for all the experimental observations, listed in Table 3.1. We find an actin diffusion constant on the microtubule lattice of $D_{\text{eff}} = 0.006$ µm^{2}s^{-1} for an actin length of 7 µm, comparable with the experimental values of 0.014(3) µm^{2}s^{-1} ($l_a = 6.6$ µm) and $\overline{D} = 0.009(3)$ µm^{2}s^{-1} ($l_a = 7.1$ µm). The average transport duration is 90 s in simulations for a microtubule growth velocity of 3 µm s^{-1} and an actin length of 4 µm, consistent with the experimental value of 80 s. With the final parameter set, an actin filament of 4 µm unbinds from the microtubule roughly 44 s after it loses its interaction with the microtubule tip in the simulations, close to the experimental value of 40 s observed in the actin diffusion experiments. Finally, our parameter set leads to a factor $R = 26.1$ from Eq. S3.18, which is very similar to the factor 20 measured experimentally.

ANALYTICAL EXPRESSION FOR CONDENSATION FORCE

The magnitude of the condensation force that drives actin transport by microtubule tips depends on the strength of the interaction between the crosslinkers and the filaments and on the density of binding sites in the overlap between the actin filament and the microtubule tip region. Here we derive an analytical expression for this force.

Because the model does not allow crosslinkers that are only bound to the actin filament, we focus on the binding sites on the microtubule and classify the sites according to their crosslinker binding state, as shown in Fig. 3.14. The state is denoted by 0 if the site is free, 1 if the microtubule site is occupied by a crosslinker that is dangling and not connected to the actin, and 2 if the site is occupied by a crosslinker that is also bound to the actin. We use $r_{i,j}$ for the transition rate from state i to state j, as shown in Fig. 3.3A of the main text. We define the equilibrium constants $K_{i,j}$ between the states through the local detailed balance relation,

$$\begin{aligned} K^{\alpha}_{0,1} &= \exp\left(-\left(\mathscr{F}^{\alpha}_1 - \mathscr{F}_0\right)/k_BT\right) = \frac{r^{\alpha}_{0,1}}{r^{\alpha}_{1,0}}, \\ K_{1,2} &= \exp\left(-\left(\mathscr{F}^{\alpha}_2 - \mathscr{F}^{\alpha}_1\right)/k_BT\right) = \frac{r^{0}_{1,2}}{r^{0}_{2,1}}\sqrt{\frac{2\pi k_BT}{k\delta^2}}, \end{aligned} \tag{3.20}$$

where $\alpha \in \{t, \ell\}$ represents the microtubule tip or lattice region, respectively. The equilibrium constants are ratios of partition functions, and are thus related to differences between the free energies $\mathscr{F}_i$ of different binding states i. The process to create a crosslinker

in the dangling state 1 depends on the microtubule region α that the crosslinker is binding to, because crosslinkers bind faster to and unbind slower from the microtubule tip than from the lattice. However, we assume that the rate to bind to the actin filament is the same for all dangling crosslinkers, independent of the microtubule region they are bound to. Hence, the equilibrium constant $K_{1,2}$ does not depend on α. The rate $r^{\alpha}_{0,1}$, and hence $K^{\alpha}_{0,1}$, is proportional to the TipAct concentration in the solution, but we keep this dependence implicit since we do not vary the concentration in the experiments. Since the crosslinkers act as harmonic springs, a crosslinker bound to a specific binding site on the microtubule can bind to multiple binding sites on the actin filament. We group all these possible binding states into a single state 2. Therefore, the expression for $K_{1,2}$ is a sum over all possible crosslinker binding positions on the actin filament, and we approximate the sum by assuming that there are no interactions between the crosslinkers and that the actin filament is infinitely long,

$$K_{1,2} \approx \sum_{i=-\infty}^{\infty} \frac{r^0_{1,2}}{r^0_{2,1}} \exp\left(-\frac{k(i\delta)^2}{2k_BT}\right) \approx \int_{-\infty}^{\infty} \frac{1}{\delta} \frac{r^0_{1,2}}{r^0_{2,1}} \exp\left(-\frac{kx^2}{2k_BT}\right) \mathrm{d}x = \frac{r^0_{1,2}}{r^0_{2,1}} \sqrt{\frac{2\pi k_BT}{k\delta^2}} \tag{3.21}$$

Here, we make use of our model assumption that the actin filament has lattice spacing δ.

To calculate the condensation force, we consider the case where an actin filament overlaps with both the microtubule lattice and tip regions, such that the front of the actin filament is behind the front of the microtubule, as shown in Fig. 3.14. We assume that there are n_ℓ microtubule lattice sites and n_t microtubule tip sites overlapping with the actin filament, such that the actin filament contains $\ell_a = n_\ell + n_t$ sites. Furthermore, the microtubule has a total of ℓ_ℓ lattice sites and ℓ_t tip sites. For the calculation of the force, we also assume that the crosslinker binding states of different microtubule binding sites are independent, such that the partition function describing the binding state of the full system can be expressed as the product of the local partition functions for each site on the microtubule. The microtubule sites can always be in states 0 and 1, but state 2 is only available when the actin filament overlaps with that site. The local partition function for each microtubule binding site is a sum over the possible binding states of the Boltzmann factors. These factors contain the free energies $\mathscr{F}_i$, and we make the choice to set the free energy $\mathscr{F}_0 \equiv 0$, giving a Boltzmann factor of 1 for state 0. Using Eq. S3.20, we see that the Boltzmann factors for binding states 1 and 2 are simply products of the equilibrium constants. Hence, the full partition sum for the system shown in Fig. 3.14 is

$$\mathscr{Z}(n_\ell, n_t) = \left[1 + K^{\ell}_{0,1}\right]^{\ell_\ell - n_\ell} \left[1 + K^{\ell}_{0,1} + K^{\ell}_{0,1}K_{1,2}\right]^{n_\ell} \left[1 + K^{t}_{0,1} + K^{t}_{0,1}K_{1,2}\right]^{n_t} \left[1 + K^{t}_{0,1}\right]^{\ell_t - n_t}. \tag{3.22}$$

The four factors correspond to the $(\ell_\ell - n_\ell)$ lattice sites outside of the actin overlap, the n_ℓ lattice sites within the actin overlap, the n_t tip sites within the actin overlap, and the $(\ell_t - n_t)$ tip sites outside of the actin overlap, as shown in Fig. 3.14A. The condensation force can be calculated as a positional derivative of the free energy $\mathscr{F}(n_\ell, n_t) = -k_BT \log[\mathscr{Z}(n_\ell, n_t)]$, given by Eq. S3.22. The actin filament position x is defined in Fig. 3.3A of the main text as the difference between the front of the actin filament and the location on the microtubule where the lattice region turns into the tip region, and

Fig. 3.14A shows that this region contains n_t sites that are spaced δ apart. Hence, $n_t = x/\delta$, and since the number of sites on the actin filament ℓ_a is constant, $n_\ell = \ell_a - n_t = \ell_a - x/\delta$. The forward pointing condensation force can thus be calculated as

$$F_f = -\frac{\mathrm{d}\mathscr{F}(\ell_a - x/\delta, x/\delta)}{\mathrm{d}x} = \frac{k_B T}{\delta} \log\left[\frac{1 + K_{0,1}^{\ell}}{1 + K_{0,1}^{\ell} + K_{0,1}^{\ell} K_{1,2}} \frac{1 + K_{0,1}^{t} + K_{0,1}^{t} K_{1,2}}{1 + K_{0,1}^{t}}\right]. \tag{3.23}$$

We see that the condensation force does not depend on the position of the actin filament x as long as there is a partial overlap with the microtubule tip region. The situation changes when $x > l_t = \ell_t \delta$, such that the actin fully covers the microtubule tip region and sticks out in front of the microtubule. Then, the *forward* pointing condensation force disappears because it is no longer possible for the actin filament to gain binding free energy by increasing the overlap with the microtubule tip. Further forward motion of the actin filament now leads to a loss of the number of binding sites on the microtubule lattice, which comes with a free energy cost. In this situation, while the number of tip sites overlapping with the actin filament $n_t = \ell_t$ remains constant, n_ℓ still depends on x as before, and Eq. S3.22 shows that there will be a *backward* pointing condensation force due to the loss of overlap with the microtubule lattice,

$$F_b = -\frac{\mathrm{d}\mathscr{F}(\ell_a - x/\delta, \ell_t)}{\mathrm{d}x} = \frac{k_B T}{\delta} \log\left[\frac{1 + K_{0,1}^{\ell}}{1 + K_{0,1}^{\ell} + K_{0,1}^{\ell} K_{1,2}}\right]. \tag{3.24}$$

F_b is negative because all equilibrium constants K are positive. Since the binding affinity of crosslinkers for the microtubule lattice is much lower than for the microtubule tip, $K_{0,1}^{\ell} \ll K_{0,1}^{t}$, we have that $|F_b| \ll |F_f|$. Using the parameter values of Table 3.1, we find the values F_f = 0.10 pN and F_b = -4.6 fN, showing that the backward force is typically irrelevant. The condensation force is plotted as a function of the actin position in Fig. 3.14B. The backward force is only able to move the actin filament when the microtubule is depolymerizing, an effect that we confirmed experimentally (see Fig. 3.2D). Depolymerizing microtubules have no tip region where EB3 binds strongly, leading to a low number of crosslinkers and thus to a low crosslinker induced friction force. A force in the femtonewton range can easily overcome the viscous friction between the actin filament and the solution, since F_f applied to an actin filament with a diffusion constant of 1 $\mu m^2 s^{-1}$ would lead to a drift velocity of -1.1 $\mu m\ s^{-1}$.

CONDENSATION FORCE IN THE OPTICAL TWEEZER EXPERIMENTS

In the optical tweezer experiments, the bead plays the role of the actin filament that is transported by the growing microtubule tip region in the actin transport experiments. Below, we theoretically estimate the condensation force associated with the geometry of the optical tweezer experiment. Because TipAct (in complex with EB3) has a much higher affinity for microtubules than for actin filaments, we assume in the simulations of actin transport that TipAct never binds to the actin filament directly, but that it first binds to the microtubule before it can bind to the actin filament. By contrast, TipAct is irreversibly bound to the bead in the optical tweezer experiments, and there is no TipAct in solution. Hence, the only possible binding path is from the dangling state on the bead to a fully connected state between the bead and the microtubule. The two distinct

regions of the microtubule then lead to two equilibrium constants describing the affinity for the microtubule, K_t and K_ℓ. An additional key parameter determining the force is the density of bound crosslinkers on the bead ρ.

Calculating the free energies relative to the dangling state, such that this state has the Boltzmann factor 1, we derive the force on the bead using a similar method as used to derive Eq. S3.23,

$$F_{f,\text{bead}} = k_B T \rho \log\left[\frac{1+K_t}{1+K_\ell}\right]. \tag{3.25}$$

We do not have experimental data to estimate these parameters accurately, but we can make an order of magnitude estimate. First, we estimate the density of crosslinkers on the bead ρ. This density represents the number of crosslinkers that is conformationally capable to bind per micrometer of microtubule length. We make the order of magnitude estimate that ρ equals 10% of a fully covered microtubule, $\rho \approx 0.1/\delta$.

To find the equilibrium constants K_t and K_ℓ, we recognize that TipAct binds much more strongly to microtubules than to single actin filaments, since single microtubule tips show a strong fluorescent TipAct signal while single actin filaments do not (Fig. 3.1B, Fig. 3.7C). Measuring dwell times (Fig. 3.13A) and performing fluorescent recovery after photobleaching (FRAP) measurements (Fig. 3.13B), we report dissociation constants of $K_D^t = 67$ nM for the binding between TipAct and microtubule tip regions, and $K_D^a = 5.2\,\mu$M for the binding between TipAct and actin [103]. We note that K_D^a was probably underestimated in the experiments, because TipAct forms dimers that have two actin binding sites, which likely caused actin filaments to bundle and led to a higher measured affinity than should be expected for the binding of TipAct to single actin filaments. To find a relation for the parameters K_t and K_ℓ, we use that the equilibrium constant K_t describes the transition to bind from the bead (representing the actin filament) to the microtubule, and $K_{1,2}$ represents the transition to bind from the microtubule to the actin filament. Based on the experimental values, we have $K_t/K_{1,2} \approx K_D^a/K_D^t = 78$, giving us the order of magnitude $K_t = 100K_{1,2}$ in the simulations. This is likely an underestimation due to the described bias in the value of K_D^a.

Finally, to find K_ℓ, we use that the difference in affinity between the microtubule tip and lattice regions should be the same for the optical tweezer experiments and the actin transport experiments, $K_t/K_\ell = K_{0,1}^t/K_{0,1}^\ell$. Using Table 3.1, we find the force

$$F_{\text{f,bead}} \approx 0.17 \text{ pN}. \tag{3.26}$$

This is the force on the bead when the bead is behind the front of the microtubule and still overlapping with the microtubule tip region. However, when the bead and the microtubule first come into contact, the bead is in front of the microtubule. Then, the condensation force caused by the increasing overlap with the microtubule tip region equals

$$F_{b,\text{bead}} = -k_B T \rho \log[1+K_t] \approx -0.21 \text{ pN}, \tag{3.27}$$

using the same parameters as before. As shown in Fig. 3.15, we experimentally find a forward force of $F_{\text{f,bead}}$ 0.12 pN and a backward force of $F_{\text{b,bead}} \approx$ -0.7 pN. Hence, we correctly estimate the order of magnitude for these forces, but the ratio between these forces is not well predicted. This may be due to an overestimation of the ratio K_t/K_ℓ, which is in turn due to an overestimation of $K_{0,1}^t/K_{0,1}^\ell$.

PROBABILITY OF ACTIN UNBINDING

In our simulations, we consider the actin filament to be bound to the microtubule as long as there is at least a single crosslinker binding the two filaments together. Here, we obtain an approximate expression for this binding probability using similar expressions as in the derivation of the condensation forces. The probability of having no crosslinkers connecting an actin filament that overlaps with the microtubule tip region over a length y_t and overlaps with the microtubule lattice region over a length y_ℓ, $p_0(y_t, y_\ell)$ defined in Eq. 3.5 of the main text, equals

$$p_0(y_t, y_\ell) = \left[\frac{1+K_{0,1}^t}{1+K_{0,1}^t+K_{0,1}^t K_{1,2}}\right]^{y_t/\delta}\left[\frac{1+K_{0,1}^\ell}{1+K_{0,1}^\ell+K_{0,1}^\ell K_{1,2}}\right]^{y_\ell/\delta} = \mathrm{e}^{-y_t/\lambda_t}\mathrm{e}^{-y_\ell/\lambda_\ell}. \quad (3.28)$$

Here, the discrete numbers of binding sites that overlap with the microtubule tip region and lattice region are approximated as $n_t = y_t/\delta$ and $n_\ell = y_\ell/\delta$, respectively. We recognize that the probability decreases exponentially with both overlap lengths, which allows us to define the length scales λ_t and λ_ℓ,

$$\lambda_\alpha = \frac{\delta}{\log\left[1+K_{0,1}^\alpha+K_{0,1}^\alpha K_{1,2}\right]-\log\left[1+K_{0,1}^\alpha\right]}, \quad (3.29)$$

with $\alpha \in \{t, \ell\}$ representing the microtubule region again. Using the parameters listed in Table 3.1, we calculate $\lambda_t = 0.038$ μm and $\lambda_\ell = 0.89$ μm. Since there is a higher density of bound crosslinkers on the microtubule tip than on the lattice, as shown in Fig. 3.9, the probability to have no crosslinkers decays much more rapidly with an increase in the overlap length in case of the tip region as opposed to the lattice region. This explains why the length scale λ_t is much shorter than λ_ℓ.

KRAMERS THEORY

In the main text, we identify that an actin filament that is being transported by a growing microtubule needs to cross a free-energy barrier to fall behind the microtubule tip region. Given that we know the free-energy profile and the diffusion constant, we can calculate the rate of these transitions using Kramers theory.

As shown in Fig. 3.3C of the main text, x is the position of the front of the actin filament relative to the point on the microtubule where the lattice region ends and the tip region begins. Since the latter point moves with the growing microtubule tip, x constitutes a co-moving frame of reference. In this frame of reference, we call $D(x)$ the effective diffusion constant of the actin filament. We obtain $D(x)$ by calculating how the overlaps between the actin filament and the microtubule lattice region y_ℓ and between the actin filament and the microtubule tip region y_t change with x. As shown in Fig. 3.3C of the main text,

$$\begin{aligned} y_t(x) &= x\mathbb{1}(0 \le x < l_t) + l_t\mathbb{1}(x \ge l_t), \\ y_\ell(x) &= l_a - x\mathbb{1}(x \ge 0), \end{aligned} \quad (3.30)$$

where we assume that $l_a \gg l_t, x$. Then, we enter these expressions into Eqs. 3.2 and 3.3 of the main text to find $D(x) = D\big(y_t(x), y_\ell(x)\big)$, which is given in Eq. 3.1 of the main text.

Next, we call $F_{\text{eff}}(x)$ the forward pointing force on the actin filament, given by Eq. 3.4 of the main text and containing a contribution from the friction. We integrate this effective force to find the generalized free energy

$$\mathscr{F}(x) = -\int_0^x F_{\text{eff}}(x')\,\mathrm{d}x'. \tag{3.31}$$

The function $\mathscr{F}(x)$ behaves exactly like an equilibrium free energy, even though it describes the non-equilibrium process of microtubule growth and actin transport. This is the result of the co-moving frame, in which the free-energy profile loses its time dependence.

Combining the expressions for the diffusion constant and the generalized free energy, and assuming the Einstein relation [130], we find a Fokker-Planck equation for $f_a(x,t)$, the probability density of the actin position x,

$$\partial_t f_a(x,t) = \partial_x \left[D(x)\, \mathrm{e}^{-\mathscr{F}(x)/k_B T} \partial_x \left(\mathrm{e}^{\mathscr{F}(x)/k_B T} f_a(x,t) \right) \right]. \tag{3.32}$$

As shown in Eqs. 3.1–3.4 of the main text, the free energy is determined by the parameters D_a, λ_t, λ_ℓ, ζ_t, ζ_ℓ, F_f, and F_b. D_a is a parameter in the simulations as well, and we have analytical approximations to the length scales λ_t and λ_ℓ in Eq. S3.29, and for the condensation forward and backward forces F_f and F_b in Eq. S3.23 and Eq. S3.23, respectively. The only fitting parameters are the two proportionality factors ζ_t and ζ_ℓ that determine how the friction coefficient scales with the actin length on the microtubule tip and lattice. Direct measurements of the diffusion constant in simulations, shown in Fig. 3.3D of the main text, give the values $\zeta_t = 810 k_B T$ s μm^{-2} and $\zeta_\ell = 30.2 k_B T$ s μm^{-2}. We emphasize that this set of simulations is independent of the set of simulations in which we estimate the free-energy profile and transport times, which means that we can make independent theoretical predictions on the generalized free-energy profile and on the functional behavior of the actin transport time. We obtain the rate of actin falling behind the tip using Kramers theory [131] based on Eq. S3.32, and the resulting rate is given in Eq. 3.6 of the main text.

RATE OF ACTIN UNBINDING

One of the processes by which actin transport ends is by the direct unbinding of the actin filament from the microtubule when it is still in contact with the microtubule tip region. Here, we develop a theoretical explanation of the unbinding rate observed in the simulations. If the actin filament is at a position $x < 0$, transport will most likely rapidly end with the filament falling further behind the tip, which we treat as an process independent from unbinding. Hence, we consider the scenario $x > 0$ for the unbinding rate, such that the actin filament overlaps both with the microtubule lattice region and with the tip region.

The actin filament can only unbind when there are no crosslinkers binding the actin filament. First, the actin filament needs to loose all connections with the microtubule lattice region. Second, the crosslinkers bind very strongly to the microtubule tip region, so the actin can only unbind when the overlap between the actin filament and the tip region almost vanishes, $x \approx 0$. Then, we assume that the rate of unbinding is limited by

the probability that both these events happen,

$$r_u \propto \mathbb{P}[\text{no connections lattice} \wedge x \approx 0] = \mathbb{P}[\text{no connections lattice}]\,\mathbb{P}[x \approx 0 \mid \text{no connections lattice}]\,. \tag{3.33}$$

Here, we use the definition of conditional probability to rewrite the proportionality into two factors, and we will discuss each factor separately.

First, we calculate the probability that no crosslinkers are bound between the actin filament and the microtubule lattice using Eq. S3.28. This probability limits the rate at which the actin filament can unbind in Eq. S3.33, so the unbinding rate decreases exponentially with the actin filament length,

$$r_u \propto \mathrm{e}^{-l_a/\lambda_\ell}. \tag{3.34}$$

We only focus on how the unbinding rate is shaped by the actin length l_a and the microtubule growth velocity v_g, since these are the variables we use to compare the transport time between simulations and experiments. We absorb all other effects into the proportionality constant. We use the length scale λ_ℓ here, since elongating an actin filament at fixed position x only increases the overlap with the microtubule lattice region, not with the tip region.

Then, we require the probability that $x \approx 0$ given that the actin filament has lost its connections with the microtubule lattice region. This probability follows from the free-energy profile $\mathscr{F}(x)$ shown in Fig. 3.3E of the main text. Specifically, the peak of the barrier is always located at $x = 0$, while the valley is at $x = l_t$, where l_t is the length of the microtubule tip region. Hence, the probability to find the actin filament close to the peak is given by the free-energy barrier height $\Delta\mathscr{F}^\ddagger = \mathscr{F}(0) - \mathscr{F}(l_t)$,

$$r_u \propto \mathrm{e}^{-\Delta\mathscr{F}^\ddagger/k_BT}. \tag{3.35}$$

Eq. S3.31 shows that this free-energy barrier requires integrating the effective force defined in Eq. 3.4 of the main text. The only term that depends on v_g or l_a is the friction term,

$$F_{\text{eff}}(x) = -\zeta(x)\, v_g + \dots. \tag{3.36}$$

Given that there are no crosslinkers connecting the actin filament to the microtubule lattice, only the overlap with the microtubule tip provides a significant friction coefficient ζ for the actin filament,

$$\zeta(x) \approx \zeta_t x. \tag{3.37}$$

Now, integrating Eq. S3.36 gives us

$$\Delta\mathscr{F}^\ddagger = \frac{1}{2}\zeta_t l_t^2 v_g + \dots. \tag{3.38}$$

By combining Eq. S3.34, Eq. S3.35, and Eq. S3.38, we find the actin unbinding rate

$$r_u\big(v_g, l_a\big) = r_u^0 \mathrm{e}^{-l_a/\lambda_\ell}\mathrm{e}^{v_g/\gamma}, \tag{3.39}$$

where the velocity γ, which sets the scale for the micortubule growth velocity v_g, is defined as

$$\gamma = \frac{2k_BT}{\zeta_t l_t^2}. \tag{3.40}$$

4

ACTIN-MICROTUBULE COORDINATION IN AXONS BY THE CYTOLINKER GAS2L1

Let's dance little stranger,
Show me secret sins.

Nouvelle Vague

Crosstalk between the actin and microtubule cytoskeletons is essential for establishing the complex polarized morphology of neurons. Here, we characterised the neuronal function of Growth Arrest Specific 2-like 1 (Gas2L1), a cytolinker protein that can directly bind to actin, microtubules and microtubule plus-end-tracking End Binding proteins. We found that Gas2L1 promotes axon branching, but restricts axon elongation in cultured rat hippocampal neurons. Using pull-down experiments and in vitro reconstitution assays, in which purified Gas2L1 was combined with actin and dynamic microtubules, we demonstrated that Gas2L1 is autoinhibited. This autoinhibition is relieved by simultaneous binding to actin filaments and microtubules. In neurons, Gas2L1 primarily localizes to the actin cytoskeleton and functions as an actin stabilizer. The microtubule-binding tail region of Gas2L1 directs its actin-stabilizing activity towards the axon. Although our in vitro reconstitutions indicate that Gas2L1 is able to affect MT dynamics, MT organization and dynamics appear normal in Gas2L1-depleted neurons. These combined results suggest that Gas2L1 does not operate via guiding MTs into actin-rich areas. Instead, we propose that Gas2L1 acts as an actin regulator, the function of which is spatially modulated by microtubules.

This chapter is partly based on the publication *Cytolinker Gas2L1 regulates axon morphology through microtubule-modulated actin stabilization* by D. van de Willige, J.J.A. Hummel, Celine Alkemade, *et al*, (2019) [116]. Celine Alkemade contributed the *in vitro* reconstitution experiments, co-wrote the article and adapted for thesis chapter. Neuron and COS cell experiments were performed by D. van de Willige and J.J.A. Hummel. Here, we present additional unpublished data (Fig. 4.13 and SI-Fig. S4.19-S4.29).

4.1. INTRODUCTION

The cytoskeleton is a key player in cellular morphogenesis, as it provides cells with structural support and acts as a scaffold for organelle positioning. An paradigmatic example where cytoskeletal filaments play intricate roles in cellular morphogenesis is neuronal development. Neurons function by propagating signals in the brain via connections with other neurons. Those connections can be created when neurons find each other, via a process termed 'neuronal pathfinding'. Consequently, neurons have complex morphologies that allow them to form elaborate networks in the brain. Developing neurons undergo extensive cell shape changes, which are coordinated by guidance cues relayed to the actin and microtubule (MT) cytoskeletons (reviewed in [161]).

In particular, the crosstalk between MTs and actin plays an essential role during axon maturation (reviewed in [8, 162, 163]). At the tips of axonal processes, specialized structures called growth cones determine the direction and rate of axon advance. Growth cones contain a central dynamic MT array which probes the actin-rich periphery. Axon outgrowth is preceded by MT stabilization in filopodia at the tip of the growth cone, and conversely, repellent cues restrict peripheral MT entry. In a similar process, axon branching is believed to start with the formation of an actin patch along the axon, either *de novo* or as a remnant of a pausing growth cone (reviewed in [164, 165]). At the site of branch formation, newly generated dynamic MT plus ends are stabilized on the actin patch to initiate a new branch.

Actin-MT crosslinking proteins, also referred to as cytolinkers, are obvious candidates to regulate cytoskeletal crosstalk during axon development (reviewed in [3]). Most studies in this context have focussed on spectraplakins, a family of large proteins, which directly bind both to actin filaments and MT shafts and indirectly associate with growing MT plus ends through End Binding (EB) proteins (see also Chapter 3) [53, 67, 71, 166]. The actin-MT crosslinking abilities of MACF1 (a spectraplakin otherwise known as ACF7) and its Drosophila ortholog Short Stop (Shot) are necessary for axon extension [68, 167]. Other MT plus end-associated proteins, such as CLASP and APC, participate in regulating axon outgrowth, possibly also by coordinating actin-MT coupling [168, 169].

Gas2L1 (Growth Arrest Specific 2-like 1) is a much smaller cytolinker than MACF1 yet with a similar domain composition (see Fig. 4.1), but its role is less well understood. Like MACF1, Gas2L1 contains an N-terminal actin-binding calponin homology (CH) domain, a MT lattice-binding Gas2-related (GAR) domain and a C-terminal SxIP motif, which mediates the interaction with MT plus-ends via EB proteins [76, 170, 171]. The actin-MT crosslinking abilities of Gas2L1 and its Drosophila ortholog Pigs (Pickled eggs) have been previously demonstrated in cells [76, 78]. So far, Gas2L1 was shown to regulate the distance between centrioles in cycling cells [172], and Pigs was identified as a cytoskeletal target of Notch signalling, which participates in Drosophila wing muscle development and oogenesis [173]. However, Gas2L1 has not been studied in the context of neuronal development, although Gas2L1 mRNA is abundant in mammalian brain tissue [170]. Here, we reveal that Gas2L1 participates in regulating axon outgrowth and branching in developing mammalian neurons. By combining data obtained in primary rat hippocampal neurons with *in vitro* reconstitution assays and biochemical experiments, we show that Gas2L1 is autoinhibited and requires the simultaneous binding of both actin filaments and MTs to fully relieve this autoinhibition. Axon outgrowth requires dynamic

MTs to invade the actin-rich growth cone periphery. Our *in vitro* reconstitutions indicate that Gas2L1 impacts MT dynamics. However, we found in Gas2L1-depleted neurons that MT plus-end growth velocity, MT organization and MT stability appear normal. This discrepancy might be explained by other proteins than Gas2L1 that are regulating MT dynamics in the neuronal growth cone, such as MACF1. In addition, these results suggest that Gas2L1 does not operate via guiding MT entry into growth cones to promote axon outgrowth (as is thought for MACF1 [68, 167]). Instead, our neuronal data suggest that Gas2L1 locally regulates the actin cytoskeleton during axon maturation by stabilizing actin in response to MT binding. Gas2L1 hereby promotes axon branching while tempering axon extension.

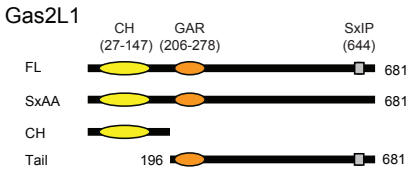

Figure 4.1: **The domain organization of the full-length Gas2L1 protein and of the deletion mutants we study in this chapter.** Indicated are the CH (actin binding) domain in yellow, the GAR (MT lattice) binding domain in orange, and the SxIP motif (EB binding domain) in grey. Additional deletion mutants are shown in Fig. S4.15A. Numbers indicate amino acid residue start and end positions, counting from the N-terminus (left) to the C-terminus (right). FL, full-length; CH, calponin homology; GAR, GAS2-related; SxIP, SxIP motif.

4.2. RESULTS

4.2.1. GAS2L1 AFFECTS AXON BRANCHING AND OUTGROWTH IN DEVELOPING NEURONS

To determine whether Gas2L1 plays a role in neuronal development, we examined the effects of Gas2L1 depletion and overexpression on axon development in dissociated primary rat hippocampal neurons. Day-in-vitro (DIV) 0 neurons were electroporated with an empty vector or with Gas2L1 shRNA-encoding plasmids and subjected to puromycin selection before mRNA isolation at DIV3. Depletion resulted in a ~64% reduction of Gas2L1 mRNA as determined by qPCR (Fig. 4.2A and Fig. S4.16A,B).

The depletion of Gas2L1 from DIV0 to DIV3 resulted in less complex axons (Fig. 4.2B) characterized by an increased axon branch length and reduced branch density (i.e., the number of branches per unit of axon length; Fig. 4.2C-F). We note that in this set of experiments, total axon length was slightly reduced, whereas other experiments showed no significant difference (Fig. S4.16E, Fig. 4.11B). The effects of Gas2L1 depletion on neuronal morphology could be rescued by co-expressing low levels of Gas2L1 (Fig. S4.17A,B and Fig. S4.16E-G), indicating that this phenotype is specific. Importantly, neuronal polarity was not affected by the loss of Gas2L1, as evidenced by staining of the axon initial segment marker TRIM46 in neurons depleted of Gas2L1 (Fig. 4.2B) [174].

When Gas2L1 was overexpressed from DIV0 to DIV3, the length of the primary axon and axonal branches was decreased, whereas the branch density was increased (Fig. 4.2C-F). These axon maturation phenotypes were opposite to those seen after Gas2L1 de-

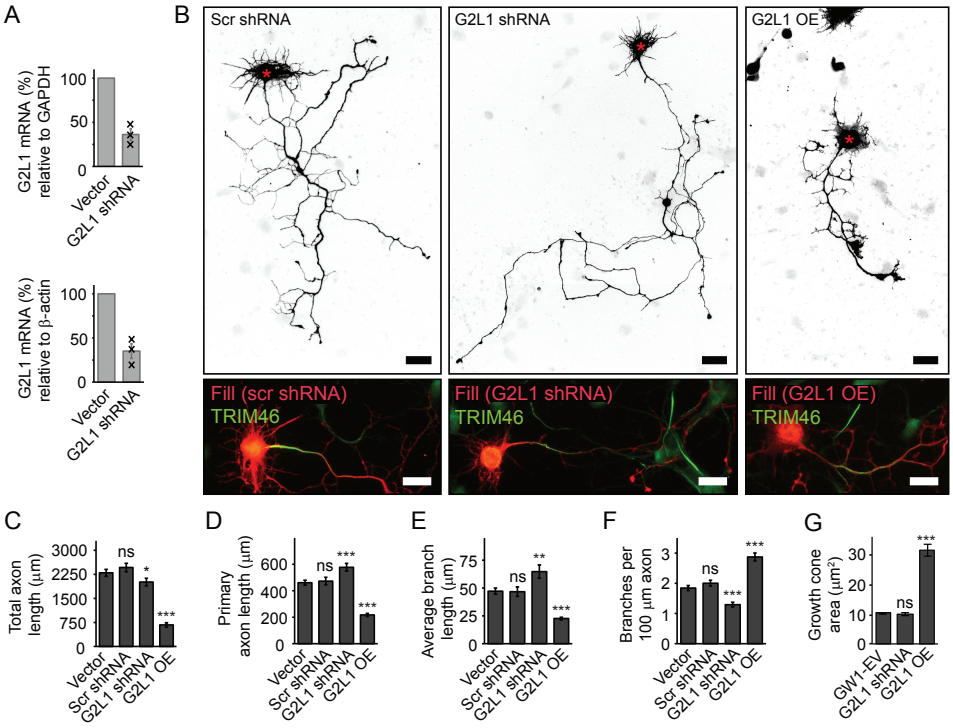

Figure 4.2: **Gas2L1 balances axon outgrowth and branching in developing neurons.** **(A)** qPCR experiments showing the decrease in Gas2L1 (G2L1) mRNA levels upon DIV0-DIV3 shRNA treatment of primary rat hippocampal neurons (A; n=3, black crosses represent individual data points). **(B)** Silhouettes (from β-galactosidase fill, top panels) of DIV3 neurons treated with scrambled (Scr) or G2L1 shRNA and co-expressing HA-β-galactosidase, or overexpressing HA-G2L1 and HA-β-galactosidase for three days. Red asterisks indicate the position of the soma. Bottom panels show fill (red) combined with TRIM46 staining (green) of the neurons shown in the panels above. **(C-F)** Quantifications of total axon length (C), primary axon length (D), average (non-primary) branch length (E) and the number of branches per 100 µm axon (F) for DIV3 neurons treated as described in (B). Vector = empty pSuper shRNA vector co-expressing HA-β-galactosidase. n=50 neurons per condition from 3 independent experiments. **(G)** Quantification of the growth cone area in DIV4 neurons transfected with GW1-EV (empty GW1 vector), G2L1 shRNA or HA-G2L1 and HA-β-galactosidase for one day. n=159 growth cones from 43 neurons for GW1-EV, 130 growth cones from 37 neurons for G2L1 shRNA, 142 growth cones from 41 neurons for HA-G2L1, from 3 independent experiments. Scale bars: 30 µm. Data is displayed as means ±SEM. Mann-Whitney test, ns: not significant, * p <0.05, ** p<0.01, ***p<0.001.

pletion (Fig. 4.2C-F). Gas2L1 overexpression also led to enlargement of axonal growth cones (Fig. 4.2G). We also noted the development of excessive filopodia (Fig. S4.16C), as evidenced by their co-localization with a filopodia marker Fascin (Fig. S4.17C). In addition, Gas2L1 neurons formed structures that resembled lamellipodia (Fig. S4.16C) and displayed some punctate staining with the lamellipodia markers cortactin and p34-Arc/ARPC2 (Fig. S4.16H,I). We note that these features were beyond the level of detail included in our morphological analyses, which were based on axon tracings (Fig. S4.16D). Despite the obvious morphological defects induced by overexpression, axons of Gas2L1-overexpressing neurons were still polarized, as TRIM46 staining (marking the axon initial segment) appeared normal in these neurons (Fig. 4.2B).

We conclude that Gas2L1 stimulates formation of new axon branches but restricts their elongation. The latter effect is different from that of MACF1, a structurally related cytolinker that promotes both axon outgrowth and branching [68, 167]. The ability of a protein to interact with both actin filaments and MTs can thus be associated with distinct neurodevelopmental functions.

4.2.2. GAS2L1 SPECIFICALLY LOCALIZES TO ACTIN-MT OVERLAPS IN *in vitro* RECONSTITUTION ASSAYS

To better understand how Gas2L1 mediates actin-MT crosstalk, we purified full-length Gas2L1, its actin-binding CH domain, and its MT-binding C-terminal fragment, which was termed Tail (Fig. 4.1 and Fig. S4.15). We studied the behaviour of these proteins in an *in vitro* reconstitution assay, which included dynamic MTs and actin filaments stabilized with phalloidin [92]. We immobilized stable MT seeds on a glass surface, allowing dynamic MTs to grow in a solution containing tubulin dimers and unattached free-moving actin filaments (Fig. 4.5A).

As the first step, we tested the behaviour of Gas2L1 and the deletion mutants in the presence of dynamic MTs or stabilized actin filaments alone. When testing the ability of Gas2L1 to bind to MTs, we observed no co-localization of the protein to the MTs, as is shown in Fig.4.3. Even after 25min, when the MTs had grown longer and more MT/MT-overlaps were present, we observed no co-localization of Gas2L1 to any MT. Interestingly, the Tail fragment (the Gas2L1-mutant lacking the actin-binding domain, see Fig. 4.1) did bind MT, although this interaction was temporary and diminished over time (Fig. S4.18A). Moreover, Tail was able to track growing MT plus-ends when EB3 was present (Fig. S4.18B,C). In addition, we confirmed that the CH domain does not interact

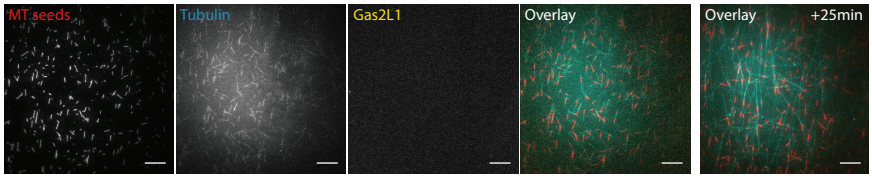

Figure 4.3: **Gas2L1 does not bind microtubules.** TIRF images of the *in vitro* reconstitution of the interaction of Gas2L1 with MTs. Shown are MT seeds (red), tubulin (blue), Gas2L1 (yellow) and their overlay. Gas2L1 shows no co-localization to MTs (2min, left panels), also not over time (25min, right panel). Scale bars: 10µm.

with MTs (Fig. S4.19). These observations indicate that, although the MT-binding domains of Gas2L1 can bind MTs in our *in vitro* assays, the full-length Gas2L1 cannot bind to MTs alone, and needs either to be activated or regulated.

Next, we tested the binding of Gas2L1 and the deletion mutants to actin filaments. The dissociation constant K_d of Gas2L1 for actin filaments, determined by a co-sedimentation assay, was 0.49 (±0.14) μM (Fig. S4.20). Using TIRF microscopy, we observed that Gas2L1 does not bind single actin filaments, but does co-localize to actin bundles (Fig. 4.4), whereas the CH domain binds all F-actin structures (both single F-actin and bundles) and expectedly Tail does not co-localize to any F-actin (Fig. S4.21). By measuring fluorescence intensity ratios of Gas2L1 or CH over actin, we confirmed that Gas2L1 does not bind single F-actin (Fig. S4.22). Nevertheless, we found that Gas2L1 is able to actively form F-actin bundles (Fig. S4.23) and localizes non-homogeneously along these bundles (Fig. S4.24). Interestingly, we observed that Gas2L1 is able to recruit EB3 to these actin bundles, indicating that Gas2L1 can bind F-actin and EB3 simultaneously in the absence of any MTs and that EB3 does not interfere with Gas2L1's actin binding (Fig. S4.25). To probe the binding kinetics of Gas2L1 at the actin bundles, we measured the off-rate for actin-bound Gas2L1 by fluorescence recovery after photobleaching (FRAP) (Fig. S4.26A-C). We found a fast ($0.5\,s^{-1}$) and a slow ($0.01\,s^{-1}$) component for the unbinding rate, as well as an immobile fraction (± 65%), suggesting a large portion of the Gas2L1 molecules are trapped within the actin bundles, at least on the time scale of our experiments. Interestingly, the CH domain, consisting of only the actin-binding domain, showed a full recovery, with only one component for the unbinding rate ($0.08\,s^{-1}$) and no indication of an immobile fraction. Therefore our results suggest that the other Gas2L1 domains somehow interfere with the actin-binding CH domain in the full-length protein. The weak affinity of full-length Gas2L1 for actin was also confirmed in competition assays, where we observed that a well-established actin-binding protein (α-actinin-1) readily outcompetes Gas2L1 binding (Fig. S4.27).

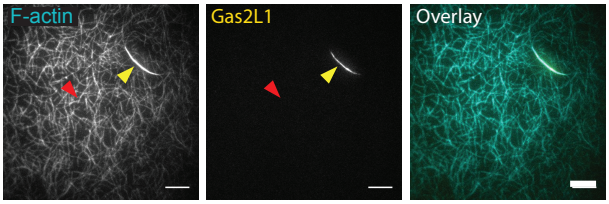

Figure 4.4: **Gas2L1 binding to actin filaments.** TIRF images of the *in vitro* reconstitution of the interaction of Gas2L1 with F-actin. Shown are F-actin (blue), Gas2L1 (yellow) and their overlay. Gas2L1 does not bind single F-actin (red arrowheads), but does co-localize to actin bundles (yellow arrowheads). Scale bars: 10 μm.

Our findings indicate that under the tested conditions, individual domains of Gas2L1 are capable of binding actin filaments, the MT lattice and MT plus ends, but the full-length protein is not. Surprisingly, when we added Gas2L1 to a composite assay with both MTs and low concentrations of actin filaments in the absence of EB3, we observed that Gas2L1 exclusively accumulated at the sites where actin filaments and MTs overlapped (Fig. 4.5B). Specific accumulation of Gas2L1 on actin-MT overlaps was especially obvious from events during which an actin filament gradually aligned with a growing

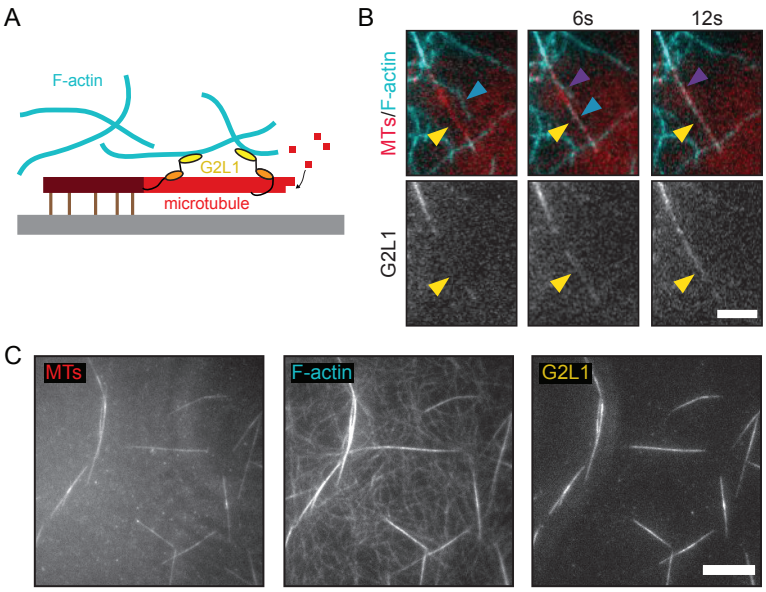

Figure 4.5: **Gas2L1 as a MT/actin cytolinker.** **(A)** Schematic depiction of the *in vitro* TIRF assay. Stable MT seeds are attached to the glass surface, from which dynamic MTs grow by addition of tubulin dimers (either with or without EB3 present). Actin filaments are free to move around in solution. Gas2L1 links F-actin to MTs. **(B)** Full-length Gas2L1 (30nM) in a composite assay with both actin (10 nM) and MTs, but without EB3. Gas2L1 only localizes at MT-actin overlaps. Gas2L1 accumulation (yellow arrows) occurs after an actin filament 'lands' and zippers (purple arrowheads) onto a MT (blue arrowheads). **(C)** Full-length Gas2L1 in a composite assay as in (B), but with higher actin concentration (1 µM). Actin bundles are formed around the dynamic MTs. Scale bars: 5µm in B; 10µm in C.

MT: the appearance of the Gas2L1 signal along the MT coincided with the zippering of the unbound part of an actin filament along the MT (Fig. 4.5B). Similar zippering of actin filaments and MTs was observed previously with an engineered cytolinker containing a CH domain targeting actin and an SxIP motif targeting EB proteins [96] (TipAct, also used in Chapters 3 and 5). In a composite assay where more actin filaments were available for binding, we observed MTs covered with multiple co-aligned actin filaments (Fig. 4.5C), whereas no MT-actin co-alignment occurred without Gas2L1 (Fig. S4.28).

Time-lapse analysis of actin-MT-Gas2L1 bundles revealed that MTs inside these bundles remained dynamic (Fig. 4.6A,B). When a catastrophe occurred and the MT shrunk back, Gas2L1 did not remain bound to actin, but disappeared together with the MT (Fig. 4.6A,B), and the actin filaments that were initially co-aligned with the MT dispersed (Fig. 4.6C). Once the MT repolymerized, the accumulation of Gas2L1 and actin along its shaft was restored (Fig. 4.6C). Qualitative FRAP measurements confirmed the transient binding of Gas2L1 to these actin-MT bundles (Fig. S4.29). Furthermore, we observed that the addition of EB3 to the assay did not alter Gas2L1-induced MT-actin co-alignment and did not induce any enrichment of Gas2L1 at growing MT plus ends relative to the lattice (Fig. S4.30A,B), in spite of the fact that EB3 was able to track MT plus ends in the same assay (Fig. S4.30C). These data show that Gas2L1 does not behave as a canonical

plus end tracking protein although it does contain an EB-binding SxIP motif.

Our results confirm that Gas2L1 can crosslink actin filaments and MTs. However, while individual domains of Gas2L1 are able to bind MTs or actin filaments, full-length Gas2L1 does not localize to either of these separate cytoskeletal components *in vitro*. Instead, Gas2L1 binds to MTs and actin filaments simultaneously, suggesting that the protein might be autoinhibited and that the interaction with both actin and MTs is required to relieve autoinhibition. Of note, Gas2L1 did not bind independently to MTs regardless of incubation time. However, over time Gas2L1 accumulated on slowly forming actin bundles (but never individual filaments) in the absence of MTs (Fig. S4.23). Since there appears to be some interaction between Gas2L1 and actin in the absence of MTs, we propose that the binding of Gas2L1 to actin acts as the first step towards initiating actin-MT crosslinking (Fig. 4.6D).

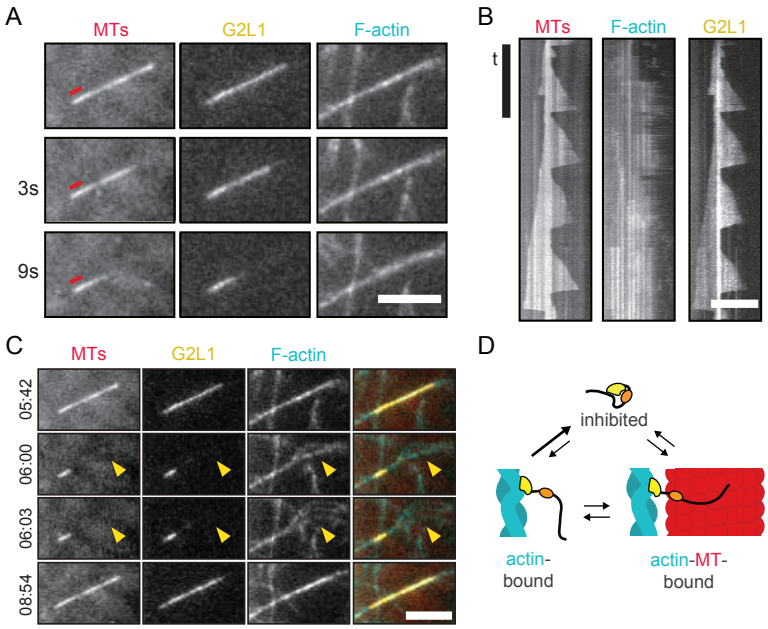

Figure 4.6: **Dynamic interactions inside actin-MT-Gas2L1 bundles.** **(A)** Still frames showing the dynamics of a Gas2L1-F-actin-MT bundle, from a composite *in vitro* reconstitution assay similar to Fig. 4.5C (so no EB3 present and at 30 nM Gas2L1). The red line indicates the (stable) MT seed. **(B)** Kymographs showing the dynamics of the Gas2L1-F-actin-MT bundle seen in (A). **(C)** Still frames showing the dispersion of actin filaments (yellow arrowheads) after Gas2L1 and the MT disappear from the Gas2L1-F-actin-MT-bundle and renewed actin bundling and Gas2L accumulation upon MT regrowth. Experimental conditions are as described for (A-B). **(D)** Model of Gas2L1 autoinhibition. Scale bars: 10µm (A), 5µm (C). For (B), vertical scale bar: 3 min, horizontal scale bar: 5µm.

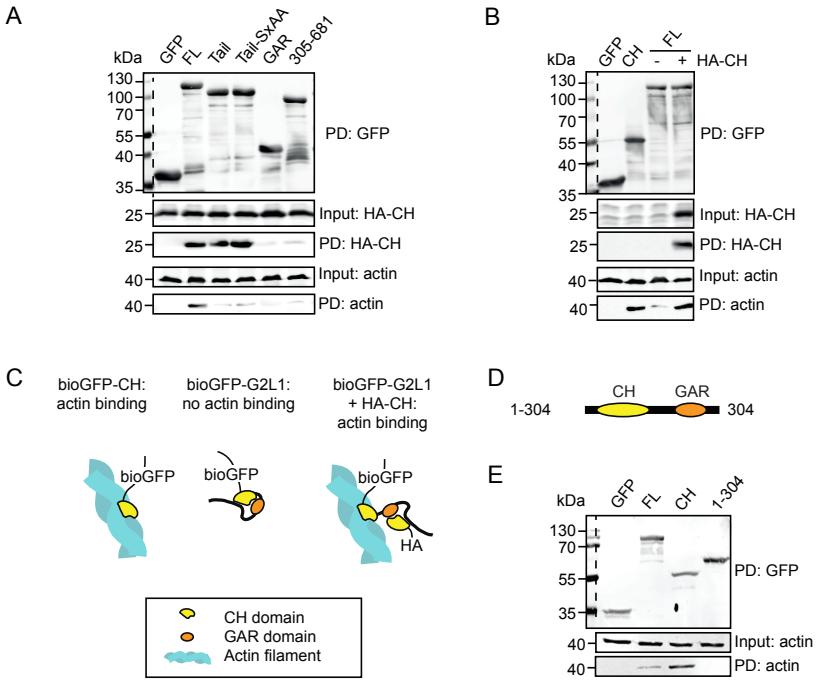

Figure 4.7: **Intramolecular interaction between Gas2L1 domains.** **(A)** Pull-down experiment showing the binding of Gas2L1's CH domain (HA-CH) to full-length Gas2L1 (FL) and both Tail and Tail-SxAA mutants in HEK293 cell lysates, as well as co-precipitation of actin with full-length Gas2L1 bound to HA-CH. **(B)** Pull-down experiment showing co-precipitation of actin with Gas2L1's CH domain in HEK293 cell lysates, and full-length Gas2L1 only when HA-CH is co-expressed. **(C)** Model of increased co-precipitation of actin with Gas2L1 in the presence of HA-CH. **(D)** Schematic depiction of the domain structure of Gas2L1(1-304). **(E)** Pull-down experiment showing the co-precipitation of actin with Gas2L1's CH domain (CH), but not with full-length Gas2L1 (FL) or Gas2L1-1-304 (1-304) in HEK293 cell lysates. Dotted lines separate marker lanes from sample lanes on the same blots (top panels). For bottom panel blots, markers were detected on the same blot, but in a different channel than the one used for signal detection that are shown here. PD, pull-down, shows what was attached to bead-bound Gas2L1 fragments (indicated for each lane) after incubation with indicated input.

4.2.3. AUTOINHIBITION OF GAS2L1 IS A RESULT OF THE INTERACTION BETWEEN THE CH DOMAIN AND MT-BINDING TAIL

If Gas2L1 is indeed autoinhibited, its MT-binding tail should directly compete with actin for binding its CH domain. A similar intramolecular interaction was reported for Shot: its N-terminal tandem CH domains interact with the C-terminal EF-hand/GAR region [75] (also studied in Chapter 5).

We mapped potential intramolecular interactions of Gas2L1 by testing whether its different deletion mutants (Fig. S4.15A) interacted with the CH domain in a pull-down assay. Gas2L1 fragments were tagged with an N-terminal AviTag fused to GFP (bioGFP), which was biotinylated by co-expressing the biotin ligase BirA. Streptavidin beads were used to bind biotinylated Gas2L1 fragments and incubated with HA (human influenza hemagglutinin) tagged CH domains, which in case of interaction were retained on the

beads after washing and could be detected by Western blotting.

Full-length Gas2L1 and the MT-binding Tail fragment pulled down the CH domain, whereas the biotinylated GFP, used as a negative control, displayed no binding (Fig. 4.7A). Moreover, a Tail mutant harbouring a mutated SxIP motif (Tail-SxAA), which was previously shown to abolish Gas2L1-EB interaction [172], still bound to the CH domain. When the Tail domain was split into smaller fragments, the binding to the CH domain was lost (Fig. 4.7A). These data suggest that the interaction of the CH domain of Gas2L1 with the MT-binding C-terminal part of the protein requires both the GAR domain and the unstructured region, and occurs independently from the association with EB proteins.

Interestingly, consistent with the pattern of *in vitro* reconstitution experiments, the CH domain of Gas2L1 pulled down endogenous F-actin much more efficiently than full-length Gas2L1 (Fig. 4.7B). However, full-length Gas2L1 acquired the ability to efficiently pull down F-actin in the presence of a co-expressed CH domain (Fig. 4.7A,B). This was likely due to the additional CH domain competing with the tail part of the full-length Gas2L1 for binding to the CH domain located within the same molecule (Fig. 4.7C), confirming our model of Gas2L1 autoinihibition. Furthermore, the MT-binding Tail fragment did not pull down F-actin even though the CH domain co-precipitated (Fig. 4.7A). This observation reinforces the idea that the CH domain of Gas2L1 cannot bind to F-actin when it is associated with the tail part of the protein in the autoinhibited conformation.

Considering the previously identified association between the CH domain and GAR/EF-hand region of Shot [75], we tested whether an interaction between the CH and GAR domains of Gas2L1 was sufficient to inhibit binding of the CH domain to actin. Indeed, we did not observe F-actin being pulled down by a Gas2L1 deletion mutant containing the CH and GAR domains but lacking the unstructured C-terminal region (amino acids 1-304, Fig. 4.7D,E). This suggests that the 1-304 mutant is autoinhibited via a direct association between the GAR and CH domains. However, we could not detect the CH-GAR interaction when the CH and GAR domains were expressed independently and not tethered to each other within the same molecule (Fig. 4.7A). This suggests that the interaction between the CH and GAR domain is rather weak and that it is likely strengthened by the presence of the unstructured C-terminal region (amino acids 305-681, see Fig. 4.1). Taken together, we conclude that Gas2L1 is autoinhibited through a direct interaction between its CH domain and its MT-binding tail. Our *in vitro* reconstitution observations predict that this mechanism could promote the selective activity of the protein at actin-MT interfaces.

4.2.4. THE GAS2L1 TAIL FRAGMENT CONTAINS AT LEAST TWO MT BINDING REGIONS

Since the unstructured C-terminus of Gas2L1 promoted the autoinhibitory interaction between the GAR and CH domains, we next tested whether this part of Gas2L1 also affects the binding of the GAR domain to MTs. We investigated MT binding of the GFP-tagged Gas2L1 Tail fragment (amino acids 196-681) or its parts (Fig. S4.15A) in COS-7 cells, where individual MTs are easier to distinguish than in neurons (Fig. 4.8). At very high expression levels, both the GAR domain and the unstructured C-terminus could bind to and bundle MTs, and the same was true for the complete Tail fragment (Fig. 4.8B).

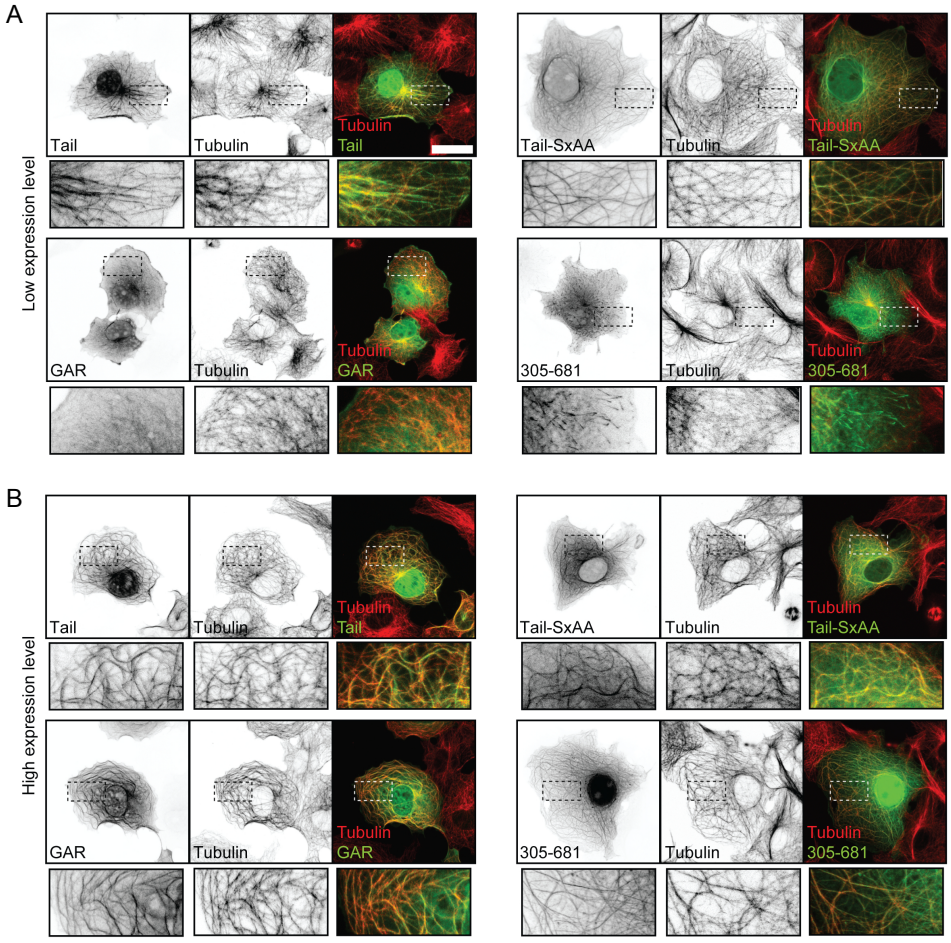

Figure 4.8: **Localization of G2L1 tail domain mutants.** **(A)** COS7 cells overexpressing different G2L1 tail domain fragments at low expression levels. **(B)** COS7 cells overexpressing G2L1 tail domain fragments at high expression levels. Shown are different G2L1 tail domain fragments (green) and staining for MTs (α-tubulin, red), as well as merged images showing co-localization of the G2L1 fragments with MTs. Bottom panels show enlargements of boxed regions. Scale bars: 30µm in (A).

However, at low overexpression levels, the GAR domain showed comparatively little association with MTs, and the unstructured C-terminus displayed a comet-like distribution characteristic for plus-end tracking proteins, whereas the complete Tail fragment co-localized with MTs (Fig. 4.8A). Mutating the SxIP motif to SxAA, and therefore abolishing the binding of the Tail fragment to EB proteins and MT plus-ends [172], did not significantly alter the binding of the Tail to MT shafts. These data suggest that both the unstructured C-terminus and the GAR domain of Gas2L1 have some affinity for the MT lattice and cooperate in associating with MTs. Our results match those reported for comparable deletion mutants of the Drosophila Gas2L ortholog Pigs in cells [78].

4.2.5. GAS2L1 LOCALIZES TO NEURONAL F-ACTIN AND REGULATES AXON DEVELOPMENT BY INFLUENCING ACTIN STABILITY

Next, we turned back to primary hippocampal neurons to investigate how Gas2L1 affects their cytoskeleton. In NIH3T3 and COS7 cells, Gas2L1 was shown to localize predominantly to actin stress fibres [76, 170]. In neurons, which lack stress fibres, GFP-tagged Gas2L1 primarily co-localized with the total F-actin population (Fig. 4.9A). The localization of Gas2L1 to F-actin was also apparent in subcellular areas devoid of MTs. This observation reveals that in contrast to our *in vitro* experiments, Gas2L1 can localize to actin structures independently of MTs in neurons. This result suggests that additional layers of regulation are likely present in cells (see discussion), and further strengthens the idea that actin binding may be the first step towards stably relieving the autoinhibition of Gas2L1. Some Gas2L1 accumulation along MTs was also observed (Fig. 4.9B). Interestingly, axons of DIV3-4 neurons expressing high levels of Gas2L1 showed clear cytoskeletal abnormalities: MTs frequently buckled inside growth cones (Fig. 4.9C-E), which were enlarged due to what appeared to be increased amounts of F-actin (Fig. 4.2G and 4.9C).

Given the dominant localization of Gas2L1 to F-actin, we then focussed on actin-related effects of the protein. We noticed that Gas2L1 depletion and overexpression phenotypes during axon development line up with results published in various studies investigating the effect of mild changes of actin stability on this process [175–180]. Therefore, we tested the effect of low nanomolar doses of latrunculin B (LatB) on the primary hippocampal neurons in our culture system. DMSO, which was used as a ve-

Figure 4.9 *(facing page)*: **Neuronal localization of Gas2L1 and effects of its overexpression. (A)** Localization of GFP-Gas2L1 (G2L1) in a DIV4 neuron stained for MTs (α-tubulin) and F-actin (Phalloidin), as well as merged images showing colocalization between GFP-Gas2L1 and Phalloidin or GFP-Gas2L1 and α-tubulin. The linescan shows colocalization along the boxed neurite. **(B)** Close-up of GFP-Gas2L1 localization to MTs (tubulin staining). Red arrowheads point along examples of MTs positive for GFP-Gas2L1. **(C)** Cytoskeleton of DIV3 neurons electroporated at DIV0, co-expressing LifeAct-GFP and control empty vector (left) or HA-Gas2L1 (right) and stained for MTs (tubulin). Boxes indicate zoomed region. **(D)** Quantification of MT configuration in axonal growth cones of DIV4 neurons transfected with GW1-EV (empty vector), G2L1 shRNA or HA-G2L1 (G2L1 OE) and HA-β-galactosidase for one day. MT configuration is classified as straight, buckled or fan-like. n=128-214 growth cones from 30-36 neurons per condition (154 growth cones from 36 neurons for GW1-EV, 128 growth cones from 30 neurons for G2L1 shRNA, 214 growth cones from 36 neurons for G2L1 OE) from 3 independent experiments. **(E)** Examples of different MT configurations (from α-tubulin staining) in growth cones as quantified in (D). Dotted red line shows the growth cone silhouette (from β-galactosidase fill). Scale bars: 20µm in (A), 3µm in (B), 10µm in (C), 5µm in (E).

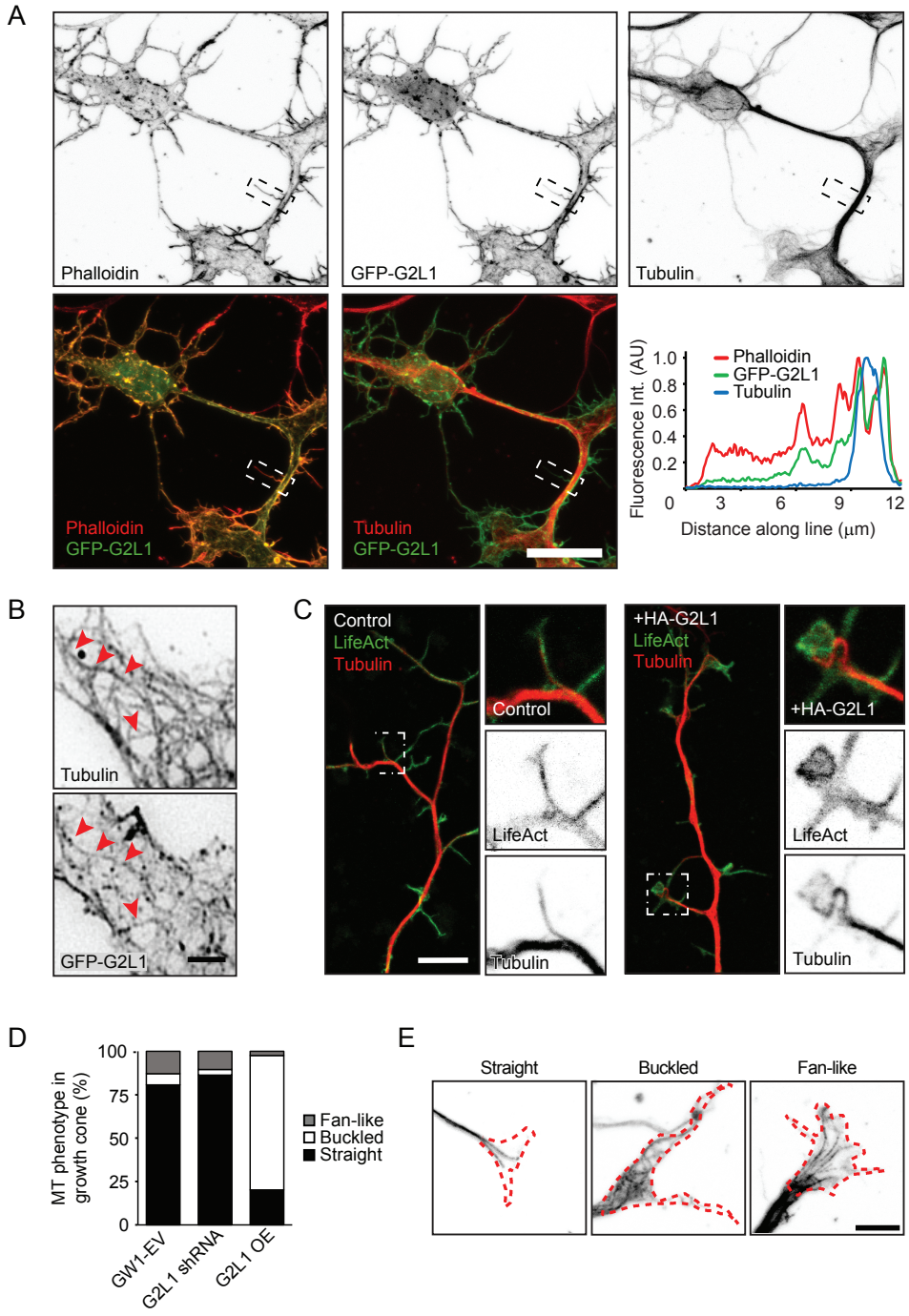
A
Phalloidin
GFP-G2L1
Tubulin
Phalloidin
GFP-G2L1
Tubulin
GFP-G2L1
Phalloidin
GFP-G2L1
Tubulin
Fluorescence Int. (AU)
1.0
0.8
0.6
0.4
0.2
0
3
6
9
12
Distance along line (μm)
B
Tubulin
GFP-G2L1
C
Control
LifeAct
Tubulin
Control
LifeAct
Tubulin
+HA-G2L1
LifeAct
Tubulin
+HA-G2L1
LifeAct
Tubulin
D
MT phenotype in growth cone (%)
100
75
50
25
0
GW1-EV
G2L1 shRNA
G2L1 OE
Fan-like
Buckled
Straight
E
Straight
Buckled
Fan-like

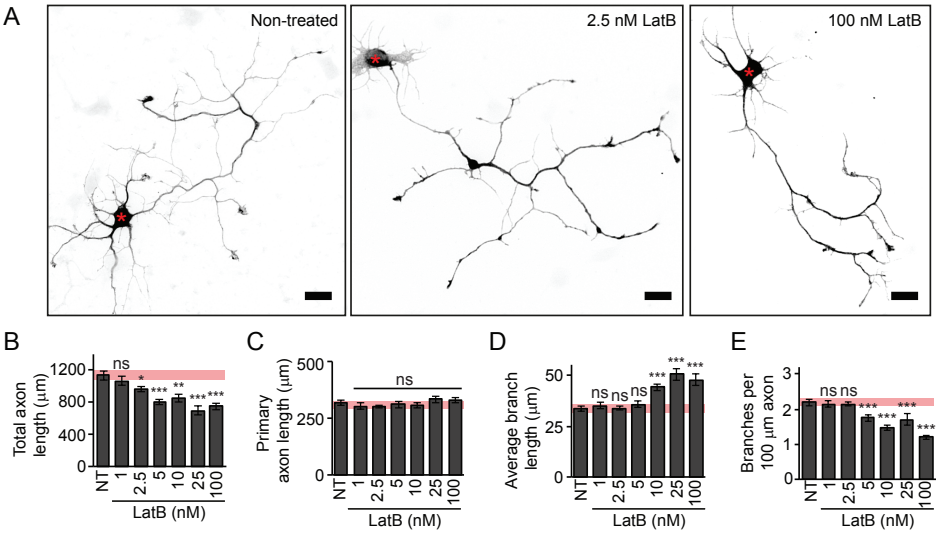

Figure 4.10: **Gas2L1 phenotypes reflect changes in actin stability. (A)** Silhouettes (from β-galactosidase fill) of DIV3 neurons, transfected at DIV1 and treated with the indicated doses of Latrunculin B for 48 hours. **(B-E)** Quantifications of total axon length (B), primary axon length (C), average axon branch length (D) and the number of branches per 100 µm axon (E) for neurons as described in (A). Pink bars show range of means ±SEM of control conditions. NT=non-treated; n=37-40 neurons per condition (38/39//37/38/40/39/39 for NT/1/2.5/5/10/25/100 nm LatB respectively) from 3 independent experiments. Scale bars: 20µm. Data is displayed as means ±SEM. Mann-Whitney test, ns: not significant, * p<0.05, ** p<0.01, ***p<0.001.

hicle, had no effects on axon morphology at the highest concentration used in these experiments (Fig. S4.31A-E). In contrast, 48-hours treatment with 10-100 nM LatB reduced branch density and induced branch elongation at DIV3 (Fig. 4.10). Mild actin destabilization with LatB thus resembled the effects of Gas2L1 knockdown (summarized in Fig. 4.14A). However, primary axon length did not increase after LatB treatment (resulting in a net decrease of combined axon length as seen in Fig. 4.10B,C), whereas the depletion of Gas2L1 did induce lengthening of the primary axon (Fig. 4.2D). These data suggest that Gas2L1 could act by stabilizing actin and display higher activity in the primary axon compared to elsewhere in the neuron, possibly due to the presence of distinct actin filament populations.

F-actin stabilization by low nanomolar doses of jasplakinolide mimicked effects of Gas2L1 overexpression on axons of control vector-expressing DIV4 neurons treated for 48 hours (Fig. 4.11, grey bars, and summarized in Fig. 4.14A). Moreover, at 25 nM of jasplakinolide, axons displayed thickening and lamellipodia- and filopodia-like protrusions akin to Gas2L1 overexpression (Fig. S4.16C and 4.11A). Importantly, 5-10 nM jasplakinolide was able to rescue the effects of Gas2L1 depletion on axon morphology (Fig. 4.11, white bars). Taken together, these data suggest that Gas2L1 mediates axon branching and outgrowth by increasing F-actin stability. These findings are consistent with the observation that the Drosophila Gas2L-ortholog Pigs stabilizes F-actin when overexpressed in S2R+ cells [78].

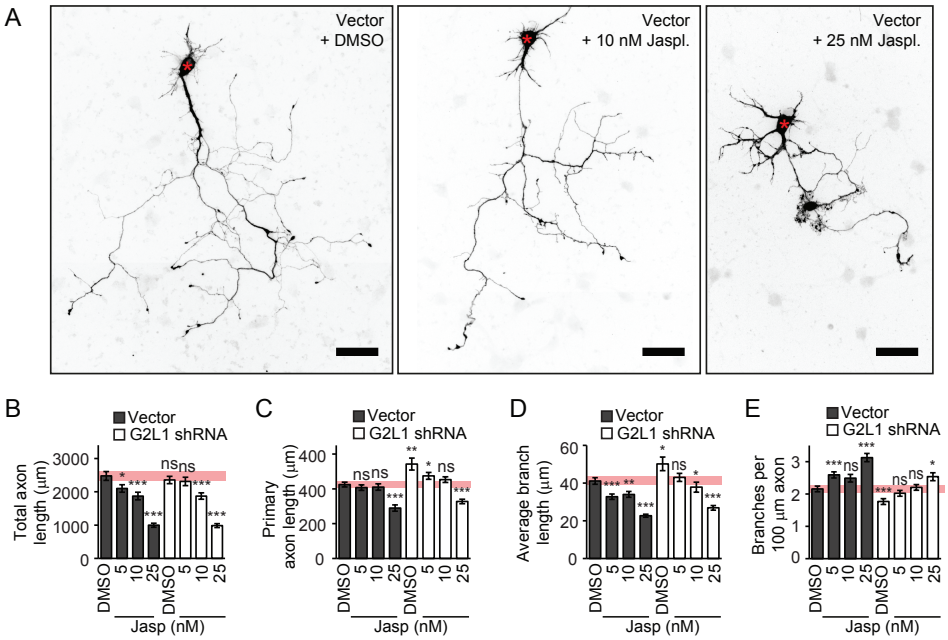

Figure 4.11: **Gas2L1 phenotypes reflect changes in actin stability. (A)** Silhouettes (from β-galactosidase fill) of DIV4 neurons, transfected at DIV1 with empty shRNA vector (grey bars in B-E) or Gas2L1 shRNA (white bars in B-E) and coexpressing β-galactosidase. 24 hours after transfection, neurons were treated with the indicated doses of Jasplakinolide or DMSO (equivalent of 25 nM dose) for 48 hours. **(B-E)** Quantifications of total axon length (B), primary axon length (C), average axon branch length (D) and the number of branches per 100 µm axon (E) for neurons as described in (A). Pink bars show range of means ±SEM of control conditions. n=64-69 neurons per condition (66/64/68/67 for vector + DMSO/5/10/25 nM jasplakinolide respectively, and 65/66/69/67 for G2L1 shRNA + DMSO/5/10/25 nM jasplakinolide respectively) from 4 independent experiments. Scale bars: 50µm. Data is displayed as means ±SEM. Mann-Whitney test, ns: not significant, * p<0.05, ** p<0.01, ***p<0.001. For Fig B-E, all values were compared to those of DMSO control (vector) neurons.

4.2.6. MT BEHAVIOUR APPEARS UNAFFECTED IN NEURONS DEPLETED OF GAS2L1 BUT IS AFFECTED BY GAS2L1 *in vitro*

We next determined if and how MT-related effects contribute to the role of Gas2L1 in axon development. In line with reports in NIH3T3 cells [76], overexpression of Gas2L1 caused the displacement of endogenous EB1 away from MT plus-ends and onto Gas2L1-decorated structures (Fig. 4.12A), which we showed above to colocalize with actin. We confirmed that this behaviour depended on the SxIP motif of Gas2L1, as mutating the SxIP motif to SxAA abolished EB1 displacement (Fig. 4.12B). These results are in agreement with our *in vitro* observations that Gas2L1 is not a plus-end tracking protein (Fig. 4.3 and S4.30) and that Gas2L1 can recruit EB3 to actin bundles (Fig. S4.25). The function of the EB-Gas2L1 interaction might be to augment the intrinsically weak MT affinity of Gas2L1. Of note, the redistribution of EB proteins and axon development defects induced by Gas2L1 overexpression show that, although overexpression experiments provide valuable insights into the functioning of the protein, endogenous Gas2L1 operates at low levels with more nuanced outcomes.

Analyzing kymographs from our *in vitro* reconstitution assays (such as shown in Fig. 4.13B and S4.30B,C) allowed us to study the impact of Gas2L1 on MT dynamics in the presence of F-actin and EB3. Preliminary analysis (limited in number of replicates) showed that Gas2L1 hardly affects the MT catastrophe rate (Fig. 4.13C). However, MT growth velocity is affected by Gas2L1, as we observe a decrease from 3.14 µm min^{-1} to 2.31 µm min^{-1} by the addition of Gas2L1 (Fig. 4.13D). Most notably, we observed a large effect of Gas2L1 on MT rescue frequency, namely an over 30-fold increase (Fig. 4.13E).

To determine the contribution of Gas2L1 to MT regulation in neurons at endogenous levels, we looked for signs of MT disruption in neurons depleted of Gas2L1. In cultured

Figure 4.12 *(facing page)*: **MTs modulate the actin-stabilizing activity of Gas2L1. (A)** Endogenous EB1 relocalization upon overexpression of GFP-Gas2L1 (G2L1) in a DIV4 neuron. Boxes indicate zoomed regions of transfected (continuous outline) or untransfected neurons (dotted outline). **(B)** Endogenous EB1 localization upon overexpression of GFP-Gas2L1-SxAA (G2L1-SxAA) in a DIV3 neuron. Boxes indicate zoomed region of transfected neuron. **(C)** Lifetime of photoactivated GFP-αTubulin signal in axons of DIV3-4 neurons electroporated at DIV0 with RFP, paGFP-αTubulin and control GW1-EV or Gas2L1 shRNA or HA-Gas2L1. n=54-59 axons per condition (59 for vector and HA-Gas2L1, 54 for Gas2L1 shRNA) from 3 independent experiments. **(D)** Growth velocity of anterograde MT comets near the axon terminus, as labelled with EB3-tagRFP-T in DIV3-4 neurons electroporated at DIV0 with pSuper empty vector (control) or Gas2L1 shRNA. n=27 neurons for control and 28 neurons for Gas2L1 shRNA (664-714 comets) per condition from 2 independent experiments. **(E)** Localization of GFP-Tail in DIV3 neurons co-expressing HA-β-galactosidase fill (blue) and stained for TRIM46 (red). Boxed region is enlarged to the right. Arrowheads indicate the axon. **(F)** DIV3 neurons expressing GFP control, GFP-Gas2L1 or GFP-CH and treated with 10 µM Latrunculin B for 30 minutes or non-treated, stained for F-actin (phalloidin) and the axon initial segment (TRIM46). **(G, H)** Raw phalloidin staining intensities in axons (G) and non-axonal neurites (pre-dendrites) (H) of DIV3 neurons expressing the indicated GFP fusions and treated with 10 µM Latrunculin B for 30 minutes (grey bars) or non-treated (white bars). n=35-40 neurons per condition (40 for GFP, GFP-G2L1, GFP-CH and 35 for GFP-SxAA) from 2 independent experiments. **(I)** Polarity index representing localization of the indicated GFP fusions in non-treated neurons (green bars), and localization of F-actin as labelled by phalloidin in DIV3 neurons treated with 10 µM Latrunculin B for 30 minutes (grey bars) or non-treated (white bars). n=35-40 neurons per condition (40 for GFP, GFP-G2L1, GFP-CH and 35 for GFP-SxAA) from 2 independent experiments. Positive values indicate axonal enrichment, negative values indicate neuritic enrichment and a value of 0 signifies no particular enrichment. Scale bars: 10 µm in (A, B), 4 µm in (C), 50 µm in (E) , 30 µm in (F). Data is displayed as means ±SEM. Mann-Whitney test (C, G, H), unpaired t-test (D), ns: not significant, * p <0.05, ** p<0.01, ***p<0.001.

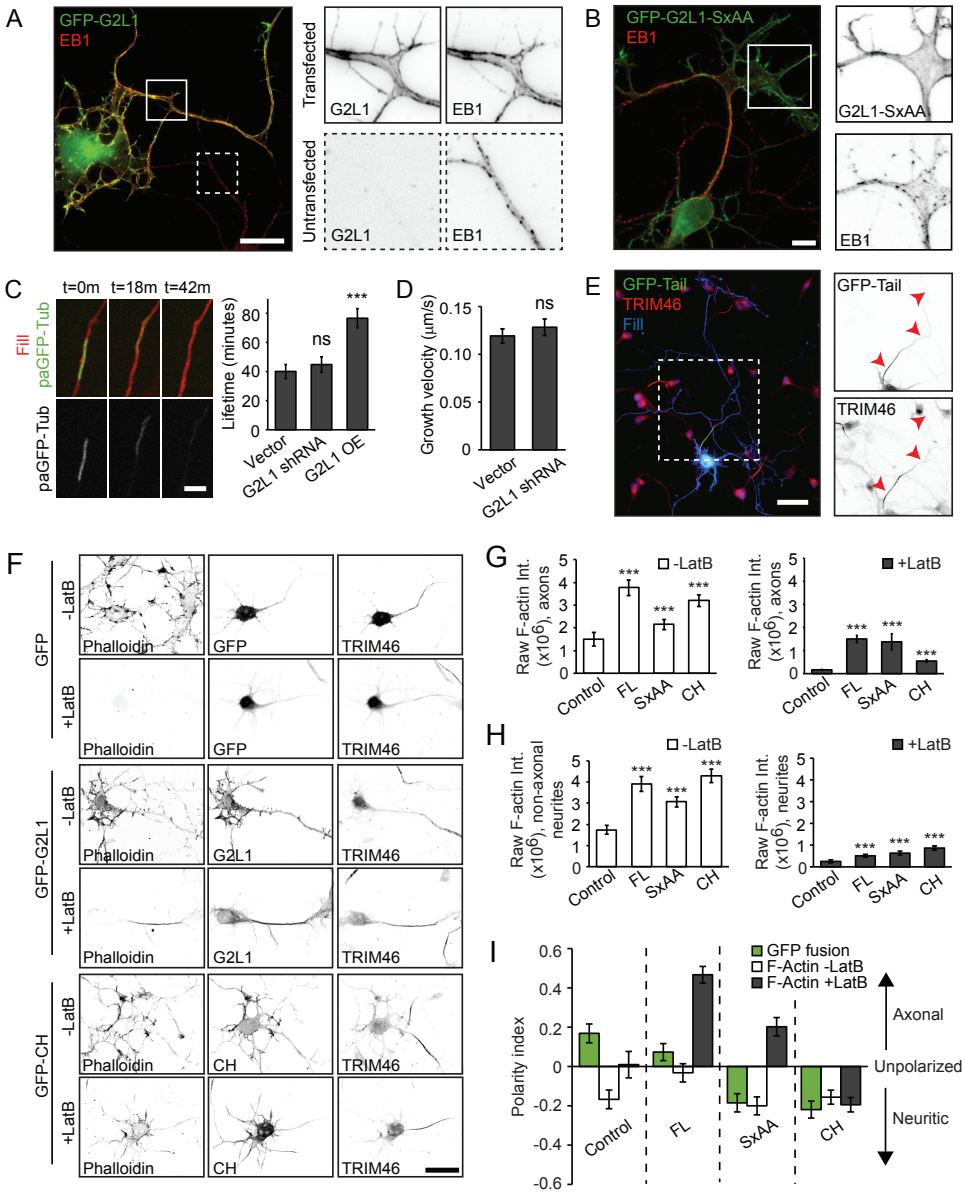
A
GFP-G2L1
EB1
Transfected
Untransfected
G2L1
EB1
B
GFP-G2L1-SxAA
EB1
G2L1-SxAA
EB1
C
t=0m t=18m t=42m
Fill
paGFP-Tub
paGFP-Tub
Lifetime (minutes)
ns
***
Vector
G2L1 shRNA
G2L1 OE
D
Growth velocity (µm/s)
ns
Vector
G2L1 shRNA
E
GFP-Tail
TRIM46
Fill
GFP-Tail
TRIM46
F
GFP
GFP-G2L1
GFP-CH
-LatB
+LatB
Phalloidin
GFP
G2L1
CH
TRIM46
G
Raw F-actin Int. (x10^6), axons
-LatB
+LatB
Control
FL
SxAA
CH
H
Raw F-actin Int. (x10^6), non-axonal neurites
Raw F-actin Int. (x10^6), neurites
I
Polarity index
GFP fusion
F-Actin -LatB
F-Actin +LatB
Axonal
Unpolarized
Neuritic

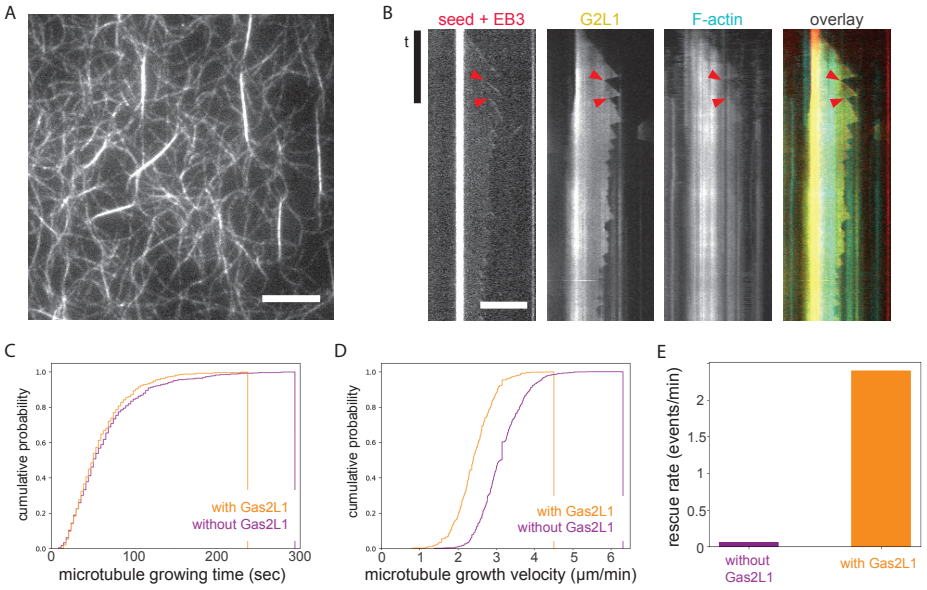

Figure 4.13: **Preliminary analysis of Gas2L1 influence on *in vitro* MT dynamics in the presence of F-actin and EB3.** **(A)** Typical field-of-view of F-actin network in which MTs grow in the presence of Gas2L1 and EB3. **(B)** Kymograph showing many rescue events. Depicted are MT seed (red), EB3 (red), Gas2L1 (yellow), F-actin (blue) and their overlay. Red arrowheads indicate the first two rescue events. Gas2L1 localizes specifically to the overlap region of MTs and F-actin. More kymographs in Fig. S4.30B,C. **(C)** MT growing time in the absence of Gas2L1 (purple) and in the presence of Gas2L1 (orange). The average catastrophe frequencies are $0.94 \pm 0.04\,\mathrm{min}^{-1}$ without Gas2L1 (purple) and $1.03 \pm 0.05\,\mathrm{min}^{-1}$ with Gas2L1 (orange). **(D)** Corresponding MT growth velocity, with average growth velocities (weighted by growing time) of $3.14 \pm 0.57\,\mu\mathrm{m\,min}^{-1}$ without Gas2L1 (purple) and $2.43 \pm 0.50\,\mu\mathrm{m\,min}^{-1}$ with Gas2L1 (orange). **(E)** Corresponding rescue frequencies, with measured rescue frequencies of $0.06\,\mathrm{min}^{-1}$ without Gas2L1 (purple) and $2.40\,\mathrm{min}^{-1}$ with Gas2L1 (orange). Experiments were performed in the presence of 1 µM F-actin and 133 nM EB3. Growth velocities are weighted averages ± weighted STD; catastrophe rates are means ± SEM. Total number of analysed growth events: n=710 (in 3 independent experiments) without Gas2L1; n=454 (from 2 independent experiments) with Gas2L1. Scale bars: 10 µm (horizontal) and 5 min (vertical).

cell lines, overexpression of Gas2L1 or its tail fragments was reported to promote resistance to nocodazole-induced MT depolymerization and to decrease MT dynamics [76, 170]. We used a photoactivatable fusion of GFP-α-tubulin to measure the longevity of MTs in axon shafts and found that, although Gas2L1 overexpression could indeed increase MT lifetimes, there was no difference between control and Gas2L1-depleted neurons (Fig. 4.12C). Similarly, we found that whereas Gas2L1 overexpression increased the ratio of acetylated/tyrosinated MTs, there was no difference between control neurons and neurons depleted of Gas2L1 (Fig. S4.32A,B). An increase in the ratio of acetylated/tyrosinated MTs reflects their enhanced stability, as newly polymerized MTs are tyrosinated, while older MTs become acetylated and detyrosinated [181, 182]. There was no change in the growth velocity of EB3-positive MT plus ends in growth cones upon Gas2L1 depletion either (Fig. 4.12D), and we saw no differences in MT organization in axonal growth cones of Gas2L1-depleted neurons (Fig. 4.9D,E). These results suggest that, although Gas2L1 has the potential to stabilize MTs at medium to high expression levels, MT behaviour is relatively normal in Gas2L1 knockdown neurons, likely due to the low levels at which we assume Gas2L1 to be expressed and to potential functional overlap with other cytolinkers, as was already shown for Shot and Tau in *Drosophila* [67, 71, 89].

4.2.7. MTs GUIDE GAS2L1 ACTIVITY IN NEURONS

Interestingly, we found that while the Gas2L1 MT-binding Tail mutant could decorate all neuronal MTs, it was enriched on TRIM46-positive MTs in proximal axons (Fig. 4.12E). Given our *in vitro* findings, which suggest a model of full release of Gas2L1 autoinhibition in the presence of actin and MTs, we wondered whether this increase in MT affinity could impact Gas2L1 activity locally. More specifically, we wondered whether the preferential interaction of the tail of Gas2L1 with MTs in the proximal axon could drive differential effects of Gas2L1 on actin stabilization.

Quantifications of the total amount of F-actin in proximal axons and non-axonal neurites (future dendrites; dendritic maturation occurs at later stages of development) revealed that overexpression of GFP-Gas2L1, GFP-Gas2L1-SxAA and GFP-CH increased F-actin levels compared to GFP overexpression (Fig. 4.12G,H, white bars). To determine whether the enhanced levels of F-actin also reflected enhanced actin stability, as suggested by drug-induced effects including rescue experiments (Fig. 4.11), we treated neurons overexpressing Gas2L1 or Gas2L1 mutants with high concentrations of LatB to reveal stable F-actin populations (Fig. 4.12F-H, grey bars). Treatment of control GFP-expressing neurons with 10 µM LatB for 30 minutes resulted in a near-complete loss of F-actin in all projections of control, GFP-expressing neurons. By contrast, some F-actin remained in the presence of overexpressed Gas2L1 mutants, although the patterns of stabilization were strikingly different between full-length Gas2L1 and its deletion mutants (Fig. 4.12F).

To quantify the differences in actin stabilization compared to the localization of the various fusion proteins tested, we compared the polarity indices of the localization of each Gas2L1 fusion before treatment and of F-actin distribution with or without LatB treatment (Fig. 4.12I). The polarity indices are derived from raw fluorescence intensities in axons and non-axonal neurites (see Materials & Methods for details) and range from 1 to -1 for purely axonal or purely non-axonal localizations, respectively. A value of 0 sig-

nifies no particular enrichment. Our analysis showed that the CH domain of Gas2L1 is enriched in non-axonal neurites, where it also stabilizes actin. Surprisingly, full-length Gas2L1 was evenly distributed between the axons and other neurites, yet it most efficiently stabilized actin in the axon (Fig. 4.12I). This suggests that the MT-binding tail region promotes axonal localization of Gas2L1 in addition to the non-axonal neurite targeting of the protein via the CH domain. Importantly, the pattern of actin stabilization by Gas2L1 mirrored the preference of the Gas2L1 tail for axonal MTs rather than the broad localization of the full-length protein to neuronal actin. This suggests that MT interactions indeed promote Gas2L1 activity towards actin.

The SxAA mutant deficient in EB binding localized similarly to the CH domain, yet it still preferentially stabilized axonal actin (Fig. 4.12I and 4.32D; note that a negative ratio in Fig. 4.12I does not indicate a protein's absence from axons, but just reflects the preferential localization to non-axonal neurites). We propose that the SxAA mutation reduces the overall binding of Gas2L1 to MTs, because this binding can occur directly, but also indirectly, through EBs, and the latter is perturbed in the SxAA mutant. Therefore, this mutation reduces the ability of the protein to localize to axons. However, the SxAA-mutated tail fragment of Gas2L1 can still interact with the CH domain and maintains some association with MTs (Fig. 4.7A and Fig. 4.8), suggesting that the mutated protein can still respond to MT-controlled regulation of autoinhibition, albeit less strongly. As a result, the actin-stabilizing activity of Gas2L1-SxAA is still shifted to the axonal compartment, but not as strongly as that of the wild-type protein.

One could argue that the behaviour of Gas2L1 is simply a result of actin-MT crosslinking via CH and GAR domains, respectively. If this were the case, the MT-binding tail region of Gas2L1 would likely exert a similar effect on other actin-binding CH domains: that is, it would change their localization and actin stabilization patterns. To test this possibility, we fused Gas2L1-Tail to the tandem actin-binding CH domains of α-actinin (ABD and ABD-Tail; Fig. S4.32C). Although the CH domains of Gas2L1 and α-actinin belong to different classes [183], ABD behaved very similarly to the CH domain of Gas2L1 – it preferentially localized to non-axonal neurites, where it also stabilized actin. However, unlike the CH domain of Gas2L1, ABD was not affected by the fusion to Gas2L1-Tail (Fig. S4.32D-G), indicating that within this fusion, the tail of Gas2L1 makes no direct contribution to the specificity of actin binding. Our data suggest that the MT-binding tail of Gas2L1 can locally and specifically modulate the activity of the CH domain of Gas2L1, likely due to the direct interaction with this domain.

4.3. DISCUSSION

In this study, we show that the cytolinker Gas2L1 contributes to the regulation of axon morphology by stabilizing F-actin. Interestingly, the actin-binding CH domain of Gas2L1 preferentially localizes to non-axonal neurites, but the presence of the MT-binding C-terminus in the full-length protein leads to an equal distribution of Gas2L1 to F-actin in all neurites. In spite of its uniform localization, full-length Gas2L1 stabilizes F-actin more potently in the proximal axon, whereas the CH domain preferentially stabilizes F-actin in non-axonal neurites. These results suggest that the binding of Gas2L1 to MTs influences both the localization and activity of the protein in neurons. This finding is further reinforced by the fact that the Gas2L1 MT-binding tail fragment is enriched on

MTs in the proximal axon, which coincides with the region of the strongest F-actin stabilization by Gas2L1.

How can MTs regulate the activity of Gas2L1 towards F-actin? We propose that this property depends on the autoinhibition of Gas2L1. Our *in vitro* reconstitution experiments demonstrated that Gas2L1 efficiently localizes to actin-MT bundles, but not to individual actin filaments or MTs. This can be explained by the interaction between the CH domain and the MT-binding tail, which employs the same interfaces as those used for the actin and MT binding. The association of the Gas2L1 tail domain with MTs is expected to liberate the CH domain and to allow Gas2L1 to interact with actin filaments, placing the activity of the protein under direct control of the simultaneous presence of actin and MTs. Our results complement previous observations hinting towards an inhibitory relation between the CH and GAR domains of Gas2L proteins in other cell types [78, 170]. For example, Girdler and colleagues observed that Pigs, the Drosophila Gas2L ortholog, stabilizes actin at MT interfaces [78]. Therefore, the regulatory mechanism we identified for Gas2L1 may be conserved in evolution. Similarly, the CH and EF-hand/GAR domains of the Drosophila spectraplakin Shot also undergo an autoinhibitory interaction [75]. The direct regulation by actin and MTs might thus be a common mechanism in CH/GAR domain-containing cytolinkers.

Although autoinhibition of Gas2L1 is obvious from the biochemical and *in vitro* reconstitution experiments, it is less apparent in neurons. Purified Gas2L1 does not associate with individual actin filaments *in vitro* unless MTs are present, yet overexpressed Gas2L1 localizes to neuronal F-actin including the areas where MTs are excluded. This discrepancy may arise from the differential affinity of Gas2L1 for various types of actin, e.g. different organisation of actin filaments, their posttranslational modifications and the presence of actin-associated proteins. Evidence for the binding selectivity of Gas2L1 was already provided by previous studies, where the binding to EB was shown to play a role in the association of Gas2L1 to MTs and F-actin [76, 78]. It is also possible that additional modes of regulation exist in cells, which are not present in the *in vitro* reconstitution experiments. For example, if Gas2L1 autoinhibition is regulated by posttranslational modifications such as phosphorylation, the absence of kinases, phosphatases or other regulatory enzymes *in vitro* would account for this discrepancy. Furthermore, in cells, Gas2L1 might interact with additional partners that are not present in our *in vitro* assays and that would skew its activity, for example, by promoting actin binding or by modulating autoinihibitory interactions between CH domain and the tail region. We note that over time, Gas2L1 does accumulate on actin bundles also in *in vitro* reconstitution experiments in the absence of MTs, suggesting that the association with actin is the first step towards releasing autoinhibition. Importantly, we find that Gas2L1 localization to neuronal F-actin is not sufficient to stabilize actin. Instead, Gas2L1-mediated actin stabilization appears to depend on MT binding by its C-terminus, suggesting that full relief of autoinhibition requires the presence of both actin and MTs even in neurons.

We showed that the actin-stabilizing drug jasplakinolide is able to rescue axon morphology of Gas2L1-depleted neurons and mimics Gas2L1 overexpression when applied to control neurons. Conversely, actin destabilization via LatB induces morphological changes in line with Gas2L1 depletion: axon branches elongate in response to LatB as

they do in Gas2L1-depleted neurons. Interestingly, the primary axon does not respond to low-dose LatB treatment but does become longer after Gas2L1 depletion (summarized in Fig. 4.14A). In line with this observation, axonal branches but not the primary axon are shortened after treatment with low doses of jasplakinolide (5-10 nM). It thus appears that the growth cones of primary axons are less sensitive to mild drug-mediated actin perturbations than axonal branches, possibly due to the presence of more robust regulatory machinery. We speculate that the reduced sensitivity of primary axons to low doses of LatB might be caused by the elevated activity of Gas2L1 in this neuronal compartment, which is caused by a higher affinity of the Gas2L1 C-terminus to MTs in the primary axon. However, we cannot exclude alternative explanations, such as the distinct drug response of specific actin subpopulations that could be present in the primary axon and axonal branches. Precedents for such distinct sensitivity have been described: for example, LatA has been suggested to specifically inhibit the function of the actin regulator β-thymosin and to thereby preferentially inhibit filopodia formation [184].

It is worth emphasizing that the dose of jasplakinolide needed to compensate the effects of neuronal Gas2L1 depletion is minimal (5-10 nM). Together with the dramatic changes induced by Gas2L1 overexpression, these findings suggest that the protein is extremely potent and that endogenous expression levels of Gas2L1 are low. This is in line with other studies investigating Gas2L-proteins [78, 170, 173]. Notably, at early development stages, Pines et al. reported phenotypes associated with cytoskeletal defects in Pigs null mutant flies without being able to detect the underlying cytoskeletal changes using conventional light microscopy [173]. The nuances of how Gas2L1 depletion affects the neuronal cytoskeleton are likely similarly subtle and challenging to identify.

Remarkably, key regions of Gas2L1 – the actin-binding CH domain, the MT-binding GAR domain and the EB-binding SxIP motif – are also found in the spectraplakin MACF1 (see also Chapter 5). Both Gas2L1 and MACF1 are actin-MT crosslinking proteins. However, depletion of MACF1 or its Drosophila counterpart Shot impairs axon outgrowth [68, 167, 185], whereas we find that Gas2L1 depletion promotes axon elongation. Actin-MT crosslinking proteins can thus exert opposite regulatory effects during neuronal development.

The difference between MACF1 and Gas2L1 may be explained by the observation that Gas2L1 is primarily an actin-localized protein, whereas MACF1 strongly interacts with MTs [59, 65]. Axon outgrowth requires dynamic MTs to invade the actin-rich growth cone periphery. MTs are disorganized and destabilized in growth cones lacking MACF1 [68, 167], and as such MACF1 is thought to guide MT entry into growth cones. We found that MT plus-end growth velocity, MT organization and MT stability appear normal in growth cones of Gas2L1-depleted neurons, suggesting that Gas2L1 does not operate via this mechanism. However, simplified *in vitro* reconstitution experiments without additional proteins do show that Gas2L1 can impact MT growth by promoting more persistent MT growth via increased rescue frequencies. This discrepancy might be explained by other proteins than Gas2L1 that are regulating MT dynamics in the neuronal growth cone, such as MACF1. We propose that the main function of Gas2L1 in the axon is to stabilize the surrounding actin network in response to the invasion of MTs (Fig. 4.14B).

Although actin-MT coupling is required for axon extension, a subpopulation of actin

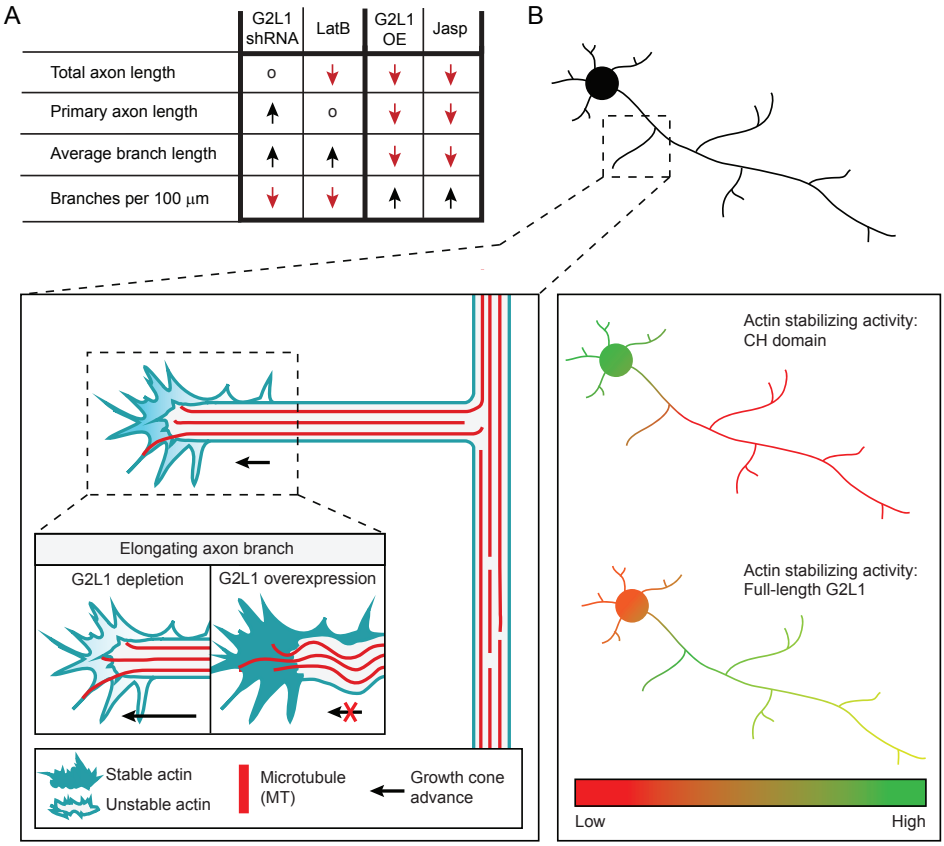

Figure 4.14: **Model of Gas2L1 activity during axon development. (A)** Summary of the effects of Gas2L1 shRNA-mediated depletion, Gas2L1 overexpression (G2L1 OE) and low nanomolar doses of jasplakinolide (jasp) and Latrunculin B (LatB) on axon development of DIV3-4 neurons. o = no effect; ↓ = lower values, ↑ = higher values. **(B)** Proposed working model of the role of Gas2L1 during axon branching and outgrowth. MT binding by the tail of Gas2L1 promotes local actin binding and stabilization by the CH domain and shifts the actin-stabilizing activity of Gas2L1 towards the axon. In growth cones, where dynamic MTs probe the actin-rich periphery, Gas2L1 contributes to actin stability levels necessary for normal outgrowth. Reduced actin stability causes overextension of branches in the absence of Gas2L1. Axons of neurons overexpressing Gas2L1 have increased actin stability, resulting in shorter branches with higher F-actin levels and buckling MTs.

acts as a barrier for MT invasion in the growth cone and as a brake on outgrowth, namely contractile actin arcs [186–189]. The actin network also produces a retrograde flow dependent on active actin-myosin contraction force that is counteracted by MTs during extension (reviewed in [6, 190]). Actin reorganization can therefore both positively and negatively affect axon elongation, and the net result is a matter of balance. By increasing actin stability, Gas2L1 could enhance the barrier function of actin, thus impeding MT invasion, or enhance actin contractility, thus retrograde flows. This model explains axon overextension in the absence of Gas2L1, as well as the appearance of buckled MTs that are impeded in invasion in the short axons of Gas2L1-overexpressing neurons (Fig. 4.14B). At endogenous levels, Gas2L1 likely contributes to a certain degree to actin stability required for normal growth cone behaviour. Finally, in contrast to their opposing roles in axon extension, both Gas2L1 and MACF1 promote axon branching [167]. This suggests that MACF1-mediated MT guidance as well as actin stabilization via Gas2L1 are necessary for the initial steps of axon branch formation.

ACKNOWLEDGEMENTS

qPCR experiments were performed with the kind help of M. de Wit and support of Prof. Dr. R.J. Pasterkamp (UMC Utrecht). We thank M. Vinkenoog-Kuit (AMOLF) for actin purification.

This work was supported by the European Research Council (Synergy grant 609822 to M.D. and A.A. and ERC-consolidator grant 617050 to C.C.H.), the Netherlands Organization for Scientific Research (NWO-ALW-VICI 865.10.010 to C.C.H.), the Netherlands Organization for Health Research and Development (ZonMW-TOP 912.16.058 to C.C.H.) and the Hong Kong Research Grants Council (General Research Fund and Theme-based Research Scheme to R.Z.Q.).

4.4. SUPPLEMENTAL INFORMATION

4.4.1. MATERIALS & METHODS

PROTEIN PURIFICATION AND *in vitro* RECONSTITUTION ASSAYS

Detailed Materials & Methods for *in vitro* reconstitution assays are provided in Chapter 2. To summarize, N-terminal GFP-G2L1 fusions were purified from HEK293 cells using Strep(II)-streptactin affinity purification using protocols described in [104]. Lyophilized porcine brain tubulin was obtained from Cytoskeleton. Monomeric (G-)actin was purified from rabbit skeletal muscle acetone powder [97, 98]. 6xHis-tagged recombinant human mCherry-EB3, purified from bacteria [24, 100, 191], were a kind gift from Michel Steinmetz (Laboratory of Molecular Research, Paul Scherrer Institute, Switzerland). *In vitro* reconstitutions were performed in passivated glass flow cells using the MRB80-based "TIRF buffer" [92]. Actin filaments were pre-polymerized and later stabilized with phalloidin. After surface attachment of the MT seeds, the final mix of all proteins in TIRF buffer, was flowed in. Experiments were carried out at 30°C with protein concentrations of 30 nM for Gas2L1 (or its truncations), 20 µM tubulin, 0 or 133 nM mCherry-EB3 and 10-1000 nM of pre-polymerized F-actin. Data was collected using a triple-colour TIRF microscope, equipped with a FRAP system and objective heater.

CO-SEDIMENTATION ASSAY OF GAS2L1 WITH ACTIN

Monomeric G-actin was pre-polymerized at 50 µM in F-actin for 1 hour at room temperature (RT) in MRB80-buffer supplemented with 5 mM DTT (Dithiothreitol) and 75 mM KCl. For filament stabilization, phalloidin was added (50 µM) after 30 min. After polymerization, samples of increasing actin concentration (0.2 - 40 µM) were incubated with 0.75 µM of Gas2L1 at RT for 2.5 hour to reach steady-state binding. Next, free and actin-bound Gas2L1 fractions were separated by high-speed centrifugation at 150,000*g* for 30 min at RT. Supernatants, containing the free Gas2L1 fractions, were loaded onto a SDS-PAGE gel (Fig. S4.20A). Free Gas2L1 fractions were measured with the *Gel Analyzer* tool in Fiji [105] and normalized by the Gas2L1 intensity at 0 µM actin. To obtain the dissociation constant (K_d), the measured fractions (Fig. S4.20B) were fitted to the Michaelis-Menten equation [192]:

$$\frac{\text{G2L1}_{bound}}{\text{G2L1}_{total}} = \frac{[\text{F-actin}]}{[\text{F-actin}] + K_d}.$$

This yielded a dissociation constant $K_d = 0.49 \pm 0.14$ µM, which reflects a relatively high affinity of Gas2L1 for F-actin. Taken together with TIRF microscopy imaging and FRAP measurements (Fig. S4.26), where we observe Gas2L1 co-localization to and slow unbinding from actin bundles, we expect that the low dissociation constant originates from Gas2L1 molecules that are trapped within the actin bundles and might therefore not reflect the true affinity of Gas2L1 to actin.

ANIMALS, PRIMARY NEURON CULTURES, ELECTROPORATION AND TRANSFECTION

Animal experiments were approved by the Dutch Animal Experiments Committee (DEC) and conducted in agreement with guidelines of Utrecht University, Dutch law (Wet op de Dierproeven, 1996) and European regulations (Guideline 86/609/EEC). Neuron cultures were derived from hippocampi of E18.5 mixed-sex pups from pregnant Wistar rats

(Janvier) according to protocols for mechanic/enzymatic dissociation described previously [193]. In short, adult rats were at least ten weeks of age, not involved in previous experiments, provided with unrestricted access to food and water and kept with a companion, wood-chip bedding and paper tissue for cage enrichment. Animals were housed in an environment with a 12 hour light-dark cycle and a temperature of 22 ± 1°C.

Primary hippocampal dissociated neuron cultures were prepared according to protocols for mechanical/enzymatic dissociation described previously [193]. Neurons were maintained at 37°C and 5% CO2.

In case of electroporation for imaging experiments, 200,000 neurons per condition were taken from the cell suspension directly after mechanical dissociation, spun down for 5 minutes at 200g and resuspended in home-made electroporation buffer (12.5 mM NaCl, 123 mM KCl, 20 mM KOH, 10 mM EGTA, 4.5 mM $MgCl_2$, 20 mM PIPES, pH 7.2). Neurons in electroporation buffer were then mixed with 4 µg DNA per condition, transferred to cuvettes (Bio-Rad GenePulser, 0.2 cm gap) and electroporated using program O-003/'Rat hippocampal neurons' of a Lonza Nucleofector 2b machine. Electroporated neurons were plated in full medium (Neurobasal medium (Gibco) supplemented with 2% B27 (Gibco), 0.5 mM glutamine (Gibco), 15.6 µM glutamate (Sigma-Aldrich) and 1% penicillin–streptomycin (Gibco)) on 18 mm coverslips coated with poly-L-lysine (37.5 µg/ml, Sigma) and laminin (1.25 µg/ml, Roche). The procedure for electroporation for qPCR experiments was described previously [194].

For transfection, 100,000 neurons per well of a 12-well plate were directly plated in full medium onto 18 mm coverslips coated as described above, and transfected at the indicated times using Lipofectamine 2000 (Invitrogen). For one well of a 12-well plate, 1.8 µg DNA was mixed with 3.3 µl Lipofectamine in 200 µl Neurobasal medium and incubated for 30 minutes at room temperature. Meanwhile, conditioned full medium of neurons was transferred to a new plate, and transfection medium (neurobasal medium supplemented with 0.5 mM glutamine) was added. The DNA/lipofectamine mix was added to the neurons in transfection medium and incubated for 45 minutes at 37°C and 5% CO2. After transfection, neurons were rinsed by dipping coverslips in pre-warmed neurobasal medium and placed back into conditioned full medium.

CULTURED CELLS AND TRANSFECTION

COS-7 cells (a fibroblast-like cell line derived from monkey kidney tissue) were cultured in DMEM/Ham's F10 (1:1) supplemented with 10% FBS and 1% penicillin/streptomycin. Cells were diluted and plated on 18 mm coverslips glass coverslips one day before transfection. COS7 cells were transfected with DNA constructs using FuGENE6 (Roche) following the manufacturers protocol.

DNA AND SHRNA CONSTRUCTS

The following DNA constructs were used in this study and described before: pβ-actin-HA-β-Galactosidase [195], pCI-neo-BirA [196], EB3-tagRFP-T [197], and paGFP-α-Tubulin [198].

All Gas2L1 expression constructs were N-terminal fusions generated from PCR-based strategies using GFP-Gas2L1 or GFP-Gas2L1-SxAA as templates, which were based on human Gas2L1 (GenBank Accession No NM_152236.1) [172]. The following backbones were used to create Gas2L1 plasmids: GW1-GFP/HA for neuronal expression, bioGFP

and GW1-HA for pull-down experiments, and StrepII-EGFP for protein purification [104]. To create GW1-GFP/HA-ABD and GW1-GFP/HA-ABD-Tail, α-actinin CH domains were amplified from Gallus gallus cDNA (amino acids 35-246, NCBI ref. NM_204127.1) using a standard PCR based strategy. To obtain ABD-Tail, amino acids 35-246 of Gallus gallus α-actinin were fused to amino acids 196-681 of human Gas2L1 (NCBI ref. NM_152236.1) by overlap extension PCR. GW2-LifeAct-EGFP was obtained from Dr. M. Adrian and Dr. P. Schätzle (Utrecht University) and based on the LifeAct peptide sequence MGVADLIKKFESISKEE (5'- ATGGGTGTCGCAGATTTGATCAAGAAATTCGAAAGCATCTCAAAGGAAGAA), which was flanked by EGFP inserted into BamHI/XbaI sites of a GW2 backbone.

For shRNA-mediated depletion, shRNA sequences were inserted into HindIII and BglII sites of the pSuper backbone [199]. The following targeting sequences were used: scrambled - GCGCGCTTTGTAGGATTCG; Gas2L1 shRNA (rat) - CGCCCAATGACATTCGAAA. For use in qPCR experiments, we excised the puromycin resistance region from pSuper.puro and transplanted it into EcoRI/BamHI sites of pSuper-Gas2L1-shRNA.

ANTIBODIES AND REAGENTS

The following antibodies, staining reagents and dilutions were used for immunofluorescence experiments:

- chicken-anti-β-galactosidase (1:2500, Aves Labs #BGL-1040);
- rabbit-anti-TRIM46 serum (1:500, described in [174]);
- rabbit-anti-fascin (1:200, Abcam #ab126772);
- rabbit-anti-cortactin (1:1000, Abcam #ab81208);
- rabbit-anti-p34-Arc/ARPC2 (1:250, EMD Millipore #07-227);
- mouse-anti-alpha-tubulin (1:1000, Sigma #T-5168, clone #B-5-1-2);
- mouse-anti-acetylated-tubulin (1:500, Sigma #T-7451);
- mouse-anti-tubulin-tyrosine (1:100, Sigma #T-9028);
- mouse-anti-EB1 (1:100, BD Biosciences #610535);
- Alexa Fluor 594 Phalloidin (1:50, Thermo Fischer Scientific #A12381);
- goat-anti-chicken Alexa 405 (1:400, Abcam #ab175675);
- goat-anti-chicken Alexa 488 (1:400, Thermo Fischer Scientific #A11039);
- goat-anti-rabbit Alexa 405 (1:400, Thermo Fischer Scientific #A31556);
- goat-anti-rabbit Alexa 568 (1:400, Thermo Fischer Scientific #A11036);
- goat-anti-mouse Alexa 405 (1:400, Thermo Fischer Scientific #A31553);
- goat-anti-mouse Alexa 568 (1:400, Thermo Fischer Scientific #A11031);
- goat-anti-mouse-IgG2B Alexa 488 (1:400, Thermo Fischer Scientific #A21141);
- goat-anti-mouse-IgG3 Alexa 594 (1:400, Thermo Fischer Scientific #A21155).

The following antibodies, staining reagents and dilutions were used for Western blotting:

- rabbit-anti-GFP (1:10,000, Abcam #ab290);

- mouse-anti-HA (1:2000, Biolegend/Covance #mms-101p, clone #16B12);
- mouse-anti-actin (1:10,000, Chemicon #MAB1501R, clone #C4);
- goat-anti-mouse IRDye800CW (1:15.000, LI-COR #926-32210);
- goat-anti-rabbit IRDye680LT (1:20,000, LI-COR #926-68021).

The following reagents were used for drug treatments: DMSO (Sigma), Latrunculin B (Santa Cruz Biotechnology #SC-203318) and Jasplakinolide (Tocris/Biotechne #2792).

IMMUNOFLUORESCENCE MICROSCOPY

For co-stainings with rabbit-anti-fascin, rabbit-anti-p34-Arc/ARPC2, and mouse-anti-EB1, neurons were fixed for 5 minutes at -20°C in 100% methanol supplemented with 1 mM EGTA, immediately followed by 5 minutes fixation at room temperature in 4% paraformaldehyde/4% sucrose. In all other cases, neurons were fixed for 10 minutes at room temperature in 4% paraformaldehyde/4% sucrose.

After fixation, neurons were washed twice in PBS. Primary antibodies were diluted in GDB buffer (0.1% BSA, 0.45M NaCl, 0.3% Triton X-100, 16.7mM phosphate buffer, pH 7.4) and incubated overnight at 4°C, followed by 3x 5 minutes washing in PSB and 1-2 hour incubation with secondary antibodies in GDB buffer at room temperature. Samples were mounted in Vectashield mounting medium (Vectorlabs).

Images of fixed cells were collected using 1) a Nikon Eclipse 80i upright widefield fluorescence microscope, equipped with a Photometrics CoolSNAP HQ2 CCD camera and Nikon NIS Br software, using one of the following oil objectives: Plan Apo VC 60x N.A. 1.40, Plan Fluor 40x N.A. 1.30 or Plan Fluor 20x N.A. 0.75; or 2) using a Carl Zeiss LSM 700 confocal laser scanning microscope running ZEN2011 software and using a Plan-Apochromat 63x/1.40 Oil DIC objective. For quantitative comparisons between conditions, imaging settings were kept identical for all acquired images.

LIVE CELL IMAGING AND PHOTOACTIVATION

Live cell imaging and photoactivation experiments were performed on an inverted Nikon Eclipse Ti-E confocal microscope equipped with a perfect focus system (Nikon), a CSU-X1-A1 Spinning Disc unit (Yokogawa), and a Photometrics Evolve 512 EMCCD camera (Roper Scientific) while using a Plan Apo VC 100x N.A.1.40 oil objective. Neurons were kept at 37°C and 5% CO2 in a stage incubator (Tokai Hit) during imaging. Movies used to determine MT growth velocity were acquired at a framerate of 1 frame per second, and acquisitions lasted 3 minutes per movie.

For photoactivation experiments, we made use of an ILas FRAP unit (Roper Scientific) and a Vortran Stradus 405 nm (100 mW) laser. The photoactivation procedure of paGFP-α-Tubulin was previously described [198]. We co-transfected neurons with GW2-mRFP to label transfected neurons and identified axons based on morphology. We placed the soma just outside the field of view, which spanned 34×34 µm, and photoactivated axon regions of approximately 6-7µm wide in the center of the image. To prevent excessive photobleaching, frames were acquired at intervals varying between 6 and 15 minutes.

qPCR

qPCR experiments were performed with the kind help of M. de Wit and prof. dr. R.J. Pasterkamp (UMC Utrecht). Experimental procedures are detailed in [194]. To summarize, neurons were electroporated at DIV0 with empty pSuper-puro or pSuper-Gas2L1 shRNA-puro, and subjected to selection with 0.5 mg/ml puromycin for 48 hours prior to RNA isolation. We performed PCR reactions with the Fast Start DNA Master PLUS SYBR green I kit (Roche) and calculated Gas2L1 mRNA levels relative to those of GAPDH and β-actin using the $\Delta\Delta C_t$ method [194].

The following primer pairs were used:

GAPDH	5'-TGCCCCCATGTTTGTGATG
	3'-TGTGGTCATGAGCCCTTCC
β-actin	5'-AGGCCAACCGTGAAAAGATG
	3'-CCAGAGGCATACAGGGACAAC
Gas2L1	5'-ACATTCGAAACCTGGACGAG
	3'-TCAGCACCCTCACAAAGATG

PULL-DOWN EXPERIMENTS AND WESTERN BLOTTING

Human Embryonic Kidney 293 (HEK293) cells were cultured in 50/50 DMEM/Ham's F10 medium (DMEM: Lonza or Biowest; Ham's F10: Lonza) supplemented with 10% FCS (Sigma) and 1% penicillin-streptomycin (Sigma), and routinely tested for mycoplasma.

HEK293 cells were co-transfected with pCI-Neo-BirA, bioGFP-tagged constructs and HA-tagged constructs using MaxPEI (Polysciences) in a ratio of 3:1 PEI:DNA. After 24-48h expression, cells were washed with ice-cold PBS supplemented with 0.5x protease inhibitor cocktail (Roche) and 5 mM $MgCl_2$. Next, cells were lysed in pull-down lysis buffer for 30 minutes on ice (50mM Tris-HCl pH 7.5, 233 mM NaCl, 0.5% Triton X-100, 5mM $MgCl_2$, protease inhibitors (Roche)). Lysates were then pre-cleared by centrifugation (15 minutes at 13.2 krpm, 4°C) and supernatants were incubated with pre-blocked magnetic bioGFP beads (Invitrogen Dynabeads M-280 Streptavidin; blocking by incubation with 20 mM Tris-HCl pH 7.5, 150mM KCl, 0.2 µg/µl chicken egg albumin for 1 hour at 4°C) for 1.5-2 hours at 4°C. Lastly, beads were generously washed 5x in wash buffer (20mM Tris-HCl pH 7.5, 150mM KCl, 0.1% Triton X-100) and eluted by boiling 10 minutes at 95°C in 2x DTT+ sample buffer (20% glycerol, 4% SDS, 200 mM DTT, 100 mM TRIS-HCl pH 6.8, bromophenol blue).

For pull-down experiments in the presence of Latrunculin B, 10 µM Latrunculin B was added to HEK293 cells 30 minutes prior to lysis. Lysis buffers used during the experiment were additionally supplemented with 10 µM Latrunculin B.

Samples ran on 12-14% SDS PAGE gels and were transferred onto nitrocellulose membranes by semi-dry blotting at 16V for one hour. Membranes were blocked in 2% bovine serum albumin (BSA)/0.02% Tween20/PBS for 1 hour at room temperature, followed by overnight incubation with primary antibodies in 2%BSA/0.02% Tween20/PBS, 3x 5 minute washes with 0.02% Tween20/PBS and one hour of incubation with secondary antibody in 2%BSA/0.02% Tween20/PBS, followed by another 3 washing steps.

Membranes were scanned on an Odyssey Infrared Imaging system (LI-COR Biosciences) and, if required, re-incubated to detect and discriminate multiple signals on the same membrane.

DATA ANALYSIS AND IMAGE PROCESSING FOR CELL IMAGING EXPERIMENTS

All images were processed with ImageJ software and plugins described below. For display purposes, the images shown had their dynamic ranges adjusted when necessary. Quantitative analyses were performed on raw data collected using the same microscope with identical settings throughout experiments.

For axon morphology analyses, β-galactosidase co-overexpression and staining was used to identify transfected neurons and to visualize morphology. We acquired composite images of the total axon from a mosaic of tiles of the same neuron that were manually pieced together. TRIM46 staining was included to identify axons, which were traced and analysed using the NeuronJ plugin for ImageJ by Dr. E. Meijering [200]. We excluded neurons with multiple axons as well as neurons without TRIM46-positive neurites from our analyses. To avoid selection bias, neurons that satisfied these requirements were included on a first-come-first-served basis during image acquisition. The number of independent experiments stated in figure legends reflects the number of experiments performed on independent neuron cultures, i.e., cultures derived from pups from a different mother animal. We would like to note that, as is expected of primary cultures, there was some morphological heterogeneity between individual neurons and also between neuron cultures.

To quantify the growth cone area and the ratio of acetylated/tyrosinated tubulin, neurons were co-transfected with β-galactosidase and stained for β-galactosidase, acetylated tubulin, and tyrosinated tubulin. Transfected neurons were identified from β-galactosidase staining, and images were acquired in three channels with identical microscope settings for all coverslips within one experiment. Using ImageJ, growth cones of transfected neurons were drawn and their area was measured. Next, the intensity of the acetylated tubulin and tyrosinated tubulin channels was measured for all growth cones of transfected neurons that did not cross untransfected neurons. The raw intensities were used to calculate the ratio of acetylated tubulin/tyrosinated tubulin.

For classification of MT orientation inside growth cones, neurons were co-transfected with β-galactosidase and stained for α-tubulin. MT orientation in growth cones of transfected neurons was analysed from α-tubulin staining and classified into straight, buckled, or fan-like phenotype.

To quantify MT growth velocity in growth cones, we co-transfected neurons with shRNA and EB3-tagRFP, and cytoplasmic GFP as a fill. Axons were identified on the basis of morphology, and growth cones could be located by observing the GFP signal. Kymographs were drawn along the shafts and growth cones, using a line thickness sufficient to cover the majority of EB traces as seen on a maximum intensity projection, and generated using the KymoResliceWide plugin for ImageJ by dr. E. Katrukha (Utrecht University, available on GitHub). The resulting kymographs were manually traced, and growth velocities obtained from individual traces were first used to calculate average velocity per neuron/kymograph before using the resulting values to calculate the average growth velocity in each condition.

For polarity index calculations, neurons were transfected with different GFP-Gas2L1 fusion constructs. TRIM46 staining was used to identify the axon initial segment and Phalloidin staining was used to visualize F-actin. Images were acquired with identical microscope settings for all coverslips within one experiment. Using ImageJ, a line of 3.18

µm width with a length of 12-32 µm was drawn in the axon initial segment. The same ROI was positioned in the nearest area where no cell was present to obtain background intensity, which was subtracted from the raw measurements. Intensities were measured at identical positions in both the GFP-Gas2L1 fusions and Phalloidin channels. The same was done for two dendrites of the same neuron. Polarity indexes were then calculated using the formula $=(I_a\text{-}I_d)/(I_a+I_d)$, where I_a is the intensity in the axon and I_d is the average intensity of two dendrites.

DATA ANALYSIS FOR *in vitro* ASSAYS

For the *in vitro* reconstitution assays, all image processing was performed in FIJI [105], including the construction of kymographs (see also Chapter 2). For the intensity ratios, we used a custom-written program in Python. Briefly, we selected a region-of-interest and measured the intensity distributions of both the GFP-signal and the actin signal. The intensity ratios were calculated using:

$$\frac{I_{GFP} - I_{bg}}{\langle I_{actin} \rangle},$$

where I_{bg} is the background noise, measured as the peak GFP-intensity in an empty channel, and $\langle I_{actin} \rangle$ is the mean actin intensity of the selected region.

FRAP measurements

We performed fluorescence recovery after photobleaching (FRAP) measurements to obtain the unbinding rates of Gas2L1 or truncated constructs from actin filaments or both MT/AFs (Fig. S4.26 and S4.29). We prepared the samples as normal TIRF assays (as described in Chapter 2). The microscope was equipped with a MAG Biosystems FRAP-3D system (Photometrics, Roper Scientific), and we performed FRAP measurements at video rate (33 ms exposure time per frame). We photobleached circular (r = 1.6 µm) regions at 60% laser power, to prevent photodamage. By regularly bleaching the same region twice, we checked for photodamage and confirmed immobile fractions.

For the analysis of FRAP, we used a custom written Python script. We normalized the fluorescence intensity by background and corrected for bleaching while imaging. To fit the Gas2L1 recovery data to two unbinding rates, we used the following equation:

$$I(t) = A(1 - e^{-tk_{off_1}}) + B(1 - e^{-tk_{off_2}}), \tag{4.1}$$

where A and B are constants and k_{off_1} and k_{off_2} are the two different off-rates of GFP-Gas2L1. We fitted every recovery curve and then averaged over the rates.

STATISTICS

Statistical analysis was performed in GraphPad 5. Datasets were first tested for normality using Shapiro-Wilk tests. Datasets that did not satisfy the normality assumption were compared using Mann-Whitney U test, and datasets that did were compared using unpaired t-tests. Tests were two-tailed. Statistical tests used for each experiment are detailed in the figure legends.

4.4.2. SUPPLEMENTAL FIGURES

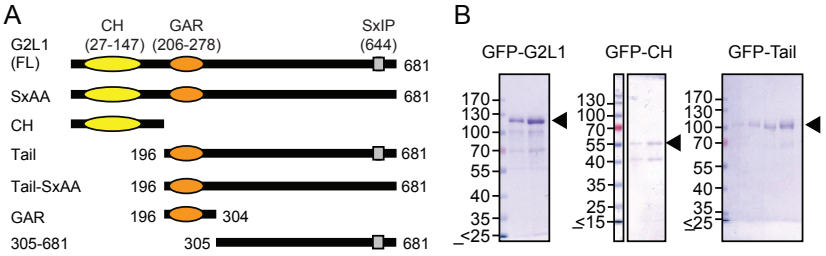

Figure 4.15: **Additional Gas2L1 mutants and purity of Gas2L1 and the deletion mutants for reconstitution assays. (A)** Schematic representation of the Gas2L1 mutants used in this chapter. Complementary to Fig. 4.1. Indicated are the CH (actin binding) domain in yellow, the GAR (MT lattice) binding domain in orange, and the SxIP motif (EB binding domain) in grey. Numbers indicate amino acid residue start and end positions, counting from the N-terminus (left) to the C-terminus (right). FL, full-length; CH, calponin homology; GAR, GAS2-related; SxIP, SxIP motif. **(B)** Commassie-stained SDS-PAGE gels showing the purity of the purified Gas2L1 (G2L1) fusions used for *in vitro* reconstitutions. For GFP-CH, the additional band at 40 kDa was identified as co-purified actin by Western blotting.

Figure 4.16 *(facing page)*: **Experimental details of neuronal phenotype validation. (A, B)** Representative melt curves of various samples amplified with Gas2L1 primers (A) and amplification curves of GAPDH or Gas2L1 cDNA amplified in control and shRNA samples (B) from qPCR experiments shown in Fig 1A. cDNA samples of control (empty shRNA vector, in duplo) and Gas2L1-shRNA-expressing neurons (G2L1 shRNA, in duplo) show one peak in the melt curve (A), demonstrating specific amplication of Gas2L1 cDNA; negative water control (MQ instead of cDNA template) shows no amplification with Gas2L1-specific primers; negative RNA control (RNA instead of cDNA as template) reveals minor unspecific product that is not amplified and therefore not interfering in the presence of cDNA. **(C)** Fine details of axon morphology of a DIV3 neuron overexpressing HA-Gas2L1 as described in Fig. 4.2B. Boxed regions (1 and 2) are enlarged below. Red asterisk indicates the soma. **(D)** Example of axon tracings for morphology analysis, using the DIV3 neuron expressing scrambled shRNA as shown in Fig 1B as a template. Boxed region is enlarged to the right. Blue tracing denotes the primary axon; the longest possible uninterrupted tracing from the soma to the tip of an axon branch. Red tracings denote non-primary branches and black circle marks the position of the soma. **(E-G)** Rescue experiments showing the total axon length (E), primary axon length (F) and average axon branch length (G) in neurons co-expressing scrambled (Scr) or Gas2L1 shRNA with GFP, or Gas2L1 shRNA with GFP-Gas2L1, and HA-β-galactosidase from DIV0 to DIV3. Data belongs to the experiment shown in Fig 1H and I. n=34-43 neurons per condition (36 for Scr shRNA, 34 for G2L1 shRNA, 43 for G2L1 shRNA + GFP-G2L1) from 2 independent experiments. **(H, I)** DIV3 neurons overexpressing GFP-G2L1 stained for cortactin (H) or p34-Arc (I), as well as merged images showing co-localization between GFP-Gas2L1 and cortactin (H) or p34-Arc (I) (left panels). Boxes indicate zoomed regions (right panels). Scale bars: 25µm in (C), 30µm in (D, H, I). Data is displayed as means ±SEM. Mann-Whitney test, ns: not significant, ***p<0.001.

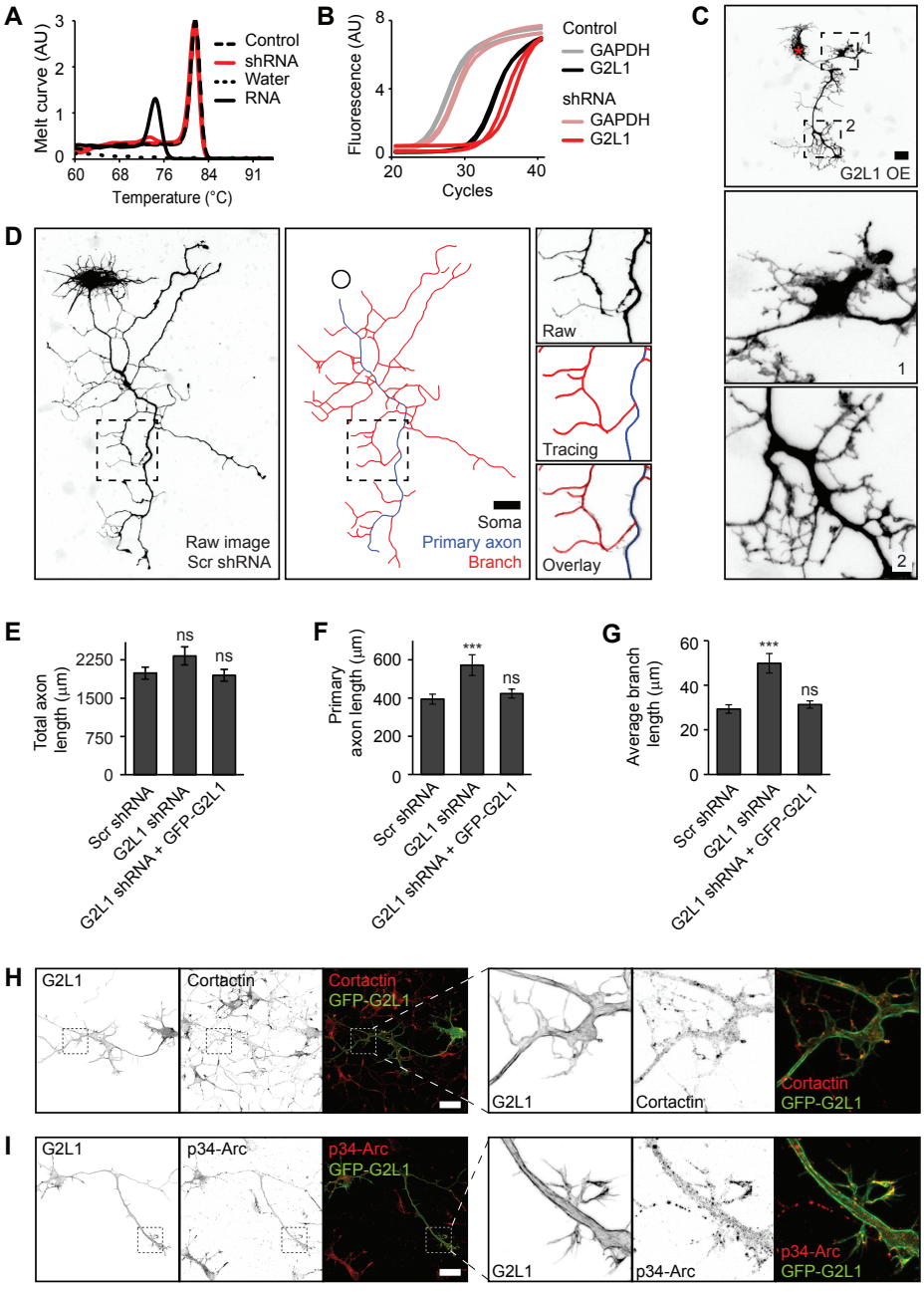
A
Melt curve (AU)
Temperature (°C)
Control
shRNA
Water
RNA
B
Fluorescence (AU)
Cycles
Control
GAPDH
G2L1
shRNA
GAPDH
G2L1
C
G2L1 OE
1
2
D
Raw image
Scr shRNA
Soma
Primary axon
Branch
Raw
Tracing
Overlay
E
Total axon length (µm)
ns
ns
Scr shRNA
G2L1 shRNA
G2L1 shRNA + GFP-G2L1
F
Primary axon length (µm)
***
ns
G
Average branch length (µm)
***
ns
H
G2L1
Cortactin
Cortactin
GFP-G2L1
I
G2L1
p34-Arc
p34-Arc
GFP-G2L1

4

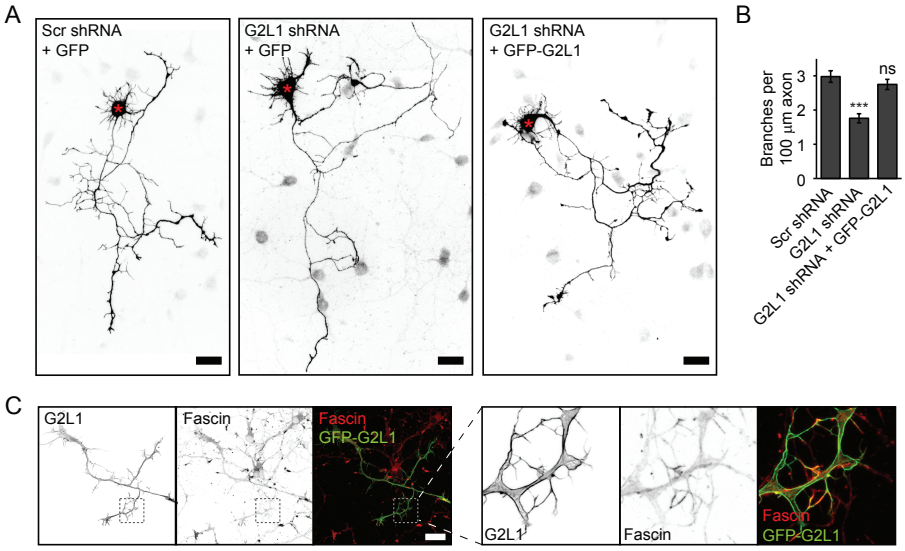

Figure 4.17: **Rescue experiments of Gas2L1 in developing neurons. (A, B)** Rescue experiments showing the number of branches per 100 µm axon in neurons co-expressing scrambled or G2L1 shRNA with GFP, or G2L1 shRNA with GFP-G2L1, and HA-β-galactosidase from DIV0 to DIV3. Silhouettes (from β-galactosidase fill) are shown in (H). n=34-43 neurons per condition (36 for Scr shRNA, 34 for G2L1 shRNA, 43 for G2L1 shRNA + GFP-G2L1) from 2 independent experiments. **(C)** Localization of GFP-Gas2L1 (G2L1) in a DIV3 neuron stained for α-fascin, as well as merged images showing colocalization between GFP-Gas2L1 and fascin (left panels). Boxes indicate zoomed regions (right panels). Scale bars: 30 µm. Data is displayed as means ±SEM. Mann-Whitney test, ns: not significant, * p <0.05, ** p<0.01, ***p<0.001.

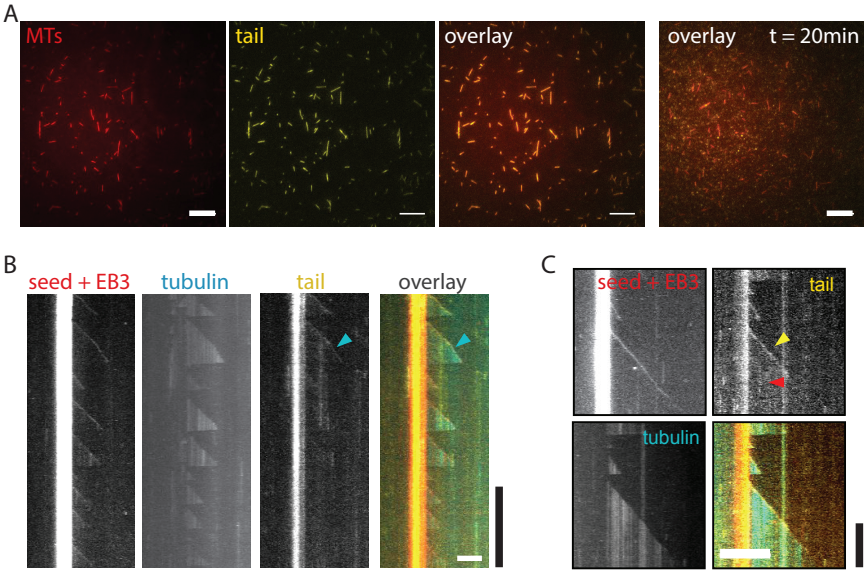

Figure 4.18: **Binding of Tail to microtubules.** **(A)** TIRF images of typical field-of-view where Tail binds to microtubules right after flushing in (left panels), but disappears from the microtubules over time (20min, right panel). Shown are MTs (red) and Gas2L1 (yellow), and their overlay. Experiments performed in the absence of EB3. The disappearance of Tail from MTs over time could be an indication that the protein is not very stable, and degrades over time. **(B)** Kymograph showing that Tail co-localizes strongly to the MT seed, and in the beginning of the time-lapse also co-localizes to the dynamic part of the MT, and even some enhanced intensity can be observed at the MT plus-end (blue arrowheads). Experiments performed in presence of EB3. **(C)** Additional kymograph showing Tail localization at both the dynamic MT lattice (red arrowhead) and at the growing MT plus-end (yellow arrowhead). Scale bars: 10µm in A; 5µm (horizontal) and 5min (vertical) in B; 10µm (horizontal) and 3min (vertical) in C.

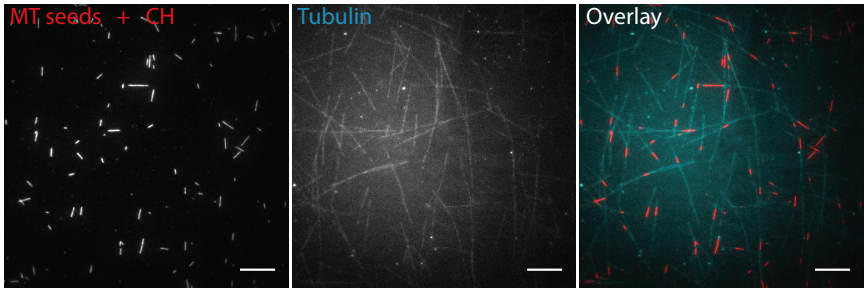

Figure 4.19: **CH domain of Gas2L1 does not bind to microtubules.** TIRF images of MT seeds (red), CH domain (red), tubulin (blue), and their overlay. Experiments performed in the absence of EB3. We observed no co-localization of CH domain to any MT, which does not change over time. Image shown is 40 min after flushing in. Scale bars: 10µm.

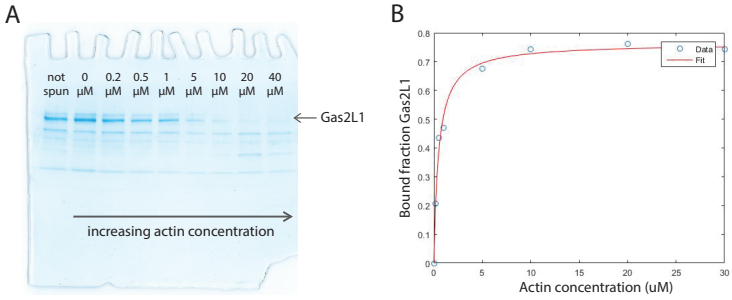

Figure 4.20: **Co-sedimentation assay of Gas2L1 with F-actin.** **(A)** SDS-PAGE gel loaded with the supernatant after high-speed centrifugation of incubated Gas2L1 with increasing concentrations of F-actin (actin concentrations are indicated on the gel for each lane). Arrow indicates where Gas2L1 is expected, based on its known molecular weight. With increasing actin concentration, an increasing fraction of Gas2L1 is co-sedimented (so not included in the supernatant). **(B)** Measured fractions of Gas2L1 bound to actin and the best fit (R^2 = 0.99, as described in Material & Methods) to determine the dissociation constant $K_d = 0.49 \pm 0.14$ µM.

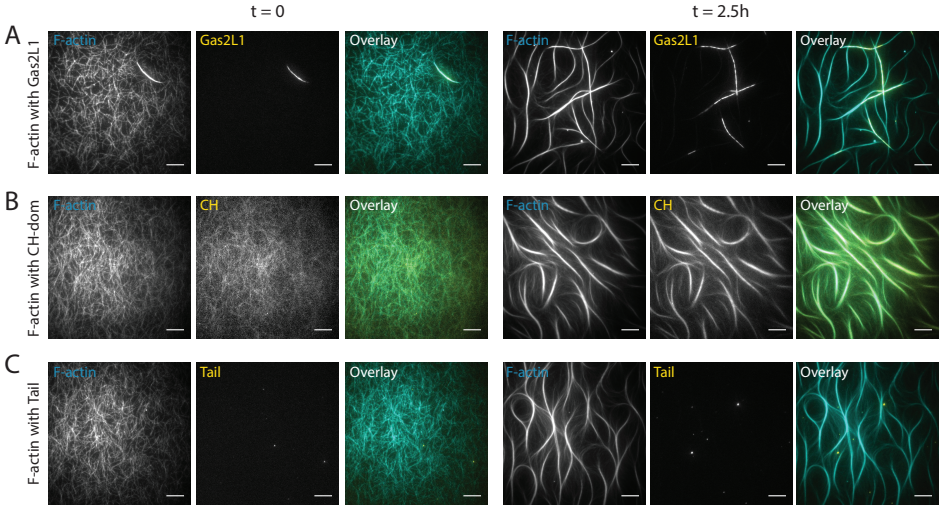

Figure 4.21: **Actin binding of Gas2L1 and its deletion mutants.** **(A)** TIRF images of actin filaments (blue) with Gas2L1 (yellow), showing that Gas2L1 does not bind to single actin filaments but does bind to actin bundles. With more actin bundles forming in time (due to methylcellulose-induced crowding), Gas2L1 remains on a subset of actin bundles. **(B)** TIRF images of actin filaments (blue) with CH domain (yellow), showing that CH binds to all actin structures, including single F-actin. **(C)** TIRF images of actin filaments (blue) with Tail (yellow), where we observe that the Gas2L1 fragment lacking the actin-binding domain does not bind to F-actin. Time indicated is after flushing in all proteins. Scale bars: 10µm.

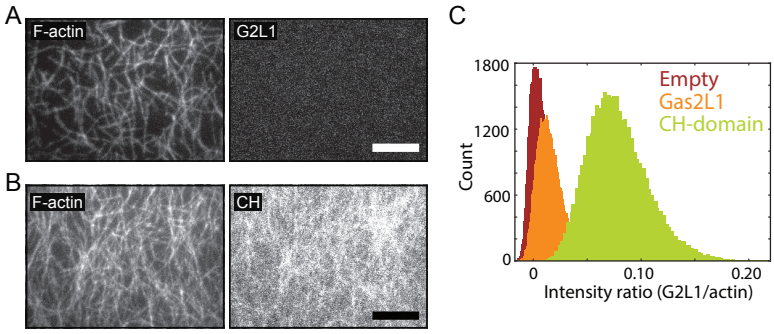

Figure 4.22: **Binding of Gas2L1 and CH domain to single actin filaments.** **(A)** TIRF images of single F-actin (left) with Gas2L1 (right), showing no co-localization of Gas2L1. **(B)** TIRF images of single F-actin (left) with CH domain (right), showing co-localization. **(C)** Intensity ratios of GFP signal over actin signal from Gas2L1 (orange) and CH domain (green). "Empty" (dark red) is from the channel with only F-actin and no GFP-protein present. This analysis reveals that there is no GFP-Gas2L1 (orange) accumulated on F-actin, since Gas2L1 has nearly the same intensity ratio as the empty channel (dark red). We do observe GFP-DH (green) binding to F-actin. The intensity range between the F-actin panels and Gas2L1/CH panels of (A) and (B) are equal. TIRF images were captured on the same day using identical microscope settings. Scale bars: 10µm.

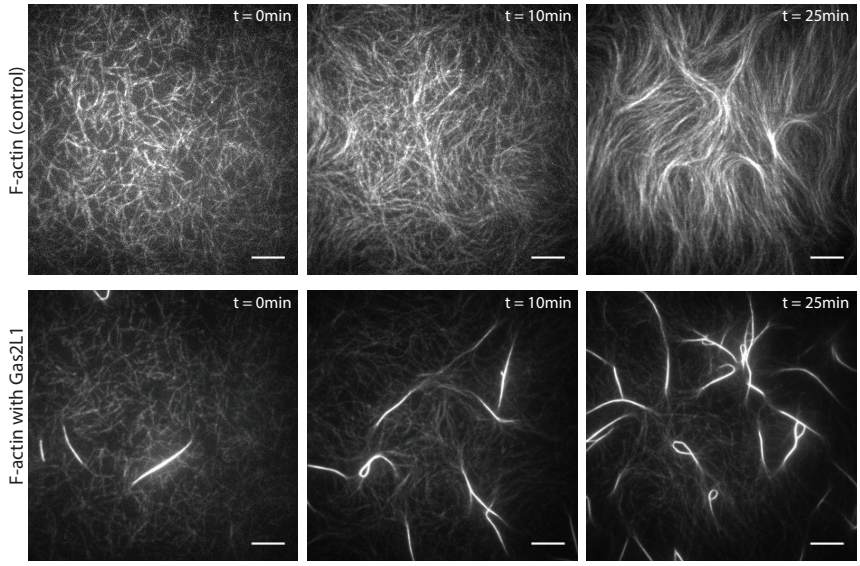

Figure 4.23: **Gas2L1 bundles actin filaments.** TIRF images showing the actin organization changing over time in the absence (top) and presence (bottom) of Gas2L1. Normally, in the control conditions where no Gas2L1 is present (top), we do not observe actin bundle formation, not even during prolonged observation. We do observe a progressive accumulation of actin filaments at the surface due to methylcellulose-induced crowding. This results in some high density areas where actin filaments take on curved configurations. When we do have Gas2L1 present (bottom), we can already observe some actin bundles from the start of imaging, which progressively increase in number. These bundles are rigid, mostly straight and occasionally curved, rather different from the high-density areas of the control condition. Indicated is the time since flushing in the final mix to the flow channels. Images are not taken at the same location over time, but are representative. Scale bars: 10µm.

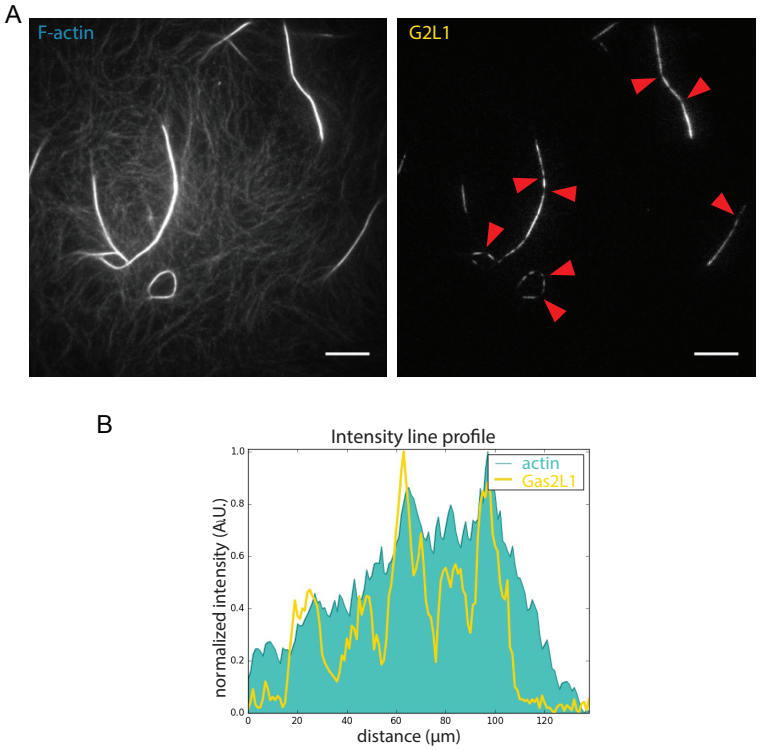

Figure 4.24: **Gas2L1 co-localization to F-actin bundles.** **(A)** TIRF images of F-actin (left) and Gas2L1 (right). Red arrowheads indicate where Gas2L1 co-localizes to actin bundles in a spotty manner. **(B)** Intensity line profile along an actin bundle. Images taken 10min after flushing in Gas2L1. Scale bars: 10µm.

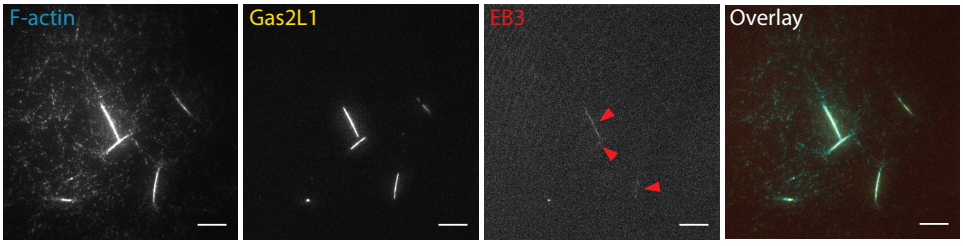

Figure 4.25: **Recruitment of EB3 to F-actin bundles via Gas2L1.** TIRF images of F-actin (blue), Gas2L1 (yellow), EB3 (red) and their overlay. We observe Gas2L1 co-localizing to (poorly-labeled) F-actin bundles, thereby also recruiting EB3 proteins (red arrowheads), indicating EB3 does not interfere with Gas2L1's actin binding. Scale bars: 10µm.

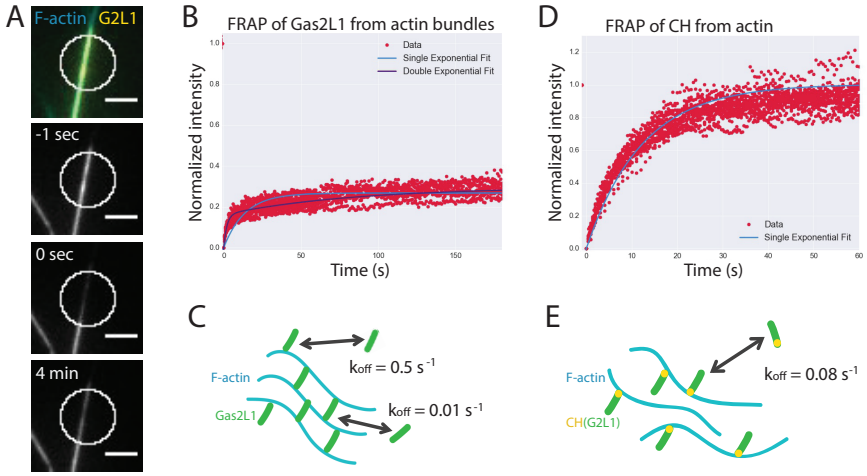

Figure 4.26: **Unbinding of full-length Gas2L1 from actin bundles.** **(A)** TIRF images of the fluorescent recovery of Gas2L1 after photobleaching (FRAP). **(B)** FRAP curves of Gas2L1 bound to actin bundles (red) with the fits of a single (light blue) or double (dark blue) exponential recovery. **(C)** Schematic model for actin binding of Gas2L1, explaining the two processes (exponents) of unbinding and the large immobile fraction of the 'trapped' proteins within the bundle. **(D)** FRAP curves of CH domain (red) with the fit of a single exponential recovery (light blue). **(E)** Schematic model for the actin binding of CH domain, indicating the single process (exponent) of unbinding. Measured unbinding rates (0.48 ± 0.07 s^{-1} and 0.01 ± 0.005 s^{-1} for Gas2L1; 0.08 ± 0.03 s^{-1} for CH domain) are averages (± STD) for multiple FRAP curves: n=8 for Gas2L1; n=17 for CH domain. Scale bars: 3µm.

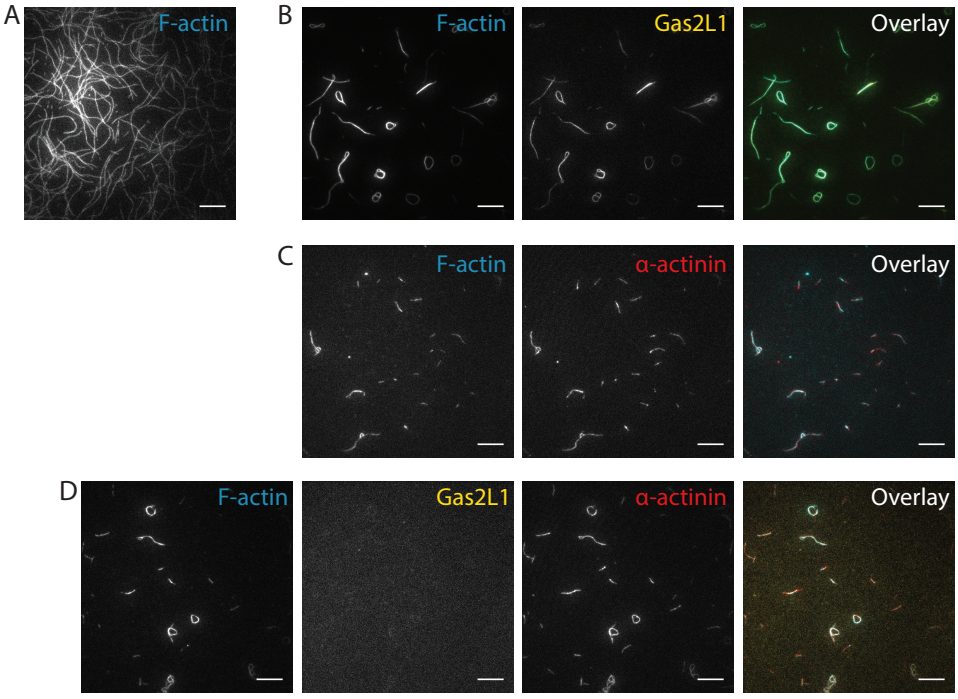

Figure 4.27: **Gas2L1 binding to actin bundles is readily outcompeted by α-actinin.** **(A)** TIRF image of the control condition with only (long) actin filaments. **(B)** TIRF images of Gas2L1 (yellow) bundling of and co-localizing to (long) F-actin (blue). **(C)** TIRF images of α-actinin (red) bundling of and co-localizing to (long) F-actin (blue). **(D)** TIRF images of the competition for F-actin (blue) bundling and binding between Gas2L1 (yellow) and α-actinin (red), where Gas2L1 is competed away from the bundles. Experiments were performed with mCherry-labeled human α-actinin-1, at 30nM concentrations (similar to GFP-Gas2L1 concentrations). Images are taken approximately 20min after flushing. Scale bars: 10µm.

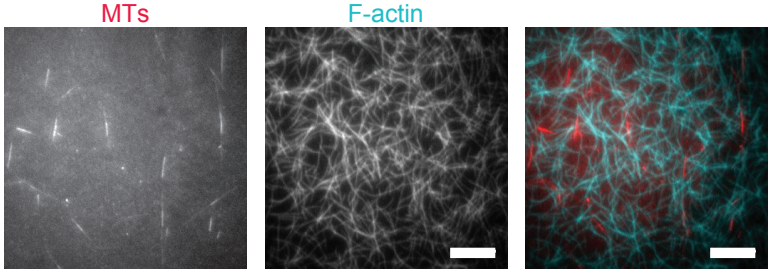

Figure 4.28: **No actin filament alignment in absence of Gas2L1.** Control *in vitro* reconstitution experiment showing no alignment of F-actin (1 µM, blue) to MTs (red) in the absence of Gas2L1. Scale bars: 10µm.

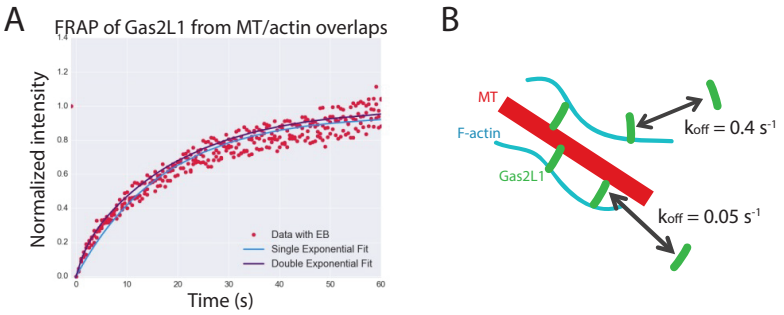

Figure 4.29: **Unbinding of Gas2L1 from MT-actin overlap regions.** **(A)** FRAP curves of Gas2L1 bound to MT-actin bundles (red) with the fits of a single (light blue) or double (dark blue) exponential recovery. **(B)** Schematic model for Gas2L1 binding to MT-actin overlap regions, explaining the two processes (exponents) of unbinding. Measured unbinding rates (0.45±0.12 s^{-1} and 0.05±0.01 s^{-1}) are averages (± STD) for n=5 FRAP curves.

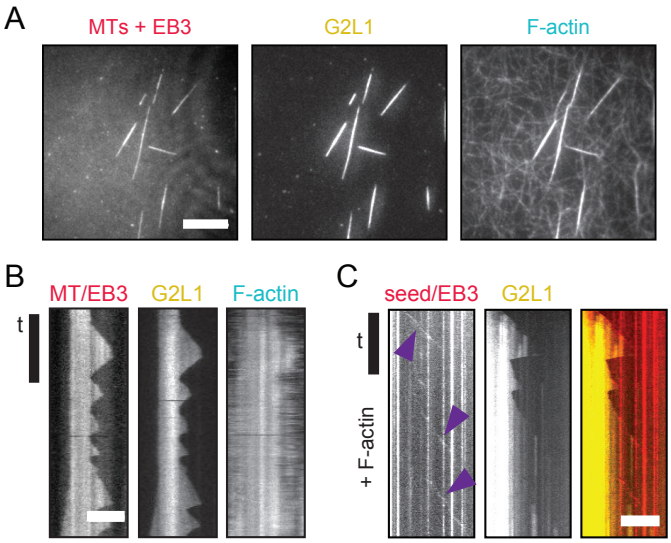

Figure 4.30: **The presence of EB3 does not change Gas2L1 localization to MT-actin bundles.** **(A)** TIRF images showing co-localization of Gas2L1 to MT-actin bundles in the presence of EB3. **(B)** Kymograph showing specific Gas2L1 localization to MT-actin overlaps and showing the absence of Gas2L1 plus-end tracking in the presence of EB3. **(C)** Kymograph showing Gas2L1 localization along MT-actin overlaps, even when EB3 tracks the growing MT plus-end (purple arrowheads). Actin channel not shown. Scale bars: 10µm in A; 5µm (horizontal) and 3 min (vertical) in B; 5µm (horizontal) and 3 min (vertical) in C.

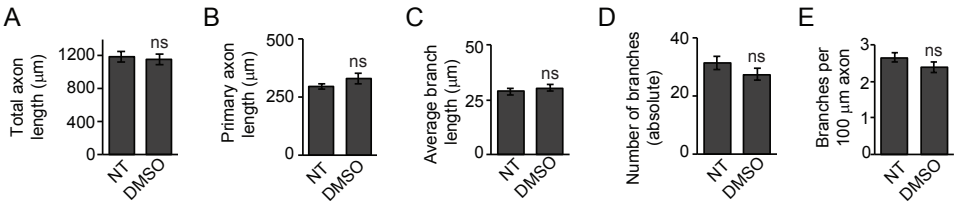

Figure 4.31: **DMSO does not affect axon morphology. (A-E)** Effect of DMSO (equivalent to DMSO concentration in 100 nM Latrunculin B condition shown in Fig 5A-E) on axon morphology of DIV3 neurons, transfected at DIV1 and treated with DMSO (1:100) for 48 hours. NT=non-treated; n=20-25 neurons per condition (25 for NT, 20 for DMSO) from 2 independent experiments. Data is displayed as means ±SEM. Mann-Whitney test, ns: not significant.

4

Figure 4.32 *(facing page)*: **The MT-binding tail fragment does not influence localization of a different actin-binding domain. (A)** Quantification of the ratio of raw acetylated tubulin (AceTub) intensity to raw tyrosinated tubulin (TyrTub) intensity in growth cones of DIV4 neurons transfected with GW1-EV, G2L1 shRNA or HA-G2L1 (G2L1 OE) and HA-β-galactosidase for one day. n=56-85 growth cones from 37-43 neurons per condition (68 growth cones from 43 neurons for GW1-EV, 56 growth cones from 37 neurons for G2L1 shRNA, 85 growth cones from 41 neurons for G2L1 OE) from 3 independent experiments. **(B)** Silhouettes (from β-galactosidase fill, left panels) of growth cones of DIV4 neurons, transfected with GW1-EV (control, top panels) or HA-Gas2L1 (bottom panels) and HA-β-galactosidase. Boxes indicate zoomed regions (right panels), showing staining for acetylated tubulin (AceTub) and tyrosinated tubulin (TyrTub). Dotted lines show the outline of the growth cone. **(C)** Schematic overview of α-actinin mutants used in Fig EV5D-G. **(D)** Additional conditions included in the experiment shown in Fig 6F: DIV3 neurons expressing GFP-ABD or GFP-ABD-Tail and treated with 10 µM Latrunculin B for 30 minutes or non-treated, stained for F-actin (phalloidin) and the axon initial segment (TRIM46). **(E, F)** Additional conditions included in the experiment shown partially in Fig 6G and H: Raw phalloidin staining intensities in axons (E) and non-axonal neurites (pre-dendrites) (F) of DIV3 neurons expressing the indicated GFP fusions and treated with 10 µM Latrunculin B for 30 minutes (grey bars) or non-treated (white bars). n=27-40 neurons per condition (40 for GFP, GFP-G2L1, GFP-CH, GFP-ABD-Tail, 35 for GFP-SxAA, 27 for GFP-ABD) from 2 independent experiments. **(G)** Additional conditions included in the experiment shown partially in Fig 6I: Polarity index representing localization of the indicated GFP fusions in non-treated neurons (green bars), and localization of F-actin as labelled by phalloidin in DIV3 neurons treated with 10 µM Latrunculin B for 30 minutes (grey bars) or non-treated (white bars). n=27-40 neurons per condition(40 for GFP, GFP-G2L1, GFP-CH, GFP-ABD-Tail, 35 for GFP-SxAA, 27 for GFP-ABD) from 2 independent experiments. Positive values indicate axonal enrichment, negative values indicate neuritic enrichment and a value of 0 signifies no particular enrichment. Scale bars: 10µm in (B), 30µm in (D). Data is displayed as means ± SEM. Mann-Whitney test, ns: not significant, **p<0.01, ***p<0.001.

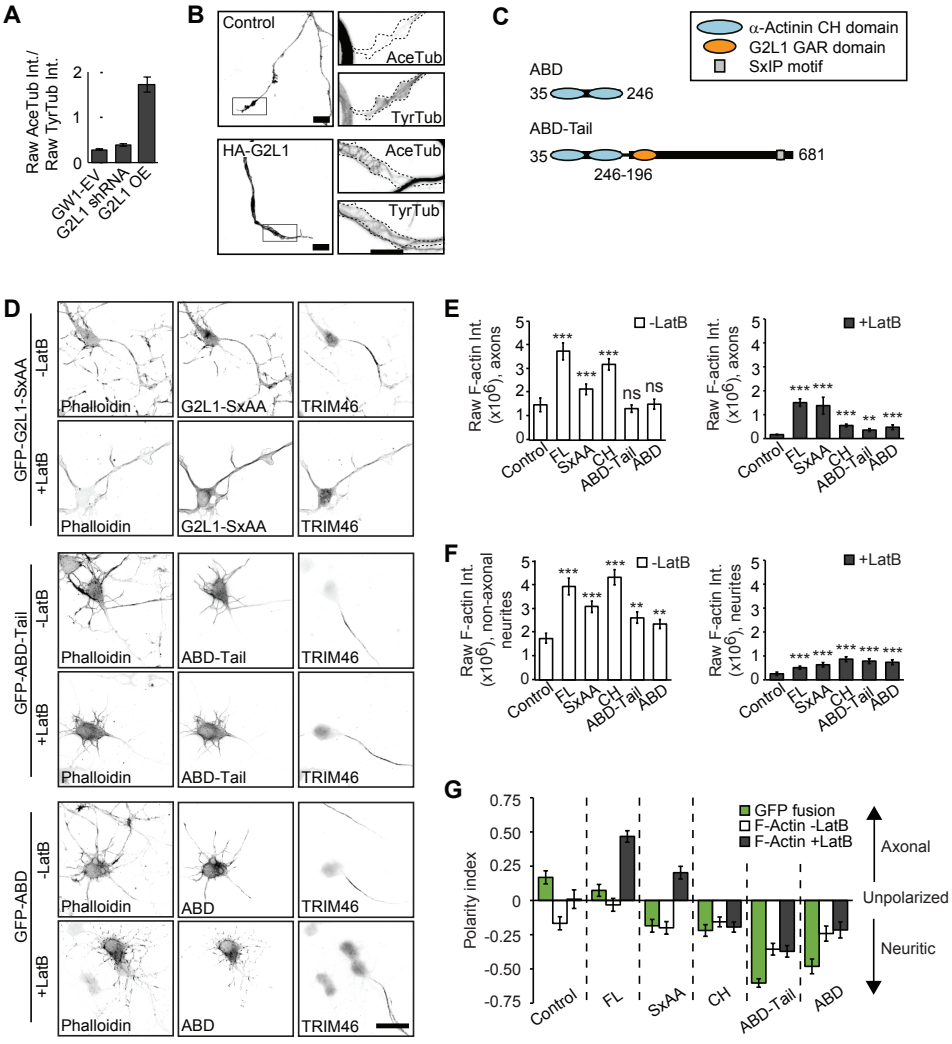
A
Raw AceTub Int./ Raw TyrTub Int.
GW1-EV
G2L1 shRNA
G2L1 OE
B
Control
AceTub
TyrTub
HA-G2L1
C
α-Actinin CH domain
G2L1 GAR domain
SxIP motif
ABD
35
246
ABD-Tail
681
246-196
D
GFP-G2L1-SxAA
GFP-ABD-Tail
GFP-ABD
-LatB
+LatB
Phalloidin
G2L1-SxAA
ABD-Tail
ABD
TRIM46
E
Raw F-actin Int. (x10^6), axons
Control
FL
SxAA
CH
ABD-Tail
ABD
F
Raw F-actin Int. (x10^6), non-axonal neurites
Raw F-actin Int. (x10^6), neurites
G
Polarity index
GFP fusion
F-Actin -LatB
F-Actin +LatB
Axonal
Unpolarized
Neuritic

5

ROLE OF THE MOLECULAR ANATOMY OF SPECTRAPLAKIN CYTOLINKERS IN ACTIN-MICROTUBULE CO-ORGANIZATION

We always did feel the same,
We just saw it from a different point of view.
Tangled up in blue.

Bob Dylan

Many distinct cytolinkers exist in cells, and these cytolinkers differ in their molecular anatomy. Some cytolinkers target the microtubule (MT) lattice, while others contain both MT lattice- and tip-binding domains. A prominent example is the spectraplakin family of cytoskeletal crosslinking proteins, which includes MACF1 (also known as ACF7) and its Drosophila homologue Shot (also known as Short stop). In this chapter, we study how the molecular anatomy of cytolinking proteins influences their impact on MT/actin crosstalk, using Shot as a reference protein. To dissect the role of the different domains, we reconstitute dynamic MTs in the presence of stabilized actin filaments and study MT/actin interactions in the presence of Shot or engineered variants. We find that Shot has a low affinity to either actin filaments or microtubules separately, but localizes selectively to MT/actin overlap regions in the composite system, where it induces MT rescues. Using engineered cytolinkers, we found that linking actin to the growing MT ends (via TipAct) results in dynamic remodelling of the actin organization. By contrast, linking actin to the MT lattice

(via TipActLong) results in long-lived actin co-alignment and persistent MT growth. By altering the spacer domain that separates the actin- and MT-binding domains, we found that for actin binding, cytolinker dimerization is important, while both dimerization and spacer rigidity play a role in the promotion of MT rescues.

5.1. INTRODUCTION

While often studied as isolated systems, the actin and microtubule (MT) cytoskeletal networks work together in a diverse set of vital cellular processes such as cell migration, mitosis, and polarization [3, 4, 6, 7]. The coordination between the two systems often requires mechanical coupling, which involves steric interactions and specific crosslinking by proteins or protein complexes. In addition to mechanical linking, MT/actin coordination can also be accomplished via signalling pathways that regulate filament (de)polymerization or motor activity, such as Rho-GTPases [3].

Crosslinking proteins that connect actin filaments to microtubules are often referred to as cytolinkers. Previous studies investigating MT/actin-crosstalk in cells and in cell-free reconstitution assays have shown that cytolinking proteins affect the organization of both cytoskeletal systems by promoting co-alignment of actin filaments and microtubules [60, 96, 116]. Moreover, it has also been shown in cells with the help of an optogenetically controllable microtubule plus end/actin crosslinker that physically linking microtubule ends to actin can slow down microtubule growth [201].

A highly conserved family of cytolinker proteins are the spectraplakins, a family of giant proteins that can bind both actin filaments and microtubules [53–55]. The two most studied members of this spectraplakin family are the mammalian MACF1 (also known as ACF7) and the sole *Drosophila* spectraplakin named Short stop (Shot, also known as Kakapo) [54, 67]. In addition, also other cytolinking proteins have been found, including (but not limited to) members of the growth-arrest-specific 2 (GAS2) family [76], another spectraplakin member Dystonin (DST, or BPAG1) [54], traditional microtubule associated proteins Tau, CLASP and MAP2 [202], and APC [88]. Most members of the spectraplakin family, including MACF1/Shot, possess two distinct microtubule-binding domains, allowing them to bind both to the microtubule lattice (via a GAR-domain) and to the growing microtubule end (via a SxIP motif for recognition of end-binding (EB) proteins) [67]. In addition, Shot and other spectraplakins can directly bind to actin filaments via a tandem of calponin homology (CH) domains (Fig. 5.1A). For MACF1, the actin binding is regulated at a nearby site, conserved in Shot, where phosphorylation was identified to increase actin binding [73]. Besides the actin- and microtubule-binding domains, spectraplakins also contain large spacer domains in between the cytoskeletal binding domains (Fig. 5.1A): a plakin domain, that acts as a scaffold for recruiting other proteins; and a linker domain containing spectrin repeats, which form a three-helix bundle that acts as a flexible and elastic linker, could potentially mediate dimerization, and acts as a scaffold for signalling pathway interactions [55, 68, 203–205]. In addition, near the microtubule lattice-binding GAR domain, EF-hand motifs are present, which bind Ca^{2+} and play a critical role in MT binding of the spectraplakin BPAG1 [74], although this effect was not yet observed for Shot [53, 166].

How linking actin filaments to the microtubule tip versus the lattice affects MT/actin crosstalk is not well understood. In addition, the influence of spacer length and flexibility

between the actin- and microtubule-binding domains remains unknown. Until now, unique aspects of natural cytolinkers, such as their many regulatory domains, their large size and complex tertiary structure, and the presence of many splice variants in the cell have made it difficult to establish a generic relationship between MT/actin-crosstalk and the molecular mechanism of crosslinking.

In this chapter, we study how the molecular anatomy of spectraplakin cytolinking proteins affects MT/actin-crosstalk, using full-length recombinant Shot as a reference cytolinker. We use *in vitro* reconstitution experiments to have control over the geometry of actin-microtubule interactions and the protein concentrations. To compare with Shot, we use engineered cytolinking proteins with a controlled anatomy. This bottom-up strategy also prevents the need for regulated protein activity, as auto-inhibition has already been shown for natural cytolinkers Shot [75] and Gas2Like1 (Chapter 4 and [116]), and suggested for Pigs (Pickled eggs) [78]. For this study, we focus on the effects of the cytolinkers on cytoskeletal organization and on microtubule dynamics. More specifically, we ask how crosslinking actin filaments either to the tip or the lattice of growing microtubules affects the microtubule growth dynamics, and we ask how crosslinking affects the co-organization of the two filament systems. For high temporal and spatial resolution, our experiments were conducted using total internal reflection fluorescence (TIRF) microscopy.

5.2. RESULTS

5.2.1. ENGINEERED CYTOLINKERS

To dissect the roles of the different domains of spektraplakins in actin/microtubule co-organization, we investigated a native spektraplakin (Shot) and a series of simplified engineered cytolinkers with different combinations of binding domains derived from the human ortholog of Shot (MACF1). The molecular anatomy of the proteins used in this chapter are shown in Fig. 5.1. To our knowledge, we here purified the large protein Shot for the first time. We note that the binding domains of Shot have up to 58-90% similarities with the sequence of the MACF1 binding domains used in our engineered cytolinkers (dependent on the domain: 76% for the CH domains; 78% for the GAR domain) [67]. Consequently, differences between our engineered proteins and Shot might arise from these differences in domain sequence, additional to functional differences in regulation that we expect for a simpler engineered cytolinker. Furthermore, we included EB3 in all assays (at a concentration of 133 nM), but for experimental reasons had 3 different batches and ages, which differed in protein activity (see Table 5.7 showing which EB was used in which assay).

To test how microtubule-end binding affects actin-micotubule interactions, we first engineered a cytolinker with the EB-binding domain but without the GAR domain (see Fig. 5.1B). This linker, which we refer to as TipAct, was already characterized in a previous study [96] and used for transporting actin filaments by growing microtubule ends (Chapter 3). The 74 kDa small protein contains the actin-binding domain (CH-tandem) and the microtubule tip-binding domain (SxIP motif) from MACF1. For simplicity, we replaced the spacer of MACF1, whose structural and mechanical properties are poorly characterized, by the coiled-coil domain of cortexillin. This coiled-coil domain is ex-

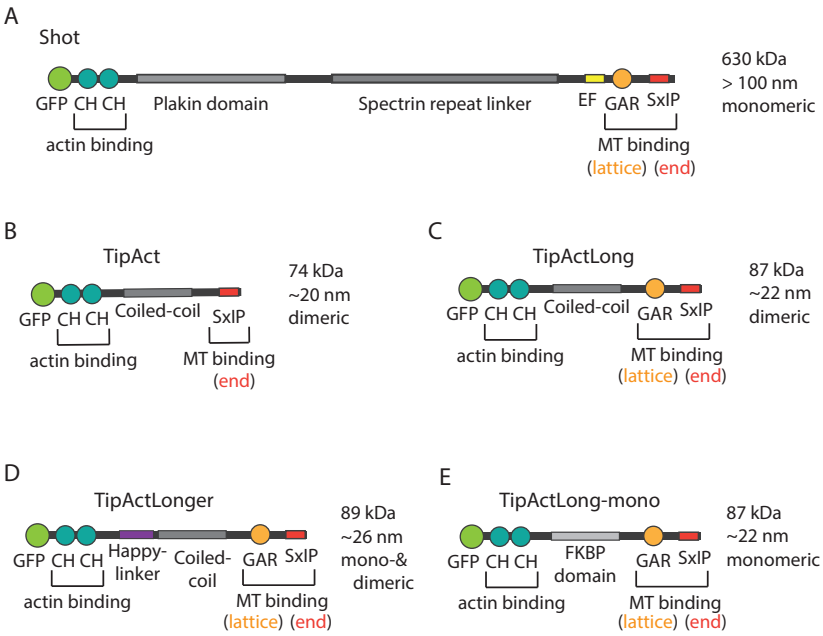

Figure 5.1: **Domain structures of the cytolinkers used in this chapter. (A)** Shot (short stop), the sole (native) spectraplakin in *Drosophila*, containing an actin-binding domain and two domains for microtubule binding: the microtubule lattice binding GAR domain, and the microtubule end-binding domain (via a SxIP motif for EB recognition). **(B)** Engineered cytolinker TipAct, designed to link the tip of growing microtubules to actin filaments. **(C)** Engineered cytolinker TipActLong which, in comparison to TipAct, has an additional GAR domain mediating microtubule lattice-binding. **(D)** Engineered cytolinker TipActLonger, which is an adaption of TipActLong by including a more flexible spacer domain (Happy-linker). **(E)** Engineered cytolinker TipActLong-mono, which is an adaptation of TipActLong by replacing the coiled-coil linker by a FKBP domain that does not dimerize unless a chemical dimerizer is added. The monomer and dimer classification of the cytolinkers indicated in the legends was determined using iSCAT measurements (Fig. 5.21). Indicated molecular weights and protein lengths were estimated from their sequences and using the length of the coiled-coil domain (~ 19 nm [206]). The engineered cytolinkers contain the actin- and microtubule-binding domains from human MACF1. Those binding domains are separated by the coiled-coil linker of cortexillin-I, which induces parallel dimerization, or by FKBP(F36V) which can induce dimerization upon addition of the chemical dimerizer AP20187. The Happy linker domain consists of 15 GSS-repeats for maximal flexibility of the linker.

pected to induce dimerization [102], which we indeed confirmed by iSCAT measurements (Fig. 5.21B).

To test how the simultaneous presence of the EB- and lattice-binding domains affects actin-microtubule interactions, we next engineered TipActLong (TAL). This cytolinker is very similar in design to TipAct, except that it contains an additional GAR domain from MACF1, which provides the possibility to link actin filaments to the lattice of microtubules, as is shown in Fig. 5.1C. Similar to TipAct, the coiled-coil spacer again induced dimerization, so that TAL forms dimers (Fig. 5.21C).

Besides regulatory domains, the main architectural difference between natural cytolinker Shot and its engineered simpler version TipActLong is the larger distance between the actin- and the microtubule-binding domains for Shot. To test whether the length and flexibility of the spacer domain has any influence on MT/actin-crosstalk, we designed the cytolinker TipActLonger (TALonger). For TALonger, we included a flexible linking domain ("Happy Linker", with an estimated persistence length of 3.4 nm) [207] in between the actin binding and the coiled-coil domains (Fig. 5.1D). Unfortunately, this altered the dimerization capabilities of the coiled-coil, as we find a coexistence of monomeric and dimeric TALonger by iSCAT (Fig. 5.21D). Assuming different diffusion constants for monomers and dimers (which influences their residence time ratio in the field-of-view for iSCAT measurements), we estimated that roughly 37-58% of the measured TALonger particles is monomeric.

Our engineered cytolinkers were originally designed as dimers to improve tip-tracking capabilities [100]. However, the natural cytolinker Shot is in our experimental conditions found to be monomeric (Fig. 5.21A). Similar to MACF1, it remains unknown wheter Shot is a monomer or oligomer within living cells [68, 204], we therefore designed a monomeric version of TAL, namely TipActLong-mono (TALmono), as is shown in Fig. 5.1E, to test the effect of cytolinker dimerization on MT/actin-crosstalk. Substituting the coiled-coil domain for a FKBP-domain, a linker domain that in principle should allow dimerization upon addition of a chemical, we observed that TALmono indeed remained monomeric (Fig. 5.21E).

5.2.2. ACTIN SLOWS DOWN MICROTUBULE GROWTH

Before investigating the effects of cytolinkers on MT/actin-crosstalk, we first study the actin/microtubule-interactions in the absence of any cytolinker. We use dynamic microtubules, grown from surface-immobilized GMPCPP-stabilized seeds, in the presence of fluorescently labeled end-binding (EB) protein EB3. To test the effect of actin filaments on microtubule growth, we add freely diffusible stabilized actin filaments. We image dynamic microtubules and stabilized actin filaments by total internal reflection fluorescence (TIRF) microscopy. A typical field-of-view is shown in Fig. 5.2A, where microtubules (shown in red, with EB3 at the growing ends marked in yellow) are seen to be growing within a entangled actin network (blue). Actin filaments are free to diffuse around and we observe no binding or alignment of these filaments to microtubules. We observe that actin filament organization is dynamic, as is shown by the changing actin organization in time series (Fig. 5.2B).

Besides studying actin organization in the proximity of microtubules, we can also use timelapses to analyze microtubule growth dynamics by constructing a kymograph, i.e.,

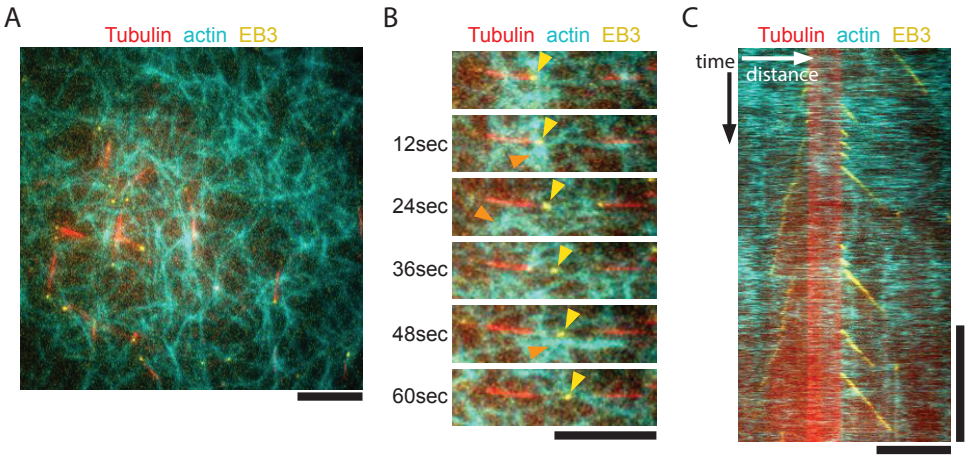

Figure 5.2: **Growing microtubules in the presence of actin filaments and in the absence of any cytolinkers.** **(A)** Typical field-of-view of microtubules (red) and their EB3-comets (yellow) growing in the presence of pre-polymerized and stabilized actin filaments (cyan). The actin filaments can move freely, as verified by time-lapse imaging, and are not (inter-)connected. This image is taken after about 5 min of imaging, where t=0 corresponds to about a minute after adding all the proteins to the attached microtubule seeds. **(B)** Time series of a growing microtubule and freely-moving actin filaments. Yellow arrowheads show the localization of the EB3-comet at the growing plus end of the microtubule. Orange arrowheads show different areas of denser actin, indicating the dynamic nature of the actin filaments moving freely around. **(C)** Kymograph showing the growth dynamics of a microtubule growing in the presence of actin filaments. In this case, the actin signal (cyan) is getting fainter due to photobleaching during imaging over a period of 20 min. Separate channels shown in Fig. 5.22. Experiments were performed with GFP-labelled EB3. Scale bars: 10 µm (horizontal) and 5 min (vertical).

a space-time plot along the length of the microtubule (Fig. 5.2C). From the microtubule tip position as a function of time, we can extract the microtubule growth velocity. From the duration of these growth events, we can calculate the frequency at which catastrophes typically occur, i.e., the rate at which the microtubule switches from the growing to the shrinking state. Moreover, we can observe whether rescues occur, i.e., switches from shrinking to growing at some distance away from the stable seed. We use these dynamic microtubule parameters to analyze the effect of an entangled actin network on microtubule growth. By analyzing a total of 1305 growth events (of which a few are shown in kymographs in Fig. 5.22), we observe that an entangled actin network has no significant effect on the microtubule catastrophe rate (Fig. 5.3A and Table 5.1) in 3 independent experiments. We measure average catastrophe rates of $0.98\,\mathrm{min}^{-1}$ and $0.94\,\mathrm{min}^{-1}$ in the absence and presence of actin filaments, respectively. Interestingly, we do observe an effect of actin on the microtubule growth velocity, which would normally correlate with an enhanced catastrophe rate [117, 208]. In the presence of an entangled actin network, we observe that microtubule growth slows down from an average of $4.03\,\mu\mathrm{m\,min}^{-1}$ to $3.14\,\mu\mathrm{m\,min}^{-1}$ (Fig. 5.3B and Table 5.1). Studying the microtubule shrinkage velocities, we observe no effect of actin (from $37.7 \pm 16.8\,\mu\mathrm{m\,min}^{-1}$ to $33.7 \pm 16.9\,\mu\mathrm{m\,min}^{-1}$) and the rescue rate remains essentially zero (from $0.08\,\mathrm{min}^{-1}$ to $0.06\,\mathrm{min}^{-1}$).

Although for freely growing microtubules a decreased microtubule growth velocity

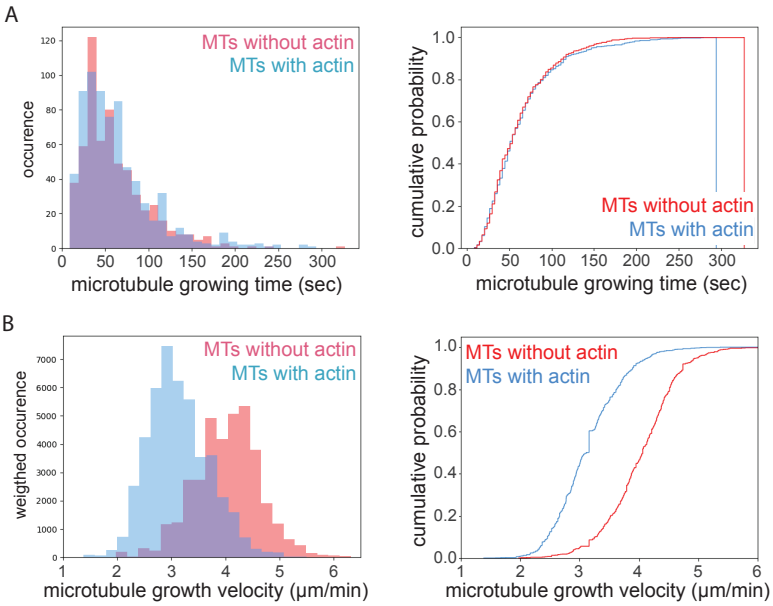

Figure 5.3: **Microtubule growth dynamics in the absence and presence of actin filaments. Left:** Histogram distribution. **Right:** Cumulative distributions. While histogram distributions are more intuitive regarding the spread and the peak values, representation via cumulative distributions contain that same information but make it easier to compare more than two conditions, as will be useful later in this chapter. **(A)** Microtubule growing time in the absence (red) and presence (blue) of actin filaments. **(B)** Corresponding microtubule growth velocity in the absence (red) and presence (blue) of actin filaments. The average catastrophe frequencies, growth velocities and rescue frequencies are shown in Table 5.1. Experiments were performed with GFP-labelled EB3.

		growth velocity (µm/min)	catastrophe rate (/min)	rescue rate (/min)	# events
no cytolinkers	no actin (red)	4.03 ± 0.60	0.98 ± 0.04	0.08	595
	with actin (blue)	3.14 ± 0.57	0.94 ± 0.04	0.06	710

Table 5.1: **Microtubule dynamics with active EB3 proteins.** Shown are the conditions without any cytolinkers, and the effect of actin filaments (as shown in Fig. 5.3). The results can be directly compared to other conditions, shown in Table 5.8. The '# events' indicates the number of analyzed MT growth events, from 3 independent experiments. Growth velocities are weighted averages ± weighted STD, catastrophe rates are means ± SEM.

correlates with an increased catastrophe rate [117, 208], this trend is not observed in our experiments. We speculate this observation could be explained by EB3 depletion, similar to a previous study where direct binding of EB1 to actin filaments in a salt-dependent manner was observed [209]. Interestingly, another study of microtubule growth within an entangled actin network (at a similar density as in our work, i.e., 2 µM) where no EB proteins were present did not find any effect of the actin on the microtubule growth velocity [36]. This observation suggests that steric hindrance from the actin network

alone does not influence the microtubule growth velocity, and the slow-down is EB-dependent. Earlier (unpublished) experiments in our lab showed the existence of an EB3 concentration range where a slight decrease in EB3 concentration resulted in decreased microtubule growth velocity without altering the catastrophe rate (data for Mal3: [210], EB3: [211]). First, we look for EB3 co-localization to actin filaments, which we do not observe (Fig. 5.23). This can be related to our salt concentration (namely 75 mM KCl, which allows only ~20% of EB bound to actin [209]) or to differences between EB1 and EB3 in actin-binding. Second, we compare the peak-to-lattice intensity ratios of EB3 comets on microtubules in the absence and presence of entangled actin filaments (Fig. 5.24). We observe no clear decrease of this ratio when actin is present. In fact, we measure a small increase in the plus-end comet intensity relative to the lattice (Fig. 5.24E and F). On the contrary, the growing minus ends (left side of kymograph in Fig. 5.24A,B) show diminished (absolute) EB comet intensities. However, we note that at high EB concentrations, the relative comet intensity is not linearly correlated with EB3 concentration due to saturation of binding [210, 211]. Although we do not find direct evidence for EB3 depletion, our observations do not rule out depletion of EB3 via weak actin binding.

To summarize, in the absence of any cytolinkers, we observe no co-alignment of actin filaments and microtubules. We do observe that stabilized actin filaments affect microtubule growth dynamics by slowing down growth, but without affecting other dynamical parameters. These results suggest that MT/actin co-organization requires the addition of cytolinkers.

5.2.3. SHOT LOCALIZES TO MT/ACTIN OVERLAPS AND PROMOTES RESCUES

After analyzing MT/actin-crosstalk in the absence of any cytolinkers, we can focus on how this coordination changes when the two systems are physically linked via cytolinking proteins. Since Shot, to the best of our knowledge, has not been characterized in reconstitution assays before, we first analyzed how the protein interacts with actin and microtubules separately. We observe that Shot hardly binds actin filaments in the absence of microtubules and only localizes to very dense actin structures (Fig. 5.4A). Conversely, in the absence of actin filaments but presence of microtubules, we find Shot localizing only to GMPCPP-stabilized microtubule seeds (Fig. 5.4B). We do not observe co-localization of Shot to growing microtubule ends, even though dim EB3-comets are present (Fig. 5.4C). Further analysis of kymographs for microtubule dynamics reveals that Shot - in the absence of actin - does not alter microtubule growth velocity or catastrophe rate (Fig. 5.6A-B, red and blue lines are without actin). We do observe a small increase in rescue rate (Fig. 5.6C, red and blue bars), where we note that all observed rescue events occurred at a site associated with a local accumulation of Shot (Fig. 5.25).

Shot localizing specifically to stabilized microtubule seeds in the absence of actin can have two different (non-excluding) explanations. Firstly, Shot could have slow unbinding rates, resulting in sequestering by the microtubule seeds encountered when shot first enters the flow channel. Over the course of 20 minutes, the finite pool of Shot-molecules would then remain bound to these seeds, preventing it from re-localizing to the dynamic microtubule lattice or growing end. Secondly, Shot might have a higher affinity to microtubule seeds. This might arise from the typical GMPCPP-tubulin conformation that might be recognized by Shot, as is the case for other proteins [93], although the affinity

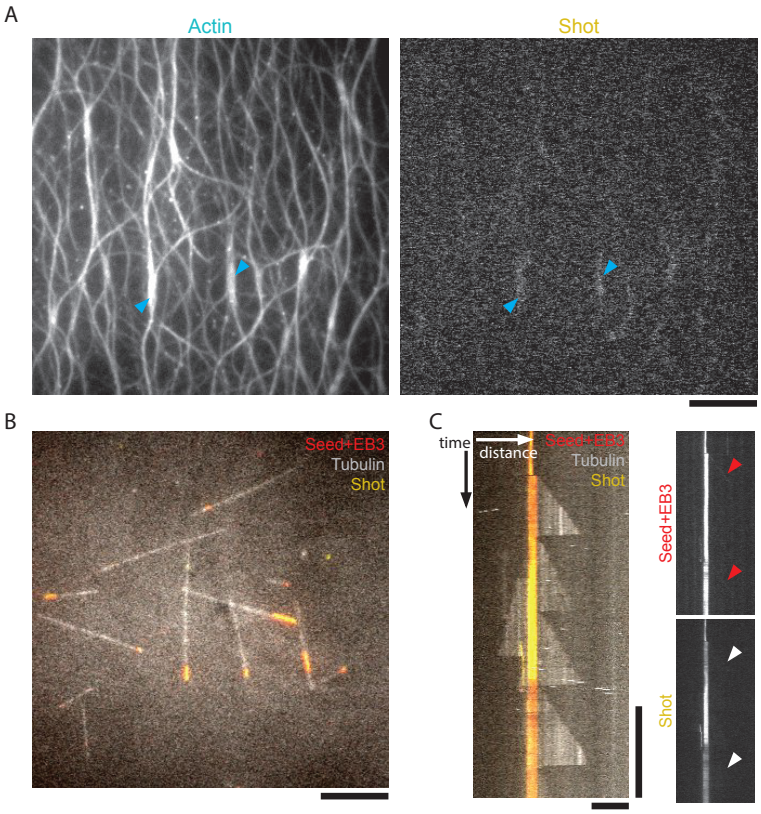

Figure 5.4: **Shot localization to actin filaments and microtubules separately. (A)** Typical field-of-view of actin filaments (left) and Shot (right). Blue arrowheads indicate some dense actin regions where Shot co-localizes to. **(B)** Typical field-of-view of growing microtubules (grey), microtubule seeds (red), EB3 comets (red) and Shot (yellow). Shot localizes only to the stabilized microtubule seeds. This image is taken after 5 min of imaging, and thus about 6 min after introducing the protein mix (i.e., tubulin and Shot) to the attached microtubule seeds. **(C)** Kymograph showing the growth dynamics of a microtubule (grey) in the presence of EB3 and Shot. Shot (yellow) localizes only to the GMPCPP-stabilized microtubule seed (red). Although dim EB3 comets are visible (red arrowhead), no co-localization of Shot (white arrowheads) is observed. Experiments were performed with less-active mCherry-labelled EB3. Scale bars: 10 µm (horizontal) and 5 min (vertical).

may also arise from the biotinylated tubulins (18%) that are present in the stabilized microtubule seeds for surface-attachment. Measurements of the (un)binding rates of Shot using FRAP measurements and assays with Taxol-stabilized seeds could help to distinguish between these scenarios. Moreover, one could flow in additional Shot proteins (and tubulin) once the seeds are saturated with Shot proteins.

After observing that Shot has a low affinity to either of the separate cytoskeletal systems, we tested its influence as a cytolinker on MT/actin-crosstalk. Strikingly, when Shot is added to the composite system, bundles of actin are formed around microtubules (Fig. 5.5A). We observe single actin filaments that are captured by and aligned to growing microtubules, as illustrated in Fig. 5.5B. Such co-alignment was not observed in the

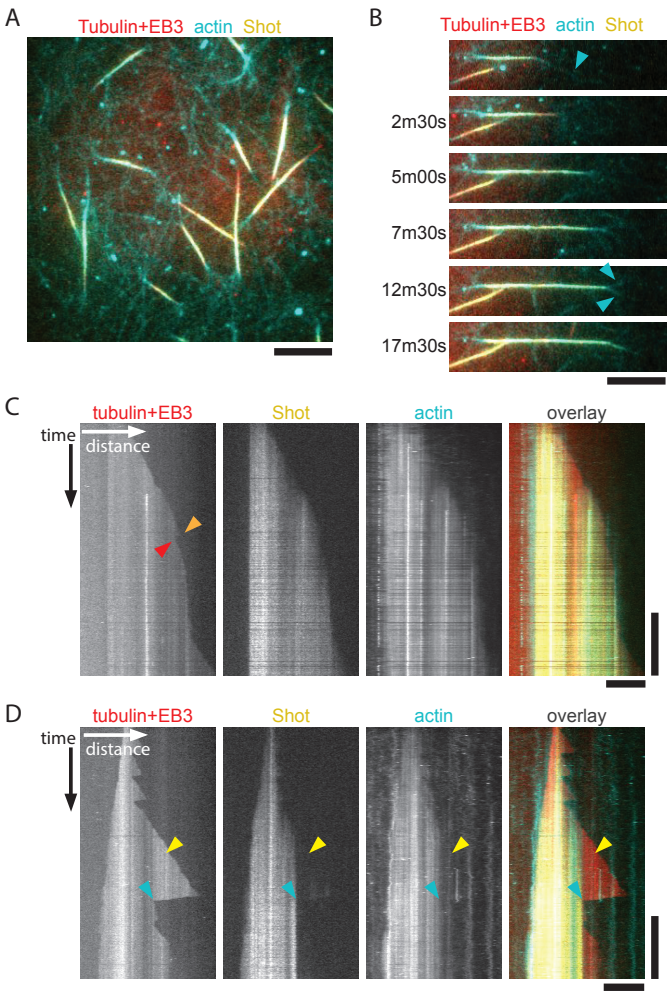

Figure 5.5: **MT/actin-crosstalk via Shot. (A)** Typical field-of-view with microtubules (red), EB3 (red) and Shot (yellow) growing in the presence of pre-polymerized actin filaments (cyan). Although actin filaments are free to move around, they form bundles around the microtubules. This image is taken after about 5 min of imaging, and thus about 6 min after adding the protein mix (containing tubulin, Shot, and stabilized actin filaments) to the attached microtubule seeds. **(B)** Time series of a growing microtubule and actin filaments in the presence of Shot. Blue arrowheads show the localization of single actin filaments that are later (next image) bundled by the growing microtubule. **(C)** Separated channels and overlay of a kymograph of the microtubule shown in B. Shot (yellow) is present all along the microtubule. Orange arrowhead indicates the only catastrophe observed for this microtubule in 20 min, which is quickly followed by a rescue event indicated with a red arrowhead. **(D)** Separated channels and overlay of a kymograph where Shot specifically localizes to MT/actin overlaps, and not (as indicated with yellow arrowheads) along the microtubule lattice where there is no actin. At these overlaps where Shot is localized, rescues of depolymerizing microtubule can be observed (blue arrowheads). Experiments were performed with less-active mCherry-labelled EB3. Scale bars: 10 µm (horizontal) and 5 min (vertical).

absence of cytolinkers. Shot co-localized along the complete microtubule lattice, and was no longer restricted to the stabilized seed (Fig. 5.5C,D). Although EB3 proteins are present, no increased co-localization of Shot is observed at the growing microtubule ends, indicating that Shot does not prefer microtubule ends over lattices. Interestingly, careful observations show that Shot specifically co-localizes to actin/microtubule overlaps (Fig. 5.5D). In the region of the microtubule lattice where no actin is present, we do not observe Shot co-localization. Conversely, we also do not observe Shot on actin filaments that are not interacting with microtubules (Fig. 5.5A).

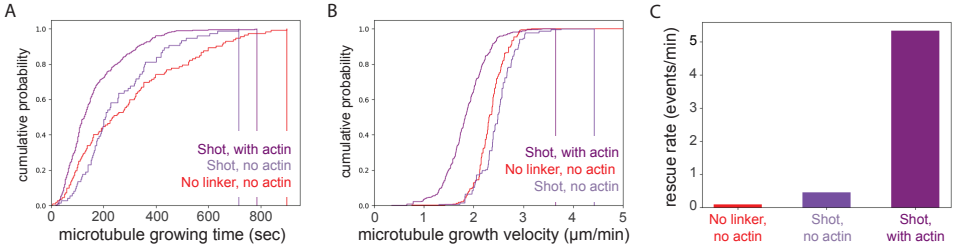

Figure 5.6: **Microtubule growth dynamics with Shot. (A)** Microtubule growing time in the absence of actin and Shot (red), with Shot but without actin (violet), or in the presence of both Shot and actin (dark purple). **(B)** Corresponding microtubule growth velocity (same colors as in A). **(C)** Corresponding microtubule rescue frequencies (same color scheme as in A and B). The average catastrophe frequencies, growth velocities and rescue frequencies are shown in Table 5.2. Experiments were performed with less-active EB3 proteins, and can therefore not directly be compared with results shown in Fig. 5.3. As a consequence, we cannot compare to the condition 'no linker, with actin'. However, we can directly compare Shot to other conditions with less-active EB3 proteins (see Table 5.9).

		growth velocity (µm/min)	catastrophe rate (/min)	rescue rate (/min)	# events
no linker	no actin (red)	2.33 ± 0.30	0.20 ± 0.02	0.03	112
Shot	no actin (light purple)	2.47 ± 0.36	0.24 ± 0.03	0.45	74
	with actin (dark purple)	1.85 ± 0.43	0.37 ± 0.02	5.33	352

Table 5.2: **Microtubule dynamics with less-active EB3 proteins in the presence of Shot** (as shown in Fig. 5.6). These data are classified as 'less-active EB3', because of the control experiments without cytolinkers and actin (top row). Here, the microtubule growth velocity and catastrophe rate are decreased compared to earlier control experiments (shown in Table 5.8), which is a known effect for having lower concentrations of EB3. The results can be directly compared to other conditions, shown in Table 5.9. '# events' is number of analyzed MT growth events. Growth velocities are weighted averages ± weighted STD, catastrophe rates are means ± SEM.

Using kymographs to analyze microtubule dynamics, we observe that the addition of actin filaments in the presence of Shot increases the MT catastrophe rate from 0.24 min^{-1} to 0.37 min^{-1} (Fig. 5.6A and Table 5.2). This effect of actin on MT catastrophe rate was not observed when no cytolinkers were present (Fig. 5.3A). The effect of actin on the growth velocity of the microtubules is similar in the presence or absence of Shot, namely slower MT growth (Fig. 5.6B). Interestingly, in presence of Shot, the addition of actin filaments greatly increases the MT rescue rate (Fig. 5.6C). This enhanced rescue rate is 10-

fold larger compared to the enhancement we observed when we added only Shot to the microtubules. Moreover, we note that we did not observe any enhancement of rescues in the absence of Shot. Kymographs show that rescues occur where both actin and Shot are localized along the microtubule lattice (Fig. 5.5D).

To summarize, we observe that Shot has a low affinity for both microtubules and actin filaments in the separate systems. However, in the composite system, we observe Shot binding to regions where microtubules and actin overlap. At those overlaps, actin filaments are aligned and bundled around microtubules and, conversely, the presence of actin promotes microtubule rescue events.

5.2.4. LINKING F-ACTIN TO MICROTUBULE PLUS-ENDS VIA TIPACT

To understand which microtubule-binding domains of Shot are important for the observed MT/actin crosstalk effects, we turn to engineered cytolinkers. Here, we can control the domain composition of the cytolinker and test their effect on MT/actin-crosstalk. First, we study the effects of linking actin filaments to growing microtubule ends, using the engineered cytolinker TipAct (Fig. 5.1B). In Chapter 3, TipAct was already used in assays with low actin concentration, and resulted in the transport of actin filaments by the growing microtubule end. Here, we use higher concentrations of actin (from 10 nM to 1 μM) to create dense entangled actin networks. We start by studying how TipAct behaves in the separate systems. We observe that in the presence of TipAct, many actin bundles are formed in conditions that in the absence of cytolinkers do not result in actin bundling (Fig. 5.7A). In addition, we observe that TipAct co-localizes to these actin bundles (Fig. 5.7A), indicating that TipAct mediates actin filament bundling, which is consistent with our observation that TipAct forms dimers in our experimental conditions (Fig. 5.21B), whereas Shot is monomeric. When TipAct is added to dynamic microtubules together with EB3, we observe TipAct localizing specifically to microtubule ends (Fig. 5.7B). This is similar to the co-localization of TipAct to EB1 proteins when expressed in COS7 cells (Fig. 5.26A). Moreover, in our *in vitro* reconstitution assay, TipAct tracks the growing microtubule ends in an identical manner as EB3 proteins, as is shown in the kymograph (see overlay in Fig. 5.7C and separate fluorescence channels in Fig. 5.27). Further analysis of these kymographs shows that TipAct slightly slows down microtubule growth compared to the control sample with EB3 alone, while the catastrophe frequency is slightly increased (Fig. 5.9A,B, and Table 5.3).

Next, we study how TipAct behaves in the composite system with both actin and microtubules present. We focus these experiments on conditions where the TipAct concentration is 10-fold (i.e., 3 nM) lower than for in the experiments described above with the separate systems (and also compared to the experiments with the other cytolinkers), since at 30nM we observe that TipAct in the composite system forms bundles of actin without microtubules involved (Fig. 5.28A). Using 3nM TipAct, we do observe TipAct localizing specifically to actin/microtubule-overlaps, indicating that most TipAct is involved in crosstalk (Fig. 5.28B and Fig. 5.8A). Interestingly, in the presence of actin, we observe that TipAct not only co-localizes to the tip of the microtubule, but also partly to the microtubule lattice (Fig. 5.8C and Fig. 5.29). These lattice-bound TipAct regions are always found right behind the tip, and do not occur as independent stretches further away from the tip. Apparently, microtubule-bound TipAct is stabilized by simultaneous

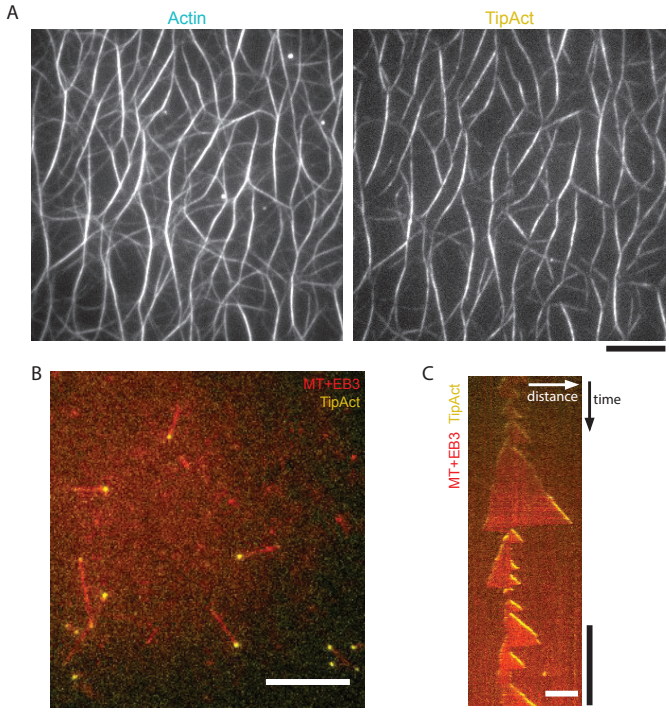

Figure 5.7: **TipAct localization to actin filaments and microtubules separately. (A)** Typical field-of-view of actin filaments (left) and TipAct (right), where we observe that TipAct (present at a concentration of 30 nM) binds and bundles actin filaments. **(B)** Typical field-of-view of growing microtubules (red), EB3 (red) and TipAct (yellow). TipAct localizes to the growing microtubule ends. This image is taken after about 5 min of imaging. **(C)** Kymograph showing the growth dynamics of a microtubule in the presence of EB3 and TipAct. TipAct localizes to the growing microtubule ends via EB3 (also see Fig. 5.27). Experiments were performed with mCherry-labelled EB3. Scale bars: 10 µm (horizontal) and 5 min (vertical).

actin-binding.

In the presence of TipAct, we observe dynamic remodelling of actin filaments around the growing microtubule ends. For example, during microtubule growth, we observe the formation of actin bundles around the microtubule (Fig. 5.8B, left). Here, we also clearly see the elongated co-localization of TipAct along the microtubule lattice. Next, during microtubule shrinkage, TipAct and these actin bundles disappear again, as can be observed by the bending and moving actin filaments (Fig. 5.8B, right). These observations suggest that the actin bundles formed around the microtubules are actually formed via TipAct linking actin filaments to the microtubule, and not TipAct binding and crosslinking actin filaments together.

By further analyzing the kymographs for microtubule dynamics, we find that linking actin filaments to microtubule ends via TipAct hardly affects the microtubule catastrophe frequency (Fig. 5.9C and Table 5.3), similar to Shot. We interpret the slight decrease in catastrophe frequency (comparing microtubules grown with TipAct either without (yellow) or with actin (orange)) as originating from the different EB3 batches we used for

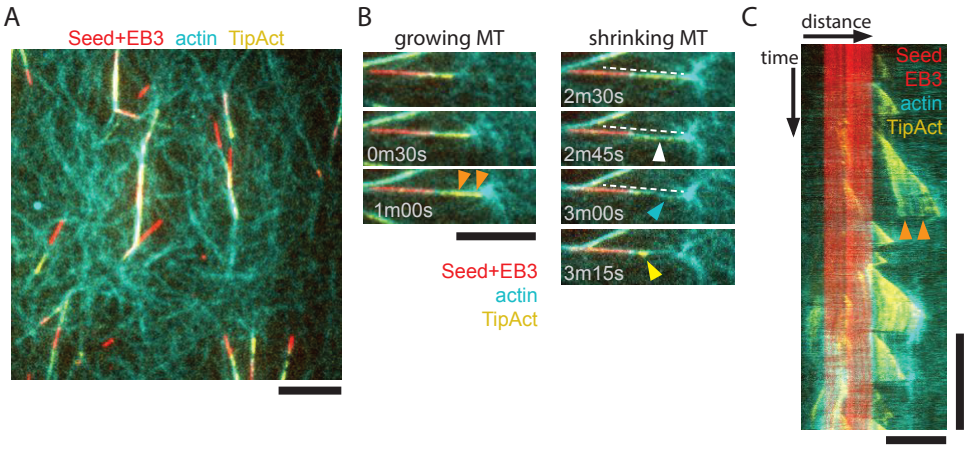

Figure 5.8: **MT/actin-crosstalk via TipAct. (A)** Typical field-of-view with microtubules (dark), seeds (red), EB3 (red) and TipAct (yellow) growing in the presence of pre-polymerized actin filaments (cyan). Although actin filaments are free to move around, they transiently form bundles around the microtubules. This image is taken after about 12.5 min of imaging, thus about 13.5 min after the protein mix (tubulin, TipAct, and stabilized actin filaments) was added to the attached microtubule seeds. **(B)** Time series of a dynamic microtubule with TipAct that is dynamically reorganizing surrounding actin filaments. On the left, the microtubule is growing and actin bundles are formed around its growing end via TipAct. Orange arrowheads indicate the extended co-localization of TipAct along the microtubule. On the right, the same microtubule is undergoing a catastrophe, where the TipAct signal on the microtubule disappears (white arrowhead) and the actin filaments start wobbling around (blue arrowhead). The yellow arrowhead indicates a TipAct comet at a new growing microtubule plus end. **(C)** Kymograph of the microtubule shown in (B) observed for a total of 20 min. Orange arrowheads indicate the extended co-localization of TipAct at and also behind the microtubule plus end. Separate channels are shown in Fig. 5.29A. Images shown are with mCherry-EB3 and GFP-TipAct (3 nM). Scale bars: 10 µm (horizontal) and 5 min (vertical).

these two sets of experiments (as indicated in Fig. 5.9C). The slight decrease in catastrophe frequency indicates that the mCherry-EB3 is less active than the GFP-EB3, an observation that was also confirmed in experiments without TipAct (Table 5.7). In addition, we observe that the rescue frequency is not altered by TipAct and remains low (<0.14 min^{-1}, data not shown), in contrast to the strong enhancement of rescues observed with Shot. However, we observe that, in the presence of TipAct, the microtubule growth velocity decreases from 3.53 $\mu\mathrm{m\,min}^{-1}$ in the absence of actin to 2.29 $\mu\mathrm{m\,min}^{-1}$ in the presence of actin (Fig. 5.9D). This decrease is more than can be expected for using mCherry-labelled EB3 instead of GFP-EB3, since without TipAct, only a small decrease for the different EB3 batches was observed (3.14 $\mu\mathrm{m\,min}^{-1}$ for GFP-EB3 and 2.92 $\mu\mathrm{m\,min}^{-1}$ for mCherry-EB3). Thus, this influence of actin on microtubule growth velocity is in line with a trend we have also observed for the condition without any cytolinking proteins, where actin slows down microtubule growth from 4.03 $\mu\mathrm{m\,min}^{-1}$ to 3.14 $\mu\mathrm{m\,min}^{-1}$ (Fig. 5.3B, and bright and dark red lines in Fig. 5.9B, respectively).

These observations indicate that linking actin to growing microtubule ends, in this case via TipAct, results in transient crosstalk and dynamic remodeling of the actin network around the microtubule, due to the dynamic nature of microtubule growth and shrinkage. In the absence of actin, TipAct slightly slows down microtubule growth com-

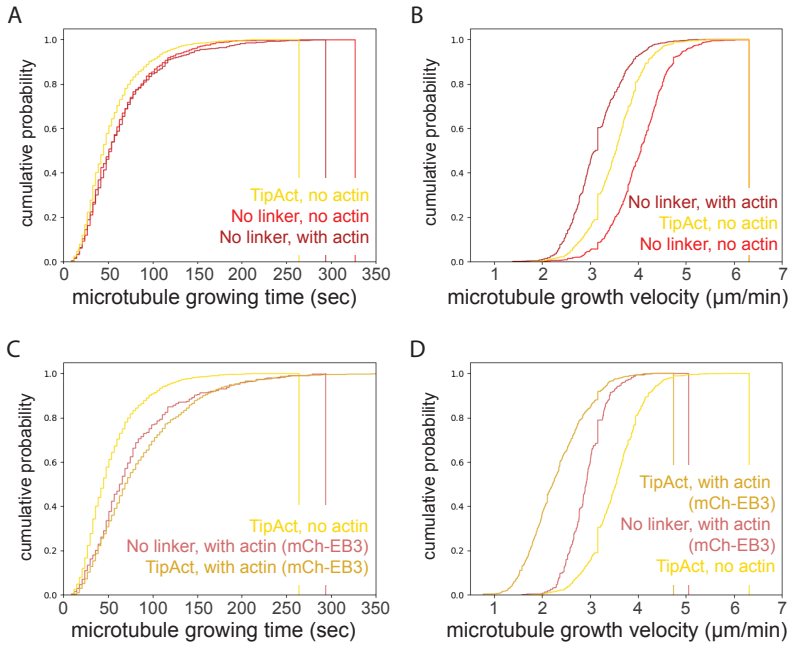

Figure 5.9: **Microtubule growth dynamics with TipAct. (A)** Influence of TipAct on microtubule growing times, comparing microtubule growth in the absence of TipAct (red-ish colored lines) and in the presence of TipAct (yellow line). **(B)** Corresponding microtubule growth velocity (same colors as in A). **(C)** Influence of actin and TipAct on microtubule growing time, comparing microtubule growth in the absence of TipAct (pink line) and in the presence of TipAct (dark yellow line). Shown is also microtubule growth time in the presence of TipAct, but absence of actin, where GFP-labelled EB3 was used in stead of mCherry-labelled EB3 (yellow line). **(D)** Corresponding microtubule growth velocity (same colors as in C). Experiments where performed with GFP-EB3, unless indicated otherwise. The average catastrophe frequencies, growth velocities and rescue frequencies are shown in Table 5.3. We can directly compare TipAct to other conditions with similar EB3 activity (see Table 5.8).

		growth velocity (µm/min)	catastrophe rate (/min)	rescue rate (/min)	# events
no linker	no actin (red)	4.03 ± 0.60	0.98 ± 0.04	0.08	595
	with actin (dark red)	3.14 ± 0.57	0.94 ± 0.04	0.06	710
	with actin * (pink)	$2.92 \pm 0.41^*$	$0.77 \pm 0.05^*$	0.00^*	284^*
TipAct	no actin (bright yellow)	3.53 ± 0.56	1.13 ± 0.04	0.02	950
	with actin* (dark yellow)	$2.29 \pm 0.62^*$	$0.71 \pm 0.02^*$	0.13^*	854^*

Table 5.3: **Microtubule dynamics with active EB3 proteins in the presence of TipAct** (as shown in Fig. 5.9). The results can be directly compared to other conditions, shown in Table 5.8. The '# events' are number of analyzed MT growth events. The asterix (*) indicates conditions with mCherry-labelled EB3 proteins, which are slightly less-active than GFP-labelled EB3 (see also Table 5.7). Growth velocities are weighted averages ± weighted STD, catastrophe rates are means ± SEM.

pared to the case where no cytolinkers are present. The combined presence of actin and TipAct slows down microtubule growth even further. Interestingly, whereas the rescue rate is greatly increased by actin in the presence of Shot, this effect was not observed for TipAct. With TipAct, most actin filaments were co-aligned to the microtubule tip, consistent with tip-tracking behaviour, as opposed to the co-alignment of actin to the whole microtubule lattice via Shot. This suggests that microtubule lattice binding plays a role in rescue promotion.

5.2.5. LINKING F-ACTIN TO THE MICROTUBULE LATTICE VIA TIPACTLONG

Next, we study the effect of linking actin filaments to microtubule lattice on MT/actin-crosstalk, using the engineered cytolinker TipActLong (Fig. 5.1C). In terms of domain structure, TipActLong is a shorter version of Shot. However, unlike Shot, TipActLong dimerizes due to its coiled-coil domain (Fig. 5.21A). We again first study the behaviour of TipActLong in the separate systems. In the presence of actin only, we observe that TipActLong causes actin filament bundling (Fig. 5.10A), similar to TipAct at the same concentration (i.e., 30 nM). To probe the binding kinetics, we measured the off-rate for actin-bound TipActLong by fluorescent recovery after photobleaching (FRAP) (Fig. 5.30A). We find a fast ($0.25\,s^{-1}$) and slow ($0.01\,s^{-1}$) component for the unbinding rate, as well as an immobile fraction (~ 45 %), suggesting a portion of the TipActLong molecules may be trapped within actin bundles. When TipActLong is added to dynamic microtubules together with EB3, we observe TipActLong along the microtubule lattices (Fig. 5.10B). This localization is different from the localization of Shot, where binding was restricted to stabilized microtubule seeds. Using FRAP measurements, we observed that microtubule binding was transient, with an off-rate of $0.04\,s^{-1}$ (Fig. 5.30B). Interestingly, despite the presence of EB3, we do not observe any enhancement of TipActLong localization at the growing microtubule ends, indicating that lattice-binding dominates over end-binding. Similarly, TipActLong expressed in cOS7 cells does not co-localize to EB1 comets, but prefers binding to what seems microtubule lattices (Fig. 5.26B). Using kymographs such as shown in Fig. 5.10C, we observed quite some rescue events at spots where two microtubules crossed over each other and therefore the TipActLong intensity was locally enhanced (Fig. 5.31). Analysis of over 160 growth events showed a small increase in rescue frequency from $0.08\,min^{-1}$ to $0.33\,min^{-1}$ due to these microtubule overlaps (bright red and light-blue bars in Fig. 5.12C, respectively, and Table 5.4). In addition, we found that TipActLong slightly reduces the microtubule catastrophe rate (Fig. 5.12A) and slows down microtubule growth from $4.03\,\mu m\,min^{-1}$ to $2.71\,\mu m\,min^{-1}$ (Fig. 5.12B).

Next, we study the effect of TipActLong on MT/actin-crosstalk. With both microtubules and actin present, we observe TipActLong localization along the complete MT length, where it forms actin bundles (Fig. 5.11A). FRAP measurements showed that TipActLong binding at MT/actin overlaps was transient, but with a fast ($0.3\,s^{-1}$) and a slow component ($0.01\,s^{-1}$) (Fig. 5.30C). Based on a comparison to the FRAP measurements on TipActLong interacting with actin and microtubules separately, we hypothesize that TAL molecules binding solely to an actin filament account for fast unbinding, while TAL molecules that bind both actin and microtubules account for slow unbinding.

During microtubule growth, we clearly observe the capturing and zippering of actin filaments along the microtubule lattice (Fig. 5.11B, left). The zippering and alignment of

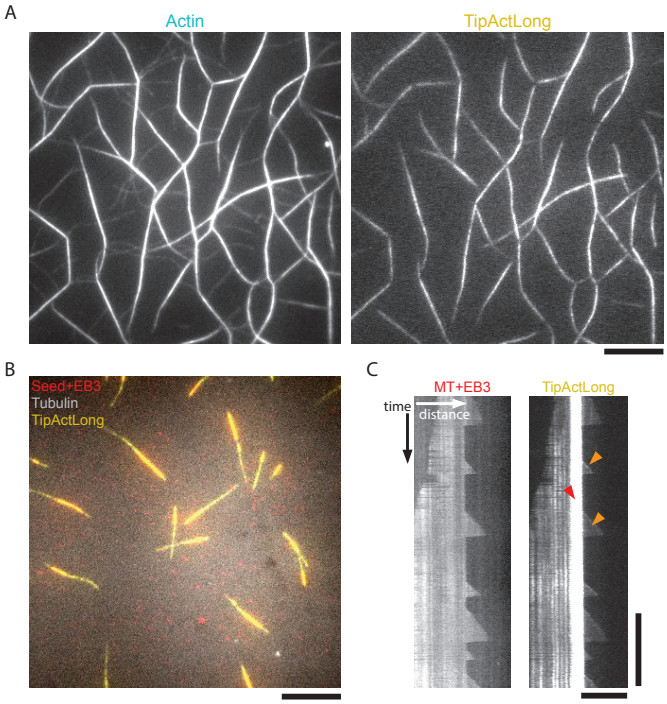

Figure 5.10: **TipActLong localization to actin filaments and microtubules separately. (A)** Typical field-of-view of actin filaments (left) and TipActLong (right), where we observe that TipActLong binds and bundles actin filaments. **(B)** Typical field-of-view of growing microtubules (red), EB3 (red) and TipActLong (yellow). TipActLong localizes along the lattice of microtubules (orange arrowheads), but is more enhanced at the GMPCPP-stabilized microtubule seeds (red arrowhead). This image is taken after about 5 min of imaging. **(C)** Kymograph showing growth dynamics of a microtubule in the presence of EB3 and TipActLong, and the localization of TipActLong along the microtubule lattice and seed. Rescue events are observed where two microtubules crossover and TipActLong-signal is enhanced (see Fig. 5.31). Experiments were performed using mCherry-EB3, and GFP-TipActLong (at 30 nM). Scale bars: 10 µm (horizontal) and 5 min (vertical).

actin filaments is even more clearly visible in conditions with lower actin concentration, where we observe single actin filaments aligning along microtubules (Fig. 5.32). However, in our denser actin conditions, multiple actin filaments align with microtubules. Looking at these actin bundles that form around microtubules at higher resolution using transmission electron microscopy, we found that typically on the order of 10 actin filaments are simultaneously associated with a single microtubule via TipActLong (Fig. 5.33C). Interestingly, when an actin filament is no longer free to reorganize itself around the microtubule because it is already bound to another microtubule, we observe that microtubules can also bend to follow actin organization (Fig. 5.11B, right). In that case, the actin filament serves as a track for the microtubule to grow along, resulting in bent microtubules.

Analyzing the kymographs, we confirm the co-localization of actin filaments (and TipActLong) along the complete microtubule (Fig. 5.11C and Fig. 5.34), which is dissim-

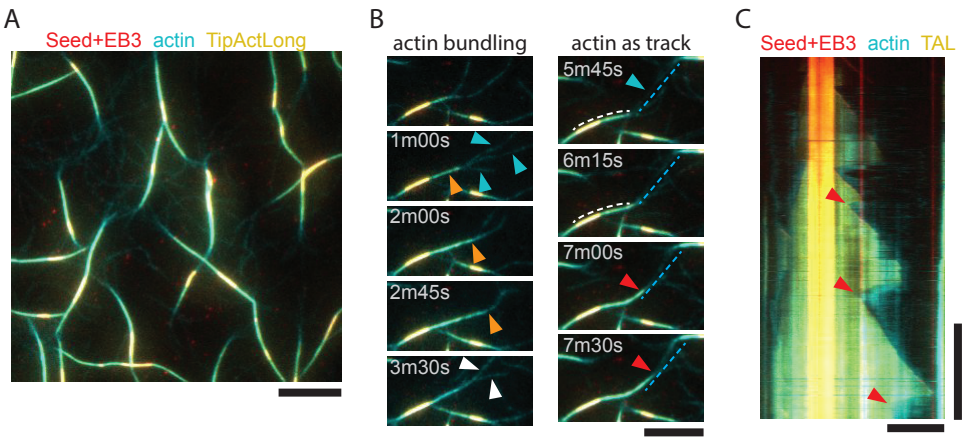

Figure 5.11: **MT/actin-crosstalk via TipActLong.** **(A)** Typical field-of-view with microtubules (dark), seeds (red), EB3 (red) and TipActLong (yellow) in the presence of pre-polymerized actin filaments (cyan). Although actin filaments are free to move around, they form bundles around the microtubules. This image is taken after about 15 min of imaging. **(B)** Time series of a growing microtubule with TipActLong and its interactions with actin filaments. On the left, a time series of a growing microtubule is shown where actin bundles are formed around the growing microtubule via TipActLong. Blue arrowheads indicate single actin filaments that will be bundled by a growing microtubule (orange arrowheads). White arrowheads indicate the un-bundled actin filaments again after microtubule catastrophe. On the right, a time series of the same microtubule, now following actin organization during growth. The blue arrowhead indicates the actin filaments that are attached to two separate microtubules and are therefore not free to move or reorganize. Red arrowheads indicate the growing microtubule whose direction is altered by growing along the actin track. **(C)** Kymograph of the microtubule shown in (B), illustrating TipActLong localization along the microtubule lattice and microtubule growth dynamics. Red arrowheads indicate rescue events. Separated channels shown in Fig. 5.34. Experiments were performed using mCherry-EB3 and GFP-TipActLong (at 30 nM). Scale bars: 10 µm (horizontal) and 5 min (vertical).

ilar to the crosstalk experiments with Shot, where we sometimes observe less actin co-alignment (and Shot co-localization) near the growing microtubule ends (as indicated in Fig. 5.5D). Upon catastrophe, we observe that most TipActLong disappears immediately (Fig. 5.34), indicating that TipActLong predominantly functions as a linker between microtubule and actin filament, and less as an actin bundler, similar to TipAct at low concentrations.

Using the kymographs to analyze over 550 growth events, we observe that actin decreases the microtubule catastrophe frequency in the presence of TipActLong from 0.76 to 0.49 min^{-1} (Fig. 5.12A and Table 5.4). The average catastrophe rate is lower in the second half of the 20 min time-lapse movie than in the first half of the movie (Fig. 5.35A,B). Given that we observed increased co-alignment between actin and microtubules over time, this observation suggests that the effect of TipActLong on microtubule growth dynamics is strengthed upon co-alignment. Furthermore, in the presence of TipActLong, the microtubule growth velocity again slightly decreases upon the addition of actin, from 2.71 to 2.17 $\mu\mathrm{m}\,\mathrm{min}^{-1}$ (Fig. 5.12B). This effect does not change during the course of the 20 min time-lapse movie, suggesting that it is independent of MT/actin co-alignment (Fig. 5.35C). Finally, we observe that actin greatly increases the microtubule rescue fre-

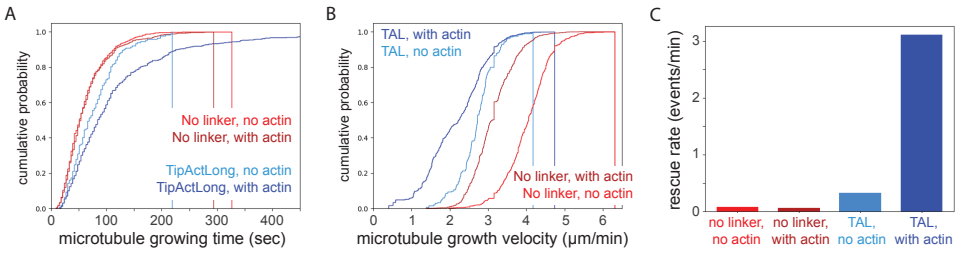

Figure 5.12: **Microtubule growth dynamics with TipActLong (TAL). (A)** Microtubule growing time in the absence of TipActLong (red-ish colored lines) and in the presence of TipActLong (blue-ish colored lines). Darker-colored lines are in the presence of actin. **(B)** Corresponding microtubule growth velocity (same color scheme as A). **(C)** Corresponding microtubule rescue frequencies (same colors as in A and B). The average catastrophe frequencies, growth velocities and rescue frequencies are shown in Table 5.4. We can directly compare TipActLong to other conditions with similar EB activity (see Table 5.8).

		growth velocity (μm/min)	catastrophe rate (/min)	rescue rate (/min)	# events
no linker	no actin (red)	4.03 ± 0.60	0.98 ± 0.04	0.08	595
	with actin (dark red)	3.14 ± 0.57	0.94 ± 0.04	0.06	710
TipActLong	no actin (light blue)	2.71 ± 0.50	0.76 ± 0.06	0.33	162
	with actin (dark blue)	2.17 ± 0.81	0.49 ± 0.02	3.11	559

Table 5.4: **Microtubule dynamics with active EB3 proteins in the presence of TipActLong** (as shown in Fig. 5.12). The results can be directly compared to other conditions, shown in Table 5.8. The '# events' shows number of analyzed MT growth events. Growth velocities are weighted averages ± weighted STD, catastrophe rates are means ± SEM.

quency, from $0.33\,\mathrm{min}^{-1}$ to $3.11\,\mathrm{min}^{-1}$, in the presence of TipActLong (Fig. 5.12C), similar to the effect of Shot. We note that the rescue rate is not large enough to cause any artifactual decrease of the catastrophe rate, since it takes on average about 20 s of depolymerization for a rescue to occur (Fig. 5.12C), which is long enough to be noticed even with our limited frame rate of $0.3\,\mathrm{s}^{-1}$.

To summarize, we observe that TipActLong behaves similarly to TipAct towards actin filaments, causing actin bundling. However, the two cytolinkers are different in the context of microtubule binding: TipActLong binds along the microtubule lattice, and not specifically at the microtubule tip like TipAct. In the composite system, our observations indicate that microtubule lattice-binding enables TipActLong to reorganize multiple actin filaments into bundles around growing microtubules. Since TipActLong-mediated actin binding simultaneously stabilize microtubules (i.e., fewer catastrophes, slower growth, and more rescues), the remodeling of the actin network is more long-lived compared to the remodeling seen in the presence of tip-binding TipAct. Moreover, TipActLong-mediated lattice binding enables actin filaments to serve as tracks that can direct microtubule growth. Interestingly, TipActLong promotes rescues of actin-bound microtubules, unlike TipAct, which strongly suggests that microtubule lattice binding plays a role in rescue promotion.

LINKING F-ACTIN TO THE MICROTUBULE LATTICE VIA A MORE FLEXIBLE CYTOLINKER (TALONGER)

Although we notice similarities between MT/actin-crosstalk mediated by TipActLong and by Shot, such as the increased microtubule rescue frequencies and extensive MT/actin co-alignment, the interactions of TipActLong and Shot with the separate cytoskeletal systems are different. Specifically, TipActLong can bundle actin filaments in the absence of microtubules and binds along the dynamic microtubules in the absence of actin, whereas Shot does not bundle actin filaments and only binds to microtubule seeds in the separate systems. To investigate the origin of these differences, we use two additional engineered cytolinkers that resemble TipActLong in terms of binding domains, but with structural changes. First, we study the influence of a longer and more flexible spacer-region between the actin- and microtubule-binding domains, motivated by the long spacer domain of Shot. We inserted a 4nm-long flexible domain, as shown

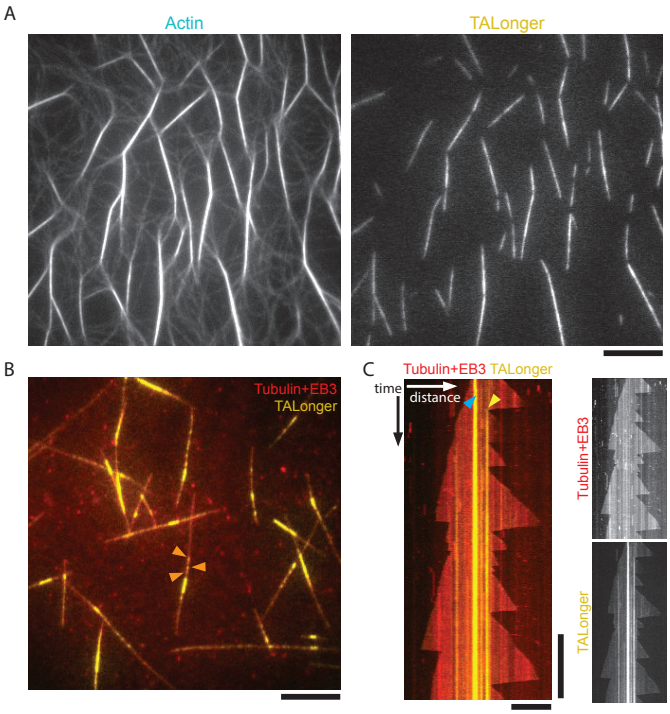

Figure 5.13: **TipActLonger localization to actin filaments and microtubules separately. (A)** Typical field-of-view of actin filaments (left) and TALonger (right), where we observe that TALonger binds and bundles actin filaments. **(B)** Typical field-of-view of growing microtubules (red), EB3 (red) and TALonger (yellow). TALonger localizes mostly at the GMPCPP-stabilized microtubule seeds, and localizes in a spotty manner along the microtubule lattice (indicated with orange arrowheads). This image is taken after about 15 min of imaging. **(C)** Kymograph showing growth dynamics of a microtubule in the presence of EB3 and TALonger. TALonger is localized along the microtubule lattice and is enhanced on the seed (blue arrowhead). Multiple rescue events are observed, of which the first one is indicated with the yellow arrowhead. Experiments were performed using less-active mCherry-EB3 and GFP-TALonger (at 30 nM). Scale bars: 10 µm (horizontal) and 5 min (vertical).

in Fig. 5.1D, increasing the overall end-to-end length of the protein from ca. 22 nm to 26 nm, and thus named it TipActLonger (TALonger).

In separate reconstitutions with actin, we observe that TALonger binds and bundles actin filaments (Fig. 5.13A), similar to TipAct and TipActLong. In assays with microtubules, we find TALonger binding along the microtubule lattice (Fig. 5.13B). However, the TALonger decoration is nonuniform. First, we observe TALonger binding more to microtubule seeds than to dynamic lattices, similar to Shot (and TAL). Second, along the lattice, we find brighter spots that are associated with rescue events, as illustrated in the kymograph of Fig. 5.13C. Unlike TipActLong, which only formed bright spots at intersections of two microtubules, TALonger additionally formed spots on single microtubules. Further analysis of these kymographs indeed show an enhanced rescue rate (Fig. 5.15C, compare red with light-purple bars, and Table 5.5) and furthermore shows that TALonger increases the microtubule catastrophe rate compared to the case where no linker is present, while the growth velocity remains similar (Fig. 5.15A and B, red with light-purple lines).

Next, we study the effect of TALonger on MT/actin-crosstalk. We observe that TALonger binds along the microtubule lattice and forms actin bundles around these microtubules (Fig. 5.14A), similar to Shot and TipActLong. The bright TALonger spots along the microtubule lattice that we observed in the absence of actin are no longer there, and TALonger co-localizes more homogeneously to the microtubule lattices. However,

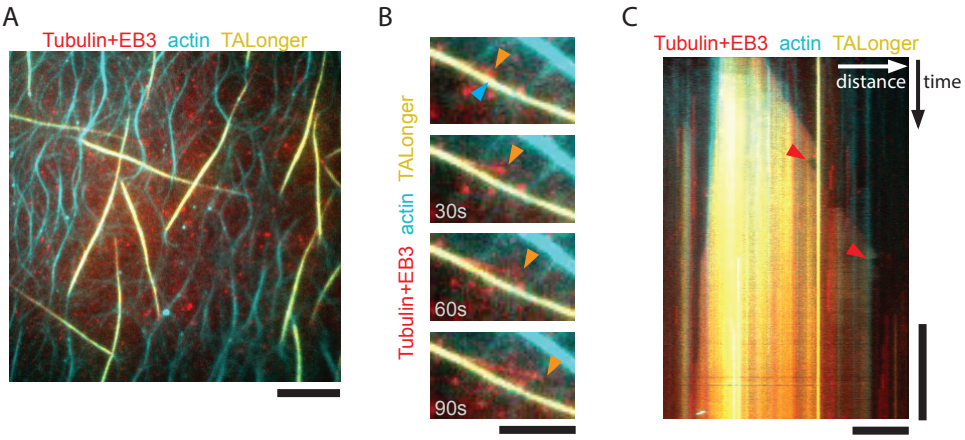

Figure 5.14: **MT/actin-crosstalk via TALonger. (A)** Typical field-of-view with microtubules (red), EB3 (red) and TALonger (yellow) in the presence of pre-polymerized actin filaments (cyan). Although actin filaments are free to move around, they form bundles around the microtubules. This image is taken after about 10 min of imaging. **(B)** Time series of a growing microtubule with TALonger and its interactions with actin filaments. Orange arrowheads indicate a growing microtubule that starts as part of a MT/actin bundle (blue arrowhead), but then grows away and is no longer decorated with TALonger nor interacting with actin. **(C)** Kymograph showing the growth dynamics of a microtubule (not the same MT as in B) growing in the presence of actin filaments and TALonger. Red arrowheads indicate rescue events. Separate channels shown in Fig. 5.36. Experiments were performed using less-active mCherry-EB3 and GFP-TALonger (at 30 nM). Scale bars: 10 µm (horizontal, A and C), 5 µm (horizontal, B) and 5 min (vertical).

TALonger intensity is still highest at the seed and gradually decreases with distance away from the microtubule seed. This indicates that TALonger co-localizes more with the lattice around the microtubule seed and less at the growing microtubule ends (Fig. 5.14C). As a consequence, we sometimes observe growing microtubule ends that are not decorated with TALonger and thus no actin filaments are co-aligned with these. In the example shown in Fig. 5.14B, we observe a microtubule that initially grows as a MT/actin bundle, but eventually continues to grow out of the bundle without TALonger decoration. This is contrary to what we observe for microtubules growing with TipActLong, where microtubules always remained bundled with actin until they underwent a catastrophe (Fig. 5.11B, right). We speculate this could be a consequence of either a depleted pool of TALonger molecules in our assay, resulting from slow unbinding rates, or a preference for TALonger to bind closer to the microtubule seed, as was observed in the absence of actin (Fig. 5.13B). FRAP measurements of TALonger unbinding from the MT/actin overlaps could help distinguish between these scenarios.

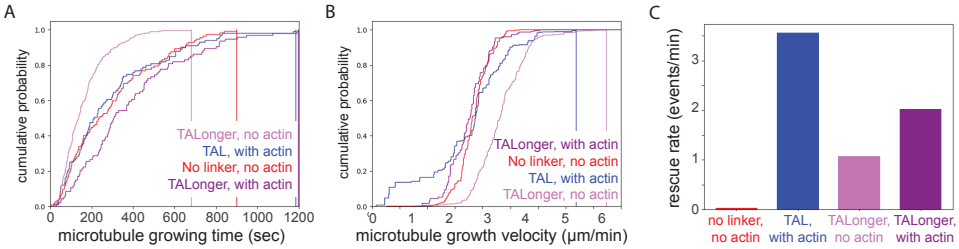

Figure 5.15: **Microtubule growth dynamics with TALonger.** **(A)** Microtubule growing time in the absence of any linker and actin (red), in the presence of TipActLong and actin (blue), in the presence of TALonger without actin (light purple), and in the presence of TALonger with actin (dark purple). **(B)** Corresponding microtubule growth velocity (same color scheme as in A). **(C)** Corresponding microtubule rescue frequencies (same color scheme as in A and B). The average catastrophe frequencies, growth velocities and rescue frequencies are shown in Table 5.5. Experiments were performed with less-active EB3 proteins and can only be directly compared to other conditions with less-active EB3 proteins (see Table 5.9).

		growth velocity (μm/min)	catastrophe rate (/min)	rescue rate (/min)	# events
no linkers	no actin (red)	2.33 ± 0.30	0.20 ± 0.02	0.03	112
TipActLong	with actin (blue)	2.22 ± 0.76	0.20 ± 0.02	3.56	99
TALonger	no actin (light purple)	2.83 ± 0.44	0.37 ± 0.02	1.07	266
	with actin (dark purple)	2.27 ± 0.78	0.16 ± 0.02	2.02	94

Table 5.5: **Microtubule dynamics with less-active EB3 proteins in the presence of TALonger** (as shown in Fig. 5.15). These data are classified as 'less-active EB3', because of the control experiments without cytolinkers and actin (top row). Here, the microtubule growth velocity and catastrophe rate are decreased compared to earlier control experiments (shown in Table 5.8), which is a known effect for having lower concentrations of EB3. The results can be directly compared to other conditions, shown in Table 5.9. The '# events' indicates number of analyzed MT growth events. Growth velocities are weighted averages ± weighted STD, catastrophe rates are means ± SEM.

Upon further analysis of the kymographs for microtubule dynamics, we find that linking actin filaments to microtubules via the flexible cytolinker TALonger results in a decreased catastrophe rate compared to not having actin present (Fig. 5.15A and Table 5.5). In addition, we again observe that the addition of actin slows down microtubule growth in the presence of TALonger (Fig. 5.15B), similar to what we observe with the other cytolinkers and in the absence of cytolinkers. Moreover, we observe that the rescue rate is enhanced upon the addition of actin (Fig. 5.15C), similar to observations for TipActLong and for Shot. However, interestingly, the rescue rate only doubles for TALonger, namely from $1.07\,\mathrm{min}^{-1}$ in the absence of actin to $2.02\,\mathrm{min}^{-1}$ in the presence of actin. Thus, the rescue rate does not reach the $3.56\,\mathrm{min}^{-1}$ rescue rate in the presence of TipActLong (Fig. 5.15C).

To summarize, we observe that TALonger behaves similarly to TipActLong. In the separate systems, TALonger causes actin bundling and binds the microtubule lattice, although in a spotty manner. In the composite system, we observe actin remodelling into bundles around the microtubule, and decreased microtubule catastrophe rates and growth velocities. This indicates that the flexible linker itself does not impact binding much. However, we observe a different effect on the microtubule rescue rate. The moderate increase of rescue rate by adding actin when TALonger is present, as opposed to the 10-fold increase in the presence of TipActLong (Fig. 5.15C), could be related to less TALonger being bound to microtubules. Not all microtubule lattices are decorated with TALonger molecules and these 'naked' microtubules are included in the ensemble average over all microtubules in the field of view. In general, we expect that the differences between TALonger and TipActLong largely arise from the fact that TipActLong is a dimer, whereas iSCAT measurements show that TALonger is only partly dimerized (Fig. 5.21D). These measurements indicate that the flexible linker domain somehow interferes with the neighbouring coiled-coil domain and prevents it from dimerizing.

LINKING F-ACTIN TO THE MICROTUBULE LATTICE VIA A MONOMERIC CYTOLINKER (TALMONO)

Besides the increased distance between the actin- and microtubule-binding domains, another explicit difference between Shot and our engineered cytolinkers is that Shot does not form dimers in our *in vitro* assays. Therefore, we wonder what is the effect of dimerization, and consequently the binding avidity, of the cytolinking protein on MT/actin-crosstalk. We altered TipActLong to a monomeric form, TALmono, by substituting the coiled-coil domain for a FKBP-domain (Fig. 5.1E) that allowed us to still chemically dimerize the protein if required. Without the chemical dimerizer, we observed that TALmono is indeed monomeric (Fig. 5.21E).

In reconstitutions with actin, we observe that TALmono does not bind nor bundle actin filaments (Fig. 5.16A). While this is contrary to the bundling activity of dimeric engineered cytolinkers such as TipAct (Fig. 5.7A) and TipActLong (Fig. 5.10A), it resembles the behaviour of monomeric Shot, which likewise did not bind or bundle actin (Fig. 5.4A). However, for TALmono, we do not observe faint localization to denser actin structures, as was observed for Shot. These observations suggest that dimerization is required for binding two different actin filaments simultaneously. Considering the single actin-binding domain that is present in each engineered protein, this result is expected. In reconstitutions with microtubules, we observe uniform TALmono localization along

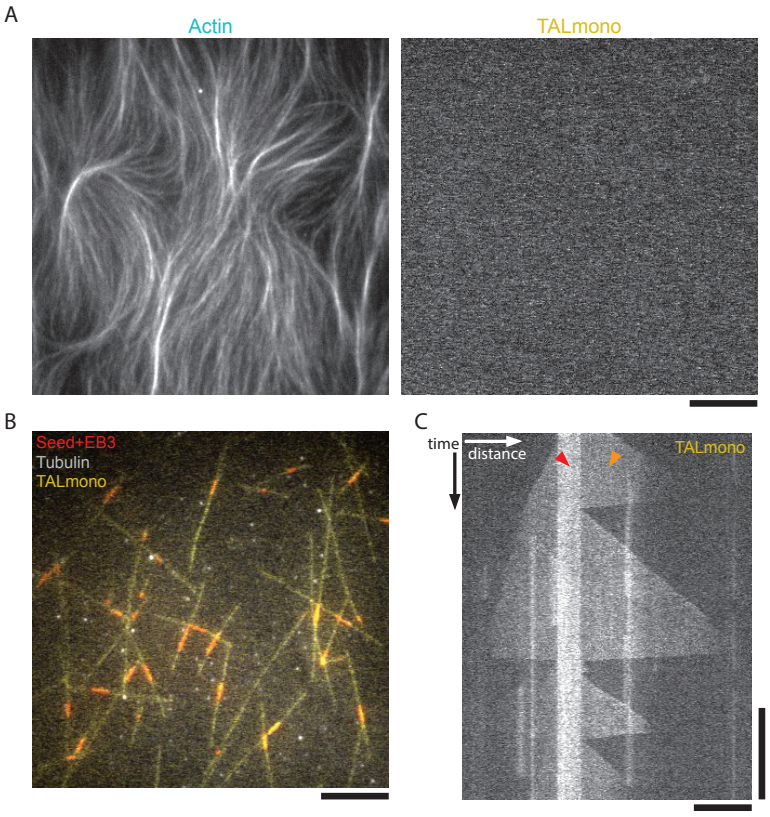

Figure 5.16: **TipActLong-mono does not bind actin filaments, but localizes to the microtubule lattice in the separate systems. (A)** Typical field-of-view of actin filaments (left) and TALmono (right), where we observe that TALmono does not bind nor bundle actin filaments. **(B)** Typical field-of-view of growing microtubules (grey), microtubule seeds (red), EB3 (red) and TALmono (yellow). TALmono localizes along the microtubule lattice. This image is taken after about 5 min of imaging. **(C)** Kymograph showing growth dynamics and the localization of TALmono along the microtubule lattice of a microtubule in the presence of EB3 and TALmono. Red arrow indicates the slightly enhanced TALmono-signal at the microtubule seed, compared to the dynamic microtubule lattice (orange arrow). Experiments were performed with less-active EB3 and 30nM TALmono. Scale bars: 10 μm (horizontal) and 5 min (vertical).

the complete microtubule lattice (Fig. 5.16B), similar to TipActLong. TALmono localization is thus different from Shot localization, which was restricted to microtubule seeds in the absence of actin. We do observe enhanced binding of TALmono to the microtubule seed, as is clearly visible on the kymograph of Fig. 5.16C.

Next, we study the effect of monomeric cytolinker TALmono on MT/actin-crosstalk. In the composite system, we observe TALmono co-localizing along the microtubule lattice, where actin is bundled too (Fig. 5.17A). However, we still observe that more TALmono is bound to the microtubule seed compared to the dynamic lattice, as is clearly shown in the separate channels of the kymographs in Fig. 5.18. Similar to TALonger, we observe 'naked' microtubules growing without TALmono decoration, resulting in

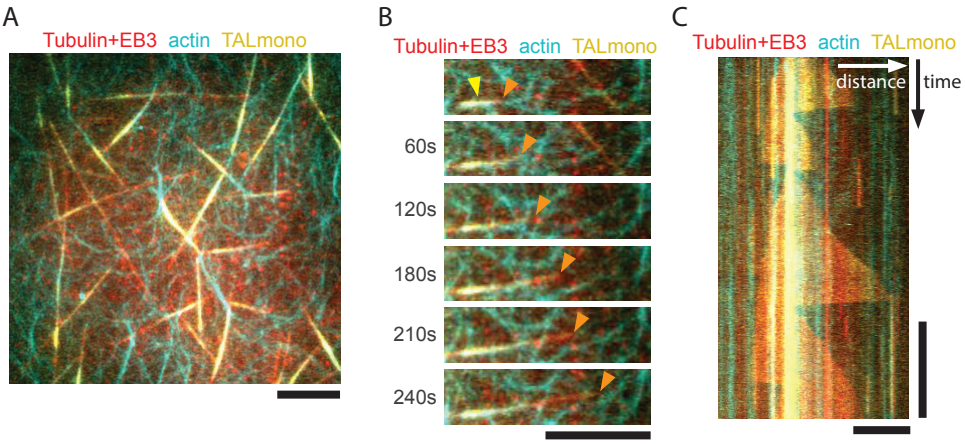

Figure 5.17: **MT/actin-crosstalk via TALmono. (A)** Typical field-of-view with microtubules (red), EB3 (red) and TALmono (yellow) in the presence of pre-polymerized actin filaments (cyan). Although actin filaments are free to move around, they form bundles around the microtubules. This image is taken after about 10 min of imaging. **(B)** Time series of a growing microtubule with TALmono and its interactions with actin filaments. Orange arrowheads indicate a growing microtubule end. Although actin filaments are around for bundling near the growing microtubule, it seems actin is mostly bundled around the microtubule seed (indicated with yellow arrowhead) and we observe no actin alignment further away from the seed. **(C)** Kymograph of the microtubule shown in B. In this case, during the timelapse of 20 min, no rescue events were observed. Experiments were performed with less-active EB3 and 30nM TALmono. Scale bars: 10 µm (horizontal) and 5 min (vertical).

diminished actin co-alignment and local actin remodelling, compared to TipActLong (Fig. 5.17B). In addition, we do not observe growing microtubules following pre-existing actin tracks.

Through further analysis of kymographs such as those shown in Fig. 5.17C and Fig. 5.18, we study the effects of TALmono on microtubule dynamics. The presence of actin does not change the catastrophe rate for microtubules growing with TALmono (Fig. 5.19A and Table 5.6). Moreover, we again confirm the trend that the addition of actin slows down microtubule growth, also in the presence of TALmono (Fig. 5.19B and Table 5.6). Finally, we observe only a few rescue events in the presence of actin and TALmono, resulting in a rescue rate of $0.23\,\mathrm{min}^{-1}$ (Fig. 5.19C and Table 5.6). This is surprising, since for the other lattice-binding cytolinkers the addition of actin usually greatly increased the rescue rate. More specifically, for Shot, which is like TALmono also monomeric, the addition of actin increases the rescue rate from $0.45\,\mathrm{min}^{-1}$ to $5.33\,\mathrm{min}^{-1}$. For the dimeric TipActLong, which contains exactly the same binding domains of TALmono, the addition of actin increases the rescue rate from $0.33\,\mathrm{min}^{-1}$ to $3.11\,\mathrm{min}^{-1}$.

To summarize, we observe that TALmono behaves similarly to Shot, although there are also some stricking differences. In the separate systems, TALmono does not bind nor bundle actin like Shot, but does bind the microtubule lattice, which is unlike Shot that only binds to the microtubule seed. In comparison, TipActLong, the dimeric version of TALmono, does bind and bundle actin filaments, and also binds the microtubule lattice. In the composite system with TALmono, we observe actin remodelling into bundles around the microtubule, and a decreased growth velocity, similar to both Shot and

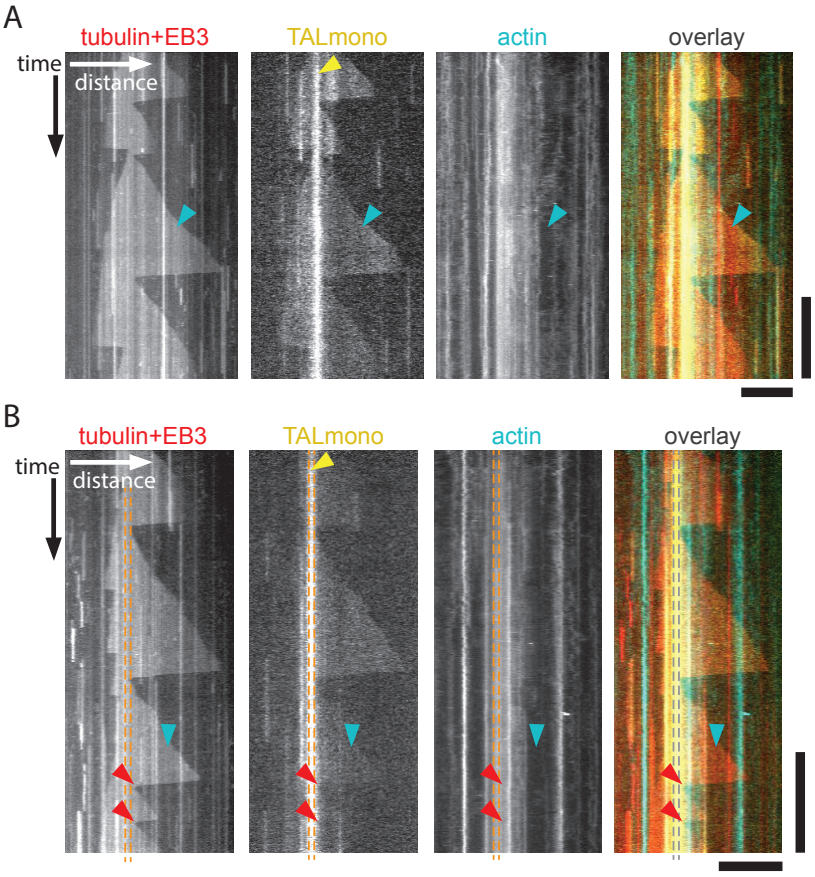

Figure 5.18: **Localization of TALmono and actin along microtubules.** **(A)** Separated channels and overlay of the kymograph shown in Fig. 5.17C. TALmono-signal is enhanced at the microtubule seed (yellow arrowhead). Blue arrowheads indicate a part of MT-lattice that has no actin, showing a lack of actin alignment. **(B)** Separated channels and overlay of a kymograph where two late ('near-seed') rescue events are observed (indicated with red arrowheads). TALmono-signal is enhanced at the microtubule seed (yellow arrowhead). Blue arrowheads indicate a part of MT-lattice that has no actin, showing a lack of actin alignment. Orange (or grey) dotted lines indicate the location of the microtubule seed. Scale bars: 10 µm (horizontal) and 5 min (vertical).

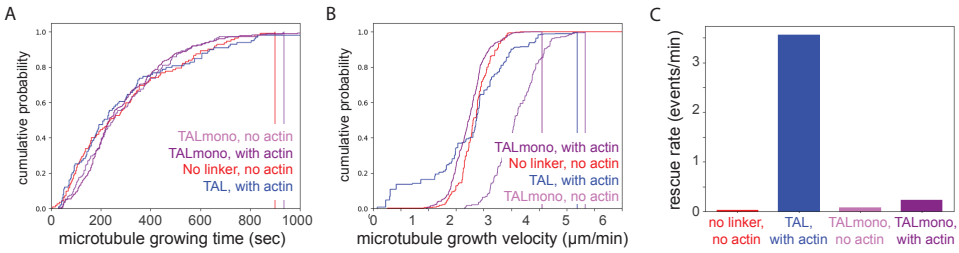

Figure 5.19: **Microtubule growth dynamics with TALmono.** **(A)** Microtubule growing time in the absence of any linker and actin (red colored line), in the presence of TipActLong and actin (blue colored line) and in the presence of TALmono (purple-ish colored lines). **(B)** Microtubule growth velocity in the absence of any linker and actin (red colored line), in the presence of TipActLong and actin (blue colored line) and in the presence of TALmono (purple-ish colored lines). **(C)** Rescue frequencies of microtubules in the absence of any linker and actin (red colored bar), in the presence of TipActLong and actin (blue colored bar) and in the presence of TALmono (purple-ish colored bars). The average catastrophe frequencies, growth velocities and rescue frequencies are shown in Table 5.6. Experiments were performed with less-active EB3 proteins and can only be directly compared to other conditions with less-active EB3 proteins (see Table 5.9).

		growth velocity (µm/min)	catastrophe rate (/min)	rescue rate (/min)	# events
no linkers	no actin (red)	2.33 ± 0.30	0.20 ± 0.02	0.03	112
TipActLong	with actin (blue)	2.22 ± 0.76	0.20 ± 0.02	3.56	99
TALmono	no actin (light purple)	3.10 ± 0.41	0.20 ± 0.02	0.08	148
	with actin (dark purple)	2.23 ± 0.31	0.20 ± 0.01	0.23	227

Table 5.6: **Microtubule dynamics with less-active EB3 proteins in the presence of TALmono** (as shown in Fig. 5.19). These data are classified as 'less-active EB3', because of the control experiments without cytolinkers and actin (top row). Here, the microtubule growth velocity and catastrophe rate are decreased compared to earlier control experiments (shown in Table 5.8), which is a known effect for having lower concentrations of EB3. The results can be directly compared to other conditions, shown in Table 5.9. The '# events' indicates number of analyzed MT growth events. Growth velocities are weighted averages ± weighted STD, catastrophe rates are means ± SEM.

TipActLong. This indicates that dimerization of cytolinkers impacts binding of the separated systems, but not so much in the composite system. Interestingly, we observe hardly any rescue events when TALmono is present, even when actin is added. This is opposed to the 10-fold increase of rescues by addition of actin in the presence of TipActLong (Fig. 5.15C and Table 5.4), indicating that dimerization of the cytolinker is important for rescues.

5.3. DISCUSSION

In this chapter, we reconstituted interactions between dynamic microtubules and freely diffusing (but stabilized) actin filaments that form an entangled network, in order to investigate the influence of spectraplakin cytolinkers on MT/actin crosstalk. Specifically, we measured the effects of cytolinker-mediated interactions with actin on MT growth dynamics and also observed the reciprocal effects on actin organization (summary in Fig. 5.20). First, in the absence of any cytolinkers, we observed that actin filaments reduce the microtubule growth velocity, but do not change the catastrophe rate. We speculate that two effects can contribute to our observations: (1) steric hindrance of the actin filaments can slow microtubules down, which should then result in higher catastrophe rates; (2) EB3 depletion from solution by actin, as observed for EB1 [209]. In general, less EB3 will result in slower microtubule growth and a decrease in catastrophe rate [117, 208]. However, in previous *in vitro* reconstitution experiments, a concentration regime of EB3 proteins was observed where less EB3 resulted in slower growth, but without yet decreasing the catastrophe rate [210, 211], similarly to our observations for the presence of actin. Admittedly, we were not able to observe any localization of EB3 to actin structures, nor did we observe any decrease in fluorescence intensity of EB3 comets at the microtubule plus ends (Fig. 5.24) that would support our speculations. Although the diminished EB3 comet fluorescence at the microtubule minus ends might indicate EB3 depletion (Fig. 5.24A,B), how actin filaments slow down microtubule growth remains an open question (Fig. 5.20).

Next, we investigated the natural cytolinker Shot and we observed that it hardly binds actin filaments nor microtubules in the separate systems. Since multiple actin-binding domains are required to form actin bundles, these observations are consistent with Shot being largely monomeric in our experimental conditions (Fig. 5.21A) and thus containing a single actin-binding domain (Fig. 5.1A). Interestingly, in the composite system, we found Shot co-localization selectively to MT/actin overlap regions, where actin filaments were co-aligned to microtubules (Fig. 5.20). In addition, actin-microtubule interactions mediated by Shot resulted in a large increase in MT rescue rate. The low affinities of Shot for isolated actin filaments or microtubules help to make localization of Shot to overlap regions more selective. However, exactly how Shot selectively localizes to the MT/actin overlap regions is not understood. One possible explanation is auto-inhibition of Shot, where for example the actin- and microtubule-binding domains interact with each other and therefore compete with binding to either actin of microtubules. Auto-inhibition of Shot was already suggested before [75], where an intramolecular interaction of the actin-binding domain with the EF-hand domain keeps the protein in an inactive conformation that is targeted to the growing microtubule end via EB. In addition, Shot's auto-inhibition is reminiscent of a protein member from another family of cytolinkers, namely Gas2Like1 (Chapter 4 and [116]), where an intramolecular interaction of the actin-binding domain with the MT lattice-binding domain competes with interactions with either of the separated cytoskeletal components. An alternative explanation for the selective binding of Shot to MT/actin overlaps could be the binding avidity of Shot. Being bound to both an actin filament and a microtubule simultaneously will likely decrease the unbinding rate of Shot, similarly to actin crosslinker α-actinin 4 (ACTN4) where doubly bound linkers unbind with almost two orders of magnitudes slower than

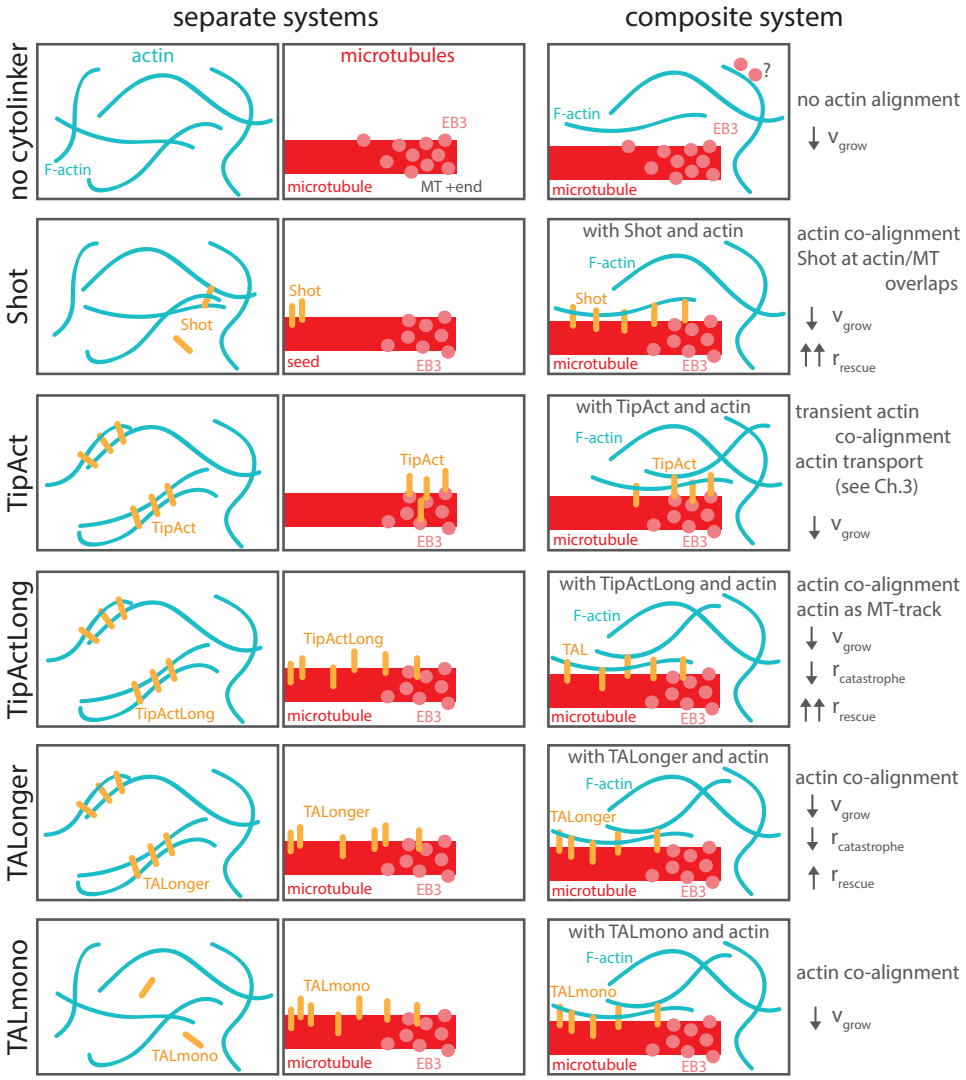

Figure 5.20: **Schematic of the influence of different cytolinkers on actin organization and MT dynamics during MT/actin crosstalk.** Indicated are the localization of cytolinkers in the separate systems, so on actin or microtubules alone (left), and in the composite system (right). The main effects on MT/actin co-organization and on microtubule dynamics are summarized on the right-hand side, where v_{grow} is the microtubule growth velocity and $r_{catastrophe}$ and r_{rescue} are the catastrophe and rescue rate, respectively. Details on microtubule dynamics can be found in Table 5.8 and Table 5.9. Actin transport by growing microtubule ends (in the presence of TipAct) is discussed in Chapter 3.

single bound linkers [212].

In cultured *Drosophila* cells, Shot is found primarily binding to microtubules and not to actin structures [213]. More specifically, in actin-rich areas, like the cell periphery, Shot is bound along the microtubule lattice, where it is actively engaged in binding actin. Our observed selectivity of Shot agrees with these observations in cells, since in our *in vitro* reconstitution assays Shot selectively binds to the MT/actin overlap regions. However, in the cell interior, an actin-low area, Shot is observed to track the growing microtubule end [213], whereas we do not observe tip-tracking behaviour of Shot in our *in vitro* reconstitution assays. While in the composite system we cannot be sure whether the localization of Shot up to the growing microtubule end is mediated by EB3 or not, since we observe similar Shot intensities for lattice and tip (Fig. 5.5), we can be sure that Shot does not tip-track in the the separated system (Fig. 5.4C). We speculate that Shot's localization to growing microtubule ends in cells might be regulated by phosphorylation, which was shown to promote actin binding in case of MACF1 [73], or unknown regulatory proteins that are recruited to the spectrin repeat domain [55]. In addition, Shot can be localized to the growing microtubule end in a complex with other tip-tracking proteins, as was already observed for APC [57].

Next, to dissect the role of the molecular anatomy of Shot, we studied the effects of engineered cytolinkers, where we controlled the protein domain composition. First, we linked actin filaments to growing microtubule ends via TipAct and found that actin filaments were dynamically re-organized around the microtubule (Fig. 5.20). While actin filaments were bundled and co-aligned to growing microtubules, those structures disappeared again after microtubule catastrophe. In addition, we observed that microtubules grown in the presence of TipAct and actin also slowed down microtubule growth, consistent with our observations of adding actin without a cytolinker. Next, we linked actin filaments to microtubule lattices via engineered cytolinker TipActLong and found multiple actin filaments that co-aligned to microtubules and formed bundles that were more long-lived than when formed via TipAct. Moreover, we found that actin filaments could serve as tracks for microtubules to grow along. In addition, we found a large increase in microtubule rescue rate, which was not observed for TipAct, while the catastrophe rate was decreased and growth slowed down, consistent with our observations of adding actin without a cytolinker.

Subsequently, we changed the spacer domain of TipActLong to investigate first the influence of increased flexibility and length between the actin- and microtubule-binding domains (TALonger), and the influence of cytolinker dimerization on MT/actin crosstalk (TALmono). For both these cytolinkers, we observed actin filament co-alignment to the microtubules, although the cytolinkers mostly localized near the MT seed and less at the dynamic microtubule ends (Fig. 5.20). In addition, we observed that actin filaments affected the microtubule growth dynamics differently in case of TALonger and TALmono compared to the other cytolinkers. Most notably, we observed a much smaller enhancement of the rescue rate in the presence of actin for TALonger (2-fold) compared to Shot and TipActLong (where the enhancement was 10-fold), and hardly any rescues at all for TALmono (Table 5.9 and Table 5.8). The relatively small effect of TALonger compared to TipActLong is likely due to the large (37-58%) percentage of monomeric TALonger. However, Shot is also monomeric (Fig. 5.21A) and still promotes rescues in the presence

of actin. We speculate on two possible explanations: (1) these difference might arise because the binding domains of Shot and TipActLong are not identical, namely from *Drosophila* and human, respectively; and (2) these results might suggest Shot-Shot interactions, where Shot can potentially form dimers or other higher-order structures when binding both actin and microtubules and auto-inhibition is released.

These results provide a framework to directly compare the effects of microtubule tip- vs lattice-binding of actin on MT/actin crosstalk. Linking actin to growing microtubule ends via TipAct results in more dynamic actin reorganization, due to the transient nature of the microtubule end and hence the transient actin-microtubule linkage. In comparison, linking actin to microtubule lattices via TipActLong results in less dynamic actin reorganization, since the microtubule lattice is motionless and only disappears upon a microtubule catastrophe, an event that occurs less often with actin linked to the microtubule lattice and also has a much higher probability of being reverted back into a growth event due to the enhanced rescue rate.

Microtubule growth is also differently affected when linking actin filaments to either the microtubule end or the lattice. Our observations indicate that linking actin to the microtubule lattice via TipActLong enables microtubule reorganization through bending growing microtubules to follow actin filaments as tracks. However, this mechanism depends on the actin filament being no longer 'free' to be remodelled by the microtubule, for example in our experiments by being attached to another microtubule. In that case, the microtubule will follow the actin organization, thus slightly bending. A previous study showed that linking growing microtubules to actin bundles via TipAct was already sufficient to deflect and bend a growing microtubule [96]. These observation indicate that polymer mechanics play a role here, with actin filaments being more flexible than microtubules. Specifically, if actin is un-bundled and free to move, the microtubule will zipper actin along its lattice, but when actin forms rigid bundles (as shown in [96]) or when actin is tensed due to attachments (as shown in Fig. 5.11B, right), the MT/actin interaction is favorable enough to zip the microtubule along the actin instead.

In addition to redirecting microtubule growth, when actin filaments are linked to the microtubule lattice via TipActLong, they also promote more persistent microtubule growth, due to a greatly increased microtubule rescue rate. How these rescues are promoted by linking actin filaments to the microtubule lattice remains an open question. Since promotion of rescues is not uncommon among microtubule associated proteins (MAPs), as was shown for MAP2 and several CLIPs and CLASPs [214–216], the involvement of actin seems to help localize (and potentially stably bind) TipActLong along the microtubule lattice. A question that arises is how many actin filaments are required for a rescue. This could be investigated more by detailed single filament assays, similar to Fig. 5.32. In addition, the linkage of actin to the microtubule lattice might induce defects, which then allows incorporation of new GTP-tubulin and results in rescues at these repaired sites [217].

Taken together, microtubule-actin crosstalk mediated by lattice-binding cytolinker TipActLong results in more long-lived actin reorganization and more persistent microtubule growth, compared to crosstalk mediated by tip-binding cytolinker TipAct. Our experiments predict that organized microtubule arrays, such as centrosomal arrays found in cells, can imprint their organization on actin more effectively with TipActLong than

with TipAct. To test this prediction, we purified centrosomes from cells and grew radial MT arrays within entangled networks of actin, as shown in Fig. 5.37. Following actin organization over time, preliminary observations show that the combined effect of more long-lived actin reorganization and more persistent microtubule growth indeed results in longer microtubules and co-aligned actin filaments further away from the central centrosome.

We speculate that more persistent microtubule growth via cytolinkers might aid microtubules to grow into dense actin networks. Examples of dense actin networks can be found in the neuronal growth cone (reviewed in [3, 8]), and the leading edge of migrating cell (reviewed in [3, 5]). Dense actin networks can in principle provide steric hindrance and prevent microtubule growth, as was shown for reconstituted Arp2/3-crosslinked actin networks [36] and dense entangled actin networks [37]. Although linking growing microtubules via cytolinkers like Shot to actin filaments could potentially strengthen the steric obstruction of microtubule growth, our study suggests the opposite. In other words, linking microtubule lattices to actin filaments could overcome steric hindrance by allowing actin remodeling and promoting persistent microtubule growth.

ACKNOWLEDGEMENTS

We would like to acknowledge Dipti Rai (Universiteit Utrecht) for help in purification of Shot, Eli van der Sluis for cloning and purification of TALonger and TALmono, and James Fawcett for design and sequencing of the TALonger and TALmono constructs and performing initial TIRF experiments. We would also like to thank Lucia Baldauf for the iSCAT measurements of the cytolinkers. Additionally, we would like to acknowledge Dieudonnée van de Willige (Universiteit Utrecht) and Cristina Martinez (AMOLF) for their help with cell imaging and STEM imaging, respectively. This work was supported by the European Research Council (Synergy grant 609822 to M.D.).

5.4. SUPPLEMENTAL INFORMATION

5.4.1. MATERIALS AND METHODS

PROTEIN PURIFICATIONS

Shot fusions were purified from HEK293 cells using Strep(II)-streptactin affinity purification, similar to Gas2L1 purification (as described in Chapter 2 and [116]). TipAct and TipActLong were expressed in E coli T7 cells and purified using a His-tag affinity column (as described in Chapter 2 and [96, 103]). For TALonger, we designed a 'Happy Linker', a peptide sequence to obtain maximal flexibility and containing 45 amino acids with 2:1 ratio of Gly:Ser (thus, 15 GGS repeats) [207]. Using PCR-based strategies and the TipActLong/pET28a plasmid as a template, we designed and cloned the new TALonger and TALmono constructs. PCR primers for amplification and insertion were designed and ordered from Eurofins Genomic (Eurofins Scientific, Brussels, Belgium). The insert fragment primers contained a 30-base pair overlap sequence at their 5' end. All PCR reactions were performed using Phusion©High-Fidelity Polymerase (NEB, Ipswitch, MA, USA), following manufacture's guidelines. The PCR products were separated by electrophoresis (7 V/cm for 75 min in 1% agarose gel that was supplemented with 0.5 µg/mL of ethidium bromide) and recovered using Qiaquick Gel Extraction of PCR Cleanup kits (Qiagen, Hilden, Germany), following manufacture's guidelines. From the purified fragments and the TAL construct, the final plasmid constructs were assembled using the Gibson Assembly©Cloning Kit (NEB). Next, 0.02 pmol of the vector fragments were incubated with their corresponding inserts at 5- or 2.5-fold molar excess of the Happy Linker and FKBP insert fragments, respectively, in 1x Gibson Assembly©master mix at 50°C for 15 minutes. Finally, TALonger and TALmono were expressed in E coli T7 cells and purified using a His-tag affinity column, similar to TipAct and TipActLong.

iSCAT MEASUREMENTS

To determine the oligomeric-state of our cytolinking proteins, we used iSCAT mass photometry to measure their mass distributions. Mass photometry uses the interference between the reflection of the illumination light on the glass-water interface and the scattered light by the proteins that bind non-specifically to the glass surface. The resulting optical contrast scales linearly with molecular mass and, together with calibration measurements of particles with known masses, allow us to determine the protein mass [218].

We used a Refeyn OneMP Mass Photometer, equipped with a 525 nm laser, to measure the interferometric scattering contrast. We obtained between 6000 and 18000 frames at 300 fps with a 10x10 µm field-of-view, choosing the number of frames such that at least 1000 particles were counted per video. Measurements were performed at room temperature (24 ± 2°C). We diluted our cytolinkers in MRB80 buffer to final concentrations ranging from 10 to 65 nM, before adding them to reusable CultureWell gaskets (Grace Biolabs, distributed by Merck, prod # GBL103250), mounted on # 1.5 coverslips. The coverslips (Corning, prod # 13296788) were first cleaned by stepwise sonication in milliQ water, 50 % isopropanol, and finally milliQ water for 5 min. We then incubated the coverslips with poly-L-lysine solution (PLL, Merck, prod # P4832) for 30 s, rinsed them with milliQ water and blow-dried them under pressurized N_2 flow, before using them within one week. To

analyse the videos and fit the mass distributions, we used the Refeyn DiscoverMP software.

ANALYSIS OF MICROTUBULE DYNAMICS

The microtubule dynamics were characterized as previously described (see Chapter 2 and [219]. In brief, growth velocities were obtained from manual fits to the growth phases, and the average velocity was taken as the average over all events weighted with the duration of the individual events. The error is the weighted standard deviation. Catastrophe rates were calculated as the number of catastrophe events divided by the total time microtubules spent growing. The error is given by the rate divided by the square-root of the number of events.

ANALYSIS OF EB COMET INTENSITIES

To measure the average of EB3's peak plus-end intensity to compare conditions with and without actin filaments present (Fig. 5.24), we first obtained the entire EB3 intensity profile from a two-pixel-wide line along the length of the microtubule. These profiles were normalized by the corresponding mean microtubule lattice intensity, which was obtained by averaging from a region at least 1 µm away from the peak.

FIXED CELL IMAGING

To measure the localization of TipAct and TipActLong in cells (Fig. 5.26), COS-7 cells were cultured in DMEM/Ham's F10 (1:1) supplemented with 10% FBS and 1% penicillin/streptomycin. Cells were diluted and plated on 18 mm glass coverslips one day before transfection with DNA constructs of GFP-TipAct or GFP-TipActLong, using FuGENE6 (Roche) following the manufacturer's protocol. After 24 hours, the COS-7 cells were first fixed with methanol (5 min at -20°C in 100% methanol supplemented with 1 mM EGTA) and immediately followed by fixation with paraformaldehyde (5 min at room temperature in 4% PFA/4% sucrose). After fixation, cells were washed twice in PBS and incubated with primary antibodies (Mouse-anti-EB1, 1:100 dilution, BD Biosciences #610535), followed by 3x 5 minute washing in PBS and incubation with secondary antibodies (goat-anti-mouse Alexa 568, in 1:400 dilution, Thermo Fischer Scientific #A11031). Samples were mounted in Vectashield mounting medium (Vectorlabs).

Fixed and stained cells were imaged on a Nikon Eclipse 80i upright widefield fluorescence microscope, equipped with a Photometrics CoolSNAP HQ2 CCD camera and Nikon NIS Br software, using a Plan Apo VC 60x N.A. 1.40 oil objective.

FRAP MEASUREMENTS

We performed fluorescence recovery after photobleaching (FRAP) measurements to obtain the unbinding rates of TipActLong from actin, microtubules, or both (Fig. 5.30). We prepared the samples as normal TIRF assays (as described in Chapter 2). The microscope was equipped with a MAG Biosystems FRAP-3D system (Photometrics, Roper Scientific), and we performed FRAP measurements at video rate (33 ms exposure time per frame). We photobleached circular (r = 1.6 µm) regions at 60% laser power, to prevent photodamage. By regularly bleaching the same region twice, we checked for photodamage and confirmed immobile fractions.

For the analysis of FRAP, we used a custom written Python script. We normalized the fluorescence intensity by background and corrected for bleaching while imaging. To fit the TipActLong recovery data to two unbinding rates, we used the following equation:

$$I(t) = A(1 - e^{-tk_{off_1}}) + B(1 - e^{-tk_{off_2}}), \tag{5.1}$$

where A and B are constants and k_{off_1} and k_{off_2} are the two different off-rates of GFP-TipActLong. We fitted every recovery curve and then averaged over the rates. Since TipActLong is dimeric, we always assumed two unbinding rates. However, when the two off-rates were within each others standard deviation range, or when the constants A and B where more than 10-fold apart, we fitted the data to a single off-rate (i.a. $B = 0$), which was only the case for microtubule-bound TipActLong.

STEM IMAGING

To measure TipActLong-mediated MT/actin bundles in more detail (Fig. 5.33), microtubules were grown from seeds in bulk together with TipActLong and pre-polymerized actin filaments in conditions similar to TIRF experiments. Electron microscopy grids were pre-treated by placing them in a humidified chamber for 36 hours before use, to reduce the hydrophobicity of the carbon layer, and improve sample adsorption. The sample was prepared by mixing 1 µL of GMPCPP seeds with 20 µM tubulin, 30 nM TipActLong and 100 nM pre-polymerized actin filaments, and incubated for 10 min at 30°C. Next, a 5 µL drop of this mix was deposited on the pre-treated EM grids, allowed to absorb for 1 min at room termperature, rinsed 5 times with milliQ water, and blotted dry.

Imaging was performed using the High-Angle Annular Dark-Field mode (HAADF) on a Verios 460 electron microscope (FEI, Hillsboro, OR, USA), similar as previously described [220]. The beam current was set to 100 pA and pixel dwell time to 3 µs, resulting in an electron dose of 400–1000 e-/nm2 with a convergence semi-angle of 2–10 mrad.

5.4.2. SUPPLEMENTAL FIGURES

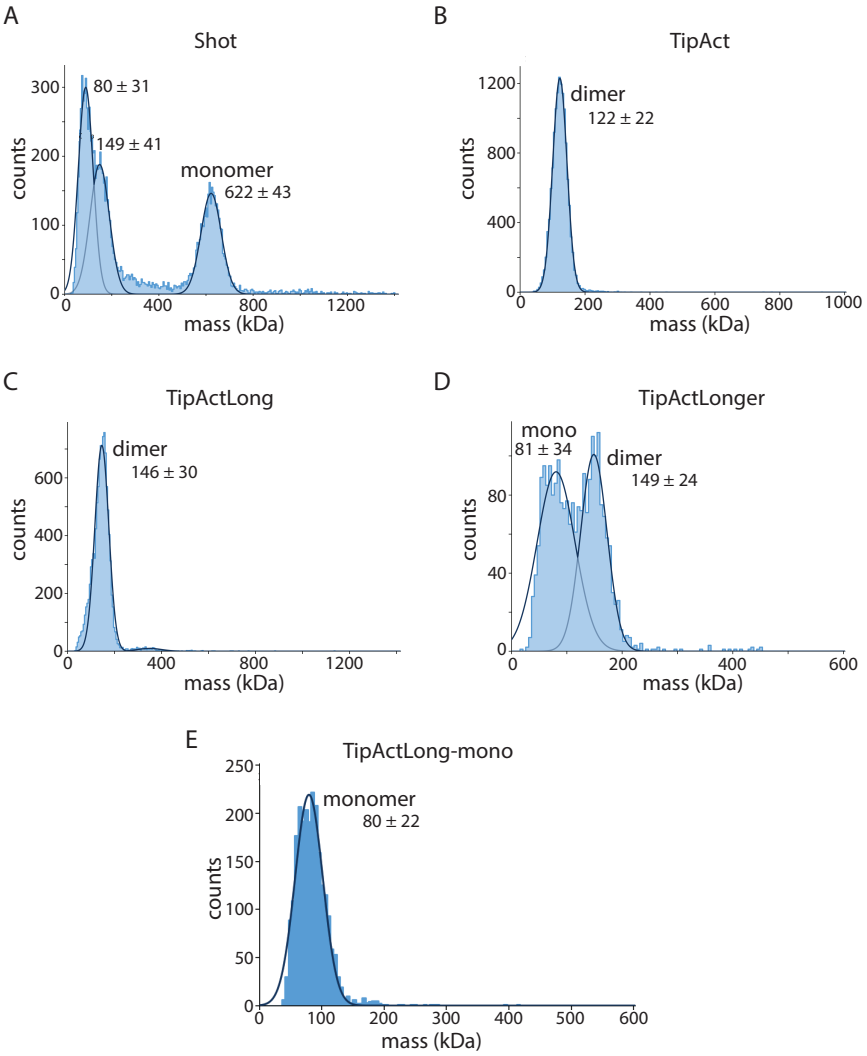

Figure 5.21: **Mass distributions from iSCAT of the cytolinkers used in this chapter. (A)** Shot (short stop). iSCAT reveals a peak around the expected monomeric mass of Shot (630 kDa) and some components with smaller masses. **(B)** Engineered cytolinker TipAct: iSCAT reveals a single peak around the expected dimeric mass of TipAct (148 kDa). **(C)** Engineered cytolinker TipActLong: iSCAT reveals a single peak around the expected dimeric mass of TipActLong (174 kDa). **(D)** Engineered cytolinker TipActLonger: iSCAT reveals two peaks around the expected monomeric (89 kDa) and dimeric mass (178 kDa) of TALonger. Based on different diffusion coefficients for monomers and dimers, thus influencing binding of the particles to the surface, we estimate that roughly 37-58% of measured TALonger particles is monomeric. **(E)** Engineered cytolinker TipActLong-mono: iSCAT reveals a single peak around the expected monomeric mass of TALmono (87 kDa). Indicated are the mean ± SD (in kDa) of the distributions.

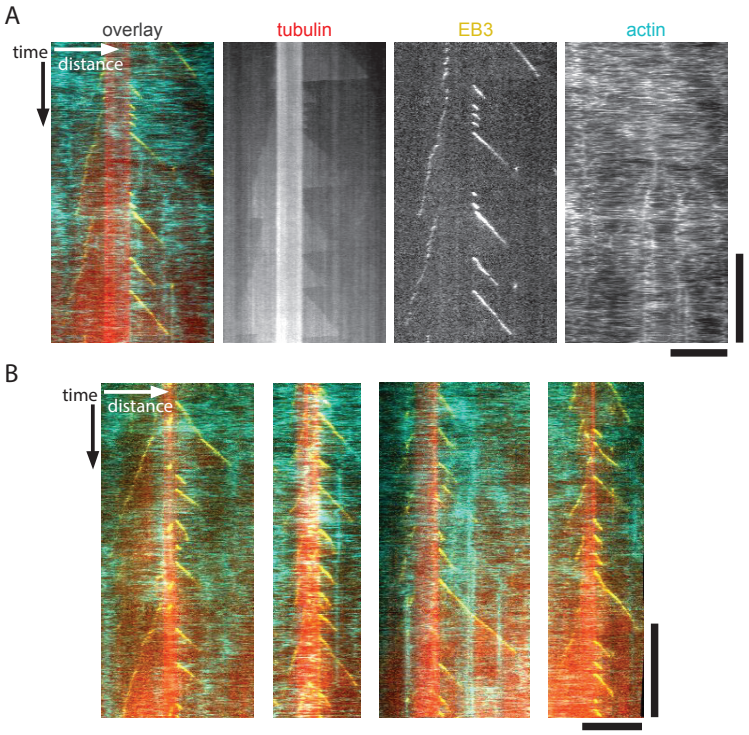

Figure 5.22: **Kymographs of microtubules growing in the presence of an entangled actin network. (A)** Growing microtubule shown in Fig. 5.2C with separated channels. Images show the overlay with microtubules in red, EB3 in yellow, and actin in cyan. **(B)** Four additional kymograph examples, only showing the overlay images. Scale bars: 5µm (horizontal) and 2 min (vertical).

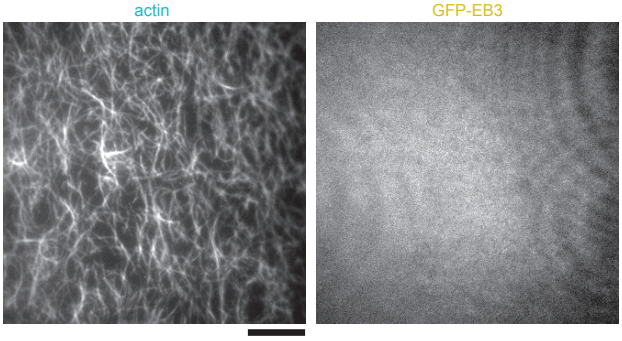

Figure 5.23: **No EB3 co-localization to actin filaments.** Typical field-of-view of an entangled actin network (left) with GFP-labelled EB3 (right) in the absence of microtubules. We do not observe EB3 localization to these actin filaments. Scale bar: 10µm.

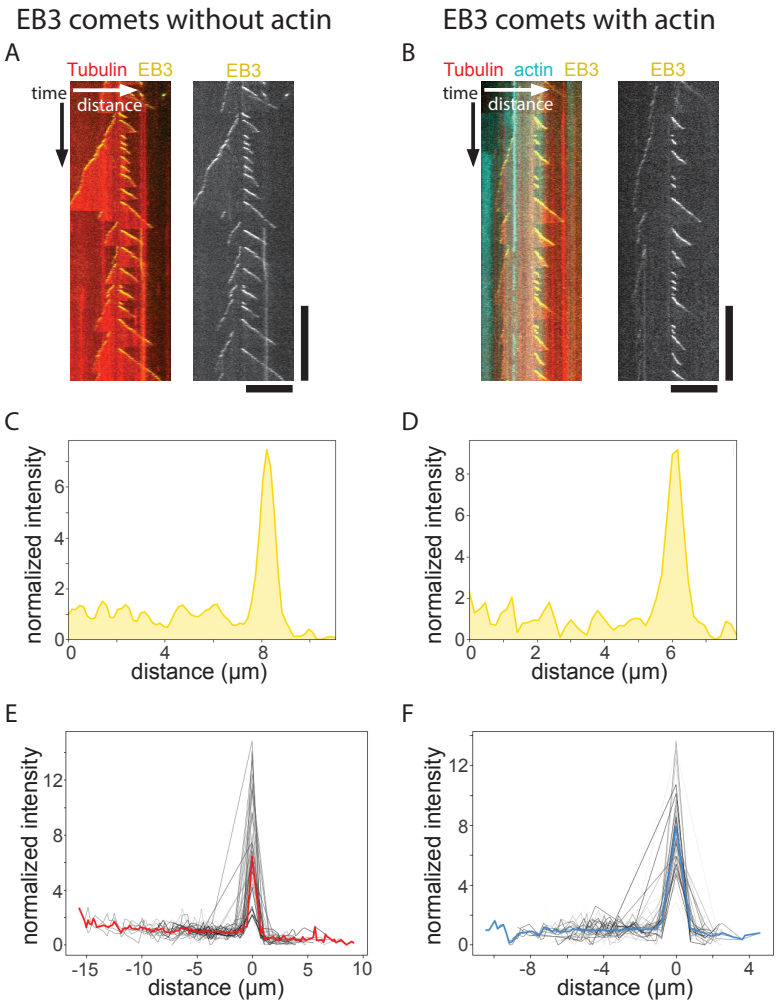

Figure 5.24: **EB comet intensities with and without actin.** **(A)** Typical kymograph showing EB3 comets in the absence of actin. Depicted on the overlay are the tubulin (red) and EB3 (yellow). **(B)** Typical kymograph showing EB3 comets in the presence of actin. Depicted on the overlay are the tubulin (red), actin (cyan) and EB3 (yellow). **(C)** Fluorescence intensity of EB3 along a microtubule in the absence of actin. A 2-pixel-wide (horizontal) line was drawn along kymographs (such as shown in A). Left of the intensity peak is the microtubule lattice, of which the average was used to normalize to 1; right of the peak is background. **(D)** Fluorescence intensity of EB3 in the presence of actin. **(E)** Fluorescence intensity of 51 EB3 line profiles, in the absence of actin, plotted together (grey). The average normalized intensity is shown in red. Peak intensity values are aligned at distance 0 μm, with the microtubule lattice at $x < 0$. The average peak intensity is 6.5±3.3 (mean±st.dev.). **(F)** Fluorescence intensity of 40 EB3 line profiles, in the presence of actin, plotted together (grey). The average normalized intensity is shown in blue. Peak intensity values are aligned at distance 0 μm. The average peak intensity is 7.9±2.6 (mean±st.dev.). Scale bars: 10 μm (horizontal) and 5 min (vertical).

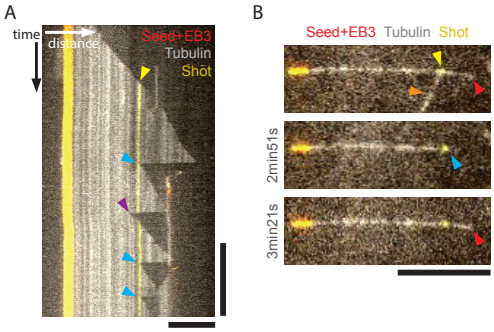

Figure 5.25: **Microtubule rescue events at Shot accumulation. (A)** Kymograph of microtubule where rescue events occurred in the absence of actin. Most rescues (blue arrowheads) occurred at an accumulation of Shot at the lattice (yellow arrowhead), except for one rescue event (purple arrowhead) which occurred nearby. Depicted is the overlay with the microtubule seed (red), EB3 (red), tubulin (grey) and Shot (yellow). **(B)** Time series of the microtubule shown in (A), where the accumulation of Shot (yellow arrowhead) is observed at the overlap with another microtubule (orange arrowhead). The growing microtubule end is indicated with red arrowheads, while the rescue event is indicated with a blue arrowhead. At other MT/MT-overlaps, we did not observe any Shot accumulation (nor rescue events), indicating this particular example does not represent a general mechanism for Shot binding to microtubules. Scale bars: 10µm (horizontal) and 5min (vertical).

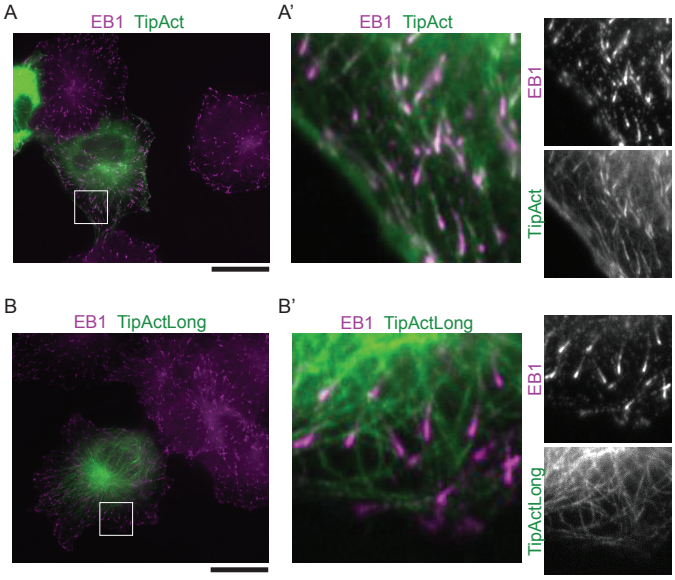

Figure 5.26: **Localization of TipAct and TipActLong in cells. (A)** Fixed COS7 cells expressing GFP-TipAct, where EB1 is visualized using antibodies. **(A')** Enlargement of white box indicated in A, showing TipAct localization to EB comets, although the localization is more extended towards the microtubule lattices compared to the shorter EB comets. **(B)** Fixed COS7 cells expressing GFP-TipActLong, where EB1 is visualized using antibodies. **(B')** Enlargement of white box indicated in B, showing TipActLong localization to microtubule lattices. Scale bars: 25µm.

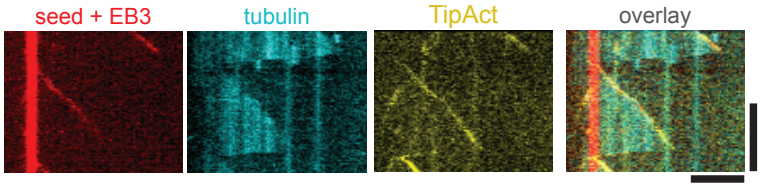

Figure 5.27: **TipAct tracks the growing microtubule tip.** Experiments performed in the absence of actin. Images show microtubule seeds and EB3 in red, tubulin in cyan, TipAct in yellow, and the merged image. Scale bars: 5µm (horizontal) and 2 min (vertical).

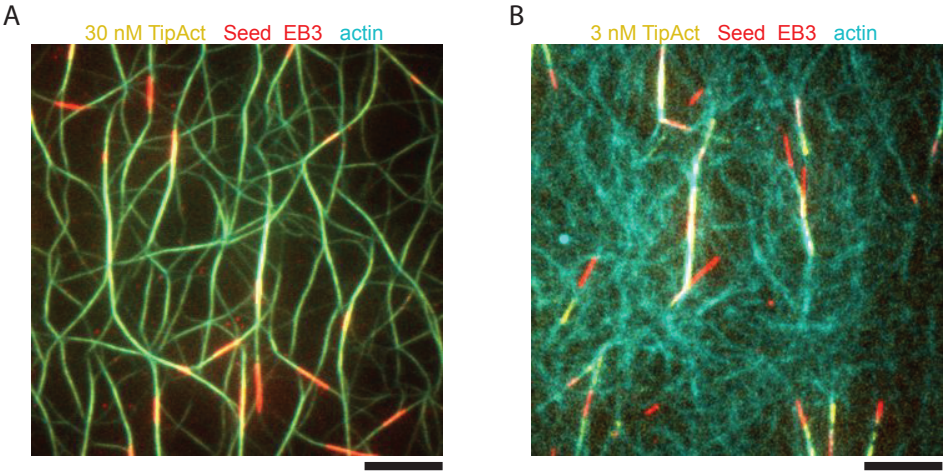

Figure 5.28: **Effect of high (30 nM) versus low (3 nM) concentration of TipAct for the crosstalk experiments. (A)** Typical field-of-view with microtubules (dark), seeds (red), EB3 (red), pre-polymerized actin (cyan) and 30 nM TipAct (yellow). Thick actin bundles with co-localizing TipAct have formed, also where no microtubules are. **(B)** Typical field-of-view with microtubules (dark), seeds (red), EB3 (red), pre-polymerized actin (cyan) and 3 nM TipAct (yellow). TipAct specifically localizes to the actin/microtubule-crosstalk regions, and hardly forms any actin bundles without any microtubules. Images taken about 12.5 min after flushing in the protein mix (containing tubulin, TipAct and actin filaments). Scale bars: 10µm.

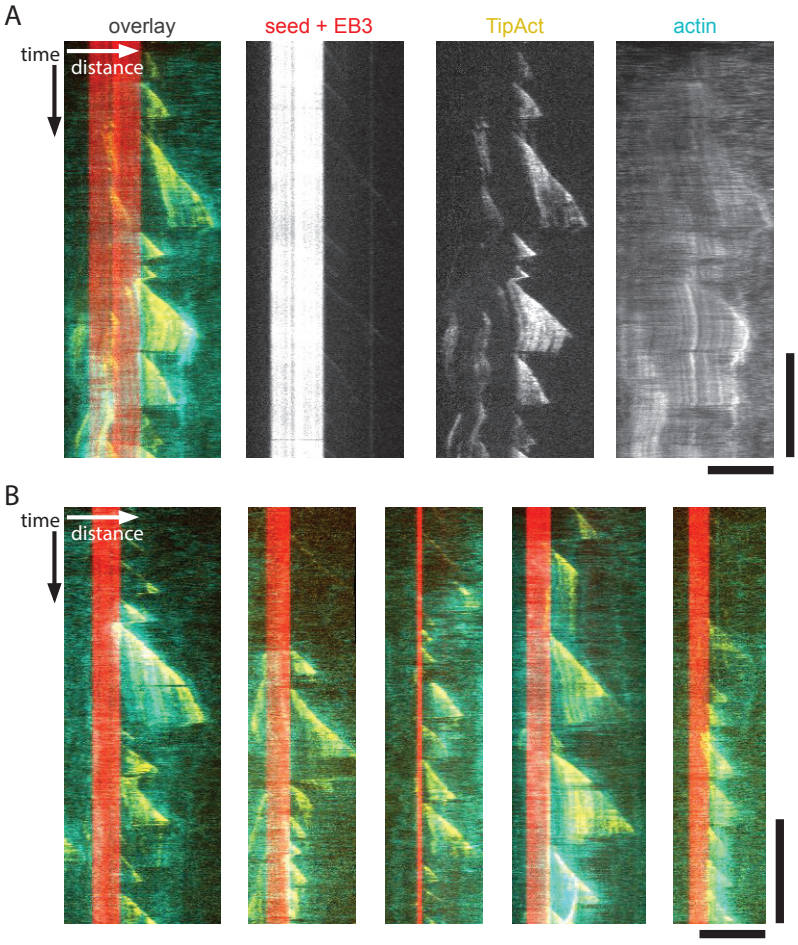

Figure 5.29: **Kymographs of MT/actin-crosstalk via TipAct. (A)** Growing microtubule shown in Fig. 5.8C with separated channels. Images show the overlay with microtubule seeds and EB3 in red, TipAct in yellow, and actin in cyan. **(B)** Five additional kymograph examples, only showing the overlay images. Scale bars: 5µm (horizontal) and 2 min (vertical).

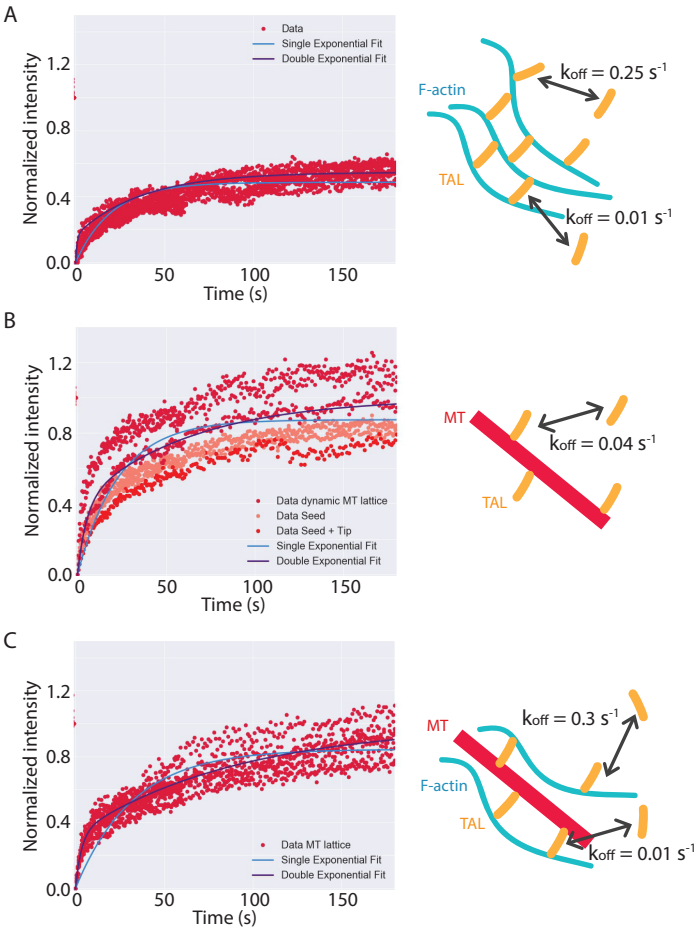

Figure 5.30: **Fluorescent recovery after photobleaching (FRAP) measurements of TipActLong binding to actin filaments, microtubules, or both. Left:** normalized intensity recovery curves. **Right:** schematic interpretation of results. **(A)** FRAP experiments of TipActLong binding to actin bundles. Double-exponential (dark blue line) was used to fit the data (red dots), resulting in a fast ($0.25\,s^{-1}$) and slow ($0.01\,s^{-1}$) component. **(B)** FRAP experiments of TipActLong binding to microtubules. Single-exponential (light blue line) was used to fit the data (red dots), resulting in an unbinding rate of ($0.04\,s^{-1}$). We distinguished the data as binding to a stable microtubule seed, to the dynamic microtubule lattice, and to a region containing partly seed and partly growing tip, depicted with different colors, as indicated. **(C)** FRAP experiments of TipActLong binding to MT/actin overlaps. Double-exponential (dark blue line) was used to fit the data (red dots), resulting in a fast ($0.3\,s^{-1}$) and slow ($0.01\,s^{-1}$) component. Red dots show the measured data, light blue curves show the fit to single exponential, dark blue curves show the fit to double exponential (Eq. 5.1). Number of fitted FRAP curves: $n = 15$, 11, and 12 for binding to actin, to the microtubule, and to the overlaps, respectively.

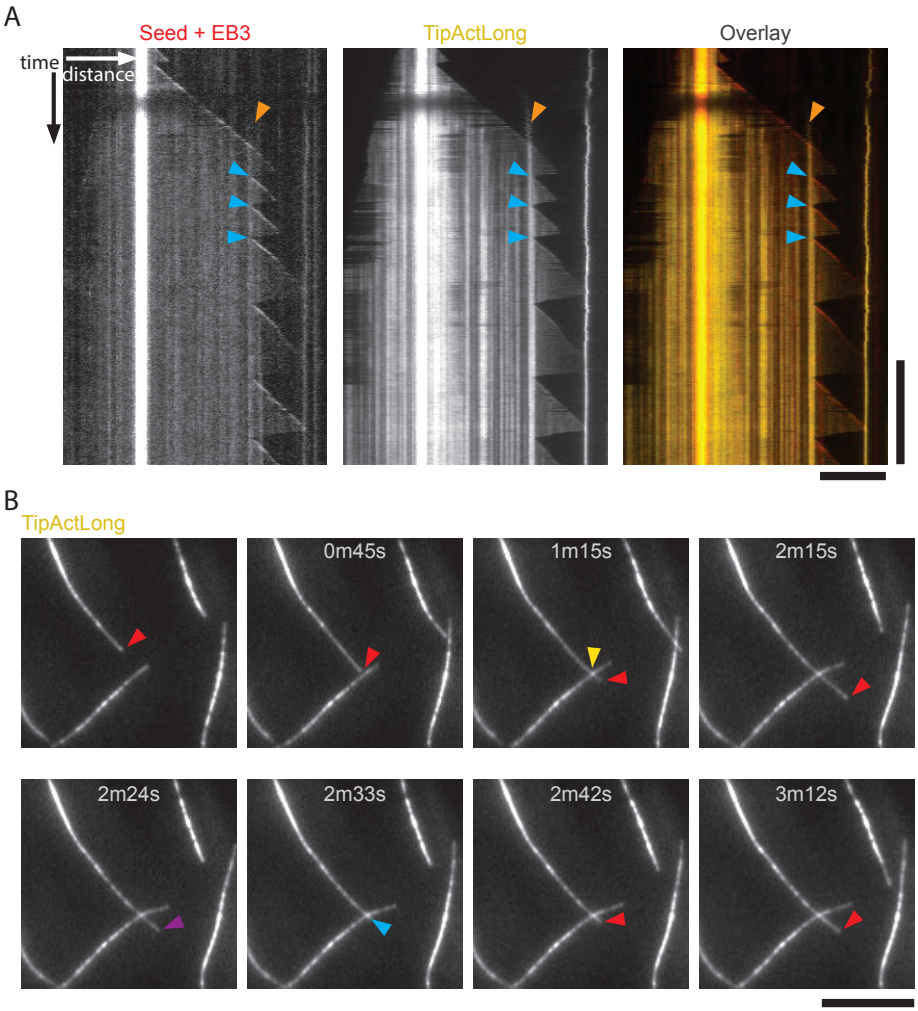

Figure 5.31: **TipActLong-induced rescues at microtubule overlaps, in the absence of actin.** **(A)** Kymograph showing multiple rescue events (first three are indicated with blue arrowheads) that occur where the microtubule overlaps with another microtubule (orange arrowhead). **(B)** Time series of the growing microtubule shown in (A), and its first rescue event. TipActLong signal is shown. The growing microtubule (end indicated with red arrowheads) crosses another microtubule, upon which more TAL localizes at the overlap (yellow arrowhead). After catastrophe, the microtubule shrinks (purple arrowhead) until it reaches the overlap region, where a rescue occurs (blue arrowhead). Scale bars: 10 µm (horizontal) and 5 min (vertical).

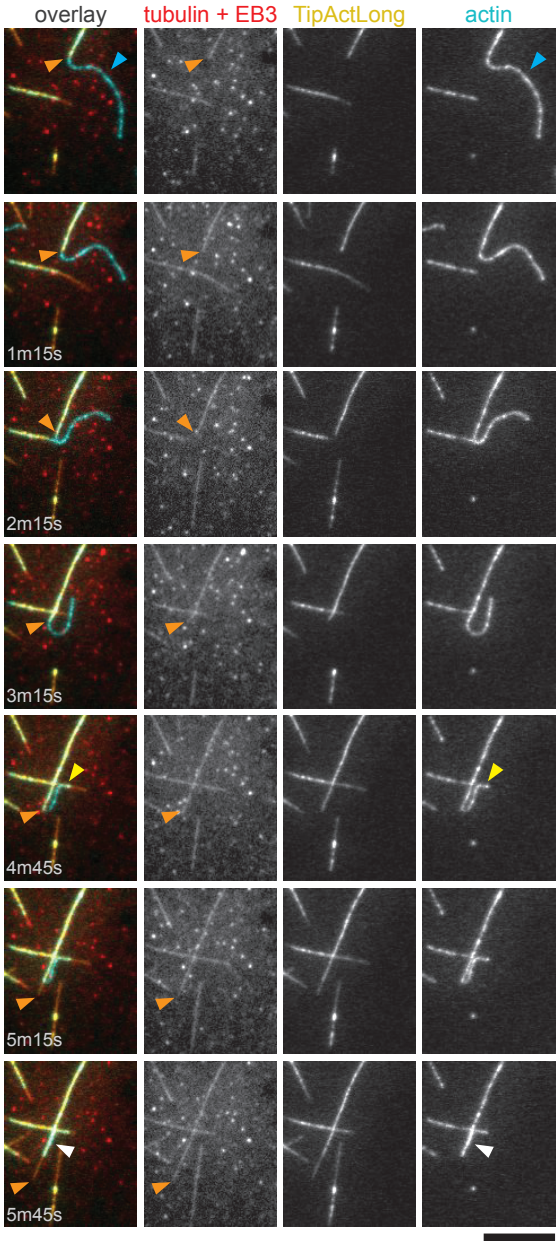

Figure 5.32: **Time series of co-alignment of a single actin filament to a growing microtubule via TipActLong.** Depicted are tubulin (red), EB3 (red), TipActLong (yellow) and actin (blue) over time, at a low actin concentration (namely 10 nM). A single actin filament (indicated by blue arrowheads) co-aligns with a growing microtubule (tip indicated by orange arrowheads), until its other end binds to another microtubule (indicated by yellow arrowheads) until it folds upon itself (indicated by white arrowheads). Scale bar: 10µm.

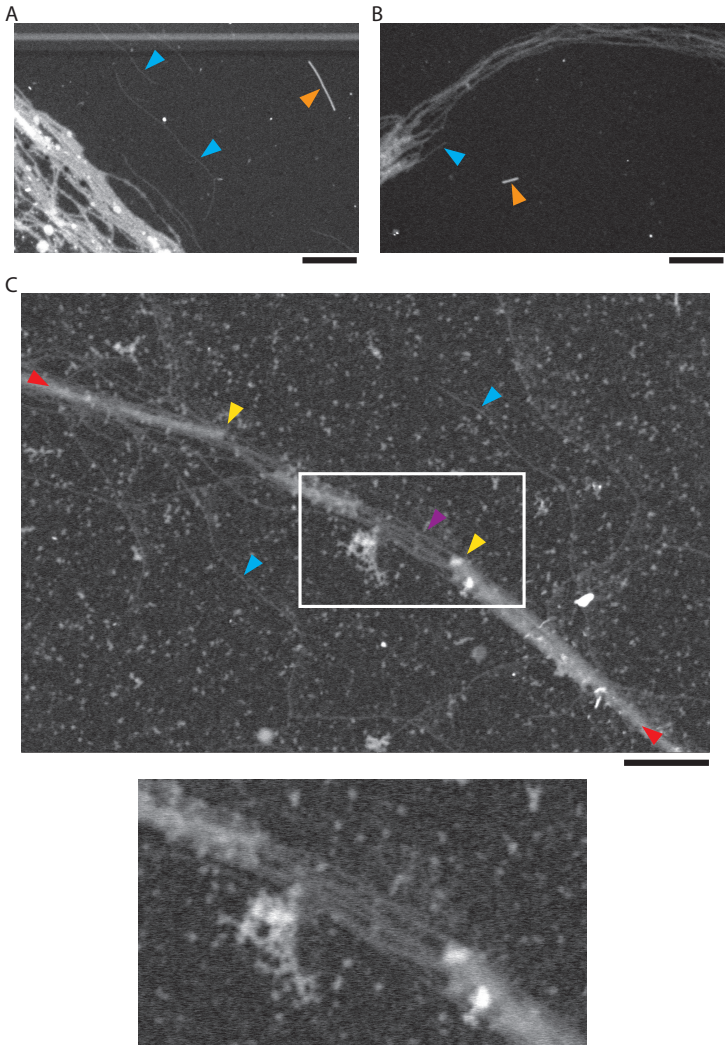

Figure 5.33: **Scanning Transmission Electron Microscopy (STEM) images of actin filaments and of actin/microtubule-crosstalk with TipActLong, operating on High-Angle Annular Dark-Field (HAADF) mode. (A)** STEM image with only pre-polymerized actin present, showing single actin filaments (blue arrowheads). Orange arrowhead indicates tobacco mosaic virus (TMV) that was used to quantify mass per unit length. **(B)** STEM image with only pre-polymerized actin present, but where filaments formed a bundle. Blue arrowhead indicates single actin filaments; orange arrowhead indicates tobacco mosaic virus (TMV). **(C)** STEM image of actin filaments crosslinked to microtubules via TipActLong. Blue arrowheads indicate single actin filaments; red arrowheads indicate overlap region of microtubule and actin; yellow arrowheads indicate the end of microtubule; purple arrowhead indicates region with only actin filaments. White box indicates area that is enlarged (below). Typical number of actin filaments associated with microtubules is around 10 filaments (from 8 observations). Scale bars: 500 nm.

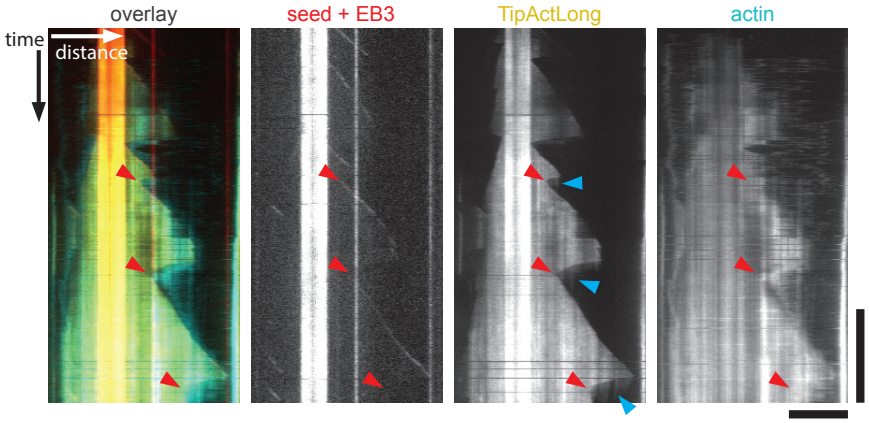

Figure 5.34: **Kymograph of MT/actin-crosstalk via TipActLong.** Growing microtubule of Fig. 5.11C, showing the overlay with microtubule seeds and EB3 in red, TipActLong in yellow, and actin in cyan, next to the separated channels. Red arrowheads indicate rescue events. Blue arrowheads show the (dimmer) smeared TipActLong localization after MT catastrophe compared to the MT/actin overlap, indicating the delayed unbinding of TipActLong from actin structures after the microtubule disappears. Scale bars: 5µm (horizontal) and 2 min (vertical).

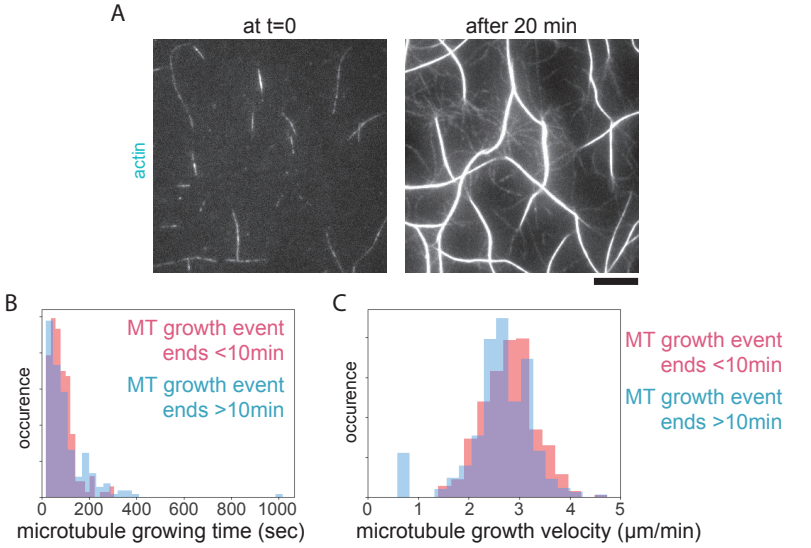

Figure 5.35: **Effect of increased actin bundling over time on microtubule dynamics in the presence of TipActLong. (A)** Over time, more actin filaments are captured, aligned and bundled along microtubules via TipActLong. These are two time points of the actin signal (corresponding to the field-of-view shown in Fig. 5.11A) at the beginning of imaging (left) and after 20 min (right). TipActLong, EB3 and MT seed signals are not shown. **(B)** Distribution of microtubule growing times, all in presence of both TipActLong and actin filaments, but distinguished between microtubules that undergo catastrophes in the first 10 min of imaging (red) or that undergo catastrophes in the second 10 min of imaging (blue). The average catastrophe frequencies are 0.72 $\pm$0.06 min^{-1} for the first half (red) and 0.32 $\pm$0.02 min^{-1} for the second half (blue). **(C)** Corresponding microtubule growth velocities (same color scheme as in B). The average growth velocities (weighed by growing time) are 2.80 $\pm$0.51 $\mu m\,min^{-1}$ for the first half (red) and 2.62 $\pm$0.67 $\mu m\,min^{-1}$ for the second half (blue). Growth velocities are weighted averages $\pm$ weighted STD; catastrophe rates are means $\pm$ SEM. Total number of analyzed growth events are 167 and 176 for the first 10 min and second 10 min, respectively. Scale bar: 10 µm

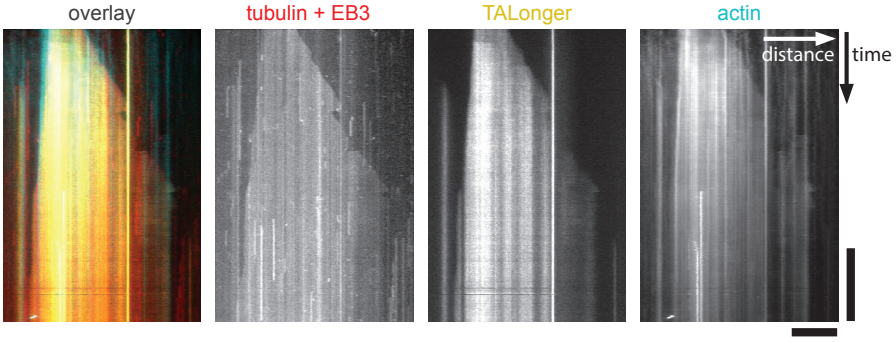

Figure 5.36: **Kymograph of MT/actin-crosstalk via TipActLonger.** Growing microtubule of Fig. 5.14C, showing the overlay with microtubule seeds and EB3 in red, TipActLong in yellow, and actin in cyan, next to the separated channels. Scale bars: 5 µm (horizontal) and 2 min (vertical).

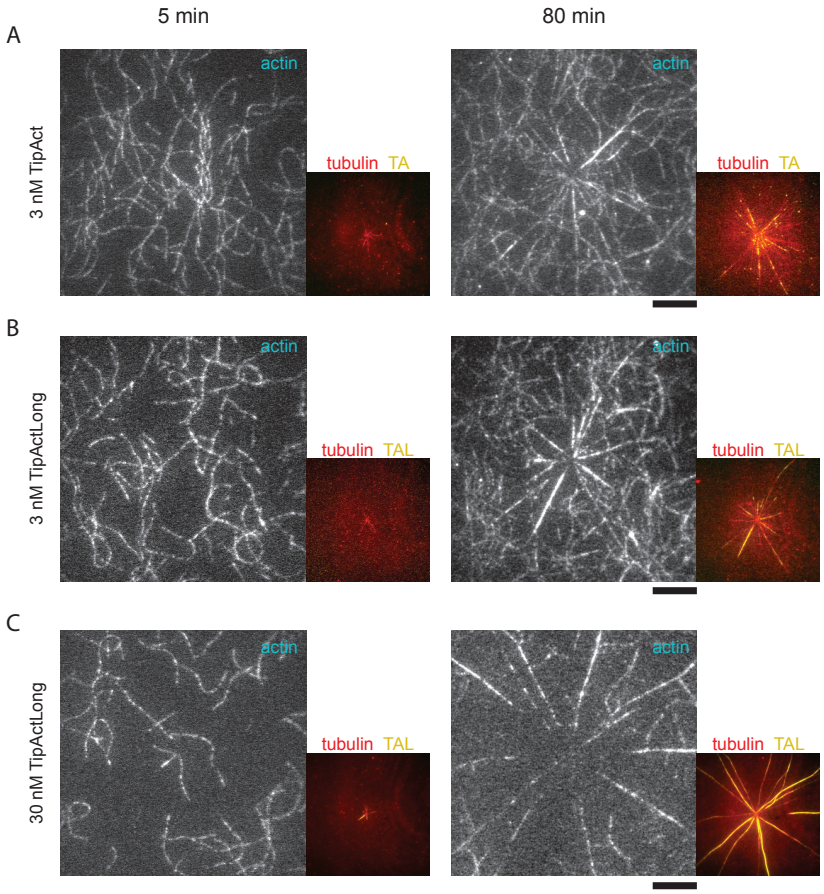

Figure 5.37: **Assay to probe microtubule-mediated actin filament reorganization in the presence of cytolinkers by a radial array of growing microtubules from a centrosome. (A)** Microtubules growing from a centrosome in a sparse actin network, in the presence of TipAct. The co-alignment of actin filaments over time is shown. **(B)** Microtubules growing from a centrosome in a sparse actin network, in the presence of TipActLong. The co-alignment of actin filaments over time is shown. **(C)** Microtubules growing from a centrosome in a sparse actin network, in the presence of 30nM TipActLong. The co-alignment of actin filaments over time is shown. Scale bars: 10µm

		growth velocity (μm/min)	catastrophe rate (/min)	EB batch used in assays with
active GFP-EB3	no actin	4.03 ± 0.60	0.98 ± 0.04	no link, TA, TAL
	with actin	3.14 ± 0.57	0.94 ± 0.04	no link, TAL
active mCh-EB3	with actin	2.92 ± 0.41	0.77 ± 0.05	no link, TA, TAL
less-active EB3	no actin	2.33 ± 0.30	0.20 ± 0.02	Shot, TALonger, TALmono

Table 5.7: **Classifying three EB3 batches used in this chapter using microtubule dynamics.** These were measured in conditions without any linkers, thus considered as controls. Indicated are in which experiments the different EB3 batches are used. The data classified as 'less-active EB3' is from the same EB3 purification batch as mCherry-EB3, but used at a much later time. Since here the microtubule growth velocity and catastrophe rate are decreased compared to earlier mCherry-EB3 experiments, which is a known effect for having lower concentrations of EB3, we decided to classify it as a different batch. GFP-EB3 are GFP-labelled EB3; mCh-EB3 ia mCherry-labelled EB3; less-active EB3 is old mCherry-labelled EB3. Growth velocities are weighted averages ± weighted STD, catastrophe rates are means ± SEM

		growth velocity (μm/min)	catastrophe rate (/min)	rescue rate (/min)	number of analyzed MT growth events
no cytolinkers	no actin	4.03 ± 0.60	0.98 ± 0.04	0.08	595
	with actin	3.14 ± 0.57	0.94 ± 0.04	0.06	710
		$2.92 \pm 0.41^*$	$0.77 \pm 0.05^*$	0.00^*	284^*
TipAct	no actin	3.53 ± 0.56	1.13 ± 0.04	0.02	950
	with actin*	$2.29 \pm 0.62^*$	$0.71 \pm 0.02^*$	0.13^*	854^*
TipActLong	no actin	2.71 ± 0.50	0.76 ± 0.06	0.33	162
	with actin	2.17 ± 0.81	0.49 ± 0.02	3.11	559

Table 5.8: **Microtubule dynamics with active EB3 proteins.** Shown are the conditions without any cytolinkers, with TipAct, and with TipActLong. In addition, for each condition, the microtubule dynamics in the absence and presence of actin are shown. * indicate conditions with mCherry-labelled EB3 proteins. Growth velocities are weighted averages ± weighted STD, catastrophe rates are means ± SEM.

		growth velocity (µm/min)	catastrophe rate (/min)	rescue rate (/min)	number of analyzed MT growth events
no cytolinkers	no actin	2.33 ± 0.30	0.20 ± 0.02	0.03	112
	with actin	-	-	-	-
Shot	no actin	2.47 ± 0.36	0.24 ± 0.03	0.45	74
	with actin	1.85 ± 0.43	0.37 ± 0.02	5.33	352
TipActLong	no actin	-	-	-	-
	with actin	2.22 ± 0.76	0.20 ± 0.02	3.56	99
TALonger	no actin	2.83 ± 0.44	0.37 ± 0.02	1.07	266
	with actin	2.27 ± 0.78	0.16 ± 0.02	2.02	94
TALmono	no actin	3.10 ± 0.41	0.20 ± 0.02	0.08	148
	with actin	2.23 ± 0.31	0.20 ± 0.01	0.23	227

Table 5.9: **Microtubule dynamics with less-active EB3 proteins.** Shown are the conditions without any cytolinkers, with natural cytolinker Shot, and with the engineered cytolinkers TipActLong, TALonger, and TALmono. In addition, for most conditions, the microtubule dynamics in the absence and presence of actin are shown. These data are classified as 'less-active EB3', because of the control experiments without cytolinkers and actin (top row). Here, the microtubule growth velocity and catastrophe rate are decreased compared to earlier control experiments (shown in Tab. 5.8), which is a known effect for having lower concentrations of EB3. Growth velocities are weighted averages ± weighted STD, catastrophe rates are means ± SEM

6

RECONSTITUTING DYNAMIC CO-ORGANIZATION OF MICROTUBULES AND ACTIN FILAMENTS IN EMULSION DROPLETS

Are we gonna give it another try?
'Cause if it's luck that's not on our side,
I'm wishing the best for the next in line.

HAIM

In vitro (or cell-free) reconstitution is a powerful tool to study the physical basis of cytoskeletal organization in eukaryotic cells. Cytoskeletal reconstitution studies have mostly been done for individual cytoskeleton systems in unconfined 3D or quasi-2D geometries, which lack complexity relative to a cellular environment. To increase the level of complexity, we presented a method to study co-organization of two cytoskeletal components, namely microtubules and actin filaments, confined in cell-sized water-in-oil emulsion droplets. We showed that centrosome-nucleated dynamic microtubules can be made to interact with actin filaments through a tip-tracking complex consisting of microtubule end-binding proteins and an actin-microtubule cytolinker. In addition to the protocols

This chapter was published as a book chapter in 'Methods in Molecular Biology' by K.J.A. Vendel, Celine Alkemade, N. Andrea, G.H. Koenderink and M. Dogterom (2020) [221]. Celine Alkemade co-wrote the book chapter with Kim Vendel. Kim Vendel optimized tip-tracking of EB3 in droplets. Celine Alkemade contributed by performing experiments which included actin and cytolinkers. Nemo Andrea optimized cytolinker behaviour in droplets.

themselves, we discussed the optimization steps required in order to build these more complex in vitro model systems of cytoskeletal interactions.

6.1. INTRODUCTION

Microtubules (MTs) and actin filaments (AFs) both play key roles in dynamic cellular processes such as cell migration, polarization and division. They are often studied independently, but it is increasingly recognized that dynamic co-organization is necessary to ensure that these processes proceed correctly [3, 222, 223]. A relatively well-studied example is cell migration, which involves interactions between dynamic plus ends of MTs with actin stress fibers and membrane-bound actin arrays at the front and rear end of the cell (Fig. 6.1A). It has been shown that AFs and MTs influence each other's organization, and that this is necessary for directional migration. The actin cytoskeleton is thought to direct MT growth towards cortical sites in the vicinity of focal adhesions. This happens by a combination of guiding growing MTs along actin stress fibers and restriction of MT growth by dense actin structures - which act as a physical barrier or sweep back MTs via actin retrograde flows [224]. MT guidance involves cytolinkers: proteins that physically link MTs and AFs [60, 96, 225]. Conversely, MTs influence the organization of AFs, for example by locally promoting actin polymerization at a growing MT tip [87] or by activating myosin contractions via Rho-GTPase pathways [29].

Cell division is another process where AFs and MTs are known to influence each other's organization (Fig. 6.1B). The actin cortex influences MT spindle positioning via interactions with MT plus ends [36, 226]. Conversely, the MT spindle provides cues to position and orient the actin-myosin ring that mediates constriction [227].

The physical mechanisms that underlie MT/actin co-organization remain poorly characterized, even though its importance has been recognized for a long time [228]. *In vitro* reconstitutions provide a powerful tool to study physical interactions of cytoskeletal components without the full complexity of cells. *In vitro* experiments have taught us a great deal about the physical properties of actin and MTs in isolation, but only a handful of studies have so far been done on the co-organization of MTs and AFs [87, 96]. These first studies were performed in unconfined environments, using 3D solutions and networks or quasi-2D surface assay geometries. It is known that physical confinement within cell-sized boundaries strongly affects the self-organization of isolated cytoskeletal components, both in case of MTs [229–232] and AFs [233–239]. Hence it is expected that confinement should influence the interaction between MTs and AFs as well. For example, a recent study using *Xenopus* egg extracts showed how different actin network architectures influence the mobility of MT asters in droplets [36].

Here, we presented a method to study dynamic co-organization of MTs and AFs in micron-scale water-in-oil emulsion droplets that mimic the physiological geometrical confinement and size of cells, as schematically shown in Fig. 6.1C. We first described the protocols to obtain dynamic MT asters nucleating from purified centrosomes encapsulated in emulsion droplets, using small adaptations to previous protocols [240–242]. We then increased the experimental complexity by adding the end-binding protein EB3, which provided the possibility to visualize and quantify MT dynamics inside cell-sized confinement. Subsequently, we described how to include AFs and establish an interaction between MTs and actin through a tip-tracking complex consisting of EB3 proteins

and cytolinkers (Fig. 6.1D). The cytolinker we use here is TipAct, an engineered protein consisting of the actin- and MT-tip-binding domains from the spectraplakin MACF (also called ACF7) that was used previously in TIRF assays (Chapters 3 and 5, and in [96]). TipAct tracks the growing MT plus tip by binding to EB3. Simple as it may sound to add extra proteins, these experiments are challenging due to the sensitivity of individual components to experimental conditions. Each new protein may need a different set of optimal experimental conditions, which can interfere with the fragile balance between the already incorporated components. Therefore, new optimization steps are required each time an extra protein is added. Here we not only provided the protocols themselves, but in addition point out which experimental 'knobs' could be tuned during optimization and what changes were needed to get each consecutive experiment working.

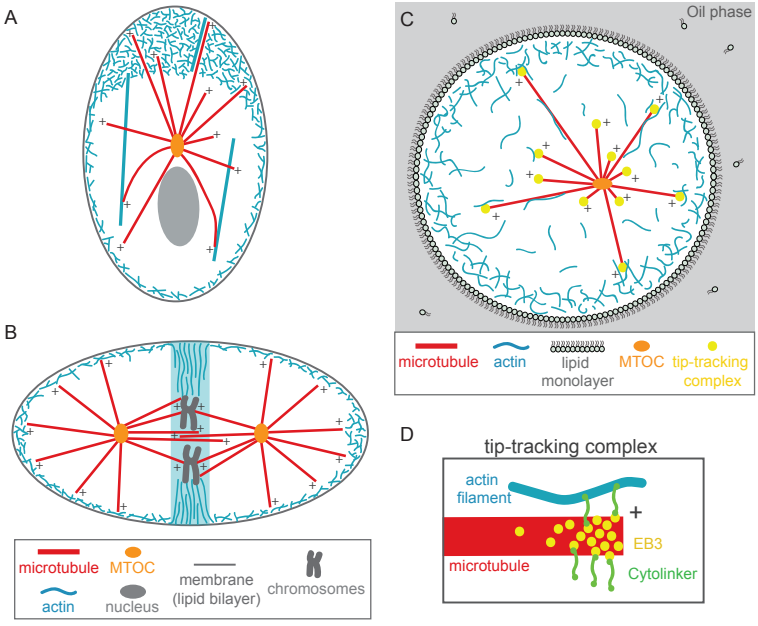

Figure 6.1: **Typical geometries and organizations of MTs and AFs in cells and in emulsion droplets. (A)** Schematic interphase cell, where MT plus ends (indicated with '+') interact with different types of actin structures. **(B)** Schematic mitotic cell, where the actin cortex positions the MT spindle and where MTs instruct the formation of the actin cytokinetic ring. **(C)** Schematic of the proposed organization of MTs and AFs in a water-in-oil emulsion droplet for *in vitro* reconstitution, mimicking the MT and AF organizations of cells. **(D)** Detailed schematic of the tip-tracking complex, consisting of end-binding proteins (EB3) and cytolinkers, that can link AFs to growing MT plus ends.

6.2. MATERIALS

6.2.1. BUFFER CONDITIONS

The buffer conditions for droplet experiments are similar to the buffer conditions used for TIRF assays (see Chapter 2). All our experiments were performed in MRB80 buffers (MRB80: 80 mM Pipes, 4 mM $MgCl_2$, 1 mM EGTA, pH 6.8 adjusted with KOH). Monomeric (G-)actin is stored and diluted in G-buffer to prevent polymerization (G-buffer: 2mM Tris, 0.2 mM Na_2ATP, 0.2 mM $CaCl_2$, 5 mM dithiothreitol (DTT), pH 7.8 adjusted with HCl).

The components of our final reaction mix are stated in Table 6.1, including the protein concentration ranges that we generally use. For the pre-polymerized AFs, we used 15 mole% labeled G-actin and added phalloidin in a 1:1 molar ratio.

component	**final concentration**	
DTT (dithiothreitol)	4	mM
catalase	0.2	mg/ml
glucose oxidase	0.4	mg/ml
D-glucose	50	mM
BSA (bovine serum albumin)	2	mg/ml
κ-casein	0.5	mg/ml
KCl	50	mM
GTP (guanosine 5'-triphosphate) sodium salt hydrate	3	mM
tubulin	20-40	µM
labeled tubulin	0.75-1.5	µM
EB3 (end binding protein, GFP-labeled)	20-150	nM
F-actin + phalloidin	10-1000	nM
cytolinker	10-50	nM
centrosomes	10	% of total volume

Table 6.1: Composition of our final reaction mix, all MRB80-buffer based.

6.2.2. PROTEINS

1. Tubulin: lyophilized porcine brain tubulin (unlabeled, or labeled with TRITC Rhodamine, HiLyte®488, or HiLyte®647) was obtained from Cytoskeleton (Denver, USA) and resuspended at 50-100 µM in MRB80, snap-frozen and stored at -80°C until use.
2. Actin: G-actin was purified from rabbit skeletal muscle powder [97] and stored in G-buffer at -80°C. Before use, G-actin was thawed at 4°C overnight, and clarified by centrifugation for 10 min at 149,000 *g*. Alexa Fluor® 647 and 594 succinimidyl esther dyes (Molecular Probes, Life Technologies) were used to produce labeled G-actin [98].
3. EB3: 6xHis-tagged recombinant human EB3, GFP-EB3 and mCherry-EB3 [24], purified from bacteria, were kind gifts from Michel Steinmetz (Laboratory of Molecular Research, Paul Scherrer Institute, Switzerland) and Anna Akhmanova (Department of Biology, Utrecht University, the Netherlands).

4. TipAct: GFP-TipAct is an engineered cytolinking protein [96], that was purified from bacteria.
5. Centrosomes: isolated from human lymphoblastic KE37 cells [101], or a kind gift from the Pierre Gönczy lab (Swiss Institute for Experimental Cancer Research (ISREC), School of Life Sciences, Swiss Federal Institute of Technology (EPFL) Lausanne, Switzerland).

6.2.3. LIPIDS, OILS AND SURFACTANTS

1. DOPS: 1,2-dioleoyl-sn-glycero-3-phospho-L-serine (sodium salt) in chloroform;
2. Mineral oil;
3. Span80 nonionic surfactant.

6.2.4. MATERIALS

1. SU-8 3025 photoresist;
2. Polydimethylsiloxane (PDMS) RVT615;
3. Rain-X rain repellent 200ml;
4. MicrewLock^{TM} microcentrifuge tubes;
5. Microfluidic MFCS pressure controller;
6. Phalloidin;
7. SiR-tubulin.

6.3. MICROTUBULE ASTERS IN EMULSION DROPLETS WITH END-BINDING PROTEIN COMETS

In this section, we explain in detail the individual steps necessary to study centrosome-nucleated MTs with EB3 comets in confinement. We confined the proteins in water-in-oil emulsion droplets. These droplets can be used as rigid containers and were generally formed by shear stress on a water phase inside an oil phase. The spherical oil-water interface was then stabilized by added surfactants (molecules with both a hydrophilic and hydrophobic part, such as phospholipids) to prevent demixing.

We start by preparing a lipid mix (Section 6.3.1) and the final reaction mix (Section 6.3.2). Next, we discuss two strategies to create water-in-oil emulsion droplets, namely via microfluidic devices and via pipetting, as well as their (dis-)advantages (Section 6.3.3). We then elaborate on the individual steps required to create droplets via the microfluidic method (Section 6.3.5). In addition, we explain the preparations for microscopic imaging, such as preparing coverslips (Section 6.3.6) and PDMS wells (Section 6.3.7). Furthermore, we discuss SiR-tubulin as an alternative method to visualize MTs with reduced background signal and hence better MT visibility (Section 6.3.8). Finally, we explain how to image these droplets for long times and analyse the data (Section 6.3.9).

6.3.1. LIPID MIX PREPARATION

The lipid mix consists of mineral oil, phospholipids and a surfactant, where the latter two form a monolayer at the interface between water and oil to stabilize the water-in-oil emulsion droplets. The procedure for making the lipid mix is as described before by Roth et al. [240] and Vleugel et al. [242].

1. Rinse glass syringes 3 times with chloroform before use;
2. Pipette chloroform-dissolved, 1,2-dioleoyl-sn-glycero-3-phospho-L-serine (DOPS) into a glass vial using a glass syringe (see Note 1);
3. Dry the lipids into a thin film on the wall of the glass vial by evaporating the chloroform in a gentle nitrogen gas flow (see Note 2);
4. Evaporate all remaining chloroform in a vacuum dessicator for about one hour (see Note 3);
5. Dissolve the lipids in mineral oil and 2.7% (v/v) Span80 to a total lipid concentration of 0.64 mg/ml (see Note 4) by sonication for 30 minutes in a bath sonicator (40 kHz);
6. Store the lipid mix at 4°C until use (see Note 5).

6.3.2. REACTION MIX PREPARATION

This reaction mix contains all components required to nucleate MT asters with protein comets in an *in vitro* environment.

1. Thaw a centrosome aliquot quickly (in your hands) and place in a 37°C water bath for about 15 minutes (see Note 6);
2. In the meantime, prepare a reaction mix on ice with concentrations as in Table 6.2 but do not add the centrosomes yet. In the end, the centrosomes should amount for 10% of the total volume;
3. Centrifuge the reaction mix 5 minutes in the AirFuge with a cold rotor at 150.000 x *g* to remove protein aggregates;
4. Transfer the reaction mix to an 0.5 ml Eppendorf tube, warm up in your hands, add to the centrosomes aliquot (see Note 7) and mix well but gently (see Note 8). Keep the reaction mix at room temperature from now on and use to prepare emulsion droplets.

Note that the reaction mix does not contain Tween20, in contrast to previously described experiments [240–242], as we found that this surfactant influenced the efficacy of functionalized phospholipids (for example with a biotin or Ni-NTA attached to the lipid head group) in addition to the DOPS lipids. The function of Tween20 was to prevent nonspecific sticking of proteins to the droplet boundary. As a result of leaving it out, we observed an increase in nonspecific cortex boundary sticking over time (see Note 9).

6.3.3. EMULSION DROPLETS

We used two different strategies to create water-in-oil emulsion droplets with the previously prepared reaction mix and lipid mix. The first is to create droplets at the T-junction

component	final concentration	
50x oxygen scavenger mix*	1	x
D-glucose	50	mM
BSA	2	mg/ml
κ-casein	0.5	mg/ml
KCl	50	mM
GTP	3	mM
tubulin	38.5	µM
rhodamine tubulin	1.5	µM
EB3-GFP	20	nM
centrosomes	10	% of total volume

Table 6.2: Composition of the reaction mix for encapsulation of MT asters with EB3-GFP comets. All components are dissolved and diluted in MRB80. *200 mM DTT, 10 mg/ml catalase, 20 mg/ml glucose oxidase.

of a microfluidic chip, see Fig. 6.2A and Section 6.3.5. The second strategy is to emulsify 0.5 µl of reaction mix into 40 µl of lipid mix by pipetting up and down 40 times with a 10 µl pipette, as schematically depicted in Fig. 6.2B (see Notes 10 and 11). Both methods have advantages and disadvantages that we will shortly discuss. Microfluidics produces uniformly sized droplets and in addition it is supposed to be a more gentle way of droplet production, which is advantageous for certain fragile proteins like tubulin or protein complexes like centrosomes. However, proteins tend to stick to PDMS walls of the microfluidic channels, leading to a decrease of protein concentration and functionality in the droplets and possibly also to a loss of centrosomes. Droplet production by pipetting produces a wider variety of droplet sizes - which can be both an advantage and a disadvantage depending on the goal of the experiment - but does not have the problem of proteins sticking to channels. Also, the droplet production is much faster, which is especially convenient for experiments that compare different experimental conditions. Finally, a much smaller volume of the reaction mix is needed to produce droplets by pipetting (0.5 µl instead of 10-15 µl for microfluidics). This allows multiple droplet batches of the same reaction mix while optimizing a single component, like actin concentration. We have been able to perform the experiments described in this chapter with both strategies for droplet production, yet the results shown in the figures were obtained in droplets prepared by pipetting unless stated otherwise.

6.3.4. MICROFLUIDIC CHIPS

The procedure for microfluidic chip preparation is exactly as described in previous methods papers [240–242], but for completeness we will repeat the steps. First, an SU-8 mold is prepared in the cleanroom (step 1 to 5). With this reusable mold, microfluidic PDMS chips can be prepared (step 6 to 13).

1. Design a photomask with three inlets as in [240] (see Note 12);
2. Order a low-cost flexible photomask with the desired design at Selba S.A. with a negative polarity, i.e. a dark photomask with transparent structures (see Note 13);
3. The mold is then produced in the cleanroom according to standard photolithogra-

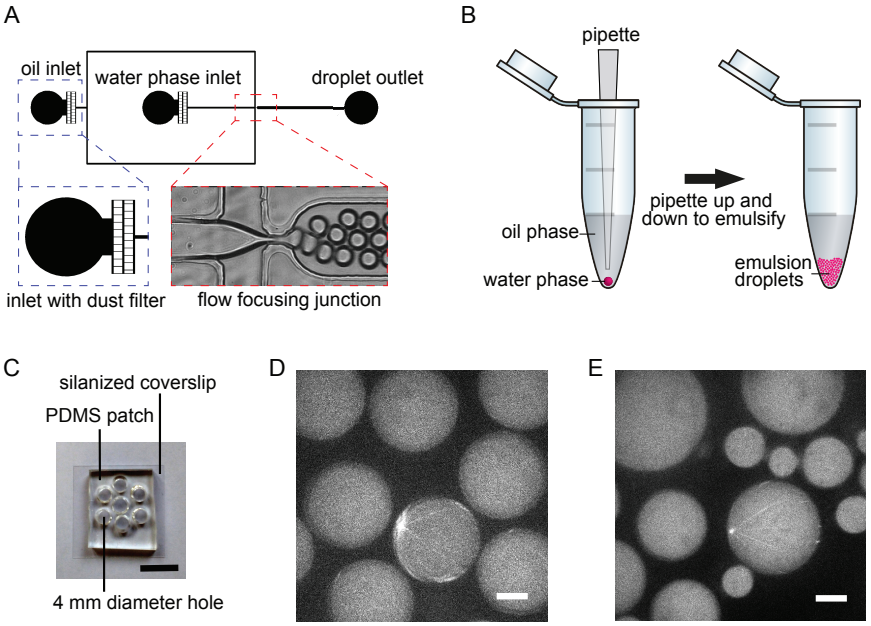

Figure 6.2: **Production of water-in-oil emulsion droplets.** Water-in-oil emulsion droplets were produced in two ways, as schematically visualized in (A) and (B). **(A)** Microfluidic chip for emulsion droplet production with one inlet for the oil phase and one for the water phase, which come together at a flow focusing T-junction where droplets are pinched off. Dust filters at the inlets prevent (PDMS) particles from entering the channels and blocking the T-junction. **(B)** Another method for emulsion droplet formation involves pipetting the oil phase and water phase up and down to generate the shear stress that leads to droplet formation. **(C)** For long-term imaging, droplets are transferred into a PDMS well consisting of a PDMS patch with holes on a silanized coverslip. **(D)** and **(E)** are typical fields of view observed when imaging emulsion droplets containing centrosomes and fluorescent rhodamine-tubulin (see Table 6.2) with a confocal spinning disc fluorescence microscope, for droplets produced with microfluidics (D) or by pipetting (E). Scale bars: 10 mm for C, and 10 µm for D and E.

phy protocols. Follow the SU-8 manufacturer's instructions for exact times, spinning velocities, temperatures, etc. (see Note 14) (see Note 15). Spincoat the SU-8 photoresist onto a 4 inch silicon wafer and perform a soft bake at 95°C;

4. Expose to UV light through the photomask (see Note 16) and bake again at 95°C;
5. Develop with the manufacturer's developer for the SU-8 type you used (again follow the manufacturer's instructions on time). Rinse the wafer first with acetone to remove the developer (see Note 17) and subsequently with isopropanol to remove the acetone. Dry in nitrogen flow and perform a final hard bake at 150°C to make the structures more robust.
6. To prepare PDMS chips from these SU-8 molds, mix PDMS pre-polymer with the PDMS curing agent in a volume ratio of 9 to 1 (see Note 18), prepare 40 ml PDMS per SU-8 mold;
7. Centrifuge for 3 minutes in a 50 ml falcon tube at 300 rcf to remove large air bub-

bles;

8. Create a cup of aluminum foil around each 4 inch silicon wafer so the wafer is the bottom of the cup and the sides of aluminum foil are at least 2 cm high (see Note 19);
9. Pour the PDMS into the cup to get a 5 mm thick layer of PDMS on top of the wafer, place in a vacuum dessicator for approximately 1 hour to remove remaining air bubbles (see Note 20) and afterwards cure for 30 minutes at 100°C;
10. In the meantime, spincoat the leftover PDMS onto glass slides (5 sec at 200 rpm followed by 30 sec at 4,000 rpm) and cure for at least 1 hour at 100°C;
11. Carefully remove the PDMS from the mold, cut out the areas of the chips (one wafer usually contains structures for four microfluidic chips) and punch 0.75 mm inlet and outlet holes (see Note 21);
12. Apply an oxygen plasma to the PDMS surfaces of glass slide and PDMS chip with a corona discharger for a few seconds. Immediately place the PDMS chip onto the glass slide and bake at 100°C for at least 1 hour to bond the surfaces together;
13. Store in a dust-free place until use (for a few months to a year).

6.3.5. MICROFLUIDIC SETUP

The flow for the droplet formation is controlled by an MFCS^{TM} pressure controller connected to a Fluiwell accessory. The microfluidic chip, and specifically droplet production at the T-junction (see Fig. 6.2A), were monitored with an inverted bright-field microscope with a 10x magnification air objective.

1. Put water phase and oil phase mixtures into two MicrewLock tubes suitable for the Fluiwell assessory and connect the polyether ether ketone (PEEK) tubing to the microfluidic chip inlets (see Note 22);
2. Adjust the pressure such that first all channels of the microfluidic chip are filled with oil phase;
3. Introduce the water phase and tune the pressures to obtain a stable production of droplets with the desired diameter at the T-junction (see Note 23);
4. Wait until a few microliters of droplets have emerged at the outlet (see Fig. 6.2A), harvest 1.5 µl using a pipette with cut-off tip, mix with 8.5 µl lipid mix (see Note 24) and transfer to the PDMS well (Section 6.3.7);
5. Clean the tubing with isopropanol after use. It is also possible to rinse the microfluidic chip with isopropanol and store it until the next use. In that case, always check at the microscope if the channels of the chip are not clogged before using it the next time.

6.3.6. COVERSLIP SILANIZATION WITH RAIN-X

Emulsion droplets must be placed onto a coverslip for imaging with the confocal spinning disc fluorescence microscope. In principle coverslips are hydrophilic, often resulting in a collapse of the aqueous interior of the droplets onto the coverslip. Coverslips

were made hydrophobic to prevent this, for example by spincoating a thin layer of polydimethylsiloxane (PDMS) or by silanization. The advantage of silanization compared to a layer of PDMS is that the imaging quality is much better because the light is not refracted and diffused by the non-transparent PDMS. One can silanize glass in various ways, and we used Rain-X [231] as it contains less harmful chemicals than other silanization solutions and can be purchased at the local car shop.

1. Place 24 x 24 mm^2 coverslips in a holder, bath sonicate the coverslips in ethanol for 20 minutes and dry in nitrogen air flow;
2. Immerse the coverslips in Rain-X for 5 minutes; (see Note 25) and leave to dry in air (see Note 26);
3. Store between paper tissues until use (see Note 27).

6.3.7. PDMS WELL PREPARATION

To immobilize the droplets during imaging over longer time periods, a PDMS well is placed onto the Rain-X silanized coverslips (see Fig. 6.2C) to hold the emulsion droplet mix [242]. In general, one can use the PDMS that is left over after cutting out the required areas for microfluidic chips (Section 6.3.4). If emulsion droplets are produced with the pipetting method instead of microfluidics, first follow steps 6 to 9 from the microfluidic chips protocol in Section 6.3.4 with a 4 inch silicon wafer (whether it has structures or not does not matter, we just need a smooth hydrophobic surface to prepare a PDMS slab).

1. Cut the 5 mm thick PDMS slab into 2 x 2 cm^2 squares;
2. Punch 5 mm diameter holes in each square (see Note 28) and store them in a dust free box;
3. Before use: press a PDMS square onto a Rain-X-coated coverslip with the smooth side (the side that was in contact with the silicon wafer) facing the coverslip;
4. After use: discard the Rain-X coverslip and carefully rinse the PDMS well with isopropanol to clean it for the next use. You can keep cleaning and re-using PDMS wells for years until they break or get lost.

6.3.8. RHODAMINE TUBULIN VERSUS SIR-TUBULIN

Multiple options exist to visualize MTs. The conventional method is to add fluorescently labeled tubulin to the reaction mix as is shown in Table 6.2. Another option is to employ SiR-tubulin, a label based on a far-red fluorophore (silicon rhodamine (SiR)) and the MT binding drug docetaxel [243]. The main advantage of SiR-tubulin is that its fluorescence intensity increases tenfold when bound to a MT compared to being in solution. As a result, the background intensity is lower and the visibility of the MTs is much better than in case of conventional fluorescent probes like rhodamine (compare Fig. 6.3A left and right). A disadvantage of SiR-tubulin is that, due to the docetaxol, it can have a stabilizing effect on the MTs (see Note 29).

To use SiR-tubulin instead of rhodamine tubulin, follow the following procedure (see Note 30):

1. Dissolve SiR-tubulin in dimethyl sulfoxide (DMSO) to a concentration of 500 µM and store at -20°C (see Note 31);
2. Mix this solution in the lipid mix (see Note 32) to a final SiR-tubulin concentration of 1 µM (see Note 33);
3. Use the lipid mix containing SiR-tubulin to prepare emulsion droplets as described in Section 6.3.3 (see Note 34).

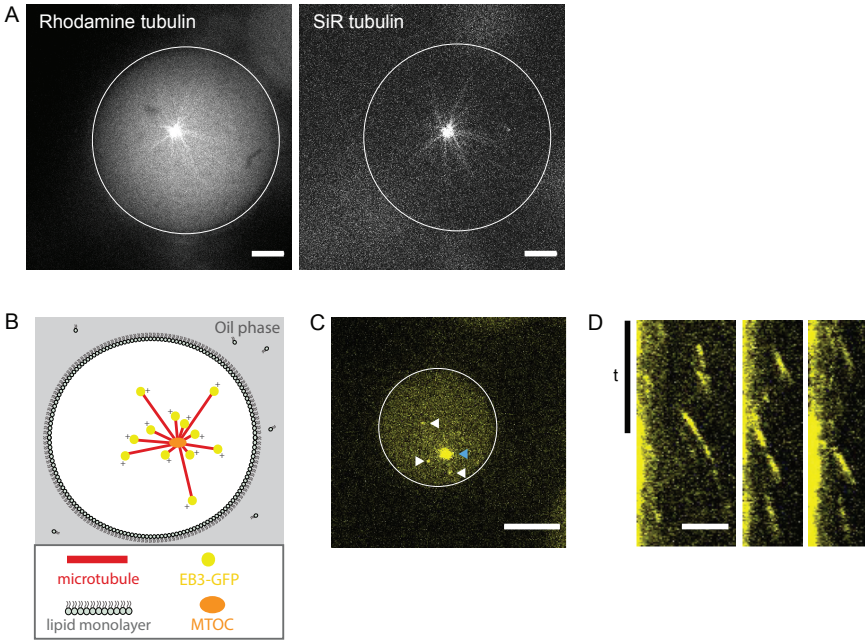

Figure 6.3: **Imaging dynamic MTs inside water-in-oil emulsion droplets.** **(A)** Water-in-oil emulsion droplet containing both rhodamine tubulin (left) and SiR tubulin (right), showing a reduced background and increased visibility of the MT aster inside the droplet for SiR tubulin compared to rhodamine tubulin. **(B)** Schematic of a MT aster containing end-binding (EB) proteins in an emulsion droplet. **(C)** EB3-GFP (yellow) protein comets (indicated with the white arrows) at the tips of MTs (not shown in this image), emerging from a MT aster inside an emulsion droplet. EB3 has an affinity to the centrosome as well, as we can see by the bright yellow signal in the center of the MT aster (blue arrow). **(D)** Tracking these EB3-GFP protein comets in time results in kymographs, showing the typical tip-tracking behaviour of EB3 proteins. White circles indicate droplet edge. Scale bars: 10 µm for A and B, and 2 min (vertical) and 5 µm (horizontal) for C.

6.3.9. IMAGING AND DATA ANALYSIS

Transfer 10 µl of emulsion droplets, either prepared by microfluidics (Fig. 6.2A) or by pipetting (Fig. 6.2B), into the PDMS well (Fig. 6.2C). We imaged with a Spinning Disc confocal fluorescence microscope with a Nikon CFI Plan Apo Lambda 100X oil immersion lens (NA 1.45, working distance 0.13 mm). A custom-made temperature control system with a heating ring around the objective lens established a sample temperature of 30°C (see Note 35), which is required for MTs to polymerize inside emulsion droplets at these

tubulin concentrations (20-40 µM). Typical fields of view of an experiment with droplets prepared by microfluidics or by pipetting are shown in Fig. 6.2D and E, respectively (see Note 36). Depending on the yield of the centrosome purification, a certain percentage of droplets contains a MT aster (see Note 37).

Previous studies on emulsion droplets have for example followed MT aster positioning over time, with or without additional MT-associated proteins [229, 240, 242], or MT organization in the presence of crosslinking motors [231, 232]. In those situations, one snapshot every few minutes suffices to track the aster position or MT organization. However, if the objective is to study MT dynamics by tracking end-binding protein comets at the growing MT tips, as is schematically depicted in Fig. 6.3B, we needed to make timelapses with much smaller timesteps, in the order of one per second. To establish this while keeping the signal-to-noise ratio high enough to visualize the protein comets, as is shown in Fig. 6.3C, we increased laser power and used exposure times of 300-500 ms (see Note 38). An important parameter for MT dynamics is the MT growth velocity. This can be extracted from the timelapses by making kymographs as depicted in Fig. 6.3D, and calculating the slope of the protein comet trace.

6.4. INCREASING COMPLEXITY: ADDING CYTOLINKERS AND ACTIN FILAMENTS

We made this experimental assay more complex by adding pre-polymerized actin filaments (AFs), as is schematically shown in Fig. 6.4A (see Note 39). From these experiments, as is shown in Fig. 6.4B, we could study co-organization resulting from steric interactions between MTs and AFs. In addition, we could physically link AFs to MTs by adding a cytolinker, as is schematically shown in Fig. 6.4C. We observed that AFs co-align with growing MTs (indicated with a blue arrow in Fig. 6.4D), and that single AFs could be transported by a tip-tracking complex at growing MT ends, as is shown in the kymograph of Fig. 6.4E.

To prepare these assays, one can follow the previously described methods with some adaptations. In this section, we discuss the main differences: an additional preparation step for the polymerization of AFs (Section 6.4.1) and their addition to the final reaction mix (Section 6.4.2). Furthermore, we discuss the challenges related to imaging the contents of these droplets (Section 6.4.3).

6.4.1. ACTIN MIX

Here, we describe how to prepare pre-polymerized AFs that can be added to the final reaction mix. It is also possible to replace the F-actin mix by a mixture of monomeric (G-)actin, so that AFs will polymerize within confinement, as described earlier [244], but this will not be described here (see Note 40).

1. Dilute your stock G-actin in G-buffer and pre-mix labeled and unlabeled G-actin (see Note 41) in the preferred ratios (see Note 42);

2. To start polymerization, add MRB80 buffer and the other components of the F-actin mix, except for phalloidin, as described in Table 6.3 (see Note 43);

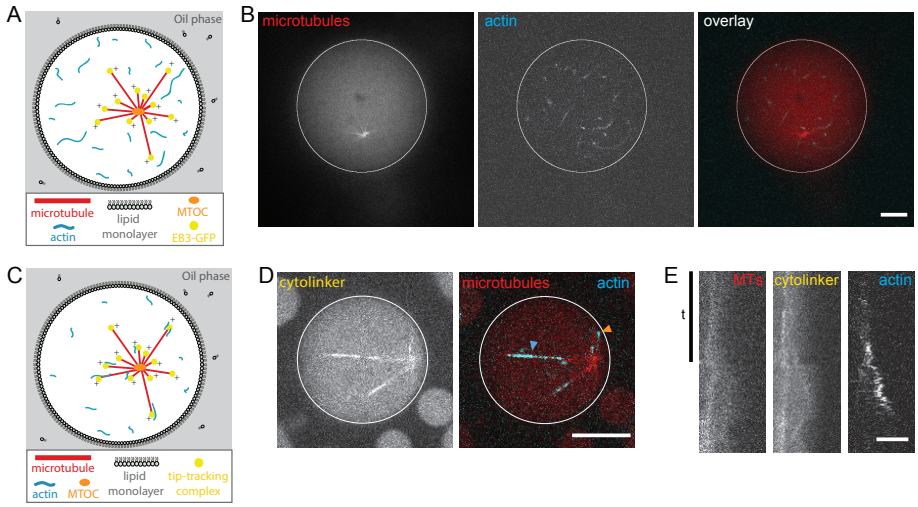

Figure 6.4: **Co-organization of MTs and AFs in droplets.** **(A)** Schematic of an emulsion droplet containing a MT aster, end-binding (EB) proteins, and filamentous actin. **(B)** Dynamic MTs with EB-comets (not shown in this image) in droplets together with pre-polymerized AFs. **(C)** Schematic of MT/actin co-organization in an emulsion droplet with a cytolinker present. **(D)** Co-alignment of AFs to MTs (right) when a cytolinker (left) is added, indicated by blue arrow. **(E)** Kymograph to show a short event of actin transport by the growing MT plus end via the cytolinker. White circles indicating droplet edge; orange arrow (in D) indicates the AF that is shown in E. Scale bars: 10 µm for B and D, and 2 min (vertical) and 5 µm (horizontal) for E.

3. After about 30 min, add phalloidin to stabilize the polymerized F-actin (see Note 44). Now, the F-actin mix is ready for use. It can be stored at room temperature for about one day.

component	final concentration in F-actin mix	
unlabeled actin	6.38	µM
labeled actin	1.125	µM
DTT	6.8	µM
KCl	50	mM
Mg-ATP	0.2	mM
Phalloidin	1	µM

Table 6.3: Composition of the reaction mix for pre-polymerizing AFs. This mix is based on MRB80 buffer.

6.4.2. FINAL REACTION MIX

The preparation of the final reaction mix is very similar to the one described before (in Section 6.3.2), except for the addition of AFs and a cytolinker.

1. Prepare the reaction mix as described in Table 6.4, but without the centrosomes and the F-actin mix;
2. As described in Section 6.3.2, centrifuge this final reaction mix for 5 minutes in the AirFuge at 150.000 x *g* using a cold rotor to remove protein aggregates;
3. Next, transfer this reaction mix to an 0.5 mL Eppendorf tube and warm up in your hands, before adding to the centrosomes aliquot;
4. Finally, add the desired amount of F-actin mix, and mix well but gently to not break the centrosomes and the AFs (see Note 45);
5. From this final reaction mix, emulsion droplets can be created using either the microfluidic or pipetting method, as discussed in Section 3.1.3 (see Note 46).

component	**final reaction mix concentration**	
50x oxygen scavenger mix*	1	x
D-glucose	50	mM
BSA	2	mg/ml
κ-casein	0.5	mg/ml
KCl	50	mM
GTP	3	mM
tubulin	38.5	µM
rhodamine tubulin	1.5	µM
EB3	150	nM
cytolinker	20	nM
F-actin mix	1	µM
centrosomes	10	% of total volume

Table 6.4: Composition of the final reaction mix for reconstituting co-organization of MTs and AFs in droplets. This mix is based on MRB80 buffer. *200 mM DTT, 10 mg/ml catalase, 20 mg/ml glucose oxidase.

6.4.3. IMAGING

To image the dynamic co-organization of MTs and AFs in emulsion droplets there are a few challenges. Firstly, compared to imaging MT asters with EB3-GFP comets, the system has become more complex with more components to consider for imaging. To visualize proteins inside 3D emulsion droplets, the brightness of the fluorescent probe is more important than for quasi-2D experiments on a glass surface, where TIRF microscopy results in good contrast. For confocal Spinning Disc imaging of emulsion droplets, the background intensity is much higher as a result of the larger depth of focus than for TIRF microscopy. Besides, light is refracted by the spherical water-oil interface, which induces aberrations that further decrease the image quality. Hence it is

necessary to think carefully about which fluorescent probe to put on which protein. As GFP is the brightest probe we have available, we labeled the protein of interest with GFP. Depending on the goal of the experiment this is either EB3 or the cytolinker. For the MTs, Rhodamine tubulin worked in our hands the best out of the commercially available fluorescently labeled tubulins to visualize MTs in droplets (see Note 47). Due to the limited amount of available wavelenghts on our microscope, this left 647 nm as the imaging wavelength for actin. Otherwise, when using SiR tubulin (visible with 647 nm), actin must be labeled with a 561 nm fluorescent probe.

Secondly, the increase of complexity also comes with an increase of colors to visualize per experiment. Especially when you are interested in relatively fast processes (on the timescale of seconds), the switching between different wavelengths can slow down the acquisition. Therefore, one could consider imaging two wavelengths simultaneously, for example by using dual-imaging on one camera, or using multiple cameras. But as dual-imaging comes at the expense of the intensity of the two wavelengths signals, this can only be used in case of sufficiently high intensities.

Thirdly, another factor to take into account for visualization is the mobility of AFs. As they are more flexible than MTs and not part of a large network or structure (like the MT aster), their diffusion constant is larger. If they move too fast, they are difficult to image. Shorter exposure times and higher laser power are needed to get an image like in Fig. 6.4B, which can lead to increased photo-bleaching as a side effect. When AFs and MTs interacted and became co-organized, the AFs diffused less and are easier to visualize (Fig. 6.4D).

Besides these previously mentioned factors to take into account for optimization of the experiments, there are some additional 'knobs' for fine tuning of experimental conditions, like protein concentrations (see Note 48), salt concentrations (see Note 49), the ratio of AFs to cytolinkers (see Note 50), the density of AFs (see Note 51) and concentrations of surfactants and excipients (see Note 52). These experimental conditions can for instance affect the type of predominant interactions inside the droplet (e.g. MT tip vs MT lattice interactions), and hence the MT-actin co-organization.

ACKNOWLEDGEMENTS

We are grateful to Marjolein Vinkenoog for actin purification and Andrea Martorana for TipAct purification. We thank Sophie Roth, Florian Hüber, Mathijs Vleugel, Anne Doerr and Esengül Yildirim for centrosome purification. We also thank the Pierre Gönczy lab (Swiss Institute for Experimental Cancer Research (ISREC), School of Life Sciences, Swiss Federal Institute of Technology (EPFL) Lausanne, Switzerland) for the kind gift of centrosomes. This work was supported by the European Research Council (Synergy grant 609822 to M.D.) and the Netherlands Organization for Scientific Research (FOM program nr. 151 to M.D.).

6.5. SUPPLEMENTAL NOTES

1 Always use glass objects instead of plastic ones when working with chloroform.

2 This works best by rotating the glass vial while keeping it under a 45° angle in a gentle nitrogen air flow.

3 Previous protocols stated evaporating the chloroform from lipid mix in vacuum for one hour [242] or only in nitrogen air flow and not in vacuum [240, 241]. The exact timing is not critical but in our hands drying for 1-2 hours works well, and even longer is also no problem.

4 Span80 is difficult to pipette due to the high viscosity, use a cut-off pipette tip to get the correct volume.

5 Usually we can store lipids for a couple of weeks in the fridge, although sometimes the lipid mix becomes milky (opaque), which is a sign that it has gone bad and therefore will not produce stable droplets. In addition, when the droplets are more prone to fuse together or splash open on the glass surface, this is another indication that the lipid mix has gone bad.

6 Keeping centrosomes for 10-20 minutes in a warm (37°C) water bath was empirically found to increase the nucleation capability of the centrosomes [242].

7 As the centrosomes are stored in a high sucrose solution, they are tricky to pipette. Therefore, it is better to add the reaction mix to the centrosome aliquot than the other way around.

8 Since the sucrose solution is viscous, pipette the mixture up and down at least 15 times to mix well.

9 If the nonspecific cortex boundary sticking becomes a problem, you can add 0.1% (v/v) Tween20 to the reaction mix in Table 6.2. The data presented in Fig. 6.2D-E and Fig. 6.4D contain Tween20.

10 Avoid making air bubbles by going to the second stop of the pipette, therefore take more than 10 µl and then pipette up and down (to the first stop of the pipette) quickly. The extra volume in the pipette tip prevents air bubble formation.

11 Emulsion droplets can also be produced by vortexing: add 2 µl reaction mix to 80 µl lipid mix in an 0.5 ml eppendorf tube and vortex for 5 seconds with a standard mini vortexer.

12 We only use two inlets (see Fig. 6.2A) - for the oil phase and water phase. The third inlet is for oil, to dilute the droplets on chip. We do not use it as we dilute the droplets later when transferring them into the PDMS imaging well.

13 A flexible photomask will not work on a UV exposure machine in combination with the vacuum used to hold the photomask in place. Therefore we attach it with Scotch tape to a glass mold that fits in the machine.

14 We used the settings for SU-8 3025 from MicroCHEM USA to obtain structures with 40 µm thickness.

15 As SU-8 ages over the years, one might need to adjust the spinning speeds [241].

16 As the exact dose of UV light depends on the machine used, calibration is needed. Make some test exposures with different exposure times and develop to see which exposure times result in robust structures.

17 This is at the same time a way to check if the development is done. If not, a white layer appears due to left over SU-8 on the wafer. In that case, put the wafer back in the developer for a while.

18 Mix the two components really well by stirring the PDMS with e.g. a spatula or pipette tip, otherwise the PDMS might form an inhomogeneous structure. It is no problem if air bubbles are created by stirring as they will be removed during the next steps.

19 Carefully press the aluminum foil around the wafer to make sure the PDMS can not flow underneath the wafer, as in that case the PDMS chip will not have the desired and homogeneous thickness.

20 Never skip this step, even if no air bubbles are visible, because small air bubbles will expand during baking and create undesired holes in your PDMS.

21 Cover the small and fragile PDMS structures that will form the channels with scotch tape to prevent damage. You remove this before bonding the PDMS to the PDMS-coated coverslip.

22 Before use, rinse both tubings first with isopropanol, then with dry them with air (just make sure the end of the tubing inside the MicrewLock tube is just above the isopropanol surface) and finally rinse with MRB80 or lipid mix respectively.

23 As the final reaction mix is only 10-20 µl in volume, there is not much space to fine tune the pressures to get an optimal droplet production. One solution is to make test droplets with just MRB80 as water phase and note the pressures where the droplet production is as desired. Next, take the water phase tubing out of the microfluidic chip and fill it with air (by applying maximum pressure while the other end of the tubing is just above the MRB80 surface). Replace the MRB80-filled MicrewLock tube by one with reaction mix, carefully increase the pressure until the tubing is filled with reaction mix and then stop the pressure so you can re-insert the end into the microfluidic chip. Now set the pressure to the empirically found values to get good droplet production from the start.

24 Usually the droplet density is very high, which gives problems when imaging droplets at the microscope. Therefore we dilute the droplets in the PDMS well.

25 We usually prepare multiple batches of coverslips and immerse them in the same volume of Rain-X for efficiency and to save Rain-X.

26 Sometimes the Rain-X film does not dry completely homogeneously onto the coverslip, visible as some transparant stains at the edges of the coverslip. This has never proven to be a problem with imaging.

27 As a result of the paper tissue, dust particles often stick to the coverslips. Shortly rinse with ethanol and dry in nitrogen flow to get rid of these without damaging the silanization.

28 It is convenient to have as many holes in each square as possible (see Fig. 6.2C), since you need a clean hole each time you prepare new droplets, also within one experimental condition.

29 In our hands, this happended at SiR tubulin concentrations above 200 µM.

30 The SiR-tubulin is added to the lipid mix, while in bulk *in vitro* reconstitution experiments it can be added to the reaction mix. We found that SiR-tubulin partitions more into the oil phase (lipid mix) than the water phase (reaction mix) and therefore needs to be added to the oil phase, as the volume of the oil phase is about 80 times larger than that of the water phase when making and imaging emulsion droplets. Some SiR-tubulin will partition into the water phase and bind to the MTs.

31 One can take out the desired volume for an experiment and then refreeze the remaining SiR-tubulin in DMSO at -20°C.

32 We usually pre-dilute the in DMSO dissolved SiR-tubulin in lipid mix before diluting it into the final lipid mix, due to the high stock concentration of SiR-tubulin. Mix these dilutions very well to get a homogeneous distribution of SiR-tubulin in the lipid mix. Also, pay attention to pipette carefully and slowly to make sure that the pipetted volume of lipid mix is consistent over different experiments because otherwise the SiR-tubulin concentration cannot be compared.

33 Usually we get good results at 1 µM, but also 0.5 µM results in nice MT labelling. As only a small fraction of the SiR-tubulin ends up in the water phase, the final concentration there is probably below the 200 nM mentioned in 29, because we do not see a strong stabilizing effect on the MTs at 0.1-1 µM SiR-tubulin in the oil phase.

34 The distribution of SiR-tubulin throughout the lipid mix is usually not perfectly homogeneous, as droplets containing stabilized MTs are observed as well as droplets with nicely labeled dynamic MTs as in Fig. 6.3A (right). We do not consider this a problem for our experiments, since we select for the proper droplets.

35 When placing the PDMS well on top of the microscope, it first needs to heat to 30°C. Due to glass expansion caused by the temperature change, droplets move out of focus. Therefore it is better to wait a few minutes for the system to equilibrate.

36 As water has a higher density than oil, the droplets sink down when they are pipetted into the PDMS well and therefore move out of focus. Thus, as in (see 35) it is better to wait a few minutes until the droplets have reached the coverglass before starting measurements.

37 Finding MT asters inside emulsion droplets can be difficult, especially if the centrosome concentration is low and the MTs are difficult to see. Easiest is to look at live microscope images with 200 ms exposure time in the wavelength channel where MTs are expected. Move in x and y and scan in z through the droplets while looking for some brighter blob in the droplets. To distinguish a protein aggregate from a centrosome, look at the diffusion rate of the blob. Due to the relatively long MTs nucleating from a centrosome (even if you can not visualize the MTs they probably are present), they are not diffusing around a lot, while protein aggregates are very mobile and can move out of your focal plane within seconds.

38 Previous efforts in our lab to visualize protein comets inside emulsion droplets did not work out. One reason is that bleaching was significant, and therefore laser intensity and exposure times were limited. We now work on a different spinning disc microscope than before, which has a different (more sensitive) camera. Since then, bleaching is not observed to be a problem anymore, hence we can image with higher laser power and exposure times. In addition, imaging on silanized coverslips instead of PDMS-coated coverslips has increased the imaging resolution by removing light refractions in the PDMS. This probably also contributed to the observation of protein comets.

39 To check the functionality of all these different proteins, it is advised to first use an assay with higher spatial (and temporal) resolution, such as the quasi-2D TIRF assay that is described before [96]. However, note that protein concentrations for TIRF assays cannot be compared to droplet experiments (see also 48).

40 G-actin will start polymerizing the moment you add it to the final reaction mix, so be quick in preparing droplets and starting the image acquisition.

41 First mix unlabelled and labelled G-actin well (dilutions in G-buffer), to get homogeneously labelled F-actin.

42 To vary the concentration of F-actin in droplets, either different concentrations of actin can be used in the F-actin mix, or this F-actin mix could be diluted right before addition to the final reaction mix.

43 After adding MRB80 to the actin-mix, polymerization starts and the mix can be kept at room temperature. Store it in the dark, to prevent photo-bleaching.

44 We add phalloidin after some time (e.g. 30 min), so it does not interfere with actin polymerization and distribution of labels. This timing is not very precise.

45 The shear-forces generated by non-gentle-mixing could break the centrosomes and the pre-polymerized AFs. Interestingly, breaking pre-polymerized F-actin (before adding it to the final reaction mix) could also serve as a method to decrease the average length of these filaments.

46 From now on, keep the final reaction mix at room temperature to prevent depolymerisation of AFs (at lower temperatures), and to prevent MTs from starting to grow (at higher temperatures). This means that also the lipid mix should be at room temperature when making droplets.

47 We have also had nicely visible MT asters inside emulsion droplets using HiLyte647-labeled tubulin from Cytoskeleton. However, after switching to a different labeled tubulin batch, the Rhodamine tubulin gave better results.

48 The tubulin concentration for *in vitro* experiments in water-in-oil emulsion droplets needs to be a factor 2-3 higher than in quasi-2D channel experiments. It is not clear why, but at lower concentrations the MTs do not nucleate in emulsion droplets.

49 Increasing the KCl concentration from 50 mM to 75 mM reduces nonspecific binding of a tip-tracking protein to the MT lattice, leading to a larger contrast between EB3 at the tip compared to the lattice.

50 The cytolinker we use is a dimer that can also bundle AFs. By changing the AF:linker ratio, one can tune the predominant interactions of the cytolinker inside the droplets.

51 The density of actin should be optimized every day, since it depends on the quality of your actin (the amount of functional actin that polymerizes into filaments) and on how much the AFs are sheared by pipetting (see 45).

52 We observe that addition of surfactants like Tween20 or excipients like BSA or κ-casein (see Table 6.1) can influence both aspecific sticking of proteins to the droplet boundary as well as specific protein-lipid interactions (the latter was only observed for Tween20 and Span80), and can even influence the stability of emulsion droplets.

7

OUTLOOK

Nothing takes the past away,
Like the future.

Madonna

The incredible ability of cells, the building blocks of life, to self-organize with great precision, using numerous dynamic processes and molecular complexity to do so, has fascinated biologists and physicists alike, including me. Vital processes, such as cell division and motility, are driven by a dynamic supramolecular organization named the cytokeleton. Networks of these cytoskeletal biopolymers arrange the cell's internal organization and provide mechanical rigidity, key factors which allow the cell to change its shape and thus divide or move. Two well-studied components of the cytoskeleton are microtubules (MTs) and actin filaments, each demonstrating distinct dynamic and mechanical properties, but coordinated to perform these vital cellular functions. Although an increasing number of studies has started to identify proteins associated with MT/actin crosstalk, a detailed picture of the underlying mechanisms remains missing.

In the meantime, at the interface between physics and biology, the concept of reconstituting cellular machineries from purified components is increasingly recognized as a tool to mimic and understand cellular processes. Using bottom-up synthetic biology to rebuild cellular systems, a minimal functional set of required components is dissected, and the underlying mechanisms can be studied.

In this thesis, we used *in vitro* reconstitution assays and engineered proteins to investigate cytolinker-mediated MT/actin crosstalk. We studied how linking actin filaments to growing microtubule plus-ends via engineered cytolinker TipAct results in the transport of actin (Chapter 3). In addition, we studied how the actin- and microtubule-binding activity of natural cytolinker Gas2Like1 is regulated via autoinhibition, which is relieved

when Gas2L1 can bind at MT/actin overlaps, providing an elegant mechanism to localize the cytolinker specifically to the place where it is needed (Chapter 4). Next, we set out to further investigate how the complex molecular anatomy of cytolinkers affect microtubule dynamics and MT/actin coordination, by using a series of engineered cytolinkers and natural spectraplakin Shot (Chapter 5). Finally, we presented a new method to study MT/actin co-organization in 3D cell-sized confinements, where centrosome-nucleated dynamic microtubles can be made to interact with actin via cytolinkers (Chapter 6). From these studies, we obtained many new insights on MT/actin crosstalk in our simple model system, but nevertheless many questions remain open. In this section, we suggest a few directions for further research.

In our *in vitro* reconstitution assays, we used dynamic microtubules grown in the presence of end binding (EB) proteins. However, we limited ourselves to using stabilized actin filaments that were not interconnected to study MT/actin co-organization and actin's impact on microtubule dynamics. This situation contrasts with cellular actin networks, which do not consist of stable actin filaments, but of filaments that are continuously (de)polymerizing, and are interconnected by crosslinker proteins and molecular motors. While our assay provides a basis to investigate molecular mechanisms for MT/actin crosstalk in cells, future studies should focus on more complex actin organizations. A few concrete ideas are discussed below.

In Chapter 3, we studied actin transport by growing microtubule plus ends, and we investigated the conditions necessary for this single-filament transport using *in vitro* reconstitution experiments, computer simulations and a minimal theoretical model. During the course of this thesis work, recent studies showed local actin polymerization at the microtubule plus end, either by promoting Arp2/3 branched actin polymerization via Adenomatous polyposis coli (APC) [88], or more directly via a cytolinking complex consisting of EB, CLIP170, and the formin mDia [87]. Our findings suggest that it would be interesting to test whether growing microtubule ends could also transport these newly nucleated actin filaments. Our first steps towards such a complex form of actin transport are shown in Fig. 7.1, where we used full-length mammalian APC (Adenomatous polyposis coli) as the cytolinker (purified from SF21 insect cells as described before [245]). In preliminary experiments, we observed APC-mediated actin nucleation (Fig. 7.1B) and APC tracking growing microtubule ends via EB3 (Fig. 7.1C), thus confirming APC's potential. However, a recent study showed that EB1 inhibits APC-mediated actin polymerization by blocking G-actin recruitment [246]), suggesting that APC might in fact not be able to tip-track and polymerize actin simultaneously. These findings would rule out APC as a tip-tracking cytolinker that also polymerizes actin filaments, thus require further investigations.

In Chapter 5, we studied the impact of an entangled actin network on microtubule growth. Here, actin filaments were not in any way connected and free to move around, thus not providing much of a physical barrier for microtubule growth. Nevertheless, we observed a decreased growth velocity without alterations in the catastrophe frequency, which we interpreted as a consequence of EB3 depletion by actin-binding, potentially combined with the effect of actin acting as a barrier. A more direct measurement of actin acting as a barrier is shown in Fig. 7.2, where we observe a microtubule growing into a perpendicular-oriented actin bundle. In this preliminary experiment, where no

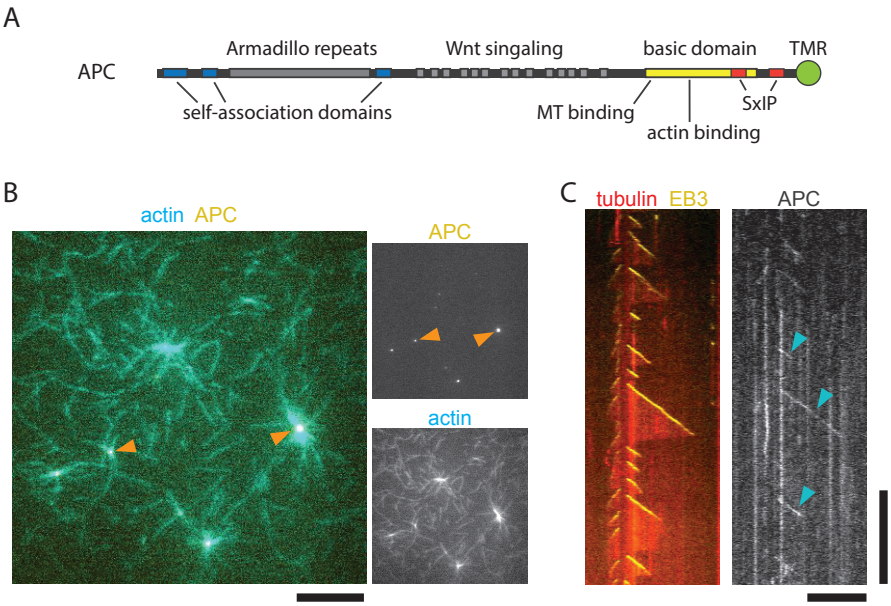

Figure 7.1: **Adenomatous polyposis coli (APC) as potential cytolinker connecting growing actin filaments to growing microtubule ends.** **(A)** Schematic of APC domain structure. APC can interact with actin and tubulin via the basic domain (yellow), and bind EB proteins via SxIP motifs (red) to track growing microtubule ends. C-terminal SNAP-tag was used for fluorescent labelling with TMR. **(B)** Actin filaments (cyan) are polymerized and captured by clusters of APC proteins (yellow). Shown are the overlay (left) and the two separated channels (right). Orange arrowheads indicate two examples of these actin/APC complexes. **(C)** APC is able to track growing mictotubule plus ends via EB3. Shown are the microtubule (red) and EB3 (yellow) on the left, and the APC on the right. Blue arrowheads indicate a few traces of APC tip-tracking. Experiments were performed at conditions similar to previous cytolinker assays (see Chapter 2 for details), with 10 nM TMR-labelled APC (TMR: tetramethylrhodamine), and in the presence of 1 µM G-actin instead of pre-polymerized and stabilized F-actin. Scale bars: 10 µm (horizontal) and 5 min (vertical).

EB or actin bundling proteins are present, a growing microtubule tries to pass the actin obstacle, but ends up pushing it slightly before undergoing a catastrophe. These types of observations invite us to further investigate how properties of the actin network, like geometrical orientation, influence microtubule dynamics. In addition, since we observed that microtubule lattice-binding cytolinkers together with actin results in more persistent microtubule growth (Chapter 5), we wonder whether these cytolinkers can help the microtubule to overcome actin barriers in different geometries.

In addition to geometrical organization, the viscoelastic properties of the actin network (influenced by the crosslinking state) might also impact microtubule dynamics differently compared to entangled networks. Previous studies showed that, in the absence of EB proteins, an Arp2/3-branched actin network acts as a barrier for microtubule growth, since the microtubule catastrophe rate was increased and resulted in shorter microtubules [36]. It would be interesting to test how a crosslinked actin network would affect microtubule dynamics. While using crosslinkers like α-actinin would limit actin filament movement compared to an entangled actin network, it would likely still allow more

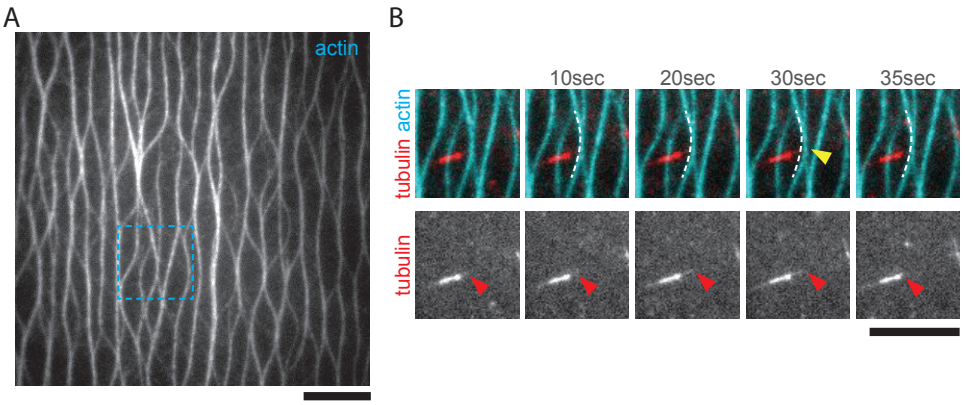

Figure 7.2: **Microtubule growing and pushing against actin bundle.** **(A)** Aligned actin network formed by introducing a drop of methyl cellulose at the flow channel end (as described in [92]). Box indicates the location of the zoom-in shown in (B). **(B)** Time series of a growing microtubule (red) and an actin bundle being pushed (cyan). Yellow arrowhead indicates the displacement of the actin bundle compared to previous timepoints. Red arrowheads indicate the growing microtubule end. Experiments were performed at conditions similar to previous cytolinker assays (see Chapter 2 for details). Scale bars: 10µm.

re-organizations compared to an Arp2/3-branched network due to the transient (thus dynamic) (un)binding of the α-actinin crosslinkers [212]. In preliminary experiments with different cytolinkers, as shown in Fig. 7.3, we observed a small increase in growth velocity (by about 25%) for microtubules grown with EB3 in an α-actinin crosslinked actin network, compared to entangled actin networks. These first observations are surprising, since we expect a crosslinked actin network to inhibit microtubule growth. Further investigations are required, focussing on the role of EB3 depletion, possible MT/α-actinin interactions, and increasing the crosslinker and actin density.

Besides changing the viscoelastic properties of the actin network by controlling actin crosslinking state, one could also include dynamic (de)polymerizing actin filaments. The turnover of actin filaments, for example resulting in treadmilling during steady state, would change the network's viscoelasticity properties [247], potentially creating less of a barrier for microtubules to grow into. This is especially interesting in the context of microtubules reaching the actin cortex, since in cells the entire cortical actin turns over within approximately one minute [248]. To create this type of dynamic actin network, many additional proteins are required, including capping and severing proteins [234]. One should be aware of the effects these actin-binding proteins can have by themselves on microtubule dynamics, as is already suggested for formins [249] and profilin [33, 34].

In our *in vitro* reconstitution assays, we used stabilized microtubule seeds that were attached to the surface, which allowed us to follow microtubule dynamics in detail. However, one could pursue another research angle when the seeds are not surface attached, namely that of actin-dependent microtubule organization. As a consequence of retrograde actin flows, microtubules have been observed to re-organize into bundles or to buckle and even break (discussed in Chapter 1). It would be interesting to study whether *in vitro* reconstituted contractile actin networks (activated by myosin motors [251]) are

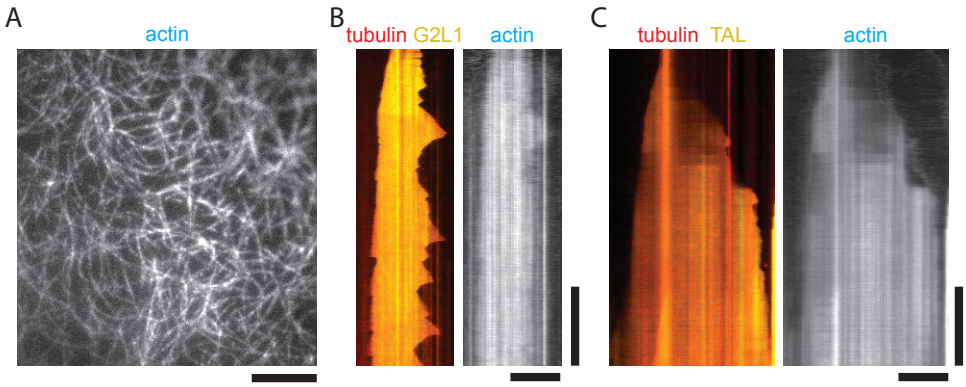

Figure 7.3: **Effect of α-actinin crosslinked actin networks on microtubule growth dynamics. (A)** Field-of-view of an actin network crosslinked by α-actinin. Here, 6 nM α-actinin-1 (ACTN1) was added to 1 µM pre-polymerized and phalloidin-stabilized actin filaments. **(B)** Typical kymograph of a microtubule decorated with cytolinker Gas2Like1 (G2L1), growing in an α-actinin crosslinked actin network. Shown is the microtubule (red) and G2L1 (yellow) on the left, and the actin channel on the right. Gas2L1 localizes at the MT/actin overlap regions, where actin filaments are aligned to the microtubule. We still observe many microtubule rescue events. **(C)** Typical kymograph of a microtubule decorated with cytolinker TipActLong (TAL), growing in an α-actinin crosslinked actin network. Shown is the microtubule (red) and TAL (yellow) on the left, and the actin channel on the right. We observe persistent microtubule growth, with catastrophes that are quickly followed by rescue event. Experiments were performed at conditions similar to previous cytolinker assays (see Chapter 2 for details). Human α-actinin-1 was purified from E. Coli as described in Ref. [250]. Scale bars: 10µm (horizontal) and 5 min (vertical).

able to reorganize microtubules via steric interactions, or whether cytolinkers are required. Preliminary experiments including skeletal muscle myosin II motors and dynamic microtubules indicated that our buffer conditions are suitable for these experiments. In addition to studying microtubule organization influenced by these reconstituted retrograde actin flows, one could study under what conditions the contractile actin network is able to buckle and break microtubules. It would be interesting to test whether linking microtubules via cytolinkers to actin filaments gives them more mechanical stability to resist these forces and prevent breakage.

We used total internal reflection fluorescence (TIRF) microscopy as a tool for fast and high-resolution imaging of single actin filaments and microtubules. However, to test the impact of MT/actin crosstalk via cytolinkers on global co-organization in cell-like geometries, the next step is to move away from the quasi-2D TIRF experiments and use the methods described in Chapter 6. Spherical droplets like the ones introduced in Chapter 6 would for instance make it possible to model mitotic spindle positioning, where microtubule plus ends interact with the actin cortex and generate pushing and pulling forces [7, 252]. In an ideal-but-complex experiment, one would be able to tune the organization of an actin cortex (like mesh size and spatial heterogeneities), and measure how it influences centrosome positioning.

To gain more control on MT/actin-crosstalk inside confinement, one could design a cytolinker that includes a light-inducible linking domain, similar to what was shown in cells [201]. This would allow for both spatial and temporal control over linking mi-

crotubules to actin filaments. Keeping in mind that microtubules connected to actin via their lattices display more persistent growth (Chapter 5), the selective activation of the cytolinker would break the initially homogeneous centrosomal microtubule organization.

To reduce the number of proteins involved in cytolinking complexes, one could design a single protein with the associated microtubule- and actin binding domains. For example, one could try to reduce the EB/CLIP/mDia-complex that was reported to mediate actin nucleation from microtubules plus-ends [87] to a single engineered protein. Or, in the context of MT/actin crosstalk via signalling pathways, design an actin-severing protein that specifically localizes to growing microtubule ends. Motivated from a practical perspective, a single protein would be easier to incorporate into confinements such as droplets than multiple proteins, since it requires fewer optimization steps, as discussed in Chapter 6.

Finally, the reduction in number of involved proteins could also serve another goal, namely that of building a synthetic cell. One single engineered protein that captures the cellular functions of interest would greatly facilitate the bottom-up construction of a synthetic cell. It would provide insight into the minimal set of components that is required for a certain cellular function. In addition, a single engineered protein would simplify the encoding and expression of components from a synthetic genome, that is ultimately required to construct a complete and functional synthetic cell [253, 254].

ACKNOWLEDGEMENTS

We thank Sebastian Baumann and Sebastian Maurer (Centre for Genomic Regulation, Barcelona, Spain) for the kind gift of purified and TMR-labeled APC. We also thank Christophe Le Clainche (Institute for Integrative Biology of the Cell, I2BC, France) for the kind gift of the construct for human α-actinin-1 and Marjolein Vinkenoog (AMOLF) and Jeffrey den Haan (TU Delft) for purification.

BIBLIOGRAPHY

[1] E. Bianconi, A. Piovesan, F. Facchin, A. Beraudi, R. Casadei, F. Frabetti, L. Vitale, M. Pelleri, S. Tassani, F. Piva, S. Perez-Amodio, P. Strippoli, and S. Canaider, *An estimation of the number of cells in the human body,* Ann Hum Biol. **40**, 463 (2013).

[2] F. Huber, A. Boire, M. Preciado López, and G. H. Koenderink, *Cytoskeletal crosstalk: when three different personalities team up,* Curr. Opin. Cell Biol. **32**, 39 (2015).

[3] M. Dogterom and G. H. Koenderink, *Actin-microtubule crosstalk in cell biology,* Nat. Rev. Mol. Cell Biol. **20**, 38 (2019).

[4] M. L. Pimm and J. L. Henty-Ridilla, *New twists in actin-microtubule interactions,* Mol. Biol. Cell **32**, 211 (2021).

[5] S. Seetharaman and S. Etienne-Manneville, *Cytoskeletal crosstalk in cell migration,* Trends in Cell Biol. **30**, 720 (2020).

[6] R. Pinto-Costa and M. M. Sousa, *Microtubules, actin and cytolinkers: how to connect cytoskeletons in the neuronal growth cone,* Neurosci Lett. **747**, 135693 (2021).

[7] F. Rizzelli, M. Grazia Malabarba, S. Sigismund, and M. Mapelli, *The crosstalk between microtubules, actin and membranes shapes cell division,* Open Biol. **10**, 190314 (2020).

[8] C. H. Coles and F. Bradke, *Coordinating neuronal actin-microtubule dynamics,* Current Biol. **25**, R677 (2015).

[9] O. C. Rodriguez, A. W. Schaefer, C. A. Mandato, P. Forscher, W. M. Bement, and C. M. Waterman-Storer, *Conserved microtubule-actin interactions in cell movement and morphogenesis,* Nat Cell Biol. **5**, 599 (2003).

[10] B. Bugyi and M.-F. Carlier, *Control of actin filament treadmilling in cell motility,* Annu Rev Biophys. **39**, 449 (2010).

[11] M. Kasai, S. Asakura, and F. Oosawa, *The G-F equilibrium in actin solutions under various conditions,* Biochim Biophys Acta. **12**, 13 (1962).

[12] T. D. Pollard and S. W. Craig, *Mechanism of actin polymerization,* Trends Biochem Sci. **7**, 55 (1982).

[13] M. Steinmetz, K. N. Goldie, and U. Aebi, *A correlative analysis of actin filament assembly, structure, and dynamics,* J Cell Biol. **138**, 559 (1997).

[14] T. D. Pollard, *Rate constants for the reactions of ATP- and ADP-actin with the ends of actin filaments,* J Cell Biol. **103**, 2747 (1986).

[15] L. Blanchoin, R. Boujemaa-Paterski, C. Sykes, and J. Plastino, *Actin dynamics, architecture, and mechanics in cell motility,* Physiol Rev. **94**, 235 (2014).

[16] T. Mitchison and M. Kirschner, *Dynamic instability of microtubule growth,* Nature **312**, 237 (1984).

[17] A. Desai and T. J. Mitchison, *Microtubule polymerization dynamics,* Annu Rev Cell Dev Biol. **13**, 83 (1997).

[18] M. K. Gardner, B. D. Charlebois, I. M. Jánosi, J. Howard, and A. J. Hunt, *Rapid microtubule self-assembly kinetics,* Cell **146**, 582 (2011).

[19] E. Nogales, M. Whittaker, R. A. Milligan, and K. H. Downing, *High-resolution model of the microtubule,* Cell **96**, 79 (1999).

[20] M. F. Carlier, D. Didry, and D. Pantaloni, *Microtubule elongation and guanosine 5'-triphosphate hydrolysis. Role of guanine nucleotides in microtubule dynamics,* Biochemistry **26**, 4428 (1987).

[21] S. Forth and T. M. Kapoor, *The mechanics of microtubule networks in cell division,* J Cell Biol. **216**, 1525 (2017).

[22] A. Akhmanova and M. Steinmetz, *Control of microtubule organization and dynamics: two ends in the limelight,* Nat Rev Mol Cell Biol. **16**, 711 (2015).

[23] S. P. Maurer, N. I. Cade, G. Bohner, N. Gustafsson, E. Boutant, and T. Surrey, *EB1 Accelerates Two Conformational Transitions Important for Microtubule Maturation and Dynamics,* Curr. Biol. **24**, 372 (2014).

[24] Y. Komarova, C. O. De Groot, I. Grigoriev, S. M. Gouveia, E. L. Munteanu, J. M. Schober, S. Honnappa, R. M. Buey, C. C. Hoogenraad, M. Dogterom, G. G. Borisy, M. O. Steinmetz, and A. Akhmanova, *Mammalian end binding proteins control persistent microtubule growth,* J Cell Biol. **184**, 691 (2009).

[25] C. Duellberg, N. I. Cade, D. Holmes, and T. Surrey, *The size of the EB cap determines instantaneous microtubule stability,* eLife **5**, e13470 (2016).

[26] R. Zhang, G. M. Alushin, A. Brown, and E. Nogales, *Mechanistic origin of microtubule dynamic instability and its modulation by EB proteins,* Cell **162**, 849 (2015).

[27] N. Galjart, *Plus-end-tracking proteins and their interactions at microtubule ends,* Curr Biol. **20**, R528 (2010).

[28] C. Janke, *The tubulin code: molecular components, readout mechanisms, and functions,* J Cell Biol. **206**, 461 (2014).

[29] J. Wojnacki, G. Quassollo, M.-P. Marzolo, and A. Cáceres, *Rho GTPases at the crossroad of signaling networks in mammals,* Small GTPases **5**, e28430 (2014).

[30] M. Krendel, F. T. Zenke, and G. M. Bokoch, *Nucleotide exchange factor GEF-H1 mediates cross-talk between microtubules and the actin cytoskeleton,* Nat Cell Biol. **4**, 294 (2002).

[31] R. Pinto-Costa and M. M. Sousa, *Profilin as a dual regulator of actin and microtubule dynamics,* Cytoskeleton **77**, 76 (2020).

[32] M. L. Pimm, J. Hotaling, and J. L. Henty-Ridilla, *Profilin choreographs actin and microtubules in cells and cancer,* Int Rev Cell Mol Biol. **355**, 155 (2020).

[33] J. L. Henty-Ridilla, M. A. Juanes, and B. L. Goode, *Profilin directly promotes microtubule growth through residues mutated in amyotrophic lateral sclerosis,* Curr Biol. **27**, 3535 (2017).

[34] R. Pinto-Costa, S. C. Sousa, S. C. Leite, J. Nogueira-Rodrigues, T. Ferreira da Silva, D. Machado, J. Marques, A. C. Costa, M. A. Liz, F. Bartolini, P. Brites, M. Costell, R. Fässler, and M. M. Sousa, *Profilin 1 delivery tunes cytoskeletal dynamics toward CNS axon regeneration,* J Clin Invest. **130**, 2024 (2020).

[35] M. E. Janson, M. E. de Dood, and M. Dogterom, *Dynamic instability of microtubules is regulated by force,* J Cell Biol. **161**, 1029 (2003).

[36] A. Colin, P. Singaravelu, M. Théry, L. Blanchoin, and Z. Gueroui, *Actin-network architecture regulates microtubule dynamics,* Curr. Biol. **28** (2018), 10.1016/j.cub.2018.06.028.

[37] D. Inoue, D. Obino, J. Pineau, F. Farina, J. Gaillard, C. Guerin, L. Blanchoin, A.-M. Lennon-Duménil, and M. Théry, *Actin filaments regulate microtubule growth at the centrosome,* EMBO J **38**, e99630 (2019).

[38] W. C. Salmon, M. C. Adams, and C. M. Waterman-Storer, *Dual-wavelength fluorescent speckle microscopy reveals coupling of microtubule and actin movements in migrating cells,* J Cell Biol. **158**, 31 (2002).

[39] S. Even-Ram, A. D. Doyle, M. A. Conti, K. Matsumoto, R. S. Adelstein, and K. M. Yamada, *Myosin IIA regulates cell motility and actomyosin–microtubule crosstalk,* Nat Cell Biol. **9**, 299 (2007).

[40] C. M. Waterman-Storer and E. Salmon, *Actomyosin-based retrograde flow of microtubules in the lamella of migrating epithelial cells influences microtubule dynamic instability and turnover and is associated with microtubule breakage and treadmilling,* J Cell Biol. **139**, 417 (1997).

[41] S. L. Gupton, W. C. Salmon, and C. M. Waterman-Storer, *Converging populations of F-actin promote breakage of associated microtubules to spatially regulate microtubule turnover in migrating cells,* Curr Biol. **12**, 1891 (2002).

[42] D. T. Burnette, L. Ji, A. W. Schaefer, N. A. Medeiros, G. Danuser, and P. Forscher, *Myosin II activity facilitates microtubule bundling in the neuronal growth cone neck,* Dev Cell **15**, 163 (2008).

[43] A. M. Winans, S. R. Collins, and T. Meyer, *Waves of actin and microtubule polymerization drive microtubule-based transport and neurite growth before single axon formation,* Dev Cell **5** (2016), 10.7554/eLife.12387.

[44] Z. Holubcová, G. Howard, and M. Shuh, *Vesicles modulate an actin network for asymmetric spindle positioning,* Nat Cell Biol. **15**, 937 (2013).

[45] K. Dahlgaard, A. A. Raposo, T. Niccoli, and D. St Johnston, *Capu and Spire assemble a cytoplasmic actin mesh that maintains microtubule organization in the Drosophila oocyte,* Dev Cell **13**, 539 (2007).

[46] J. Azoury, K. W. Lee, V. Georget, P. Rassinier, B. Leader, and M.-H. Verlhac, *Spindle positioning in mouse oocytes relies on a dynamic meshwork of actin filaments,* Curr Biol. **18**, 1514 (2008).

[47] M. Shuh and J. Ellenberg, *A new model for asymmetric spindle positioning in mouse oocytes,* Curr Biol. **18**, 1986 (2008).

[48] Y.-C. Lin, G. H. Koenderink, F. C. MacKintosh, and D. A. Weitz, *Control of nonlinear elasticity in F-actin networks with microtubules,* Soft Matter **7**, 902 (2011).

[49] M. Dogterom and B. Yurk, *Measurement of the force-velocity relation for growing microtubules,* Science **278**, 856 (1997).

[50] D. E. Ingber, *Tensegrity I. cell structure and hierarchical systems biology,* J Cell Sci. **116**, 1157 (2003).

[51] C. P. Brangwynne, F. C. MacKintosh, S. Kumar, N. A. Geisse, J. Talbot, L. Mahadevan, K. K. Parker, D. E. Ingber, and D. A. Weitz, *Microtubules can bear enhanced compressive loads in living cells because of lateral reinforcement,* J Cell Biol. **173**, 733 (2006).

[52] B. P. Bouchet, I. Noordstra, M. van Amersfoort, E. A. Katrukha, Y.-C. Ammon, N. D. Ter Hoeve, L. Hodgson, M. Dogterom, P. W. Derksen, and A. Akhmanova, *Mesenchymal cell invasion requires cooperative regulation of persistent microtubule growth by SLAIN2 and CLASP1,* Dev Cell **39**, 708 (2016).

[53] K. Suozzi, X. Wu, and E. Fuchs, *Spectraplakins: master orchestrators of cytoskeletal dynamics,* J. Cell Sci. **197**, 465 (2012).

[54] J. Zhang, J. Yue, and X. Wu, *Spectraplakin family proteins - cytoskeletal crosslinkers with versatile roles,* J. Cell Sci. **130**, 2447 (2017).

[55] R. Cusseddu, A. Robert, and J.-F. Côté, *Strenght through unity: the power of the mega-scaffold MACF1,* Front. Cell Dev Biol. **9** (2021), 10.3389/fcell.2021.641727.

[56] T. R. Lane, E. Fuchs, and K. C. Slep, *Structure of the ACF7 EF-hand-GAR module and delineation of microtubule binding determinants,* Structure **25**, 1130 (2017).

[57] K. C. Slep, S. L. Rogers, S. L. Elliott, H. Ohkura, P. A. Kolodziej, and R. D. Vale, *Structural determinants for EB1-mediated recruitment of APC and spectraplakins to the microtubule plus end,* J Cell Biol. **168**, 587 (2005).

[58] I. Karakesisoglou, Y. Yang, and E. Fuchs, *An epidermal plakin that integrates actin and microtubule networks at cellular junctions,* J Cell Biol. **149**, 195 (2000).

[59] A. Kodama, I. Karakesisoglou, E. Wong, A. Vaezi, and E. Fuchs, *ACF7: an essential integrator of microtubule dynamics,* Cell **115**, 343 (2000).

[60] X. Wu, A. Kodama, and E. Fuchs, *ACF7 regulates cytoskeletal-focal adhesion dynamics and migration and has ATPase activity,* Cell **135**, 137 (2008).

[61] Y. Margaron, N. Fradet, and J.-F. Côté, *ELMO recruits actin cross-linking family 7 (ACF7) at the cell membrane for microtubule capture and stabilization of cellular protrusions,* J Biol Chem. **288**, 1184 (2013).

[62] W. Ning, Y. Yu, H. Xu, X. Liu, D. Wang, J. Wang, Y. Wang, and W. Meng, *The CAMSAP3-ACF7 complex couples noncentrosomal microtubules with actin filaments to coordinate their dynamics,* Dev Cell **39**, 61 (2016).

[63] Y. Ma, J. Yue, Y. Zhang, C. Shi, M. Odenwald, W. G. Liang, Q. Wei, A. Goel, X. Gou, J. Zhang, S.-Y. Chen, W.-J. Tang, J. R. Turner, F. Yang, H. Liang, H. Qin, and X. Wu, *ACF7 regulates inflammatory colitis and intestinal wound response by orchestrating tight junction dynamics,* Nat Commun. **8**, 15375 (2017).

[64] L. Hu, P. Su, R. Li, K. Yan, Z. Chen, P. Shang, and A. Qian, *Knockdown of microtubule actin crosslinking factor 1 inhibits cell proliferation in MC3T3-E1 osteoblastic cells,* BMB Rep **48**, 583 (2015).

[65] M. Ka, E.-M. Jung, U. Mueller, and W.-Y. Kim, *MACF1 regulates the migration of pyramidal neurons via microtubule dynamics and GSK-3 signaling,* Dev Biol. **395**, 4 (2014).

[66] X. Wu, Q.-T. Shen, D. S. Oristian, C. P. Lu, Q. Zheng, H.-W. Wang, and E. Fuchs, *Skin stem cells orchestrate directional migration by regulating microtubule-ACF7 connections through GSK3β,* Cell **144**, 341 (2011).

[67] A. Voelzmann, Y. Liew, Y. Qu, I. Hahn, C. Melero, N. Sánchez-Soriano, and A. Prokop, *Drosophila Short stop as a paradism for the role and regulation of spectraplakins,* Semin. Cell Dev. Biol. **69**, 40 (2017).

[68] N. Sánchez-Soriano, M. Travis, F. Dajas-Bailador, C. Gonçalves-Pimentel, A. J. Whitmarsh, and A. Prokop, *Mouse ACF7 and Drosophila Short stop modulate filopodia formation and microtubule organisation during neuronal growth,* J Cell Sci **122**, 2534 (2009).

[69] N. Sánchez-Soriano, C. Gonçalves-Pimentel, R. Beaven, U. Haessler, L. Ofner-Ziegenfuss, C. Ballestrem, and A. Prokop, *Drosophila growth cones: a genetically tractable platform for the analysis of axonal growth dynamics,* Dev Neurobiol. **70**, 58 (2010).

[70] Y. Qu, I. Hahn, S. E. Webb, S. P. Pearce, and A. Prokop, *Periodic actin structures in neuronal axons are required to maintain microtubules,* Mol Biol Cell **28**, 296 (2017).

[71] J. Alves-Silva, N. Sánchez-Soriano, R. Beaven, M. Klein, J. Parkin, T. H. Millard, H. J. Bellen, K. J. T. Venken, C. Ballestrem, R. A. Kammerer, and A. Prokop, *Spectraplakins Promote Microtubule-Mediated Axonal Growth by Functioning As Structural Microtubule-Associated Proteins and EB1-Dependent +TIPs (Tip Interacting Proteins),* J. Neurosci. **32**, 9143 (2012).

[72] W. Lu, M. Lakonishok, and V. I. Gelfand, *Gatekeeper function for Short stop at the ring canals of the Drosophila ovary,* Curr Biol. **S0960-9822(21)00669-2** (2021), 10.1016/j.cub.2021.05.010.

[73] J. Yue, Y. Zhang, W. G. Liang, X. Gou, P. Lee, H. Liu, W. Lyu, W.-J. Tang, S.-Y. Chen, F. Yang, H. Liang, and X. Wu, *In vivo epidermal migration requires focal adhesion targeting of ACF7,* Nat Commun. **7** (2016), 10.1038/ncomms11692.

[74] M. Kapur, W. Wang, M. T. Maloney, I. Millan, V. F. Lundin, T.-A. Tran, and Y. Yang, *Calcium tips the balance: a microtubule plus end to lattice binding switch operates in the carboxyl terminus of BPAG1n4,* EMBO Rep. **13**, 1021 (2012).

[75] D. A. Applewhite, K. D. Grode, M. C. Duncan, and S. L. Rogers, *The actin-microtubule cross-linking activity of Drosophila Short stop is regulated by intramolecular inhibition,* Mol Biol Cell **24**, 2885 (2013).

[76] M. J. Stroud, A. Nazgiewicz, E. A. McKenzie, Y. Wang, R. A. Kammerer, and C. Ballestrem, *Gas2-like proteins mediate communication between microtubules and actin through interactions with end-binding proteins,* J Cell Sci. **127**, 2672 (2014).

[77] N. Zhang, C. Zhao, X. Zhang, X. Cui, Y. Zhao, J. Yang, and X. Gao, *Growth arrest-specific 2 protein family: Structure and function,* Cell Prolif. **54**, e12934 (2021).

[78] G. C. Girdler, D. A. Applewhite, W. M. Perry, S. L. Rogers, and K. Röper, *The Gas2 family protein Pigs is a microtubule +TIP that affects cytoskeleton organisation,* J Cell Sci. **129**, 121 (2016).

[79] B. L. Goode and M. J. Eck, *Mechanism and function of formins in the control of actin assembly,* Annu Rev Biochem. **76**, 593 (2007).

[80] J. Gaillard, V. Ramabhadran, E. Neumanne, P. Gurel, L. Blanchoin, M. Vantard, and H. N. Higgs, *Differential interactions of the formins INF2, mDia1, and mDia2 with microtubules,* Mol Biol Cell **22**, 4575 (2011).

[81] F. Bartolini, J. B. Mosely, J. Schmoranzer, L. Cassimeris, B. L. Goode, and G. G. Gundersen, *The formin mDia2 stabilizes microtubules independently of its actin nucleation activity,* J Cell Biol. **181**, 523 (2008).

[82] S. Szikora, I. Földi, K. Tóth, E. Migh, A. Vig, B. Bugyi, J. Maléth, P. Hegyi, P. Kaltenecker, N. Sanchez-Soriano, and J. Mihály, *The formin DAAM is required for coordination of the actin and microtubule cytoskeleton in axonal growth cones,* J Cell Sci. **130**, 2506 (2017).

[83] M. Kwon, M. Bagonis, G. Danuser, and D. Pellman, *Direct microtubule-binding by myosin-10 orients centrosomes toward retraction fibers and subcortical actin clouds,* Dev Cell **34**, 323 (2015).

[84] A. I. Fokin, V. David, K. Oguievetskaia, E. Derivery, C. E. Stone, L. Cao, N. Rocques, N. Molinie, V. Henriot, M. Aumont-Nicaise, M.-V. Hinckelmann, F. Saudou, C. Le Clainche, A. P. Carter, G. Romet-Lemonne, and A. M. Gautreau, *The Arp1/11 minifilament of dynactin primes the endosomal Arp2/3 complex,* Sci Adv. **7**, eabd5956 (2021).

[85] E. Hwang, J. Kusch, Y. Barral, and T. C. Huffaker, *Spindle orientation in Saccharomyces cerevisiae depends on the transport of microtubule ends along polarized actin cables,* J Cell Biol. **161**, 483 (2003).

[86] F. Yarm, I. Sagot, and D. Pellman, *The social life of actin and microtubules: interaction versus cooperation,* Curr Opin Microbiol. **4**, 696 (2001).

[87] J. L. Henty-Ridilla, A. Rankova, J. A. Eskin, K. Kenny, and B. L. Goode, *Accelerated actin filament polymerization from microtubule plus ends,* Science **352**, 1004 (2016).

[88] N. Efimova, C. Yang, J. X. Chia, N. Li, C. J. Lengner, K. L. Neufeld, and T. M. Svitkina, *Branched actin networks are assembled on microtubules by adenomatous polyposis coli for targeted membrane protrusion,* J. Cell Biol. **219** (2020), 10.1083/jcb.202003091.

[89] D. Ricolo and S. J. Araujo, *Coordinated crosstalk between microtubules and actin by a spectraplakin regulates lumen formation and branching,* eLife **9**, e61111 (2020).

[90] D. Ricolo, J. Castro-Ribera, and S. J. Araujo, *Cytoskeletal players in single-cell branching morphogenesis,* Dev Biol. **477**, 22 (2021).

[91] B. T. Best, *Single-cell branching morphogenesis in the Drosophila trachea,* Dev Biol. **451**, 5 (2019).

[92] M. Preciado López, F. Huber, I. Grigoriev, M. O. Steinmetz, A. Akhmanova, M. Dogterom, and G. H. Koenderink, *Chapter Seventeen - In Vitro Reconstitution of Dynamic Microtubules Interacting with Actin Filament Networks,* in *Methods in Enzymology*, Reconstituting the Cytoskeleton, Vol. 540, edited by R. D. Vale (Academic Press, 2014) pp. 301–320.

[93] M. Zanic, J. H. Stear, A. A. Hyman, and J. Howard, *EB1 recognizes the nucleotide state of tubulin in the microtubule lattice,* PLOS ONE **4**, e7585 (2009).

[94] R. M. Buey, R. Mohan, K. Leslie, T. Walzthoeni, J. H. Missimer, A. Menzel, S. Bjelić, K. Bargsten, I. Grigoriev, I. Smal, E. Meijering, R. Aebersold, A. Akhmanova, and M. O. Steinmetz, *Insights into EB1 structure and the role of its C-terminal domain for discriminating microtubule tips from the lattice,* Mol Biol Cell **22**, 2912 (2011).

[95] C. E. Aitken, R. A. Marshall, and J. D. Puglisi, *An oxygen scavenging system for improvement of dye stability in single-molecule fluorescence experiments,* Biophys J. **94**, 1826 (2008).

[96] M. Preciado López, F. Huber, I. Grigoriev, M. O. Steinmetz, A. Akhmanova, G. H. Koenderink, and M. Dogterom, *Actin–microtubule coordination at growing microtubule ends,* Nat. Commun. **5**, 4778 (2014).

[97] J. D. Pardee and J. Aspudich, *Chapter Eighteen - Purification of Muscle Actin,* in *Methods in Enzymology*, Structural and Contractile Proteins Part B: The Contractile Apparatus and the Cytoskeleton, Vol. 85 (Academic Press, 1982) pp. 164–181.

[98] B. S. Gentry, S. van der Meulen, P. Noguera, B. Alonso-Latorre, J. Plastino, and G. H. Koenderink, *Multiple actin binding domains of Ena/VASP proteins determine actin network stiffening,* Eur. Biophys. J. (2012), 41, 979-990.

[99] A. A. Hyman, S. Salser, D. N. Drechsel, N. Unwin, and T. J. Mitchison, *Role of GTP hydrolysis in microtubule dynamics: information from a slowly hydrolyzable analogue, GMPCPP.* Mol. Biol. Cell **3**, 1155 (1992).

[100] S. Honnappa, S. M. Gouveia, A. Weisbrich, F. F. Damberger, N. S. Bhavesh, H. Jawhari, I. Grigoriev, F. J. A. van Rijssel, R. M. Buey, A. Lawera, I. Jelesarov, F. K. Winkler, K. Wüthrich, A. Akhmanova, and M. O. Steinmetz, *An EB1-Binding Motif Acts as a Microtubule Tip Localization Signal,* Cell **138**, 366 (2009).

[101] M. Moudjou and M. Bornens, *Method of centrosome isolation from cultured animal cells,* Cell biology: a laboratory handbook **2**, 111 (1998).

[102] M. Steinmetz, A. Stock, R. Schulthess, R. Landwehr, A. Lustig, J. Faix, G. Gerisch, U. Aebi, and R. Kammerer, *A distinct 14 residue site triggers coiled-coil formation in cortexillin I,* EMBO J. **17**, 1883 (1998).

[103] M. Preciado López, *In vitro studies of actin-microtubule coordination*, Dissertation, Vrije Universiteit, Amsterdam (2015).

[104] A. Aher, M. Kok, A. Sharma, A. Rai, N. Olieric, R. Rodriguez-Garcia, E. A. Katrukha, T. Weinert, V. Olieric, L. C. Kapitein, M. O. Steinmetz, M. Dogterom, and A. Akhmanova, *CLASP suppresses microtubule catastrophes through a single TOG domain,* Dev Cell **46**, 40 (2018).

[105] J. Schindelin, I. Arganda-Carreras, E. Frise, V. Kaynig, M. Longair, T. Pietzsch, S. Preibisch, C. Rueden, S. Saalfeld, B. Schmid, J.-Y. Tinevez, D. J. White, V. Hartenstein, K. Eliceiri, P. Tomancak, and A. Cardona, *Fiji: an open-source platform for biological-image analysis,* Nat. Methods **9**, 676 (2012).

[106] C. Alkemade, H. Wierenga, V. Volkov, M. Preciado López, A. Akhmanova, P. R. ten Wolde, M. Dogterom, and G. H. Koenderink, *Cross-linkers at growing microtubule ends generate forces that drive actin transport,* bioRxiv , 2021.07.09.451744 (2021).

[107] H. L. Sweeney and E. L. Holzbaur, *Motor proteins,* Cold Spring Harb. Perspect. Biol. **10** (2018), 10.1101/cshperspect.a021931.

[108] M. Dogterom, J. W. Kerssemakers, G. Romet-Lemonne, and M. E. Janson, *Force generation by dynamic microtubules.* Curr. Opinion Cell Biol. **17**, 67 (2005).

[109] M. Vleugel, M. Kok, and M. Dogterom, *Understanding force-generating microtubule systems through in vitro reconstitution.* Cell Adh Migr. **10**, 475 (2016).

[110] O. Kučera, V. Siahaan, D. Janda, S. H. Dijkstra, E. Pilátová, E. Zatecka, S. Diez, M. Braun, and Z. Lansky, *Anillin propels myosin-independent constriction of actin rings,* Nat Commun. **12**, 4595 (2021).

[111] Z. Lansky, M. Braun, A. Lüdecke, M. Schlierf, P. R. ten Wolde, M. E. Janson, and S. Diez, *Diffusible Crosslinkers Generate Directed Forces in Microtubule Networks,* Cell **160**, 1159 (2015).

[112] H. Wierenga and P. R. ten Wolde, *Diffusible Cross-linkers Cause Superexponential Friction Forces,* Phys. Rev. Lett. **125**, 078101 (2020).

[113] M. Braun, Z. Lansky, G. Fink, F. Ruhnow, S. Diez, and M. E. Janson, *Adaptive breking by Ase1 prevents overlapping microtubules from sliding completely apart,* Nature Cell Biol. **13**, 1259 (2011).

[114] R. Subramanian, S.-C. Ti, L. Tan, S. A. Darst, and T. M. Kapoor, *Marking and measuring single microtubules,* Cell **154**, 377 (2013).

[115] J. C. Sandquist, M. E. Larson, and K. J. Hine, *Myosin-10 independently influences mitotic spindle structure and mitotic progression,* Cytoskeleton (Hoboken) **73**, 351 (2016).

[116] D. van de Willige, J. J. Hummel, C. Alkemade, O. I. Kahn, F. K. Au, R. Z. Qi, M. Dogterom, G. H. Koenderink, C. C. Hoogenraad, and A. Akhmanova, *Cytolinker Gas2L1 regulates axon morphology through microtubule-modulated actin stabilization,* EMBO Rep. **20**, e47732 (2019).

[117] S. P. Maurer, P. Bieling, J. Cope, A. Hoenger, and T. Surrey, *GTPγS microtubules mimic the growing microtubule end structure recognized by end-binding proteins (EBs),* Proc. Natl. Acad. Sci. U.S.A. **108**, 3988 (2011).

[118] T. L. Hill, *Theoretical problems related to the attachment of microtubules to kinetochores,* Proc. Natl. Acad. Sci. U.S.A. **82**, 4404 (1985).

[119] C. S. Peskin, G. M. Odell, and G. F. Oster, *Cellular motions and thermal fluctuations: the Brownian ratchet.* Biophys. J. **65**, 316 (1993).

[120] R. Zandi, D. Reguera, J. Rudnick, and W. M. Gelbart, *What drives the translocation of stiff chains?* Proc. Natl. Acad. Sci. U.S.A. **100**, 8649 (2003).

[121] R. Rodríguez-García, V. A. Volkov, C.-Y. Chen, E. A. Katrukha, N. Olieric, A. Aher, I. Grigoriev, M. Preciado López, M. O. Steinmetz, L. C. Kapitein, G. Koenderink, M. Dogterom, and A. Akhmanova, *Mechanisms of Motor-Independent Membrane Remodeling Driven by Dynamic Microtubules,* Curr. Biol. **30**, 972 (2020).

[122] G. Lan, B. R. Daniels, T. M. Dobrowsky, D. Wirtz, and S. X. Sun, *Condensation of FtsZ filaments can drive bacterial cell division,* Proc. Natl. Acad. Sci. U.S.A. **106**, 121 (2009).

[123] S. Walcott and S. X. Sun, *Active force generation in cross-linked filament bundles without motor proteins,* Phys. Rev. E **82**, 050901 (2010).

[124] J. Feng, Z. Hu, H. Chen, J. Hua, R. Wu, Z. Dong, L. Qiang, Y. Liu, P. W. Baas, and M. Liu, *Depletion of kinesin-12, a myosin-IIB-interacting protein, promotes migration of cortical astrocytes,* J. Cell Sci. **129**, 2438 (2016).

[125] F. J. Ahmad, J. Hughey, T. Wittmann, A. Hyman, M. Greaser, and P. W. Baas, *Motor proteins regulate force interactions between microtubules and microfilaments in the axon,* Nat. Cell Biol. **2**, 276 (2000).

[126] D. L. Beach, J. Thibodeaux, P. Maddox, E. Yeh, and K. Bloom, *The role of the proteins Kar9 and Myo2 in orienting the mitotic spindle of budding yeast,* Curr. Biol. **10**, 1497 (2000).

[127] H. Yin, D. Pruyne, T. C. Huffaker, and A. Bretscher, *Myosin V orientates the mitotic spindle in yeast,* Nature **406**, 1013 (2000).

[128] S. Walcott and S. X. Sun, *A mechanical model of actin stress fiber formation and substrate elasticity sensing in adherent cells,* Proc. Natl. Acad. Sci. U.S.A. **107**, 7757 (2010).

[129] B. Harland, S. Walcott, and S. X. Sun, *Adhesion dynamics and durotaxis in migrating cells,* Phys. Biol. **8**, 015011 (2011).

[130] A. Einstein, *Über die von der molekularkinetischen Theorie der Wärme geforderte Bewegung von in ruhenden Flüssigkeiten suspendierten Teilchen,* Ann. Phys. (Berl.) **322**, 549 (1905).

[131] H. A. Kramers, *Brownian motion in a field of force and the diffusion model of chemical reactions,* Physica **7**, 284 (1940).

[132] M. J. Schnitzer, K. Visscher, and S. M. Block, *Force production by single kinesin motors,* Nat. Cell Biol. **2**, 718 (2000).

[133] M. C. Uçar and R. Lipowsky, *Collective Force Generation by Molecular Motors Is Determined by Strain-Induced Unbinding,* Nano Lett. **20**, 669 (2020).

[134] J. Fink, N. Carpi, T. Betz, A. Bétard, M. Chebah, A. Azioune, M. Bornens, C. Sykes, L. Fetler, D. Cuvelier, and M. Piel, *External forces control mitotic spindle positioning,* Nat. Cell Biol. **13**, 771 (2011).

[135] M. Saltini and B. M. Mulder, *Microtubule-based actin transport and localization in a spherical cell,* R. Soc. Open Sci. **7**, 201730 (2020).

[136] J. D. Fenn, C. M. Johnson, J. Peng, P. Jung, and A. Brown, *Kymograph analysis with high temporal resolution reveals new features of neurofilament transport kinetics,* Cytoskeleton (Hoboken) **75**, 22 (2018).

[137] C. Hookway, L. Ding, M. W. Davidson, J. Z. Rappoport, G. Danuser, and V. I. Gelfand, *Microtubule-dependent transport and dynamics of vimentin intermediate filaments,* Mol. Biol. Cell **26**, 1675 (2015).

[138] C. Leduc and S. Etienne-Manneville, *Regulation of microtubule-associated motors drives intermediate filament network polarization,* J. Cell Biol. **216**, 1689 (2017).

[139] A. Robert, P. Tian, S. A. Adam, M. Kittisopikul, K. Jaqaman, R. D. Goldman, and V. I. Gelfand, *Kinesin-dependent transport of keratin filaments: a unified mechanism for intermediate filament transport,* FASEB J. **33**, 388 (2019).

[140] J. Lutkenhaus, *The ParA/MinD family puts things in their place,* Trends Microbiol. **20**, 411 (2012).

[141] A. G. Vecchiarelli, K. Mizuuchi, and B. E. Funnell, *Surfing biological surfaces: exploiting the nucleoid for partition and transport in bacteria,* Mol. Microbiol. **86**, 513 (2012).

[142] A. G. Vecchiarelli, Y. Seol, K. C. Neuman, and K. Mizuuchi, *A moving ParA gradient on the nucleoid directs subcellular cargo transport via a chemophoresis force,* Bioarchitecture **4**, 154 (2014).

[143] V. A. Volkov, P. J. Huis in 't Veld, M. Dogterom, and A. Musacchio, *Multivalency of NDC80 in the outer kinetochore is essential to track shortening microtubules and generate forces,* eLife **7**, e36764 (2018).

[144] M. Castoldi and A. V. Popov, *Purification of brain tubulin through two cycles of polymerization–depolymerization in a high-molarity buffer,* Protein Expr. Purif. **32**, 83 (2003).

[145] A. Hyman, D. Drechsel, D. Kellogg, S. Salser, K. Sawin, P. Steffen, L. Wordeman, and T. Mitchison, *Preparation of modified tubulins,* in *Methods in Enzymology*, Molecular Motors and the Cytoskeleton, Vol. 196 (Academic Press, 1991) pp. 478–485.

[146] A. W. Avery, M. E. Fealey, F. Wang, A. Orlova, A. R. Thompson, D. D. Thomas, T. S. Hays, and E. H. Egelman, *Structural basis for high-affinity actin binding revealed by a β-III-spectrin SCA5 missense mutation,* Nat. Commun. **8** (2017), 10.1038/s41467-017-01367-w.

[147] Y. Wang, K. Ajtai, and T. P. Burghardt, *Ventricular Myosin Modifies In Vitro Step-Size When Phosphorylated,* J. Mol. Cell Cardiol. **72**, 231 (2014).

[148] L. A. Amos and A. Klug, *Arrangement of Subunits in Flagellar Microtubules,* J. Cell Sci. **14**, 523 (1974).

[149] V. E. Galkin, A. Orlova, M. R. Vos, G. F. Schröder, and E. H. Egelman, *Near-Atomic Resolution for One State of F-Actin,* Structure **23**, 173 (2015).

[150] T. Duke, *Molecular model of muscle contraction,* Proc. Natl. Acad. Sci. U.S.A. **96**, 2770 (1999).

[151] S. Jeney, E. H. K. Stelzer, H. Grubmüller, and E.-L. Florin, *Mechanical Properties of Single Motor Molecules Studied by Three-Dimensional Thermal Force Probing in Optical Tweezers,* ChemPhysChem **5**, 1150 (2004).

[152] H. Ahmadzadeh, D. H. Smith, and V. B. Shenoy, *Viscoelasticity of Tau Proteins Leads to Strain Rate-Dependent Breaking of Microtubules during Axonal Stretch Injury: Predictions from a Mathematical Model,* Biophys. J. **106**, 1123 (2014).

[153] S. Broersma, *Viscous Force Constant for a Closed Cylinder,* J. Chem. Phys. **32**, 1632 (1960), publisher: American Institute of Physics.

[154] S. Broersma, *Viscous force and torque constants for a cylinder,* J. Chem. Phys. **74**, 6989 (1981).

[155] G. Li, Q. Wen, and J. X. Tang, *Single filament electrophoresis of F-actin and filamentous virus fd,* J. Chem. Phys. **122**, 104708 (2005).

[156] A. Vijaykumar, P. G. Bolhuis, and P. R. ten Wolde, *The intrinsic rate constants in diffusion-influenced reactions,* Faraday Discuss. **195**, 421 (2017).

[157] T. A. Reid, C. Coombes, S. Mukherjee, R. R. Goldblum, K. White, S. Parmar, M. McClellan, M. Zanic, N. Courtemanche, and M. K. Gardner, *Structural state recognition facilitates tip tracking of EB1 at growing microtubule ends,* eLife **8**, e48117 (2019).

[158] N. B. Gudimchuk, E. V. Ulyanov, E. O'Toole, C. L. Page, D. S. Vinogradov, G. Morgan, G. Li, J. K. Moore, E. Szczesna, A. Roll-Mecak, F. I. Ataullakhanov, and J. Richard McIntosh, *Mechanisms of microtubule dynamics and force generation examined with computational modeling and electron cryotomography,* Nat. Commun. **11**, 3765 (2020).

[159] D. Boyer, *Optimal estimates of the diffusion coefficient of a single Brownian trajectory,* Phys. Rev. E **85** (2012), 10.1103/PhysRevE.85.031136.

[160] D. Boyer and D. S. Dean, *On the distribution of estimators of diffusion constants for Brownian motion,* J. Phys. A-Math. Theor. **44**, 335003 (2011).

[161] M. Schelski and F. Bradke, *Neuronal polarization: from spatiotemporal signaling to cytoskeletal dynamics,* Mol Cell Neurosci. **84**, 11 (2017).

[162] T. Lewis Jr., J. Courchet, and F. Polleux, *Cell biology in neuroscience: cellular and molecular mechanisms underlying axon formation, growth, and branching,* J Cell Biol. **202**, 837 (2013).

[163] A. Pacheco and G. Gallo, *Actin filament-microtubule interactions in axon initiation and branching,* Brain Res Bull. **126**, 300 (2016).

[164] K. Kalil and E. Dent, *Branch management: mechanisms of axon branching in the developing vertebrate CNS,* Nat Rev Neurosci. **15**, 7 (2014).

[165] D. Gibson and L. Ma, *Developmental regulation of axon branching in the vertebrate nervous system,* Development **138**, 183 (2011).

[166] K. Röper, S. L. Gregory, and H. Brown, Nicholas, *The 'spectraplakins': cytoskeletal giants with characteristics of both spectrin and plakin families,* J Cell Sci. **115**, 4215 (2002).

[167] M. Ka and W. Kim, *Microtubule-actin crosslinking factor 1 is required for dendritic arborization and axon outgrowth in the developing brain,* Mol Neurobiol. **53**, 6018 (2016).

[168] U. Engel, Y. Zhan, J. Long, S. Boyle, B. Ballif, K. Dorey, S. Gygi, A. Koleske, and D. Van Vactor, *Abelson phosphorylation of CLASP2 modulates its association with microtubules and actin,* Cytoskeleton (Hoboken) **71**, 195 (2014).

[169] F. Zhou, J. Zhou, S. Dedhar, Y. Wu, and W. Snider, *NGF-induced axon growth is mediated by localized inactivation of GSK-3β and functions of the microtubule plus end binding protein APC,* Neuron **42**, 897 (2004).

[170] D. Goriounov, C. Leung, and R. Liem, *Protein products of human Gas2-related genes on chromosomes 17 and 22 (hGAR17 and hGAR22) associate with both microfilaments and microtubules,* J Cell Sci. **116**, 1045 (2003).

[171] K. Jiang, G. Toedt, S. Montenegro Gouveia, N. Davey, S. Hua, B. van der Vaart, I. Grigoriev, J. Larsen, L. Pedersen, K. Bezstarosti, M. Lince-Faria, J. Demmers, M. Steinmetz, T. Gibson, and A. Akhmanova, *A proteome-wide screen for mammalian sxip motif-containing microtubule plus-end tracking proteins,* Curr Biol. **22**, 1800 (2012).

[172] F. Au, Y. Jia, K. Jiang, I. Grigoriev, B. Hau, Y. Shen, S. Du, A. Akhmanova, and R. Qi, *GAS2L1 is a centriole-associated protein required for centrosome dynamics and disjunction,* Dev Cell **40**, 81 (2017).

[173] M. Pines, B. Housden, F. Bernard, S. Bray, and K. Röper, *The cytolinker Pigs is a direct target and a negative regulator of Notch signalling,* Development **137**, 913 (2010).

[174] S. van Beuningen, L. Will, M. Harterink, A. Chazeau, E. van Battum, C. Frias, M. Franker, E. Katrukha, R. Stucchi, K. Vocking, A. Antunes, L. Slenders, S. Doulkeridou, P. Sillevis Smith, A. Altelaar, J. Post, A. Akhmanova, R. Pasterkamp,

L. Kapitein, E. de Graaff, and C. Hoogenraad, *TRIM46 controls neuronal polarity and axon specification by driving the formation of parallel microtubule arrays,* Neuron **88**, 1208 (2015).

[175] F. Bradke and G. Dotti, *The role of local actin instability in axon formation,* Science **283**, 1931 (1999).

[176] J. Chia, N. Efimova, and T. Svitkina, *Neurite outgrowth is driven by actin polymerization even in the presence of actin polymerization inhibitors,* Mol Biol Cell **27**, 3695 (2016).

[177] E. Dent and K. Kalil, *Axon branching requires interactions between dynamic microtubules and actin filaments,* J Neurosci. **21**, 9757 (2001).

[178] K. Flynn, F. Hellal, D. Neukirchen, S. Jacob, S. Tahirovic, S. Dupraz, S. Stern, B. Garvalov, C. Gurniak, A. Shaw, L. Meyn, R. Wedlich-Söldner, J. Bamburg, J. Small, W. Witke, and F. Bradke, *ADF/cofilin-mediated actin retrograde flow directs neurite formation in the developing brain,* Neuron **76**, 1091 (2012).

[179] G. Gallo, H. Yee, and P. Letourneau, *Actin turnover is required to prevent axon retraction driven by endogenous actomyosin contractility,* J Cell Biol. **158**, 1219 (2002).

[180] W. Lu, P. Fox, M. Lakonishok, M. Davidson, and V. Gelfand, *Initial neurite outgrowth in Drosophila neurons is driven by kinesin-powered microtubule sliding,* Curr Biol. **23**, 1018 (2013).

[181] M. Magiera, P. Singh, S. Gadadhar, and C. Janke, *Tubulin posttranslational modifications and emerging links to human disease,* Cell **173**, 1323 (2018).

[182] S. Gadadhar, S. Bodakuntla, K. Natarajan, and C. Janke, *The tubulin code at a glance,* J Cell Sci. **130**, 1347 (2017).

[183] M. Gimona, K. Djinovic-Carugo, W. Kranewitter, and S. Winder, *Functional plasticity of CH domains,* FEBS Lett. **513**, 98 (2002).

[184] E. Yarmola, T. Somasundaram, T. Boring, I. Spector, and M. Bubb, *Actin-latrunculin A structure and function. Differential modulation of actin-binding protein function by latrunculin A,* J Biol Chem. **275**, 28120 (2000).

[185] S. Lee, K. Harris, P. Whitington, and P. Kolodziej, *Short stop is allelic to kakapo, and encodes rod-like cytoskeletal-associated proteins required for axon extension,* J Neurosci. **20**, 1096 (2000).

[186] W. Sayyad, L. Amin, P. Fabris, E. Ercolini, and V. Torre, *The role of myosin-II in force generation of DRG filopodia and lamellipodia,* Sci Rep. **5**, 7842 (2015).

[187] S. Turney, M. Ahmed, I. Chandrasekar, R. Wysolmerski, Z. Goeckler, R. Rioux, G. Whitesides, and P. Bridgman, *Nerve growth factor stimulates axon outgrowth through negative regulation of growth cone actomyosin restraint of microtubule advance,* Mol Biol Cell **27**, 500 (2016).

[188] K. Kollins, J. Hu, P. Bridgman, Y. Huang, and G. Gallo, *Myosin-II negatively regulates minor process extension and the temporal development of neuronal polarity,* Dev Neurobiol. **69**, 279 (2009).

[189] A. Schaefer, V. Schoonderwoert, L. Ji, N. Mederios, G. Danuser, and P. Forscher, *Coordination of actin filament and microtubule dynamics during neurite outgrowth,* Dev Cell **15**, 146 (2008).

[190] L. Lowery and D. Van Vactor, *The trip of the tip: understanding the growth cone machinery,* Nat Rev Mol Cell Biol. **10**, 332 (2009).

[191] S. Montenegro Gouveia, K. Leslie, L. Kapitein, R. Buey, I. Grigoriev, M. Wagenbach, I. Smal, E. Meijering, C. Hoogenraad, L. Wordeman, M. Steinmetz, and A. Akhmanova, *In vitro reconstitution of the functional interplay between MCAK and EB3 at microtubule plus ends,* Curr Biol. **20**, 1717 (2010).

[192] L. Michaelis, M. Menten, K. Johnson, and R. Goody, *The original michaelis constant: translation of the 1913 michaelis-menten paper,* Biochem. **50**, 8264 (2011).

[193] L. Kapitein, K. Yau, and C. Hoogenraad, *Microtubule dynamics in dendritic spines,* Methods Cell Biol. **97**, 111 (2010).

[194] O. Kahn, P. Schatzle, D. van de Willige, R. Tas, F. Lindhout, S. Portegies, L. Kapitein, and C. Hoogenraad, *APC2 controls dendrite development by promoting microtubule dynamics,* Nat Commun. **9**, 2773 (2018).

[195] C. Hoogenraad, A. Milstein, I. Ethell, M. Henkemeyer, and M. Sheng, *GRIP1 controls dendrite morphogenesis by regulating EphB receptor trafficking,* Nat Neurosci. **8**, 906 (2005).

[196] G. Lansbergen, I. Grigoriev, Y. Mimori-Kiyosue, T. Ohtsuka, S. Higa, I. Kitajima, J. Demmers, N. Galjart, A. Houtsmuller, F. Grosveld, and A. Akhmanova, *CLASPs attach microtubule plus ends to the cell cortex through a complex with LL5β,* Dev Cell **11**, 21 (2006).

[197] B. van der Vaart, W. van Riel, H. Doodhi, J. Kevenaar, E. Katrukha, L. Gumy, B. Bouchet, I. Grigoriev, S. Spangler, K. Yu, P. Wulf, J. Wu, G. Lansbergen, E. van Battum, R. Pasterkamp, Y. Mimori-Kiyosue, J. Demmers, N. Olieric, I. Maly, C. Hoogenraad, and A. Akhmanova, *CFEOM1-associated kinesin KIF21A is a cortical microtubule growth inhibitor,* Dev Cell **27**, 145 (2013).

[198] M. Kuijpers, D. van de Willige, A. Freal, A. Chazeau, M. Franker, J. Hofenk, R. Rodrigues, L. Kapitein, A. Akhmanova, D. Jaarsma, and C. Hoogenraad, *Dynein regulator NDEL1 controls polarized cargo transport at the axon initial segment,* Neuron **89**, 461 (2016).

[199] T. Brummelkamp, R. Bernards, and R. Agami, *A system for stable expression of short interfering RNAs in mammalian cells,* Science **296**, 550 (2002).

[200] E. Meijering, M. Jacob, J. Sarria, P. Steiner, H. Hirling, and M. Unser, *Design and validation of a tool for neurite tracing and analysis in fluorescence microscopy images,* Cytometry A. **58**, 167 (2004).

[201] R. C. Adikes, R. A. Hallett, B. F. Saway, B. Kuhlman, and K. C. Slep, *Control of microtubule dynamics using an optogenetic microtubule plus end–F-actin cross-linker,* J. Cell Biol. **217**, 779 (2018).

[202] R. Mohan and A. John, *Microtubule-associated proteins as direct crosslinkers of actin filaments and microtubules,* IUBMB Life **67**, 395 (2015).

[203] Y. Yan, E. Winograd, A. Viel, T. Cronin, S. Harrison, and D. Branton, *Crystal structure of the repetitive segments of spectrin,* Science **262**, 2027 (1993).

[204] C. Leung, D. Sun, M. Zheng, D. Knowles, and R. Liem, *Microtubule actin crosslinking factor (MACF): a hybrid of dystonin and dystrophin that can interact with the actin and microtubule cytoskeletons,* J. Cell Biol. **147**, 1275 (1999).

[205] H.-J. Chen, C.-M. Lin, C.-S. Lin, R. Perez-Olle, C. L. Leung, and R. K. Liem, *The role of microtubule actin cross-linking factor 1 (MACF1) in the Wnt signaling pathway,* Genes Dev. **20**, 1933 (2006).

[206] J. Faix, M. Steinmetz, H. Boves, R. Kammerer, F. Lottspeich, U. Mintert, J. Murphy, A. Stock, U. Aebi, and G. Gerisch, *Cortexillins, major determinants of cell shape and size, are actin-bundling proteins with a parallel coiled-coil tail,* Cell **86**, 631 (1996).

[207] M. van Rosmalen, M. Krom, and M. Merkx, *Tuning the flexibility of glycine-serine linkers to allow rational design of multidomain proteins,* Biochemistry **56**, 6565 (2017).

[208] M. Zanic, P. O. Widlund, A. A. Hyman, and J. Howard, *Synergy between XMAP215 and EB1 increases microtubule growth rates to physiological levels,* Nat. Cell Biol. **15**, 688 (2013).

[209] E. O. Alberico, Z. C. Zhu, Y.-F. O. Wu, M. Gardner, D. R. Kovar, and H. V. Goodson, *Interactions between the microtubule binding protein EB1 and F-actin,* J Mol Biol. **428**, 1304 (2016).

[210] L. Munteanu, *Dynamics and regulation at the tip: a high resolution view on microtubule assembly*, Dissertation, Universiteit Leiden, Leiden (2008).

[211] M. W. Kok, *The dynamics of microtubule stability: a reconstitution of regulated microtubule assembly under force*, Dissertation, Technische Universiteit Delft, Delft (2019).

[212] Y. Mulla, H. Wierenga, C. Alkemade, P. R. ten Wolde, and G. H. Koenderink, *Frustrated binding of biopolymer crosslinkers,* Soft Matter **15**, 3036 (2019).

[213] D. A. Applewhite, K. D. Grode, D. Keller, A. D. Zadeh, K. C. Slep, and S. L. Rogers, *The spectraplakin Short stop is an actin–microtubule cross-linker that contributes to organization of the microtubule network,* Mol. Biol. Cell **21**, 1714 (2010).

[214] K. Ichihara, H. Kitazawa, Y. Iguchi, H. Hotani, and T. J. Itoh, *Visualization of the stop of microtubule depolymerization that occurs at the high-density region of microtubule-associated protein 2 (MAP2),* J Mol Biol. **312**, 107 (2002).

[215] J. Al-Bassam, H. Kim, G. Brouhard, A. van Oijen, S. C. Harrison, and F. Chang, *CLASP promotes microtubule rescue by recruiting tubulin dimers to the microtubule,* Dev Cell. **19**, 245 (2010).

[216] Y. A. Komarova, A. S. Akhmanova, S.-i. Kojima, N. Galjart, and G. G. Borisy, *Cytoplasmic linker proteins promote microtubule rescue in vivo,* J Cell Biol. **159**, 589 (2002).

[217] M. Théry and L. Blanchoin, *Microtubule self-repair,* Curr Opin Cell Biol. **68**, 144 (2021).

[218] G. Young, N. Hundt, D. Cole, A. Fineberg, J. Andrecka, A. Tyler, A. Olerinyova, A. Ansari, E. G. Marklund, M. P. Collier, S. A. Chandler, O. Tkachenko, J. Allen, M. Crispin, N. Billington, Y. Takagi, J. R. Sellers, C. Eichmann, P. Selenko, L. Frey, R. Riek, M. R. Galpin, W. B. Struwe, J. L. P. Benesch, and P. Kukura, *Quantitative mass imaging of single biological macromolecules,* Science **360**, 423 (2018).

[219] P. Bieling, L. Laan, H. Schek, E. L. Munteanu, L. Sandblad, M. Dogterom, D. Brunner, and T. Surrey, *Reconstitution of a microtubule plus-end tracking system in vitro,* Nature **450**, 1100 (2007).

[220] C. Martinez-Torres, F. Burla, C. Alkemade, and G. H. Koenderink, *Revealing the assembly of filamentous proteins with scanning transmission electron microscopy,* PLoS One **14**, e0226277 (2019).

[221] K. J. Vendel, C. Alkemade, N. Andrea, G. H. Koenderink, and M. Dogterom, *In vitro reconstitution of dynamic co-organization of microtubules and actin filaments in emulsion droplets,* Methods Mol Biol. **2101**, 53 (2020).

[222] S. Huda, S. Soh, D. Pilans, M. Byrska-Bishop, J. Kim, G. Wilk, G. G. Borisy, K. Kandere-Grzybowska, and B. A. Grzybowski, *Microtubule guidance tested through controlled cell geometry,* J. Cell Sci. **125**, 5790 (2012).

[223] E. Bazellières, D. Massey-Harroche, M. Barthélémy-Requin, F. Richard, J. P. Arsanto, and A. Le Bivic, *Apico-basal elongation requires a drebrin-E-EB3 complex in columnar human epithelial cells,* J. Cell Sci. **125**, 919 (2012).

[224] F. Zhou, C. Waterman-Storer, and C. Cohan, *Focal loss of actin bundles causes microtubule redistribution and growth cone turning,* J. Cell Biol. **157**, 839 (2002).

[225] K. Zaoui, K. Benseddik, P. Daou, D. Salaun, and A. Badache, *ErbB2 receptor controls microtubule capture by recruiting ACF7 to the plasma membrane of migrating cells,* Proc. Natl Acad. Sci. USA **107**, 18517 (2010).

[226] P. Kunda and B. Baum, *The actin cytoskeleton in spindle assembly and positioning,* Trends Cell Biol. **19**, 174 (2009).

[227] H. Bringmann and A. Hyman, *A cytokinesis furrow is positioned by two consecutive signals,* Nature **436**, 731 (2005).

[228] M. Abercrombie, *The bases of the locomotory behaviour of fibroblasts,* Exp. Cell Res **Suppl 8**, 188 (1961).

[229] L. Laan, N. Pavin, J. Husson, G. Romet-Lemonne, M. van Duijn, M. P. López, R. D. Vale, F. Jülicher, S. L. Reck-Peterson, and M. Dogterom, *Cortical dynein controls microtubule dynamics to generate pulling forces that position microtubule asters,* Cell **148**, 502 (2012).

[230] J. Alvarado, B. Mulder, and G. Koenderink, *Alignment of nematic and bundled semiflexible polymers in cell-sized confinement,* Soft Matter **10**, 2354 (2014).

[231] H. Baumann and T. Surrey, *Motor-mediated cortical versus astral microtubule organization in lipid-monolayered droplets,* Journal of Biological Chemistry **289**, 22524 (2014).

[232] M. P. Juniper, M. Weiss, I. Platzman, J. P. Spatz, and T. Surrey, *Spherical network contraction forms microtubule asters in confinement,* Soft matter **14**, 901 (2018).

[233] M. S. e Silva, J. Alvarado, J. Nguyen, N. Georgoulia, B. M. Mulder, and G. H. Koenderink, *Self-organized patterns of actin filaments in cell-sized confinement,* Soft Matter **7**, 10631 (2011).

[234] L.-L. Pontani, J. Van der Gucht, G. Salbreux, J. Heuvingh, J.-F. Joanny, and C. Sykes, *Reconstitution of an actin cortex inside a liposome,* Biophysical journal **96**, 192 (2009).

[235] M. Pinot, F. Chesnel, J. Kubiak, I. Arnal, F. J. Nedelec, and Z. Gueroui, *Effects of confinement on the self-organization of microtubules and motors,* Current Biology **19** (2009).

[236] E. A. Shah and K. Keren, *Symmetry breaking in reconstituted actin cortices,* Elife **3**, e01433 (2014).

[237] K. Takiguchi, A. Yamada, M. Negishi, Y. Tanaka-Takiguchi, and K. Yoshikawa, *Entrapping desired amounts of actin filaments and molecular motor proteins in giant liposomes,* Langmuir **24**, 11323 (2008).

[238] F. Tsai and G. Koenderink, *Shape control of lipid bilayer membranes by confined actin bundles,* Soft Matter **11**, 8834 (2015).

[239] K. Carvalho, F.-C. Tsai, E. Lees, R. Voituriez, G. H. Koenderink, and C. Sykes, *Cell-sized liposomes reveal how actomyosin cortical tension drives shape change,* Proceedings of the National Academy of Sciences **110**, 16456 (2013).

[240] S. Roth, L. Laan, and M. Dogterom, *Reconstitution of cortical dynein function,* Methods in enzymology **540**, 205 (2014).

[241] N. Taberner, A. Lof, S. Roth, D. Lamers, H. Zeijlemaker, and M. Dogterom, *In vitro systems for the study of microtubule-based cell polarity in fission yeast,* Methods in cell biology **128** (2015).

[242] M. Vleugel, S. Roth, C. Groenendijk, and M. Dogterom, *Reconstitution of basic mitotic spindles in spherical emulsion droplets,* J Vis. Exp. **13** (2016).

[243] G. Lukinavičius, L. Reymond, E. D'este, A. Masharina, F. Göttfert, H. Ta, A. Güther, M. Fournier, S. Rizzo, H. Waldmann, *et al.*, *Fluorogenic probes for live-cell imaging of the cytoskeleton,* Nature methods **11**, 731 (2014).

[244] M. M. Claessens, M. Bathe, E. Frey, and A. R. Bausch, *Actin-binding proteins sensitively mediate F-actin bundle stiffness,* Nature Materials **5**, 748 (2006).

[245] S. Baumann, A. Komissarov, M. Gili, V. Ruprecht, S. Wieser, and S. P. Maurer, *A reconstituted mammalian APC-kinesin complex selectively transports defined packages of axonal mRNAs,* Science Advances **6**, 4763 (2020).

[246] M. Angeles Juanes, C. P. Fees, G. J. Hoeprich, R. Jaiswal, and B. L. Goode, *EB1 directly regulates APC-mediated actin nucleation,* Curr Biol. **30**, 4763 (2020).

[247] P. M. McCall, F. C. MacKintosh, D. R. Kovar, and M. L. Gardel, *Cofilin drives rapid turnover and fluidization of entangled F-actin,* PNAS **116**, 12629 (2019).

[248] G. Salbreux, G. Charras, and E. Paluch, *Actin cortex mechanics and cellular morphogenesis,* Trends Cell Biol. **22**, 536 (2012).

[249] F. Bartolini and G. Gundersen, *Formins and microtubules,* Biochim Biophys Acta. **1803**, 164 (2010).

[250] C. Ciobanasu, B. Faivre, and C. Le Clainche, *Actomyosin-dependent formation of the mechanosensitive talin–vinculin complex reinforces actin anchoring,* Nat Commun **5**, 3095 (2014).

[251] V. Wollrab, J. M. Belmonte, L. Baldauf, M. Leptin, F. Nédeléc, and G. H. Koenderink, *Polarity sorting drives remodeling of actin-myosin networks,* J Cell Sci. **132**, jcs219717 (2018).

[252] O. M. Lancaster and B. Baum, *Shaping up to divide: coordinating actin and microtubule cytoskeletal remodelling during mitosis,* Semin Cell Dev Biol. **34**, 109 (2014).

[253] H. Jia and P. Schwille, *Bottom-up synthetic biology: reconstitution in space and time,* Curr Opin Biotechnol. **60**, 179 (2019).

[254] W. K. Spoelstra, S. Deshpande, and C. Dekker, *Tailoring the appearance: what will synthetic cells look like?* Curr Opin Biotechnol. **51**, 47 (2018).

SAMENVATTING

Het menselijke lichaam bestaat uit zo'n $3-4\times10^{13}$ (30-40 biljoen) cellen [1]. Deze cellen functioneren allemaal op een betrouwbare manier, en werken elegant met elkaar samen, om het levende organisme waar ze onderdeel van zijn in stand te houden. Niet alleen mensen, maar alle levende organisme op aarde (van planten tot papegaaien) zijn samengesteld uit cellen, al bestaan sommige organismen zoals bacteriën slechts uit een enkele cel. Cellen zijn dan ook de kleinst-levende bouwstenen van planten en dieren; elke cel is een klein stukje 'leven' op zichzelf dat kan repliceren, sterven, en een ongelofelijke diversiteit aan fucties kan uitvoeren.

Om het leven van meercellige organisme in stand te houden moeten cellen flexibele en dynamische entiteiten zijn, die kunnen groeien, delen, en interacteren met hun omgeving. Ze bereiken dit door een scala aan zeer complexe en dynamische processen. Voor bijvoorbeeld celdeling, een essentiele functie voor leven, moet een cel dramatisch van vorm veranderen. Naast deze vormveranderingen moet de interne cellulaire organisatie ook strak gecontroleerd worden om goed te kunnen functioneren. Cellen moeten bijvoorbeeld een voor-achterkant polariteit bewerkstelligen om directionele migratie aan te drijven. Dit is belangrijk voor o.a. immuun-cellen die op jacht zijn naar indringers en hiervoor in beweging zijn. De cellulaire vorm en interne organisatie is kortom van cruciaal belang voor een organism, en is daarnaast ook nauw verwant aan het goed functioneren van hersenencellen (ook wel neuronen genoemd).

Het vermogen van cellen, eigenlijk kleine zakjes gevuld met eiwitten, om van vorm en interne organisatie te veranderen is afhankelijk van een interne stellage genaamd het cytoskelet. Dit 'cellulaire skelet' is in tegenstelling tot ons eigen (lichamelijke) skelet heel dynamisch, waarbij de filamenten waaruit het bestaat continu worden opgebouwd, afgebroken, en gereorganiseerd. Het cytoskelet doet dan ook veel meer dan een gewoon skelet: naast het geven van stabiliteit aan een cel, zorgt het ook voor de organisatie binnen een cel, het genereren van krachten, en voor de vormveranderingen.

De twee voornaamste componenten van het cytoskelet zijn draden van eiwitten genaamd microtubuli en actine filamenten. Ze worden meestal bestudeerd als losstaande systemen, omdat ze op andere manieren zijn opgebouwd en verschillende eigenschappen hebben. Er is echter steeds meer bewijs dat hun functies in werkelijkheid nauw met elkaar zijn verweven en dat ze voor het correct uitvoeren hiervan afhankelijk van elkaar zijn. In dit proefschrift wordt bestudeerd hoe deze twee componenten van het cytoskelet elkaar beïnvloeden. In het bijzonder focussen wij op de vraag hoe actine en microtubuli elkaar organiseren en coördineren via een bepaald soort eiwitten die beide filamenten fysiek aan elkaar koppelt, de zogenoemde cytolinkers.

Om goed te kunnen bestuderen hoe cytolinkers invloed hebben op de coördinatie van het cytoskelet gaan we weg uit de complexe omgeving van de cel, waar veel andere eiwitten aanwezig zijn en waar veel verschillende andere processen plaatsvinden. We nemen de bouwstenen van het cytoskelet en de cytolinkers uit de cel, en herbouwen ze

buiten de cel zodat ze in een geïsoleerde omgeving bestudeerd kunnen worden. Door fluoriderende elementen aan de eiwitten toe te voegen, worden ze zichtbaar met fluorescentie microscopie. Naast het gebruik van natuurlijke cytolinkers ontwerpen we ook onze eigen cytolinkers, zodat we beter begrijpen hoe specifieke karakteristieken van deze eiwitten de coördinatie beïnvloeden. De geïsoleerde omgeving is een krachtig middel om cellulaire functies te bestuderen, aangezien de vereenvoudiging ons in staat stelt de variabelen strak te controleren en zodoende de onderliggende mechanismen duidelijker te identificeren.

VOORNAAMSTE BEVINDINGEN VAN DIT PROEFSCHRIFT

Het onderzoek van componenten van levende cellen of organismen buiten hun 'levende' omgeving wordt *in vitro* onderzoek genoemd. In dit proefschrift wordt *in vitro* onderzoek gebruikt om middels een 'bottom-up' benadering het biologische proces van microtubuli/actine coördinatie te reconstrueren. De meeste experimenten zijn uitgevoerd met *total internal reflection fluorescence* (TIRF) microscopie om een hoge plaatselijke en temporele resolutie te verkrijgen. We gebruiken deze microscopie voor het karateriseren van zowel natuurlijke cytolinkers als onze eigen, simpelere, ontworpen cytolinkers. We bestuderen hun effecten op actine filament reorganisatie en op de groei dynamieken van microtubuli. Het verkrijgen van een gedetailleerd begrip op hoe cytolinkers invloed hebben op microtubuli/actin coördinatie biedt nieuwe inzichten in de manier waarop actine en microtubuli invloed op elkaar hebben. Gekeken wordt hoe actine filamenten de groei van microtubuli kunnen beïnvloeden, een belangrijk karakter van microtubuli aangezien het hun organisatie in een cel bepaald. Daarnaast kijken we ook hoe deze groei van microtubuli vervolgens weer invloed heeft op de actine organisatie.

In Hoofdstuk 1 geven we een algemene introductie in het onderwerp, onze motivatie, en het doel van dit proefschrift. In Hoofdstuk 2 lichten we de methodes en materialen toe die gebruikt zijn voor de *in vitro* reconstitutie studies.

Hoofdstuk 3 combineert experimentele en theoretische studies om te laten zien dat microtubuli actine filamenten kunnen verplaatsten die aan de groeiende microtubuli uiteinden vastzitten via een eiwit-complex van EB3 en cytolinkers. We laten zien dat deze vorm van cytolinker-aangedreven transport wordt beheerst door een samenspel van twee krachten, namelijk een affiniteit-gedreven voorwaartse condensatie kracht en een tegenwerkende frictie kracht. We tonen dat het koppelen van microtubuli en actine via passieve cytolinkers een nieuwe manier is waarmee elementen van het cytoskelet elkaar kunnen coördineren en krachten op elkaar uitvoeren, wat in dit geval resulteert in het transport van actine filamenten.

In Hoofdstuk 4 combineren we onze *in vitro* experimenten met onderzoek in hersencellen om een natuurlijke cytolinker genaamd Gas2Like1 (Gas2L1) te karakteriseren. We tonen aan dat Gas2L1 geautoïnhibeerd is, wat inhoudt dat het eiwit niet goed werkt door interacties met zichzelf. Deze auto-inhibitie wordt verholpen wanneer Gas2L1 kan binden aan plekken waar microtubuli en actine overlappen, wat zorgt voor een elegant mechanisme om de cytolinker specifiek te lokaliseren waar het nodig is. Daarnaast zien we ook dat, in aanwezigheid van actine filamenten, Gas2L1 de groei dynamica van microtubuli verandert door een grote toename in de microtubuli 'rescue' frequentie, wat inhoudt dat de microtubuli minder lang krimpt. Verder laten we zien dat Gas2L1 in

hersencellen voornamelijk lokaliseert op het actine cytoskelet en daar functioneert als een actine stabilisator, waarbij de lokalisatie gereguleerd wordt door microtubuli.

In Hoofdstuk 5 gebruiken we de natuurlijke cytolinker Shot (uit *Drosophila*) als een model eiwit om simpelere cytolinkers te ontwerpen en bestuderen. De meeste cytolinker eiwitten bezitten twee verschillende domeinen waarmee ze kunnen binden aan microtubuli, namelijk via EB-eiwitten aan de groeiende uiteinden van microtubuli, of direct aan de schacht van microtubuli. We vragen ons af hoe de moleculaire anatomie van cytolinkers invloed heeft op MT/actine coördinatie. Door onze cytolinkers zelf te ontwerpen op basis van Shot hebben we controle over de verschillende cytolinker-domeinen die het cytoskelet binden, alsook de domeinen op de cytolinker die hier tussen liggen. We focussen specifiek op de co-organisatie van het cytoskelet en op de groei-dynamica van microtubuli, en zien dat het koppelen van actine filamenten aan het groeiende uiteinde van microtubuli resulteert in dynamische actine reorganisaties. Vice versa resulteert het koppelen van actine filamenten aan de microtubuli schachten in langdurigere reorganisaties van actine, en in consistentere groei van microtubuli waarbij vele 'rescues' plaastvinden (gebeurtenissen waarbij de krimp van een microtubuli vroegtijdig wordt omgezet in groei).

In Hoofdstuk 6 presenteren we een nieuwe methode om de microtubuli/actine organisatie te bestuderen in 3D compartimenten van cel-formaat, bestaande uit water-in-olie emulsie druppeltjes. Terwijl alle *in vitro* experimenten in voorgaande hoofdstukken worden uitgevoerd in quasi-2D om de hoge resoluties te behalen met TIRF microscopie, laat dit hoofdstuk zien dat we dynamische microtubuli, die groeien vanuit centrosomen, kunnen laten interageren met actine filamenten in een 3D bolvormige container via de ontworpen cytolinker TipAct. Daarnaast verschaffen we gedetailleerde protocollen en bespreken we optimalisatie stappen die nodig zijn voor het bouwen van deze complexere *in vitro* model systemen van cytoskelet co-organisatie.

Het werk in dit proefschrift laat de kracht zien van 'bottom-up' (*in vitro*) experimenten om de interacties van microtubuli en actine via cytolinkers te bestuderen. We laten zien dat een nieuw mechanisme van microtubuli/actine coördinatie (namelijk actine transport) begrepen kan worden door de onderliggende moleculaire interacties van de cytolinker te bestuderen. Daarnaast tonen we dat de regulatie van cytolinker activiteit in hersencellen (namelijk Gas2L1) begrepen kan worden door *in vitro* karakterisering. Verder laten we ook zien dat, door zelf-ontworpen cytolinkers te gebruiken, we kunnen beginnen te begrijpen hoe de moleculaire anatomie van natuurlijke cytolinkers de microtubuli/actine coördinatie kan beïnvloeden. Tenslotte tonen we dat de *in vitro* experimenten ook gebruikt kunnen worden om microtubuli/actine coördinatie te bestuderen in cel-achtige geometrieën. Dit proefschrift kan dienen als een basis voor toekomstige studies voor het ontrafelen van microtubuli/actin coördinatie door cytolinkers. Het laatste Hoofdstuk 7 van dit proefschrift presenteert een beknopte samenvatting van enkele voorbeelden voor toekomstige onderzoeksrichtingen, geïllustreerd door middel van proof-of-concept resultaten.

CURRICULUM VITÆ

Celine ALKEMADE

05-01-1990 Born in Utrecht, The Netherlands.

EDUCATION

2002–2008 Atheneum
Segbroek College, The Hague, The Netherlands

2008–2013 Bachelor of Science in Physics
Utrecht University, Utrecht, The Netherlands
Internship: "User-friendly two-photon microendoscope for *in vivo* imaging" at the Molecular Biophysics group (UU)

2013–2015 Master of Science in Physics
University of Amsterdam, Amsterdam, The Netherlands
Internship: "Interactions of formins mDia1 and mDia2 on septin polymerization" at the Biological Soft Matter group (AMOLF)

2015–2021 Ph.D. Biophysics
Delft University of Technology (Delft, The Netherlands)
and AMOLF (Amsterdam, The Netherlands)
Thesis: Reconstituting microtubule-actin coordination by cytolinkers
Promotors: Prof. dr. Gijsje H. Koenderink
Prof. dr. Marileen Dogterom

AWARDS

2017 Scholarship to Woods Hole MBL 2017 Summer Course in Physiology

List of Publications

Publications covered in this thesis:

3. **Celine Alkemade**[*], Harmen Wierenga[*], Vladimir A. Volkov, Magdalena Preciado López, Anna Akhmanova, Pieter Rein ten Wolde, Marileen Dogterom, Gijsje H. Koenderink, *Cross-linkers at growing microtubule ends generate forces that drive actin transport*, (2021, under revision at PNAS). Preprint online on BioRxiv: 2021.07.09.451744 (2021).

2. Kim J.A. Vendel[*], **Celine Alkemade**[*], Nemo Andrea, Gijsje H. Koenderink, Marileen Dogterom, *In vitro reconstitution of dynamic co-organization of microtubules and actin filaments in emulsion droplets*, Methods in Mol. Biol. **2101:53-75** (2020).

1. Dieudonnée van de Willige[*], Jessica J.A. Hummel[*], **Celine Alkemade**[*], Olga I. Kahn, Marileen Dogterom, Gijsje H. Koenderink, Casper C. Hoogenraad, Anna Akhmanova, *Cytolinker Gas2L1 regulates axon morphology through microtubule-modulated actin stabilization*, EMBO Rep. **20**, e47732 (2019).

Other publications:

2. Cristina Martinez-Torres, Federica Burla, **Celine Alkemade**, Gijsje Koenderink, *Revealing the Assembly of Filamentous Proteins with Scanning Transmission Electron Microscopy*, PLoS ONE **14**(12), e0226277 (2019).

1. Yuval Mulla, Harmen Wierenga, **Celine Alkemade**, Pieter-Rein ten Wolde, Gijsje H. Koenderink, *Frustrated binding of biopolymer crosslinkers*, Soft Matter **15**, 3036 (2019).

[*]These authors contributed equally to this work.

ACKNOWLEDGEMENTS

My scientific journey over the last years was greatly supported by many people, whom I would like to thank in this section.

First of all, my promotors Gijsje and Marileen, thank you both for your trust and guidance, especially during the final (and more difficult) years of my PhD. Although getting you both together in the same room proofed to be challenging due to continuously crammed agendas, I've greatly enjoyed the co-supervision and I will never forget your invaluable roles. Gijsje, thank you for taking the time to discuss new results and provide feedback on new ideas: your enthusiasm (and excellent organization skills) have kept me motivated, and will continue to inspire me. Marileen, thank you for keeping the big picture and showing me how to be more pragmatic.

Next, I want to thank my paranymphs, who've made AMOLF and TU Delft warm places to work. Marco, thank you for all the coffee, drinks, parties and dinners. And I've greatly enjoyed the tour in Milan. Esengül, thank you for your great enthusiasm and keeping me up-to-date whenever I visited Delft. And for getting my PhD started with 'Strawberry Milkshakes'. I'm looking forward to celebrating my PhD with both of you!

Some of the work in this thesis would not have been possible without very fruitful collaborations. Anna and Pieter Rein, thank you for all the discussions and valuable input to the *in vitro* experiments. Dieudonnée and Jessica, thank you for your work in neurons. Amol and Dipti, thank you for your help with purifications. Guillaume and Antoine, thank you for hosting us in Paris.

Being part of two research groups, I have had the chance to meet a lot of wonderful people. Yuval and Agata, thanks for your supervision during and after my master project. Viktoria, for sharing the lab bench and your dry humour. Federica, for the good talks and drinks (and swims in Amsterdam canals). Anders, for sharing the MT at AMOLF and your advices. Cristina, for your morning happiness and enthusiasm for MT at EM grids. Maurits, for discussing both science and life (and your kind words during 'Delftse Lichtjesnacht'). Kim, for the nice office talks and the crosstalk-droplets. Vladimir, for your critical questions and force measurements (please don't bike near the Atomium in Brussel anymore). Renu, for providing smart/geeky bags whenever I was moving proteins again (and for not minding waking up in Heidelberg whenever I entered the room). Lennard, for enduring my 'in-depth' introduction into the microscope (and compliments on your curling skills). Lucia, for the inspiring scientific views and your happiness. Mathijs, for the early train rides to Delft from Utrecht (and starting centrosome purifications). Louis, for your curiosity and kindness (and colourful jackets and hats). Ilina, Irene and Gerard, I'm wishing you all the best for your future crosstalk experiments. And then there are many more that left a great mark on my time spend as PhD, including Aditya, Ali, Ashmiani, Bart, Florian, Gitta, Ian, James, Karin, Liza, Magdalena, Marian, Michal, Nemo, Nicholas, Nuria, Reza, Roland, Rosalie, Stef, Yash, and many more...

I want to specifically thank the heroes of my thesis, namely the technicians that came running whenever I needed help with proteins, microscopes, or water coolers: Andrea, Anne, Eli, Esengül, Hinco, Jan-Bonne, Jeffrey, Jeremy, Marjolein, Marko, Simone, Yvonne, and Vanda. Also thanks to Jolijn and Esther for their great help in conquering bureaucratic jungles.

Over the years, I've also met many others that I want to thank for making AMOLF a fun place to work. Maria and Olga, thanks for your sweet and loving support, and I'm looking forward to visiting you wherever you move. Nicola and Jeanette, thanks for your warm welcomes in the office (and fun trips in Paris and Brussel). Sebastian, for the fun you brought in our office. Yao, for explaining us Chinese words and talking about your cycling trips. Harmen, for our walks in Utrecht and your dancing at Veldhoven. Mathijs, for your enthusiasm to open doors by foot. Wiebe and Juliette, for the small talks at the coffee corner and reception. And many more that I no doubt forgot to mention. Also the people I've met during Physiology Course 2017, I want to thank greatly for all their inspiration and views on both science and life. Specifically, Caitlin and the Euro-gang.

In addition, I'm very fortunate to also have a loving group of friends around me, including the 'Good Old Days' (Kim, Nicky, Judith, and all their little ones), the 'The Hague gang' (Roos, Milou, Emiel, Casper, Marley, Eric, Thijs), Max&Tessa and many more. Thanks for your love, laughs and support.

Gwendolyn en Lucas, papa en mama, 'k zie jullie graag. En Ruben: voor alles.

&